Prestatiegericht ontwerp van hydrotalcietgebaseerde bimetallische katalysatoren voor ethanoldehydrogenatie

Performance Based Design of Hydrotalcite-Based Bimetallic Catalysts for Ethanol Dehydrogenation

Jolien De Waele

Promotoren: prof. dr. ir. J. W. Thybaut, dr. V. Galvita
Proefschrift ingediend tot het behalen van de graad van
Doctor in de ingenieurswetenschappen: chemische technologie

UNIVERSITEIT
GENT

Vakgroep Materialen, Textiel en Chemische Proceskunde
Voorzitter: prof. dr. P. Kiekens
Faculteit Ingenieurswetenschappen en Architectuur
Academiejaar 2017 - 2018

ISBN 978-94-6355-139-7
NUR 952
Wettelijk depot: D/2018/10.500/57

Examencommissie:

Prof. Dr. Ir. Daniël De Zutter, voorzitter	Universiteit Gent
Dr. Hilde Poelman, secretaris	Universiteit Gent
Prof. Dr. Ir. Mark Saeys	Universiteit Gent
Prof. Dr. Pascal Van Der Voort	Universiteit Gent
Prof. Dr. Ir. Michiel Dusselier	KU Leuven
Dr. Evgeniy Redekop	University of Oslo
Prof. Dr. Ir. Joris W. Thybaut, promotor	Universiteit Gent
Dr. Vladimir V. Galvita, promotor	Universiteit Gent

Universiteit Gent

Faculteit Ingenieurswetenschappen en Architectuur

Vakgroep Materialen, Textiel en Chemische Proceskunde

Laboratorium voor Chemische Technologie

Technologiepark 914

B-9052 Zwijnaarde

België

Tel.: +32 (0)9 331 17 57

Fax.: +32 (0)9 331 17 59

http://www.lct.ugent.be

The research leading to these results has received funding from the European Research Council under the European Union's Seventh Framework Programme (FP7/2007-2013) / ERC grant agreement n° 615456, from the 'Long Term Structural Methusalem Funding by the Flemish Government' and from the IAP 7/05 Interuniversity Attraction Poles Programme – Belgian State – Belgian Science Policy.

Acknowledgements - Dankwoord

Op het einde van een doctoraat is het gebruikelijk terug te blikken op de afgelopen 4 jaar. In 4 jaar ben ik, zowel op persoonlijk als op wetenschappelijk vlak, enorm geëvolueerd. Mijn leven en levensdoelen zijn gewijzigd en dit is mede dankzij dit doctoraat. Daarom zou ik hier graag de mensen bedanken die, op welke manier dan ook, bijgedragen hebben aan dit werk.

Vooreerst zou ik prof. Marin willen bedanken om me toe te laten een doctoraat aan te vangen op het Laboratorium voor Chemische Technologie. Daarnaast zou ik graag mijn promotoren Joris en Vladimir bedanken. Joris, bedankt om mij de vrijheid te geven alle mogelijke analyses te doen en apparaten te gebruiken die op dat moment gepast leken om mijn onderzoek verder te zetten. Door deze vrijheid kijk ik heel tevreden terug op de resultaten die behaald geweest zijn. Voorts ook bedankt voor het nalezen van mijn artikels, abstracten,… al dan niet als advocaat van de duivel. Vladimir, thank you for your tremendous input in all scientific work. Whenever I was stuck, unhappy about the results or just lost in what they meant, you were always there to give an answer or to calm me down. I have learnt a great deal about the magic of catalyst synthesis and characterization and you have given me real insight and fun in solving the puzzle on what the catalyst looks like.

Hilde, bedankt voor de hulp bij verschillende karakterisatiemethoden of resultaten en om mijn artikels met zoveel zorg na te lezen. Jouw logica en structuur heeft me veel geleerd over hoe een artikel best opgebouwd wordt en hoe zwaktes in een artikel vastgelegd kunnen worden. Ook bedankt aan Jenoff en prof. Saeys voor de samenwerking aan het verhaal over het effect van water. I would also like to thank prof. Damyanova and prof. Gabrovska for the collaboration on the NiCu catalysts.

Een special woordje van dank gaat uit naar de technische dienst van het LCT: Bert, Michaël, Wim, Brecht, Tom, Georges, Erwin, Hans en Lambert. Jullie hebben me waarschijnlijk meermaals verwenst als ik nog maar eens langskwam met een probleem aan één van de opstellingen. Bedankt om deze altijd zo vakkundig en snel op te lossen. Mijn doctoraat had zonder jullie nog lang niet af geweest.

I would like to thank the people from the two groups I was a part of. I would like to thank Vladimir's group for the kindness in which we exchanged reservations on characterization equipment and for the discussion I had with every one of you about results or procedures. A special thanks to Lukas for the TEM time and to Rakesh for the TAP experiments. I would like to thank the CaRE-group for the fruitful discussions during the CaRE-lunches and for the successful and fun CaRE-events. More specifically, I would like to thank my office buddies. I've had many over the years, but I'm grateful for all of them: Bart, Kenneth, Tapas, Roxanne, Naghmeh, Laura, Mostafa and Pedro. I would like to give a special notice to Laura, Mostafa and Pedro for being so work-minded at work, but being so open and social after work in our 'Office Dinners'.

Ik zou ook graag Geraldine bedanken voor haar algemene interesse in mijn doctoraat en leven en voor de leuke tijd die we, samen met Florence, hadden tijdens de lessen van Ingenieursproject I. Ook Florence, bedankt voor je enthousiasme voor dit vak en de leuke babbels tijdens de les.

Alexandra and Daria, I would like to mention both of you separately, since we were the HTK-1 musketeers together. Thank you for the fruitful collaboration we had there. Both when solving problems as for doing favors, we were a true team.

Bedankt ook aan mijn twee thesisstudenten Bram en Maxime. Beiden waren jullie aangename studenten om te begeleiden, zeer gedreven en verstandig. Bram heeft zijn stap al gemaakt naar de industrie, voor Maxime hoop ik dat hij ook een job vindt die hem met plezier 's morgens doet opstaan.

Daarnaast zou ik graag de mensen van de koffie- en middagpauze bedanken, voor de leuke babbels en een uitlaatklep te zijn voor eventuele kleine frustraties. Bedankt dus Jeroen P., Stephanie, Lukas, Pieter R., Alexandra, Brigitte, Anton, Florence, Lies, Alexander, Jens, Stijn, …

Bedankt aan mijn vrienden, voor onze vele etentjes of uitstapjes. Ook voor jullie luisterend oor voor al mijn frustraties of gloriemomenten. Bedankt dus aan Evi, Renée, Thibault, Stefaan, Karlijn, Charlotte, Emma, Stephanie, Sven, Timothy, Maxime,…

Na al deze bedankjes komen nu de belangrijkste mensen aan bod. Mama, papa en zus, bedankt voor alle mogelijkheden, voor de steun, niet 4 jaar, maar al bijna 27 jaar lang. De situatie is sinds 4 jaar wat veranderd omdat ik nu niet meer officieel thuis woon, maar jullie zijn wel mijn thuis en we, Jonas en ik, komen heel graag bij jullie. Ook bedankt aan de ouders van mijn liefje, ook bij jullie staat de deur altijd open voor ons en dat appreciëren we heel erg.

Dit brengt me bij de allerbelangrijkste persoon, Jonas. Schat, ik kan je niet genoeg bedanken voor alle steun, voor een luisterend oor voor mijn frustraties of als ik vastzat met resultaten, … maar ook voor jouw kalmte, jouw kritische kijk en voor jouw (flauwe) humor. Ik zie je graag!

Jolien

Lente 2018

Table of Contents

List of Figures

List of Tables

List of Symbols

1. *Roman symbols*

(1-b)	Fraction of the catalyst bed occupied by the catalyst (m_p^3 m_B^{-3})
a	Correction factor for the number of carbon atoms (-)
A	Pre-exponential factor (s^{-1})
a_s	Specific external surface area (m_i^2 kg_{cat}^{-1})
a_v	Volumetric interface surface area (m^2_i m^{-3}).
b	Maximum dilution degree (m^3_{inert} $m^{-3}_{inert+cat}$)
b	Parameter estimation matrix (-)
b_i	Estimated parameter of β_i (-)
C	Concentration (%)
$C_{A,b}$	Concentration of A in the bulk (mol m_f^{-3})
$C_{A,s}$	Concentration of A at the external surface (mol m^{-3})
C_M	Amount of Cu atoms in one m^2 of metal Cu ($1.47\ 10^{19}$ atoms m^{-2})
$C_{tot,DH}$	Number of active dehydrogenation sites (mol kg_{cat}^{-1})
D_A	Molecular diffusion coefficient (m_f^2 s^{-1})
D_{AB}	Gas phase molecular bond energy (kJ mol^{-1})
D_{eA}	Effective diffusion coefficient, corrected with the porosity and tortuosity of the pellet (m^2 s^{-1})
d_p	Pellet diameter (m)
d_t	Reactor (tube) diameter (m)
E_a	Activation energy (J mol^{-1})
F_i	Molar outlet flow rate of compound i (mol s^{-1})
$F_{i,j}$	Experimentally measured response (mol s^{-1})
$\hat{F}_{i,j}$	Calculated response (mol s^{-1})
h	Planck's constant ($6.626\ 10^{-34}$ m^2 kg s^{-1})
j_D	J factor of Chilton and Colburn (-)
K	Equilibrium coefficient (Pa^{-1})
k	Rate coefficient (s^{-1})
k_B	Boltzmann constant ($1.38\ 10^{-23}$ m^2 kg s^{-2} K^{-1})
k_{fA}	Mass transfer coefficient (m_f^{-3} m_i^{-2} s^{-1})
L	Length of the reactor (m)

M	Molar mass (kg mol^{-1})
Mol_{H2}	Number of mol H_2 adsorbed (mol)
n	Reaction order (-)
n	Coordination number of site (-)
n	Number of experiments (-)
N_A	Constante of Avogadro (6.02 10^{23} atoms mol^{-1})
N_A	Avogadro constant (6.022 10^{23} mol^{-1})
N_{AC}	Number of active sites (mol s^{-1})
n_e	Number of repeat experiments (-)
n_{ek}	Number of repeat experiments with the same reaction conditions (-)
p	Pressure (Pa)
p	Number of unknown parameters (-)
Pe'_a	Peclet number (-)
p_{tot}	Total pressure (Pa)
Q	Atomic chemisorption enthalpy (kJ mol^{-1})
Q_{0A}	Atomic chemisorption enthalpy of top site (kJ mol^{-1})
Q_A	Atomic chemisorption enthalpy of a n-fold coordination site (kJ mol^{-1})
Q_{AB}	Chemisorption enthalpy of molecule AB (kJ mol^{-1})
R	Universal gas constant (8.314 J K^{-1} mol^{-1})
r	Number of sets of reaction conditions with repeat experiments (-)
R^2	Multiple correlation coefficient (-)
Re_p	Reynolds number of particle (-)
R^{ins}	Intrinsic rate of formation (mol kg^{-1}_{cat} s^{-1})
R^{obs}	Observed rate of formation (mol kg^{-1}_{cat} s^{-1})
r_v^{obs}	Observed volumetric rate of formation (mol m^{-3}_{cat} s^{-1})
r_w^{obs}	Rate of consumption of A per mass of catalyst (mol kg_{cat}^{-1} s^{-1})
$s(b_i)$	Estimated standard deviation on b_i (-)
Sc	Schmidt number defined as $\mu (\rho D_A)^{-1}$.
s_e^2	Pure-error sum of squares (-)
SF	Stoichiometric factor (2)
S_i	Selectivity of compound i (-)
SK	Constant depending on shape of Cu (6)
S_{trans}	Translational entropy (J K^{-1} mol^{-1})
STY_{AcH}	Space time yield of acetaldehyde (mol_{AcH} (s mol_{metal})$^{-1}$)
T	Temperature (K)
T	Matrix transposition operator

T_b	Bulk temperature (K)
TOF	Turn-over frequency (s^{-1})
T_{wi}	Internal wall temperature (K)
u	Velocity (m s^{-1})
W	Catalyst mass (kg_{cat})
w	Weigh factor (-)
W_{Cu}	Cu loading (wt%)
X	Independent variable matrix (-)
X_A	Conversion (-)
X_{dil}	Conversion obtained with diluted bed (-)
y	Observed dependent variable matrix (-)
$\hat{\mathbf{y}}$	Calculated dependent variable matrix (-)
y_{fA}	Film factor (mol fraction)
y_{jk}	Experimental response of experiment j at set of reaction conditions k (-)
z_{DH}	Number of nearest neighbors (-)
Δp	Pressure drop (Pa)
$\Delta_r H$	Reaction enthalpy (J mol^{-1})
$\Delta S^{\ddagger}$	Activation entropy (J K^{-1} mol^{-1})
$\bar{y}_k$	Mean of the repeat experiments at set of reaction conditions k (-)

2. *Subscripts*

-	Backwards reaction
*	Free sites
+	Forward reaction
Ac	Acetyl
AcH	Acetaldehyde
C	Carbon
DC	Decomposition sites
DH	Dehydrogenation sites
EtAc	Ethyl acetate
EtO	Ethoxyl
EtOH	Ethanol
H	Hydrogen atom
H	Hydrogen

H_2	Hydrogen gas
O	Oxygen
surf	Surface

3. Greek symbols

$(1-\varepsilon_B)$	Fraction of the reactor volume occupied by the catalyst bed ($m_B^3\ m_r^{-3}$);
μ	Dynamic viscosity (kg $m_r^{-1}\ s^{-1}$)
$Ø_{av}$	Average diameter (nm);
α	Heat transfer coefficient (W $m_i^{-2}\ K^{-1}$);
α_w	Heat transfer coefficient between bed and reactor wall ($Wm_r^{-2}K^{-1}$)
β	True parameter value
θ	Molar fraction (-)
θ_{DH}	Ratio of dehydrogenation active sites to the total number of active sites (-)
λ_{er}	Effective radial heat conductivity of the catalyst bed ($Wm_r^{-2}K^{-1}$)
λ_p	Heat conductivity of the catalyst pellet (W $m^{-1}\ K^{-1}$).
ρ	Density of the gas phae (kg m_f^{-3})
ρ_{Cu}	Density of Cu (8.92 g cm^{-3})
$\rho_{i,j}$	Binary correlation coefficient
ρ_p	Density of the pellet (kg m^{-3});
σ_{ii}^2	Element i,i of the covariance matrix (-)
ϕ_m	Total mass flux (kg $m_r^{-2}\ s^{-1}$)

4. Abbreviations

ALD	Atomic Layer Deposition
BET	Brunauer-Emmett-Teller
CO-DRIFTS	Carbon monoxide - Diffuse Reflectance Infrared Fourier Transform Spectroscopy
DFT	Density Functional Theory
EDX	Energy dispersive X-ray spectroscopy
EXAFS	Extended X-ray Absorption Fine Structure
FCC	Face Centered Cubic (Structure)
FTIR	Fourier Transformed Infrared (Spectrometry)

HTK-MI	High Throughput Kinetics - Mechanistic Investigation
ICP-OES	Inductively Coupled Plasma-Optical Emission Spectroscopy
STEM	Scanning transmission electron microscopy
STY	Space Time Yield
TAP	Temporal Analysis of Products
TCD	Thermal Conductivity Detector
TPO	Temperature Programmed Oxidation
TPR	Temperature Programmed Reduction
VASP	Vienna ab initio package
XANES	X-ray absorption near-edge structure
XAS	X-ray absorption spectroscopy
XPS	X-ray photoelectron spectroscopy
XRD	X-Ray Diffraction

Glossary

Activation energy	For an elementary step, the difference in internal energy between transition state and reactants. A measure for the temperature dependence of the rate coefficient.
Active site	The region of a catalyst where adsorbate molecules bind and undergo a chemical reaction.
Adsorption	The preferential concentration of a species at the interface between two phases. Adherence of the atoms, ions or molecules of a gas or liquid to the surface of another substance.
Alloy	A material that it is made by mixing two or more metals, or a metal and another substance. The structure of alloy can vary according to the environment i.e. well mixed, core-shell etc.
Arrhenius relation	Expresses the dependence of a rate coefficient k corresponding with a chemical reaction on the temperature T and activation energy, Ea: $k=A \exp(E_a/RT)$ with R the universal gas constant, T the temperature and A the pre-exponential factor.
As prepared	The catalyst before calcination.
Average turnover frequency	The number of molecules reacting per active site per unit time. Average because we can't assume that every active site has the same activity.
Azeotrope	Or a constant boiling point mixture is a mixture of two or more liquids whose proportions cannot be altered or changed by simple distillation.
Catalyst	Substance or material, which through repeated cycles of elementary steps, accelerates the conversion of reagents into products. Catalysts are classified into homogeneous, which are in the same phase with the reagents (e.g. acids and bases, metal complexes, etc.), and heterogeneous, which are separated from the reactants by an interface (e.g. metals, metal oxides, etc.). Here, reduced, active material.
Chemisorption	Also known as chemical adsorption. Adsorption in which the forces involved are valence forces of the same kind as those operating in the formation of chemical compounds. Chemisorption strongly

	depends on the surface and the adsorbed species, and only one layer of chemisorbed molecules is formed. Its energy of adsorption is the same order of magnitude as in chemical reactions, and the adsorption may be activated.
Coking	Build-up of carbon depositions during reaction.
Conversion	Measure for the amount of a reactant that has been transformed into products as a result of a chemical reaction.
Coprecipitation	In chemistry, coprecipitation or co-precipitation is the carrying down by a precipitate of substances normally soluble under the conditions employed.
Cycled reduction	A series of H_2-air-H_2-air-H_2 treatments at 823K.
Deactivation	The decrease in conversion in a catalytic reaction with time of run under constant reaction conditions.
Decomposition sites	Sites on which the major reaction is decomposition, i.e., Pd and Ni sites.
Dehydration	A chemical reaction that involves the removal of water from an organic molecule.
Dehydrogenation	A chemical reaction that involves the removal of hydrogen from an organic molecule.
Dehydrogenation sites	Sites on which the major reaction is dehydrogenation, i.e., PdZn, Cu or NiCu sites.
Density of states	Describes the number of states per interval of energy at each energy level available to be occupied.
Dispersion	The level in which active sites are distributed over the catalyst surface.
Elementary step	The irreducible act of reaction in which reactants are transformed into products directly, i.e., without passing through an intermediate that is susceptible to isolation.
Gas chromatography	The process in which the components of a mixture are separated from one another by injecting the sample into a carrier gas which is passing through a column or over a bed of packing with different affinities for adsorption of the components to be separated.
Hydrogen spillover	Spillover involves the transport of active species sorbed or formed on a first surface onto another surface that does not, under the same conditions, sorb or form the active species.

Intermetallic compound	An intermetallic compound is a solid-state compound exhibiting metallic bonding, defined stoichiometry and ordered crystal structure.
Kirkendall effect	The motion of the interface between two metals that occurs as a consequence of the difference in diffusion rates of the metal atoms.
Material	Synthesized, unactive powder.
Oligomerization	A chemical reaction that involves the linking of small molecules into bigger ones with repeating units.
One-pot synthesis	Catalyst synthesis that proceeds in one step.
Parity diagram	A 2-dimensional scatter plot in which the model calculated values of the responses are displayed against the experimentally observed values.
Pre-exponential factor	The temperature-independent factor of a rate coefficient, also called the frequency factor.
Pseudo-steady state	Its mathematical expression is that the time rate of change of the concentration of all active centres in a reaction sequence is equal to zero.
Regeneration	Regeneration is renewal through the internal processes of a body or system. Here, applying a procedure to make the catalyst active again.
Selectivity	Measure for the amount in which a product is formed from the reactants as a result of a chemical reaction.
Single reduction	One H_2 treatment at 823K.
Sintering	Coalescence of separate metal particles to become one bigger particle.
Structure-activity relationships	The relationship between the chemical structure of a molecule and activity
Support	Also called carrier. Material, usually of high surface area, onto which the active catalytic material, present as the minor component, is dispersed. The support may be catalytically inert, but it may contribute to the overall catalytic activity.
Turnover frequency	The number of molecules reacting per active site per unit time.
Wet incipient impregnation	Also called capillary impregnation or dry impregnation, is a commonly used technique for the synthesis of heterogeneous catalysts. Typically, the active metal precursor is

dissolved in an aqueous or organic solution. Then the metal-containing solution is added to a catalyst support containing the same pore volume as the volume of the solution that was added.

Summary

The current chemical industry essentially relies on fossil resources. However, evermore processes are developed that start from bio-based resources for the production of fuels and/or chemicals. Bio-ethanol production for blending with gasoline is a well-known example, but it can also serve as a feed for chemicals production. It is mainly produced via fermentation of sugar cane, sugar beet, or corn, i.e., feeds which are in competition with the food supply. Alternative bio-ethanol sources are to be found in agricultural waste.

Bio-ethanol contains at least 85% water. This represents a major challenge because water is a well-known inhibitor for many catalytic reactions. To remove all water from bio-ethanol, energy intensive separation processes are required, particularly due to the azeotrope between ethanol and water. This issue could be mitigated if bio-ethanol could be converted to acetaldehyde, since the latter does not form an azeotrope with water. This requires a hydrothermally stable catalyst, however.

Two routes are available for ethanol dehydrogenation to acetaldehyde, i.e., a direct one with hydrogen as a byproduct, and an oxidative one with water as byproduct. Both routes have advantages and disadvantages. In the present thesis the direct dehydrogenation is preferred, mainly because the produced hydrogen is considered as a valuable byproduct and the reaction conditions are milder than for the oxidative dehydrogenation.

To avoid the formation of diethyl ether and other acid catalyzed reaction products, a rather basic support is recurred to, i.e., hydrotalcite-based mixed oxides. Such supports have the advantage that nanoparticle active sites can be formed on the surface of this support via *incorporation* of the active metals in the support upon synthesis, which diffuse to and form nanoparticles on the surface upon calcination and reduction.

Cu-based catalysts are typically used for such dehydrogenation reactions. Their advantages are the high acetaldehyde yield that can be achieved and their relatively low catalyst cost. They suffer severe irreversible deactivation, however, due to sintering of the active particles. To mitigate this issue, bimetallic catalysts are recurred to since they can mimic the catalytic behavior of a monometallic one while improving, e.g., its stability. PdZn intermetallic catalysts were tested first, since it was reported that the density of states of PdZn resembled that of Cu. Similar catalytic properties can, hence, be expected but with an improved stability due to the presence of Zn atoms which prevent sintering.

First, the effect of activation procedure on the catalyst performance was investigated. For this, a 1wt%Pd-1.2wt%Zn/Mg(Al)(Pd)(Zn)O_x catalyst was synthesized via the incorporation of Pd and Zn in the support. Two activation procedures were tested, i.e., single reduction and cycled reduction. Single reduction corresponds with a one-step reduction at 823K with H_2. Cycled reduction entails a reduction-oxidation treatment which comprises consecutive H_2 - air treatments at 823K. Via detailed catalyst characterization, it was found that the formation of the PdZn alloy active particle is enhanced via the use of cycled reduction as activation procedure. Furthermore, the number of active sites increased due to the extraction of all incorporated active metals from the support thanks to cycled reduction. The formation process of an active particle upon single and cycled reduction is schematically represented in Figure 1. Steps a to d correspond with single reduction. After calcination, all active metals are present in the support and some ZnO is already present on the surface. Upon reduction, Pd^{2+} is first extracted from the support and reduces immediately to Pd. Then Zn^{2+} also diffuses from the support to the surface and, via hydrogen spillover from Pd, reduces to Zn. Meanwhile, Zn diffuses into the Pd particle with the formation of a PdZn shell with a Pd core. When applying an oxidation treatment, as in cycled reduction, Zn is extracted from the PdZn particle with the formation of small ZnO islands on the Pd particle. The diffusion length of ZnO to Pd is thus shortened and subsequent reduction improves the formation of a homogeneous PdZn alloy particle, see Figure 1 e to f. Two cycles are sufficient to form such a homogeneous particle.

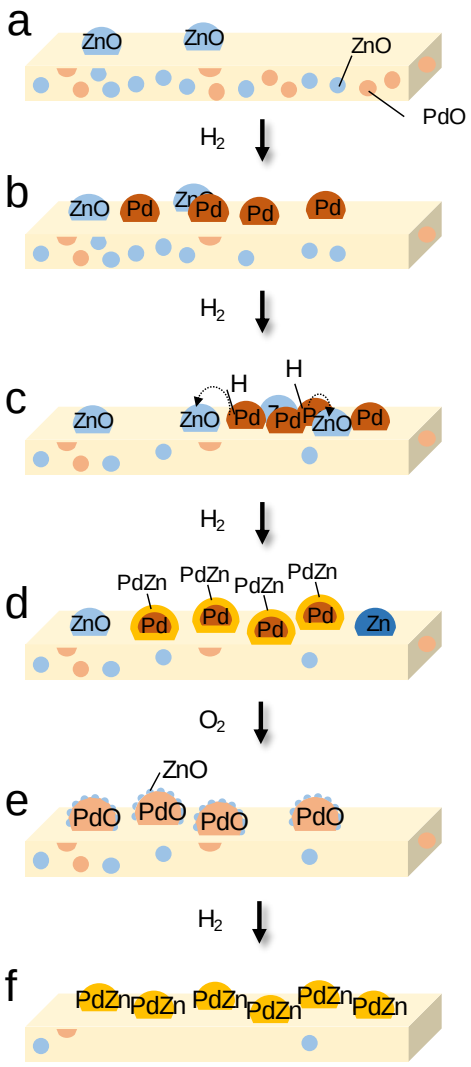

Figure 1: Representation of the formation of the intermetallic compound during single reduction (a-d) and cycled reduction (a-f) at 823K for PdZn/Mg(Al)(Pd)(Zn)O_x. dark orange: Pd, light blue: ZnO or $ZnAl_2O_4$, light orange: PdO, gold: intermetallic compound PdZn.

The above sketched nanoparticle catalyst formation also explains the catalyst behavior. For both activation procedures, an initial activity loss coinciding with an increased acetaldehyde selectivity was observed and attributed to the formation of cokes on adjacent Pd sites. Cokes were formed via acetaldehyde decomposition on the Pd sites to methane and carbon monoxide with subsequent carbon formation from methane and carbon monoxide. When these sites are blocked, only the PdZn sites remain which are active for acetaldehyde formation and not at all for decomposition into methane and carbon monoxide. Overall, cycled reduction gave rise to the most stable PdZn/Mg(Al)(Pd)(Zn)O_x catalyst with a turn-over frequency of 7 mol_{EtOH} $(mol_{Pd}\ s)^{-1}$.

Secondly, the effect of synthesis method on the catalyst performance was investigated. The PdZn hydrotalcite-based catalyst was prepared via two methods. The first one is the synthesis of the pure $Mg(Al)O_x$ support and addition of Pd and Zn via wet incipient impregnation. The second one is the incorporation of Pd and Zn in the support during its synthesis. It was found that impregnation gives rise to bigger active particles. This renders the formation of a homogeneous alloy particle more difficult and, hence, even after cycled reduction, still a core-shell particle remains. Furthermore, active metal losses were found for the impregnated catalyst. This is attributed to the weak interaction of the active metals with the support due to the impregnation. Upon regeneration of the catalyst via cycled reduction, cokes are burnt off during oxidation, resulting in a local hotspot that enables the evaporation of Pd and Zn. Metal losses may not only occur under oxidative conditions. Also upon reduction, via the formation of PdH which has a lower evaporation temperature, a certain amount of Pd may be lost. Overall, the incorporated $PdZn/Mg(Al)(Pd)(Zn)O_x$ catalyst gives rise to the most active catalyst.

Considering the intended use of bio-ethanol, the effect of water on the catalyst performance was assessed by employing a 30wt% H_2O/ethanol feed. The activity and acetaldehyde selectivity decreased as compared to the original activity with pure ethanol, see Figure 2. Upon restoring the pure ethanol feed, the activity and selectivity only recovered partially. Regeneration via cycled reduction was required to fully restore the original acetaldehyde selectivity. Detailed characterization methods as well as DFT calculations were used to assess the phenomena occurring in the presence of water. It was found that ZnO patches are formed on Pd-rich PdZn particles. The hydrogen produced via reaction is insufficient to completely restore the PdZn particles to their original state. Only a regeneration procedure allows to fully recover the PdZn intermetallic particle.

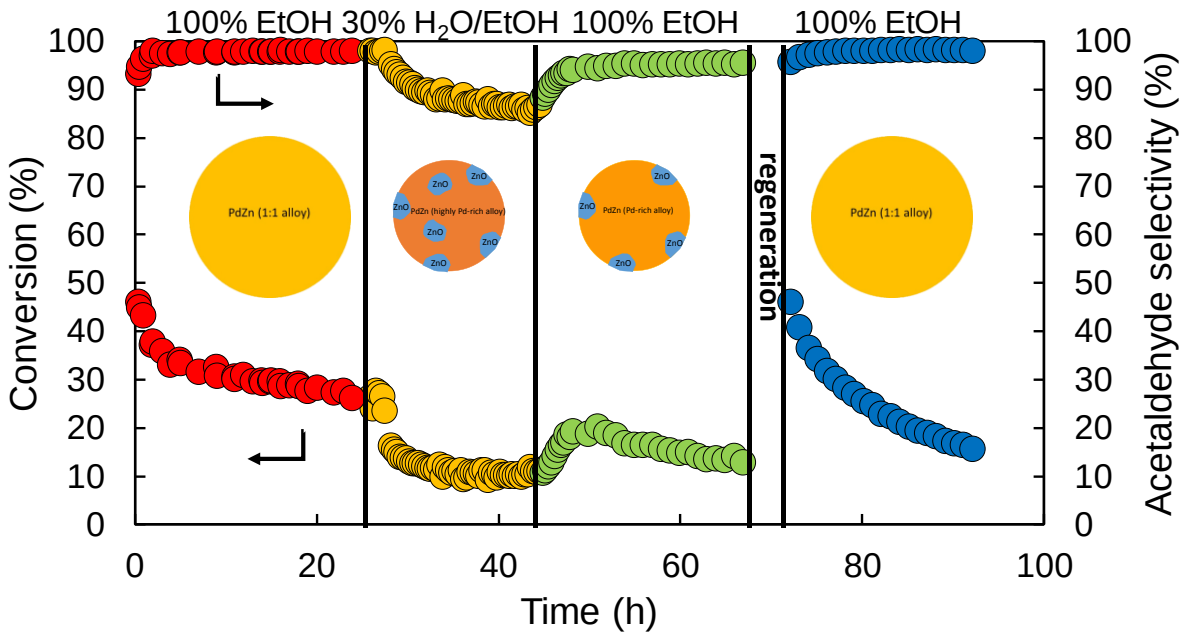

Figure 2: Performance curves of PdZn/Mg(Al)(Pd)(Zn)O_x for subsequently 100wt% ethanol (red), 30wt% H_2O/ethanol (yellow), 100wt% ethanol after water feed (green), 100wt% ethanol after regeneration (blue). The circles represent the catalyst topology at the different stages.

Combining the insight gained from the above-described activities on the PdZn catalysts, it is clear that the dehydrogenation reaction only occurs on Pd sites. Zn is inactive for bio-ethanol dehydrogenation and only serves as a buffer to avoid the presence of two adjacent Pd sites and to change the activity of the Pd sites. Indeed, such adjacent Pd-sites give rise to unwanted products such as methane, carbon monoxide and cokes. To improve the catalyst activity, it would be worthwhile to synthesize a bimetallic catalyst with two metals which are both active for dehydrogenation such as Ni and Cu. Both elements however suffer from deactivation, i.e., by coking and sintering. By alloying the two metals, both deactivation mechanisms may be avoided. Seven NiCu/Mg(Al)(Ni)(Cu)O_x catalysts were tested, all with a different Ni/Cu-ratio. Also a Cu/Mg(Al)(Cu)O_x was synthesized to be able to compare the activity. It was found that the presence of Ni does improve the activity and acetaldehyde selectivity and has comparable stability as the Cu/Mg(Al)(Cu)O_x catalyst. This Cu catalyst is, moreover, also more stable than the typical Cu-based catalyst that was found in literature. The catalyst activity as a function of time on stream of all catalysts exhibits two regimes: a fast deactivation within the first hours and, subsequently,

a more moderate one, see Figure 3. The fast deactivation was attributed to coking, whereas sintering was identified as the cause for the slow deactivation. For the best catalyst, i.e., 1wt%Ni-10wt%Cu/Mg(Al)(Ni)(Cu)O_x, no rapid deactivation regime occurred. FTIR measurements showed that for this catalyst, more Ni was present in the alloy, whereas for other catalysts Ni particles occurred separate from Cu. Therefore, most likely no adjacent Ni sites were present on this best catalyst, which prevented the decomposition of acetaldehyde to methane and carbon monoxide and subsequently further to cokes. Thus, similar phenomena as on PdZn catalysts also occur on the NiCu catalysts. When investigating the effect of a water containing feed on the NiCu catalysts, it was found that the conversion increased upon changing the feed from pure ethanol to 30wt%H_2O/ethanol. This was attributed to removal of cokes from the active sites via activation of H_2O on Cu sites. In general, the NiCu catalysts didn't outperform the PdZn catalysts based on TOF, but they do have the highest industrial potential: the cost of the NiCu catalysts is 400 times lower, even with the highest Ni and Cu loading investigated here and the conversion is higher than for the PdZn catalyst. Furthermore, the NiCu catalysts improve upon the presence of water.

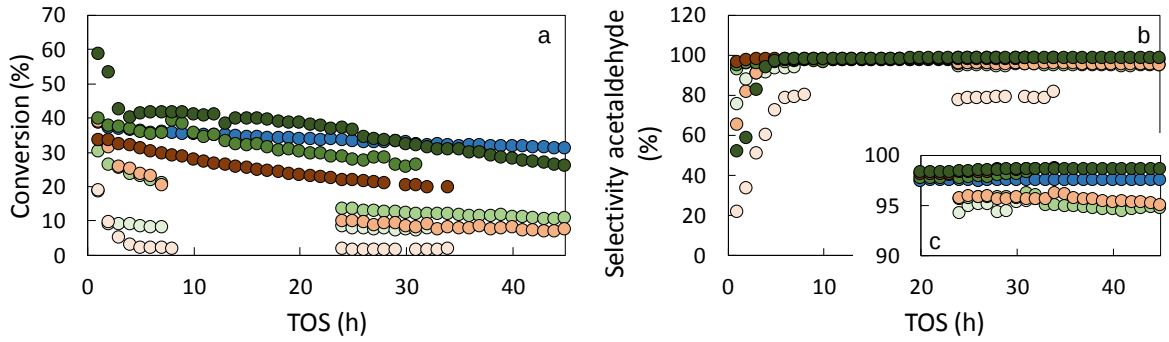

Figure 3: Performance curves for 10wt%Cu/Mg(Al)(Cu)O_x (blue), 0.5wt%Ni-Xwt%Cu/Mg(Al)(Ni)(Cu)O_x (X=0,5,10) (red, light->dark=higher Cu loading), 1wt%Ni-Xwt%Cu/Mg(Al)(Ni)(Cu)O_x (X=0,5,10,20) (green, light->dark=higher Cu loading). a: conversion, b: acetaldehyde selectivity, c: zoom on acetaldehyde selectivity.

The complete alloying of Ni and Cu for the 1wt%Ni-10wt%Cu/Mg(Al)(Ni)(Cu)O_x was supported by kinetic modelling. A generic kinetic model was constructed which could allow reproducing the steady-state behavior on all investigated catalysts. Two types of sites were

considered, i.e., the dehydrogenation sites such as PdZn, Cu and NiCu, and the decomposition sites such as Pd and Ni. To reduce the number of adjustable parameters in the model, the adsorption and reaction enthalpies were calculated via the UBI-QEP method. In this method, the adsorption enthalpy of all compounds is expressed in terms of the atomic chemisorption enthalpy of H, C and O. Non-linear regression to 41 experimental data points was performed to estimate the remaining 17 model parameters. All estimates were physically meaningful and statistically significant. More particularly, the values obtained for the atomic chemisorption enthalpies were in line with literature reported values. The amount of 'free' Ni sites, i.e., adjacent Ni sites which can contribute to the decomposition reaction, is indeed small, i.e., only 8%. The reaction path analysis showed that once ethanol is adsorbed on the surface, it is instantaneously converted into acetaldehyde on the dehydrogenation sites. It subsequently desorbs and/or moves to the decomposition sites where it is transformed into methane and carbon monoxide.

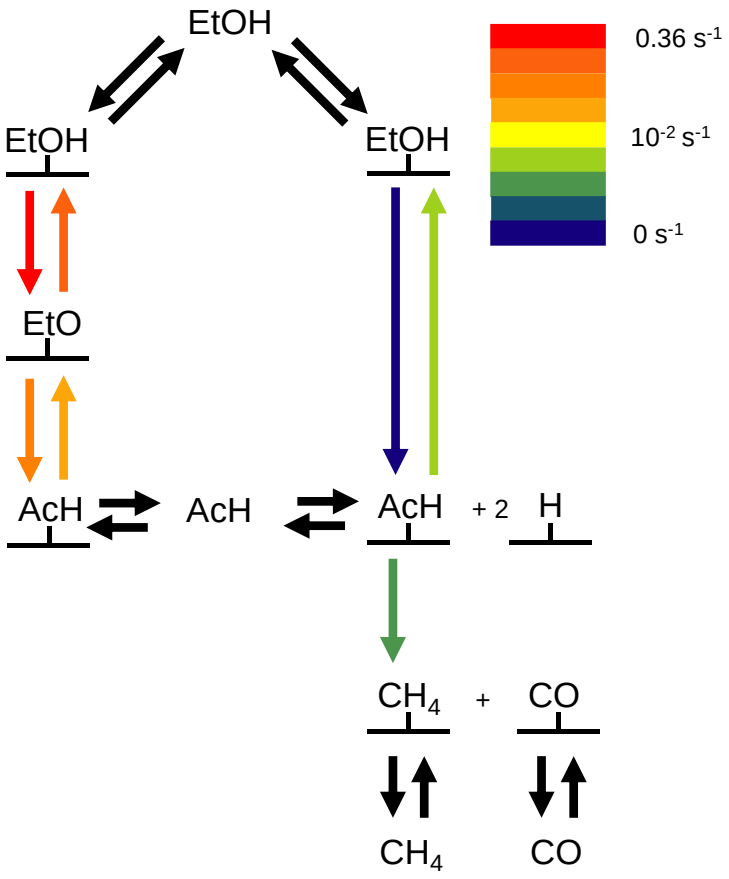

Figure 4: Reaction path analysis at T=533K, P_{tot}=0.5MPa, W/F_{EtOH}=3.6kg_{cat} s mol^{-1}. The colors represent the relative rates, i.e., dark red=high rate → dark blue=low rate.

In general, the use of bimetallic catalysts for ethanol dehydrogenation has been investigated by acquiring insight in the fundamental phenomena that occur during synthesis and activation of the catalyst. Via the investigation of the effect of water on both catalysts, the industrial potential of the materials is evaluated. Via more elaborate kinetic modelling efforts, also in-silico guidelines might be put forward to further improve the catalyst performance.

Samenvatting

De huidige chemische industrie is volledig gebaseerd op fossiele grondstoffen. Er zijn echter meer en meer initiatieven die bio-gebaseerde grondstoffen gebruiken voor de productie van biobrandstoffen en chemicaliën. Een gekend voorbeeld is het mengen van bio-ethanol met benzine, maar ook chemicaliën kunnen geproduceerd worden uit bio-ethanol. Vaak wordt dit geproduceerd via de fermentatie van suikerriet, suikerbiet en maïs. Deze grondstoffen zijn echter in competitie met de voedselindustrie en bijgevolg ethisch bekritiseerd. Het gebruik van andere grondstoffen zoals landbouwafval is dus aangewezen.

Bio-ethanol bevat bij productie minstens 85% water. Dit is een enorme uitdaging aangezien water een gekende vertrager van vele katalytische systemen is. Om alle water van ethanol te scheiden zijn energie-intensieve processen vereist omdat ethanol en water samen een azeotroop vormen. Deze kwestie kan omzeild worden als bio-ethanol omgezet wordt tot acetaldehyde aangezien water en acetaldehyde geen azeotroop vormen. Maar, dan moet wel een hydrothermisch stabiele katalysator gevonden worden.

Er bestaan twee reactiepaden voor de productie van acetaldehyde via ethanol dehydrogenering: het directe pad met waterstof als bijproduct of de oxidatieve route met water als bijproduct. Beide routes hebben voor- en nadelen, maar hier wordt de directe dehydrogenering onderzocht aangezien waterstof een waardevol bijproduct is en omdat de reactiecondities milder zijn dan voor de oxidatieve dehydrogenering.

Om de productie van diethylether en andere zuurgekatalyseerde reactieproducten te vermijden, wordt gebruik gemaakt van een basische drager. Hydrotalcietgebaseerde gemengde oxides komen in aanmerking aangezien actieve nanodeeltjes gevormd kunnen worden aan het

oppervlak van de drager via bijmenging van de actieve bestanddelen bij de synthese van de drager en diffusie van de actieve elementen naar het oppervlak bij calcinatie en reductie.

Voor de dehydrogeneringreactie worden typisch kopergebaseerde katalysatoren gebruikt. De voordelen zijn een hoge acetaldehydeopbrengt en een lage katalysatorkost. Ze zijn echter erg gevoelig voor irreversibele deactivatie door sinteren van de actieve deeltjes. Om dit op te lossen worden bimetallische katalysatoren onderzocht aangezien ze eenzelfde katalytisch gedrag kunnen vertonen als monometallische katalysatoren, maar dan, bijvoorbeeld, met verbeterde stabiliteit. PdZn intermetallische katalysatoren zijn eerst onderzocht aangezien de verdeling van de atomaire energieniveaus van PdZn erg gelijkend was aan die van Cu. Dit wijst op gelijkaardige eigenschappen, maar een verhoogde stabiliteit werd verwacht.

Eerst werd het effect van de activatieprocedure op de katalysatorprestatie onderzocht. Daarvoor werd een 1wt%Pd-1.2wt%Zn/Mg(Al)(Pd)(Zn)O_x katalysator gesynthetiseerd via de bijmenging van Pd en Zn in de drager. Twee activatieprocedures zijn getest, namelijk *enkelvoudige* reductie en *cyclische* reductie. Enkelvoudige reductie is een éénstapsreductie met waterstof op 823K. Cyclische reductie is een reductie-oxidatiebehandeling die bestaat uit H_2-lucht-H_2-lucht-H_2 op 823K. Via gedetailleerde karakterisatie werd gevonden dat de vorming van het actieve PdZn deeltje verbeterd wordt door toepassing van cyclische reductie als activatieprocedure. Voorts neemt het aantal actieve centra toe door volledige extractie van de actieve materialen uit de drager. De vorming van het actief deeltje, zowel door enkelvoudige als cyclische reductie, is samengevat in Figuur 1. Enkelvoudige reductie is voorgesteld in elementen a tot d. Na calcinatie zijn alle actieve metalen aanwezig in de drager en een kleine hoeveelheid ZnO is reeds aanwezig op het oppervlak. Bij reductie wordt Pd^{2+} geëxtraheerd uit de drager waarbij het onmiddellijk reduceert tot Pd. Dan diffundeert ook Zn^{2+} uit de drager en reduceert tot Zn onder invloed van overdracht van H_2 vanaf Pd. Ondertussen diffundeert Zn in het Pd deeltje met de vorming van een PdZn rand met een Pd kern tot gevolg. Wanneer een oxidatie uitgevoerd wordt, zoals het geval is bij cyclische reductie, wordt Zn opnieuw vrijgemaakt uit het PdZn deeltje waardoor kleine ZnO

eilandjes ontstaan op een Pd deeltje. De diffusielengte van ZnO naar Pd is echter wel verkort waardoor een volgende reductie de vorming van een homogeen PdZn deeltje bevordert, zie Figuur 1 e tot f. Twee keer herhalen van de reductie-oxidatie behandeling is voldoende om een homogeen deeltje te vormen.

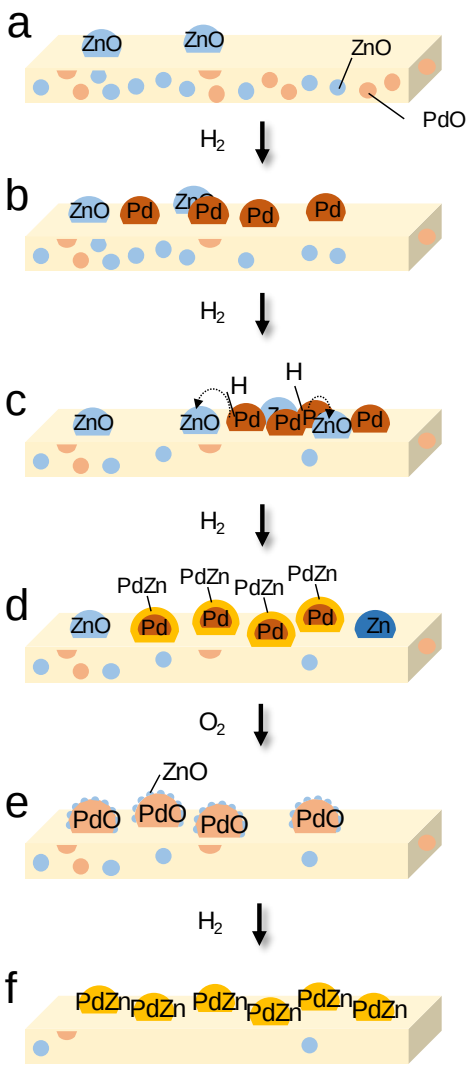

Figuur 1: Schematische voorstelling van de vorming van het intermetallische deeltje tijdens enkelvoudige reductie (a-d) en cyclische reductie (a-f) op 823K voor PdZn/Mg(Al)(Pd)(Zn)O_x. donkeroranje: Pd, lichtblauw: ZnO of $ZnAl_2O_4$, lichtoranje: PdO, goud: intermetallische component PdZn.

De vorming van de katalysator kan ook de katalysatorprestatie verklaren. Voor beide activatieprocedures werd initieel activiteitsverlies vastgesteld samen met een verhoogde acetaldehydeselectiviteit. Dit was toegeschreven aan de vorming van cokes op naburige Pd sites.

Cokes werd gevormd door decompositie van acetaldehyde op de Pd sites tot methaan en koolstofmonoxide met de vorming van cokes door omzetting van methaan en koolstofmonoxide als gevolg. Wanneer deze sites geblokkeerd raken, door cokes, blijven enkel de PdZn sites over die wel actief zijn voor acetaldehydeproductie en niet voor de vorming van methaan en koolstofmonoxide. Algemeen bracht cyclische reductie de beste katalysator voort met een omzettingsfrequentie van 7 s^{-1}.

Als tweede werd het effect van de synthesemethode op de katalysatorprestaties onderzocht. De PdZn hydrotalcietgebaseerde katalysator werd bereid op twee manieren. Bij de eerste werd eerst de pure $Mg(Al)O_x$ drager gemaakt en werden Pd en Zn via impregnatie toegevoegd. De tweede methode is ook gebruikt in het vorige onderzoek, dus de inmenging van Pd en Zn in de drager tijdens zijn synthese. Er werd vastgesteld dat via impregnatie grotere deeltjes gevormd worden. Dit bemoeilijkt de vorming van een homogeen legeringsdeeltje en, zelfs bij cyclische reductie, blijft een PdZn rand met een Pd kern over. Verder ging actief materiaal verloren tijdens reactie bij de geïmpregneerde katalysator. Dit is toegeschreven aan de zwakke interactie van de actieve metalen met de drager. Bij regeneratie van de katalysator met een oxidatie-reductie behandeling wordt cokes afgebrand wat een lokale hotspot creëert. Dit zorgt dan voor verdamping van Pd en Zn. Metaalverlies komt niet enkel voor bij oxidatieve condities. Bij reductie wordt PdH gevormd en deze hebben een lagere verdampingstemperatuur dan Pd. Algemeen is de geïncorporeerde $PdZn/Mg(Al)(Pd)(Zn)O_x$ katalysator de meest actieve katalysator.

Voorts werd ook het effect van water op de katalysatorprestaties bekeken door een voeding van 30wt% water/ethanol te gebruiken. Zowel de activiteit als de acetaldehydeselectiviteit daalden in vergelijking met de originele activiteit bij 100% ethanol, zie Figuur 2. Wanneer daarna opnieuw 100% ethanol gevoed wordt, stijgen de activiteit en selectiviteit slechts gedeeltelijk. Om te achterhalen welke veranderingen plaatsvinden wanneer een waterhoudende voeding gebruikt wordt, zijn gedetailleerde karakterisatiemethoden en DFT berekeningen voor de thermodynamische eigenschappen gebruikt. Daaruit werd geconcludeerd dat ZnO eilandjes

gevormd worden op Pd-rijke PdZn deeltjes. Dit wordt slechts gedeeltelijk teniet gedaan wanneer opnieuw zuivere ethanol gebruikt wordt, door de vorming van waterstof. Regeneratie herstelt het PdZn deeltje volledig.

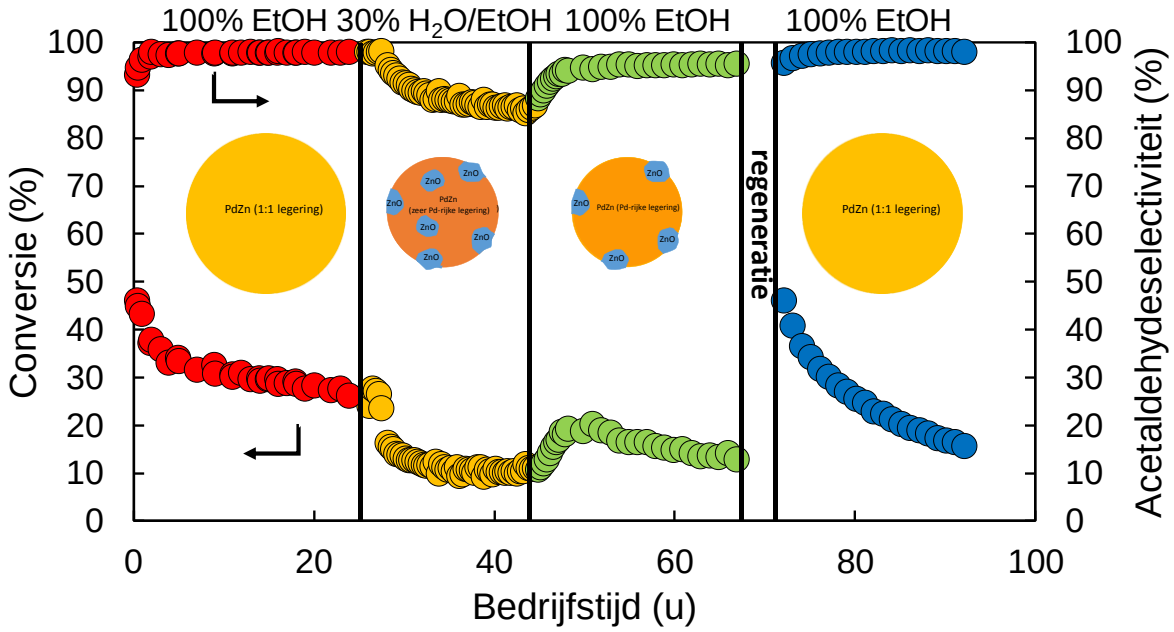

Figuur 2: Prestatiecurves voor PdZn/Mg(Al)(Pd)(Zn)O_x voor opeenvolgend 100m% ethanol (I, rood), 30m% H_2O/ethanol (II, geel), 100m% ethanol na waterhoudende voeding (III, groen), 100m% ethanol na regeneratie (IV, blauw). De cirkels stellen de katalysator voor bij de verschillende stadia.

Wanneer de resultaten van de PdZn katalysatoren gecombineerd worden, kan geconcludeerd worden dat de dehydrogeneringsreactie enkel doorgaat op de Pd sites. Zn is niet actief voor de reactie en zorgt enkel voor een buffer om de aanwezigheid van twee naburige Pd sites te vermijden en om de activiteit van Pd te wijzigen. Naburige Pd sites zorgen namelijk voor de productie van ongewenste producten zoals methaan, koolstofmonoxide en cokes. De activiteit van de katalysator zou waarschijnlijk kunnen verbeterd worden als een bimetallische katalysator gebruikt wordt waarbij beide elementen actief zijn voor de dehydrogeneringsreactie. Dit is zo voor Ni en Cu. Beide metalen zijn echter erg gevoelig aan deactivatie, resp. cokesvorming en sintering. Door het legeren van de metalen kan de deactivatie vermeden worden. Zeven NiCu/Mg(Al)(Ni)(Cu)O_x katalysatoren zijn getest geweest, allen met een andere Ni/Cu-ratio.

Voorts werd een Cu/Mg(Al)(Cu)O_x katalysator gemaakt als referentiekatalysator. De aanwezigheid van Ni in de katalysator verbetert de omzettingsfrequentie en de acetaldehydeselectiviteit. De stabiliteit was gelijkaardig aan die van de pure Cu katalysator. Maar, de hier besproken Cu katalysator, is stabieler dan de typische Cu katalysator in literatuur. Het activiteitsprofiel als functie van de tijd voor alle NiCu katalysatoren bevat twee regimes: snelle deactivatie in de 1e uren en een trage deactivatie later, zie ook Figuur 3. De snelle deactivatie kon worden toegeschreven aan cokesvorming, terwijl sintering de oorzaak was voor de trage deactivatie. De beste katalysator, 1m%Ni-10m%Cu/Mg(Al)(Ni)(Cu)O_x, vertoonde geen snelle deactivatie. Onderzoek met FTIR toonde dat, voor deze katalysator, de legering meer Ni bevat dan voor de andere katalysatoren. Er waren dus geen naburige Ni sites, waardoor de decompositie van acetaldehyde tot methaan en koolstofmonoxide vermeden is. Het is dus duidelijk dat dezelfde fenomenen voorkomen bij PdZn en NiCu katalysatoren. Ook het effect van water op de katalysatorprestaties is onderzocht voor de NiCu katalysatoren. Bij verandering van een pure ethanolvoeding naar een 30m%H_2O/ethanol-voeding, werd een hogere conversie vastgesteld. Dit kon verklaard worden door de activatie van water op de Cu sites. Algemeen kan geconcludeerd worden dat de NiCu katalysatoren geen hogere activiteit hebben als gekeken wordt naar de omzettingssnelheid, maar ze hebben wel het hoogste industrieel potentieel: de prijs van de NiCu katalysatoren is 400 keer lager dan voor de PdZn katalysatoren, zelfs met de hoge Ni en Cu beladingen en de conversie van de NiCu katalysatoren is hoger dan voor de PdZn katalysatoren. Voorts verbetert de conversie van de NiCu katalysatoren bij de aanwezigheid van water in de voeding.

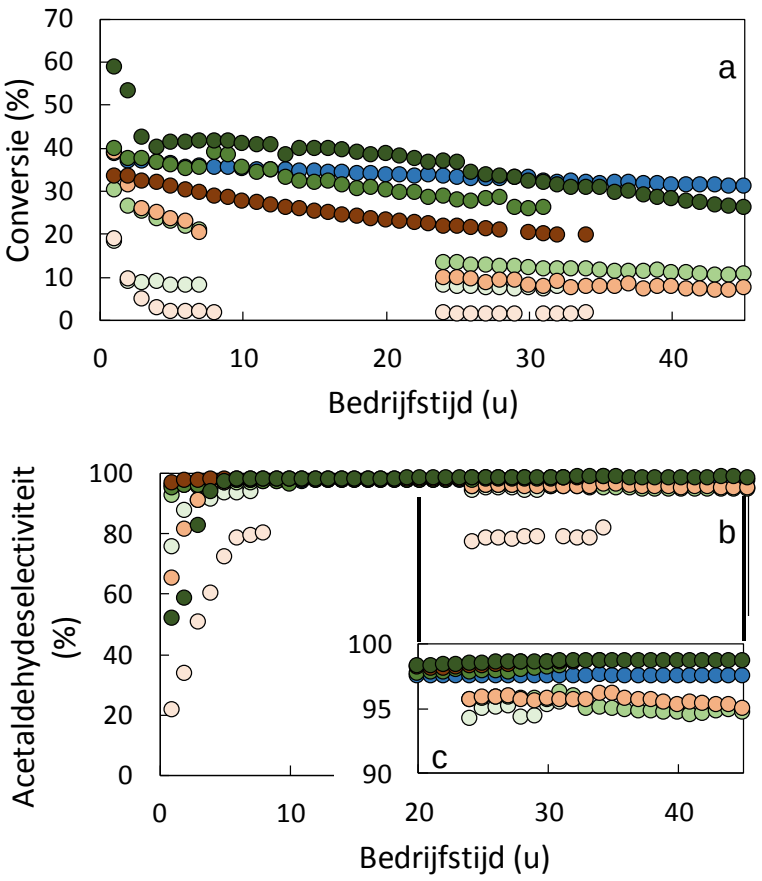

Figuur 3: Prestatiecurve voor 10m%Cu/Mg(Al)(Cu)O_x (blauw), 0.5m%Ni-Xm%Cu/Mg(Al)(Ni)(Cu)O_x (X=0,5,10) (rood, licht->donker=hogere Cu lading), 1m%Ni-Xm%Cu/Mg(Al)(Ni)(Cu)O_x (X=0,5,10,20) (groen, licht->donker=hogere Cu lading). a: conversie, b: acetaldehydeselectiviteit, c: focus op acetaldehydeselectiviteit.

Daarnaast werd het bestaan van een NiCu legering voor 1massa%Ni-10m%Cu/Mg(Al)(Ni)(Cu)O_x gesteund door kinetische modellering. Een algemeen kinetisch model werd opgesteld waarin alle reacties vervat zitten die voorkomen op alle onderzochte katalysatoren in stabiele toestand. Daarvoor werden twee types aan actieve centra ingevoerd: dehydrogeneringsites, zoals PdZn, Cu en NiCu, en decompositiesites, zoals Pd en Ni. Niet-lineaire regressie van 41 experimentele datapunten is gebruikt voor de schatting van 17 parameters. Alle parameters zijn fysisch zinvol en statistisch significant. Voor de bepaling van de adsorptie- en reactie-enthalpiën werd de UBI-QEP methode gebruikt waarbij de adsorptie-enthalpie van alle componenten gerelateerd kan worden met de atomaire chemisorptie-enthalpie van H, C en O. De

geschatte waarden voor deze parameters komen overeen met de waarden gerapporteerd in literatuur. De hoeveelheid 'vrije' Ni-sites, dus naburige Ni-sites die bijdragen aan de decompositiereactie, is zeer klein, maar 8%. Reactiepadanalyse, zie Figuur 4, heeft blootgelegd dat, wanneer ethanol geadsorbeerd wordt aan het katalysatoroppervlak, het onmiddellijk reageert naar acetaldehyde op de dehydrogeneringssites. Dan desorbeert het en adsorbeert opnieuw op de decompositiesites met de vorming van methaan en koolstofmonoxide als gevolg.

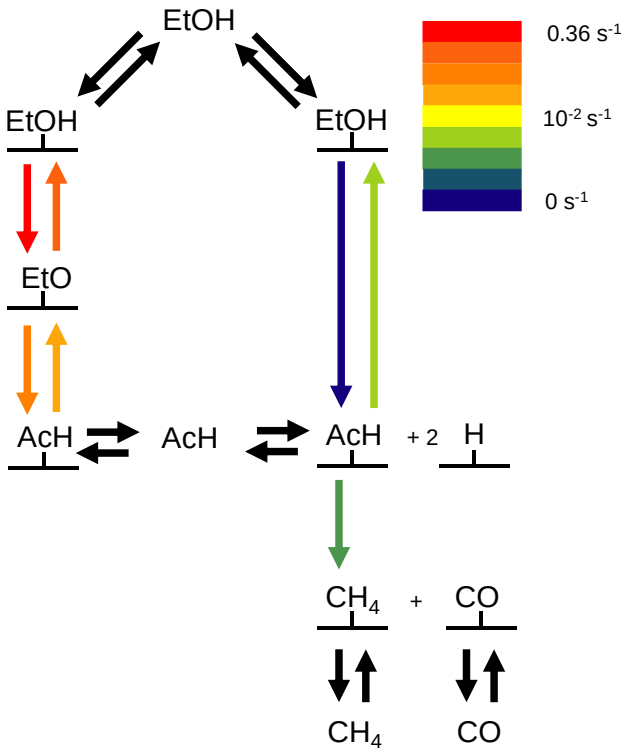

Figuur 4: Reactiepadanalyse bij T=533K, P_{tot}=0.5MPa, W/F_{EtOH}=3.6kg_{kat} s mol^{-1}. De kleuren zijn representatief voor de relatieve snelheden: donker rood= hoge snelheid → donker blauw=lage snelheid.

Over het algemeen werd het gebruik van bimetallische katalysatoren voor ethanoldehydrogenering onderzocht door inzicht te verwerven in de fundamentele fenomenen die optreden tijdens synthese en activatie van de katalysatoren. Via onderzoek naar het effect van water op de katalysatoren is het industrieel potentieel van de materialen geëvalueerd. Via meer uitgebreide kinetische modellering kunnen ook richtlijnen opgesteld worden die de prestaties van de katalysatoren verder kunnen verbeteren.

Chapter 1:

Introduction

The current chemical industry thrives on the use and conversion of fossil feedstocks, i.e., oil, coal and natural gas. According to the World Energy Council, still 86% of the energy consumption originates from fossil feedstocks, see Figure 1- 1 [1]. Over the past 70 years, we have been depleting the world from its energy resources at an ever increasing pace. Although significant reserves for these resources are still available, we can no longer tolerate the irreversible consumption of these resources in terms of CO_2 and other greenhouse gas emissions. Furthermore, it is important that we lower our dependency on the fossil resource supplying countries given the political situation in most of these countries. Thirdly, with the mining of fossil resources the earth is depleted and might alter the geographic stability of some regions and impact the soil and water quality, e.g., by breaking of shale layers for the extraction of shale gas [2].

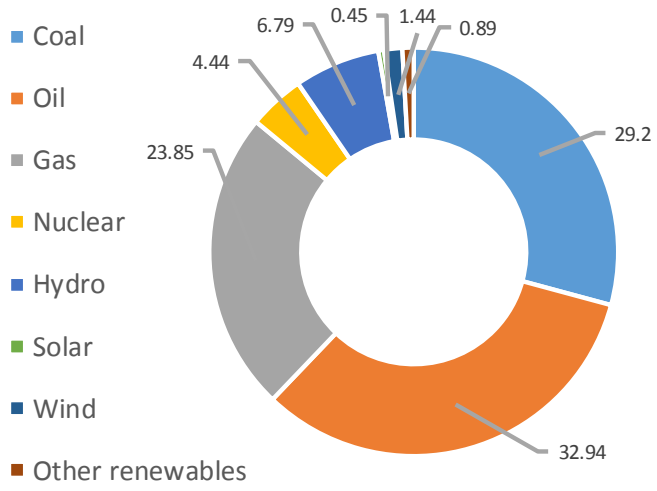

Figure 1- 1: World energy consumption per resource [1].

1.1. Bio-ethanol as an alternative to fossil feedstocks

1.1.1. Production of bio-ethanol

The last decades, this awareness has lead academia and industry towards research in renewable resources which mitigate the use of fossil resources and consequently the impact on our environment. Many alternatives are being found for fuel purposes, such as electric cars. However, also a great share of the annual resource demands is converted into base chemicals that are subsequently further processed into consumer goods. For this, the retro-aldol reaction of sugars to glycolaldehyde and biomass fermentation to bio-ethanol might constitute good alternatives since they are easily produced from biomass [3, 4]. Furthermore, via these processes, we can capture emitted CO_2 into chemicals, which lowers the greenhouse gas levels. Here, fermentation to bio-ethanol and the conversion to other chemicals will be discussed further.

Bio-ethanol is commonly produced via fermentation of biomass [5]. The feedstocks that are mostly used are sugar cane, sugar beet and corn [6]. The global production of bio-ethanol amounted to 100 Gl in 2016, with the highest producer being the US [7]. This is only a small amount compared to the annual oil production which amounts to 2.4 Tl [8]. This production of bio-ethanol can still rise when the change towards a bio-based chemical industry continues.

The advantage of sugar cane and sugar beet is that they are sucrose-containing feedstocks, whereas corn is a starch-containing feedstock. Starch needs an additional pretreatment step to depolymerise the starch chains into individual glucose monomers. Of course, the production of bio-ethanol from edible substances is conflicting with the food production and raises ethical concerns. Therefore, research is being conducted on the production of bio-ethanol from lignocellulosic biomass, such as agricultural waste, wood, … . Lignocellulosic biomass consists of 3 main compounds, see Figure 1- 2 [9]:

- cellulose which is the easiest to transform into bio-ethanol since it is a polymer of glucose,
- hemi-cellulose which is a polymer consisting of different pentoses and hexoses and
- lignin which is a polymer of aromatic compounds.

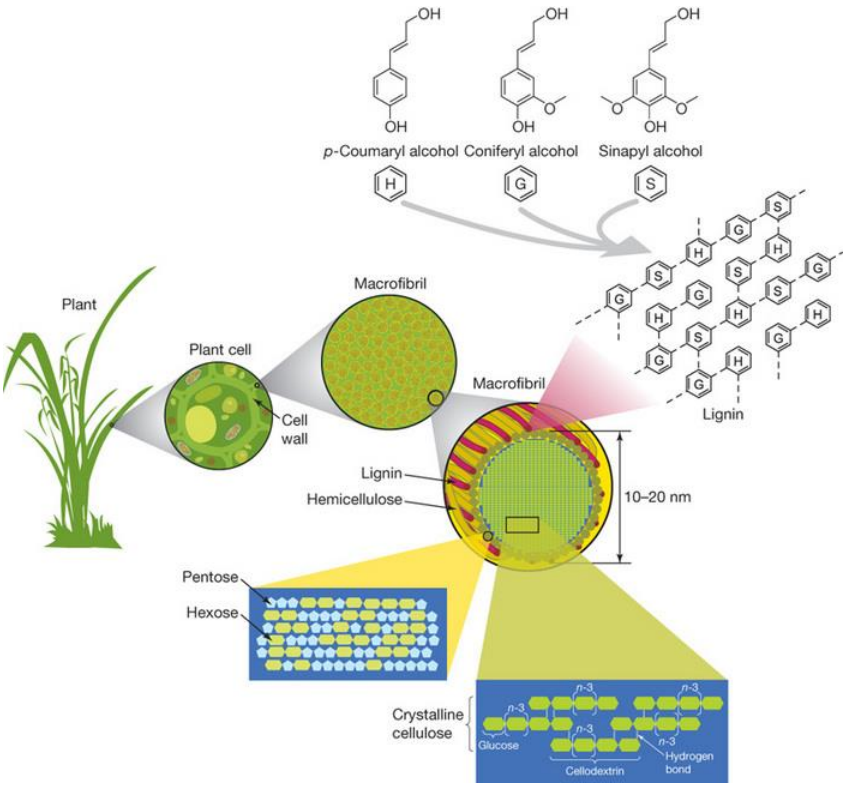

Figure 1- 2: A schematic representation of the structure of lignocellulosic biomass [9].

The lignocellulic biomass can be found in the macrofibril of the cell wall of a plant, see Figure 1- 2. It exists as a thread where cellulose is located at the center. The hemicellulose is wrapped around the cellulose. The lignin then covers the hemicellulose. Thus, to get to the cellulose (and hemi-cellulose), which is the most valuable compound for bio-ethanol production, one first has to decompose the lignin. This reduces the quality of the cellulose and, hence, a lot of research is still being performed to find the best method for breaking these lignin fibers, such as mechanical pre-treatment, steam explosion, supercritical CO_2 treatment [5, 10].

Secondly, a hydrolysis step should be performed to convert cellulose and hemi-cellulose into sugar molecules via the addition of water. This reaction is catalyzed by acids or by enzymes [5, 11]. The use of enzymes has many advantages over acid hydrolysis because of the milder conditions that can be used and corrosion issues are avoided. Furthermore, enzymatic hydrolysis gives higher yields than the acid-based one [11].

Afterwards, the production of bio-ethanol from sugars can be performed [5]. This is achieved under anaerobic conditions at atmospheric pressure and a temperature of 310K. The most commonly used yeast is the *Saccharomyces cerevisiae.* It can convert all hexoses, reaches almost the theoretical ethanol yield, i.e., $0.51 g_{EtOH}/g_{sugar}$ and can produce ethanol at concentrations up to 18v%. It can, however, not convert pentoses, such as xylose. Since this is the second most abundant sugar in lignocellulose, new enzymes have been designed. The *Zymomonas mobilis* is a promising enzyme since it can convert both glucose and xylose with yields up to 97% of the theoretical value and concentrations of 12v% [5].

After bio-ethanol production, the mixture consists mainly of water with max. 20% ethanol, together with solids. When feeding the mixture into a distillation column, the solids remain in the aqueous phase at the bottom of the column whereas a 37% bio-ethanol mixture is retrieved from the top. The latter mixture is then further concentrated to the azeotrope of 95v%.

1.1.2. Ethanol/water azeotrope

Due to the presence of hydrogen bonds between the OH- groups of ethanol and water, there is a pronounced interaction between these components. This gives rise to a positive azeotrope, i.e., the boiling point of the azeotrope is lower than of the pure compounds. The maximum ethanol concentration that can be achieved with distillation is hence limited to 95v% ethanol or 96 mol%, see Figure 1- 3.

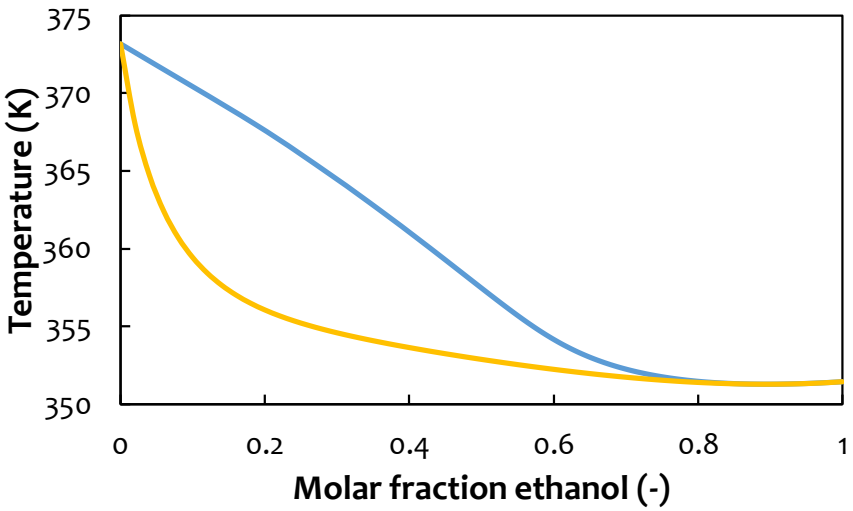

Figure 1- 3: Phase diagram of the water-ethanol system at 1atm determined by Aspen Plus®. Yellow: liquid composition, blue: vapor composition.

For the use of ethanol as fuel purposes or to convert it further into other chemicals, typically anhydrous ethanol is required. The azeotrope, hence, has to be *broken*, as it is called. For this, several options are under investigation [12]. The oldest processes used for this are azeotropic distillation with cyclohexane and extractive distillation with ethylene glycol.

In azeotropic distillation, another compound, mostly cyclohexane for an ethanol/water mixture, is added to the ethanol/water mixture which forms a ternary azeotrope. That way, it is possible to distill pure ethanol from the bottom and the azeotropic mixture at the top. This mixture is then decanted into two liquids and those are distilled separately to recover the cyclohexane and remove the water. The energy requirement for this is 294 kJ mol^{-1} [13].

In extractive distillation, a non-volatile, high-boiling compound is added to the ethanol/water mixture. Important here is that the third compound doesn't form an azeotrope with any of the compounds. The process is performed in two columns. In the first, ethyl glycol is entered at the top plate of the distillation column and the azeotropic mixture is fed on the middle plate. The ethyl glycol flows downwards thereby entraining most of the water. This results in a 100% ethanol stream at the top of the distillation column. In the second column, a conventional distillation is

performed between ethyl glycol and water to separate them into pure compounds. The total energy requirement is 85kJ mol^{-1} [13].

Many other methods are also available and are being improved, such as pervaporation, molecular sieves, …[12] It is clear that the need for anhydrous ethanol has significantly driven research in that field. An alternative would be to produce chemicals from a water-ethanol mixture. If the chemicals produced from ethanol don't form an azeotrope with water, the final separation becomes significantly easier and will consume less energy. This is however not evident as many catalytic reactions are hindered by the presence of water since it tends to poison or increase the sintering. Taking the potential energy savings into account, this is certainly worth investigating [14-16].

1.2. Ethanol dehydrogenation to acetaldehyde

Ethanol can be catalytically converted into three major chemical product groups, see Figure 1- 4 [4]:

- production of CO_2 and H_2 via steam reforming,
- production of hydrocarbons via the dehydration to ethene,
- the production of acetaldehyde and subsequently other oxygenates.

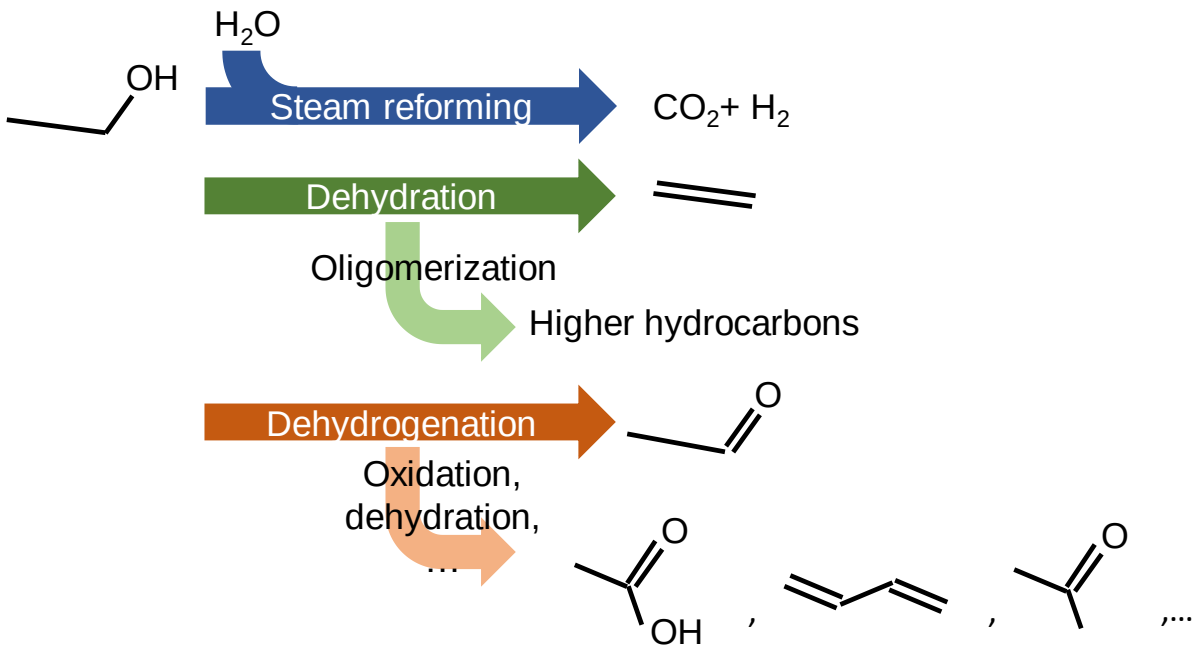

Figure 1- 4: Scheme of the possible ethanol conversion reactions.

1.2.1. *Acetaldehyde*

In this thesis, the focus will be on the production of chemicals, thus we are most interested in the conversion of ethanol to acetaldehyde. A major advantage of the production of acetaldehyde is that it doesn't form an azeotrope with water, resulting in an easy removal of water. This of course only applies if the reaction can proceed in the presence of water.

Acetaldehyde is a potential bio-based platform molecule for the production of a wide variety of chemicals such as 1,3-butadiene, pyridine, ethyl acetate, … [17] The global production in 2018 amounts for USD1.33 billion [18] The use of acetaldehyde for the production of pyridines and pentaerythritol is rising. These chemicals are used in the production of agricultural chemicals such as fertilizers, pesticides, but also paint and coatings. Especially China is a big consumer of acetaldehyde accounting for 46% of the market [19].

Acetaldehyde is currently produced via direct oxidation of ethene via the Wacker process [17]. This process was developed around 1960 and has the following reactions:

$$C_2H_2 + PdCl_2 + H_2O \rightleftharpoons CH_3CHO + Pd + 2HCl$$

$$Pd + 2CuCl_2 \rightleftharpoons PdCl_2 + 2CuCl$$

$$2CuCl + \frac{1}{2}O_2 + 2HCl \rightleftharpoons 2CuCl_2 + H_2O$$

$PdCl_2$ and $CuCl_2$ act both as a catalyst; $PdCl_2$ as a catalyst for acetaldehyde formation and $CuCl_2$ as reoxidizer of Pd to $PdCl_2$. The overall reaction is an exothermic reaction:

$$C_2H_4 + \frac{1}{2}O_2 \rightleftharpoons CH_3CHO \qquad \Delta H = -244\ kJ\ mol^{-1}$$

It is produced in a one- or two-stage process at moderate conditions, i.e., a temperature of 378K to 403K and pressures of 0.4MPa to 1MPa.

The economic assessment of the Wacker process as compared to the production from ethanol goes beyond of the scope of this work. However, considering the conversion from ethanol as an alternative route which lowers the net CO_2 emissions to the atmosphere and the potential bio-based routes might have in the future, research towards the green production of acetaldehyde as a platform molecule should be performed to enhance the performance and economics of the system.

Ethanol conversion to acetaldehyde can proceed via two reactions:

1. Direct dehydrogenation:

$$CH_3CH_2OH \rightleftharpoons CH_3CHO + H_2 \qquad \Delta H_r^\circ = 70.6\ kJ\ mol^{-1}$$

2. Oxidative dehydrogenation:

$$CH_3CH_2OH + \frac{1}{2}O_2 \rightleftharpoons CH_3CHO + H_2O \qquad \Delta H_r^\circ = -171.2\ kJ\ mol^{-1}$$

1.2.2. Direct dehydrogenation

The major advantage of direct dehydrogenation is the production of H_2 as a byproduct, which improves the economics of the process. Furthermore, H_2 can easily be removed from the reaction mixture. This could, if necessary, enhance the ethanol conversion since the reaction is thermodynamically controlled. However, the reaction is endothermic and, hence, heat should be supplied to the process, which in fact decreases its economic viability [17]. Overall, quite moderate temperatures and pressures are used for the catalytic activity tests, i.e., ranging from 373 to 800K and mostly at atmospheric pressure [20-47]. A variety of secondary products are also formed during reaction, e.g. ethyl acetate, diethyl ether, CO, methane,… . Many different types of catalysts are under investigation in literature such as Au/$ZnZrO_x$, NiCo/ZnO, N-doped graphene nanosheets, Pd/m-ZrO_2,…, see Table 1- 1 [31-33, 48]. However, the most commonly investigated one is Cu-based, which will be discussed in more detail in section 1.4.

1.2.3. Oxidative dehydrogenation

Ethanol dehydrogenation via the oxidative reaction requires the addition of oxygen to the system which is transformed into water. This is less interesting as compared to the hydrogen produced in the direct dehydrogenation. However, the reaction is exothermic, such that the produced heat can be used for pre-heating purposes, reducing the cost of the overall process [17]. Also for this reaction, quite moderate temperatures and pressures are employed, i.e., a temperature range from 300 to 800K and pressures of max. 3.0 MPa [49-76]. However, the highest activities are mostly observed at more elevated temperatures than was the case for the direct dehydrogenation. Typical secondary products are acetic acid, acetone and ethyl acetate. Among the great variety of investigated catalysts for this reaction, see Table 1- 2, two types of catalyst are most promising, i.e., Au supported on different metal oxides and V_2O_5 on different supports. For V_2O_5 catalysts, especially V_2O_5/TiO_2 gives promising results and it is, hence, also mostly investigated. It has proven to be a stable catalyst up to 200h [60]. The catalyst gives rise to high conversions and selectivities at low temperatures, i.e., 403-453K [76]. For supported Au catalysts,

more variety exists in the used supports, e.g. CeO_2, TiO_2, SiO_2. Mullen et al. [63] have found that the addition of small amounts of water to the feed increases the formation of acetaldehyde, but upon addition of more water, the activity decreases. Nadeem et al. [61] have investigated anatase and rutile TiO_2 and found out that Au impregnated on rutile TiO_2 gives rise to the highest acetaldehyde yield, but still a high amount of ethene is also produced. Redina et al. [59] have investigated the addition of both Au and Cu on the catalyst and found that alloy formation of Au and Cu decreases the activity for ethanol oxidation. Bauer et al. [53] support this statement and suggest to make alloy particles which are then oxidized and form an Au particle with a CuO_x shell. They claim that the interface between Au and CuO_x is the active site.

In this thesis, direct dehydrogenation is investigated because of the industrial relevance of hydrogen as a byproduct and the mild reactions conditions. It should be taken into account that the presence of acid sites on the catalyst may result in the production of diethyl ether, which is undesired. Thus, when choosing a support, it is important to keep in mind the industrial production of the catalyst and also the rather basic nature.

Table 1- 1: Catalysts used for ethanol direct dehydrogenation. The missing values were not reported and couldn't be calculated from the reference.

Catalyst	Temperature (K)	Space time (kg_{cat} s mol^{-1})	Conversion (%)	Acetaldehyde selectivity (%)	TOF (s^{-1})	Deactivation (% in 6h)	Reference
9%Cu/rice husk	523	85	75		0.15	20	[77]
Ag/Fe–Si_3N_4	523	610	18	38			[54]
Ag/Fe–Si_3N_4–Al	523	610	12	33			[54]
Ag/Fe–Si_3N_4–Zr	523	610	15	33			[54]
Ag/TiO_2	523		4.6	92			[35]
Ag-CeO_2/SiO_2	533	1	45	90			[41]
Au/CeO_2 (rod)	573	1.63	10	90			[52]
Au/TiO_2	523		5.5	100			[35]
Au/$ZnZrO_x$	545	150	40	80		20	[32]
Cu/Cr_2O_3	583	51			0.066	12	[46]
Cu/HAP	533	33000	50	50			[26]
Cu/MCM-41	533	33000	70	20			[26]
Cu/Mg(Al)(Cu)O_x	573	45	80	72.5		0	[34]
Cu/SBA-15	533	33000	60	25			[26]
Cu/TiO_2	523		9.1	100			[35]
Cu/ZrO_2	533		9	100		0	[40]
Cu/ZrO_2	523	105	77	15			[43]
$Li_{0.9}Zr_{1.8}In_{0.1}Nb_{0.1}P_{2.9}Mo_{0.1}O_{12}$	523	384	20	90			[28]
Mg(Al)O_x	533	89	2	75			[23]
MoO2	573	564	41	47.6		20	[25]
N-doped C nanosheets	573	12	11	100			[31]
Pt/CeO_2 (rod)	573	1.63	18	60			[52]
Pt/SiO_2	533				0.28		[20]
TiO_2	523		2.9	100			[35]
V_2O_3	573	564	13.4	43.6		40	[25]

Table 1- 2: Catalysts used for ethanol oxidative dehydrogenation. The missing values were not reported and couldn't be calculated from the reference.

Catalyst	Temperature (K)	Space time (kg_{cat} s mol^{-1})	Conversion (%)	Acetaldehyde selectivity (%)	TOF (s^{-1})	Deactivation (% in 6h)	Reference
0.2Au0.2Cu/SiO_2	523	700	100	100		60 in 2nd run	[59]
20V_2O_5/TiO_2	523	0.3	100	0			[55]
Ag/Fe–Si_3N4	523	610	75	100			[54]
Ag/HAP	523		15	100	1.38	0	[62]
Ag/OMS-2-cp	473	611	75	80	0.011	0	[66]
Ag/OMS-2-imp	473	611	60	10	0.0038		[66]
Ag-CeO_2/SiO_2	523	1	100	76			[41]
Au/CeO_2	353	0.1			0.024		[63]
Au/CeO_2 (rod)	573	1.63	100	0			[52]
Au/SiO_2	523	700	80	100			[59]
Au_3Cu/SiO_2	533	39	100	85			[53]
AuCu/SiO_2	533	39	90	85		4	[53]
AuCu/SiO_2 - reduced	533	39	90	85			[53]
$AuCu_3$/SiO_2	533	39	100	80			[53]
Cu/SiO_2	533	39	20	70			[53]
$LaMn_{0.95}Pd_{0.05}O_3$	533	0.18	12	90			[51]
$LaMnO_3$	523	0.18	8	90			[51]
N-doped C nanosheets	543	306	70	92.5			[64]
OMS-2	473	611	75	90			[66]
Pt/CeO2	573	4	78	25		13	[49]
Pt/CeO_2 (rod)	573	1.63	4.3	0			[52]
single-walled carbon nanotubes	523				0.000072		[57]
V/Al_2O_3	523	73	51	66			[60]
V/Mg(Al)O	523	73	12	66			[60]
V/SBA-15	523	73	17	80			[60]

1.3.Hydrotalcite-based supports

Hydrotalcite-based catalysts seem to be ideal candidates as a support, because of their ease in industrial preparation and their rather basic nature. Hydrotalcites, or layered double hydroxides, are a type of clay [78]. They are a versatile material for use as adsorbents, catalysts, catalytic supports, heat stabilizer for PVC, … [79]. Recently, these materials have been frequently investigated as a catalyst in general and for the conversion of lignocellulosic feedstocks in particular, see work of Baskaran et al. and Hernández et al. for more information [78, 80]. The general formula for those materials is $[M^{2+}_{1-x}M^{3+}_{x}(OH)_2]^{x+}(A^{m-})_{\frac{x}{m}}.nH_2O$. Most commonly, M^{2+} and M^{3+} are resp. Mg and Al, but they can also (partially) be replaced by other elements, such as transition metals. The structure consists of layers that are similar to $Mg(OH)_2$ octahedral layers [81], see Figure 1- 5. Due to the induced charge within the layers by changing a bivalent to a trivalent ion, interlayer ions are present to compensate for the charge. Also water is present between the layers. Upon thermal treatment, i.e., calcination, the hydrotalcite structure releases CO_2 and water from in between the layers and, furthermore, transforms the $Mg(Al)(OH)_x$ layers into a mixed oxide $Mg(Al)O_x$ [82]. The mixed oxide is usually well-dispersed with a high surface area. Upon addition of a transition metal, this diffuses from the support to the surface upon reduction which results in the formation of nanoparticles. However, substituting Mg or Al with a transition metal that has a divergent ion radius might disrupt the formation of uniform layers and thus reduce the surface area of the mixed oxide significantly [83]. The use of hydrotalcite-based mixed oxides has several advantages [78, 79, 81, 82, 84-87]:

- They have a moderate basicity which inhibits coking;
- They exhibit a high thermal stability to steam and reduction-oxidation cycles;
- The resistance to sintering is significant due to the presence of Al-cations;
- After reduction, well-dispersed metallic particles are obtained.

Another feature of mixed oxides formed from hydrotalcite-like compounds is that, when adding water, the hydrotalcite structure is recovered. The memory effect is often detrimental for the catalyst activity and lifetime, due to the incorporation of active sites in the support, but is now frequently used to improve the catalytic activity. This is performed via the encapsulation of the reactants in between the layers of the hydrotalcite thereby making the contact of the active sites with the reactants more abundant [88, 89].

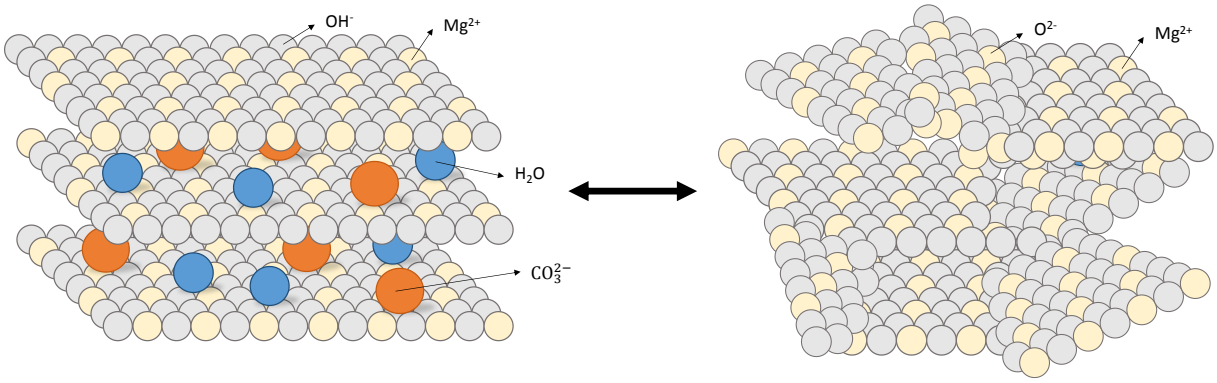

Figure 1- 5: Schematic representation of layered hydrotalcite support and collapse after calcination. The structure is regained upon water addition.

1.4. Cu-based catalysts

Major advantages promoting the use of Cu as a catalyst are its relatively low price and its low toxicity [90, 91]. Unfortunately, Cu has one significant disadvantage: it is particularly prone to deactivation by sintering [47, 77, 92]. Twigg et al. have reviewed the deactivation causes of Cu catalysts in industrial processes and concluded that sintering and poisoning are the two main reasons for deactivation. While poisoning should and can be prevented by tuning the feedstock composition [92], many attempts have been made to improve the resistance of Cu catalysts against sintering [26, 43, 47, 93-101].

Different support materials have been investigated, although only few report on the stability of their catalysts [26, 43, 93-96]. Marchi et al. have tested Cu/SiO_2 for isopropyl alcohol and found

that within 2 hours on stream, the activity dropped to 20% of the original level [94]. Guardino et al. have tested Cu/Nb_2O_5 for ethanol reforming and reported on a strong interaction between Cu and Nb_2O_5 as compared to Cu on Al_2O_3, as found via TPR [102]. The catalyst is quite active and stable with only 5% activity loss after 30h. Freitas et al. have tested a Cu/ZrO_2 catalyst for ethanol dehydrogenation and have proven that it only loses 4% of activity in 20h, which is quite remarkable [43].

Also promoting agents have been added to Cu catalysts to reduce the Cu particle size and increase the catalyst stability, e.g Cr, Fe, B, La [46, 97-101]. Tu et al. have investigated the effect of Cr on the stability of Cu catalysts [46]. They found that the stability improves upon addition of Cr, i.e., an optimum was found at a Cr/Cu molar ratio of 1/10. The catalyst still suffered from deactivation due to sintering however, i.e., 5% activity loss occurred after 8h on stream. Zhu et al. have used B as a promotor for the Cu dispersion and stability and were able to prolong the stable activity regime to more than 56h compared to 28h for the Cu/SiO_2 [98]. However, ultimately, also this catalyst was subject to deactivation due to sintering. Chen et al. added Fe as a promotor for the reverse water-gas shift reaction [103]. These authors have synthesized a quite stable catalyst, i.e., only an activity loss from 15% to 12%. For the low-temperature water-gas shift reaction, La promotion of Cu catalysts enhances their stability, as found by Kam et al. [101]. After 25h, the conversion has only dropped from 45% to 38%.

1.5.Bimetallic catalysts

It is clear that many attempts were made to overcome the rapid irreversible deactivation of the Cu-based catalysts. Since different supports or promoting agents don't seem to solve this issue, the design of bimetallic catalysts can be investigated, since it can drastically change the catalyst properties of a monometallic material.

Bimetallic catalysts are defined as materials that have combined catalytic properties [104-106]. They mostly exhibit excellent properties such as a high resistance to sintering. They can be

divided into three groups: core-shell materials, heterostructures and alloy or intermetallic catalysts, see Figure 1- 6. In core-shell, one element forms the inner part, whereas another metal covers the first element as a shell [107]. Heterostructures are structures that grow from two nuclei with a different chemical identity which coincide at some point to make a sharing interface. Alloy particles consist of homogeneously mixed metals and form metal-metal bonds with their neighboring atoms. Intermetallic species are a special type of alloy particles where a stoichiometric ratio between the two metal species is required. Here, the focus is on alloys, such as PdZn, NiCu, …

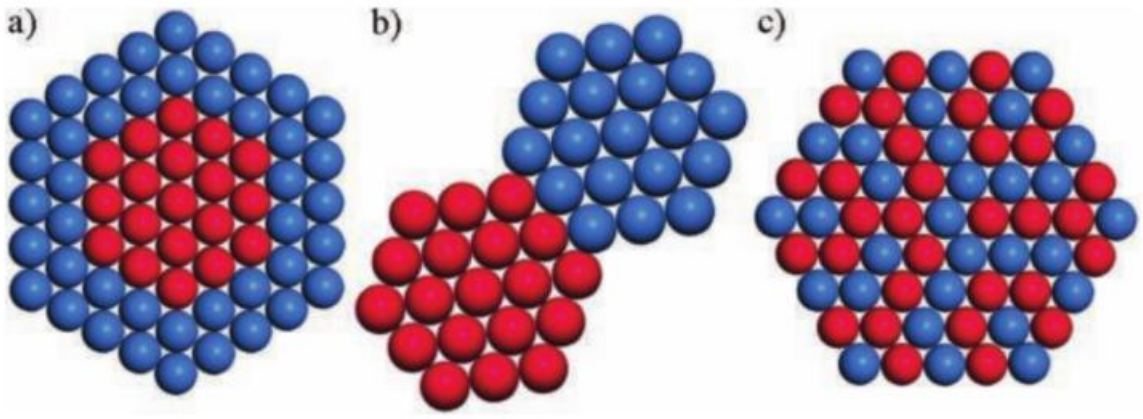

Figure 1- 6: Different bimetallic structures. a: core-shell, b: heterostructure and c: alloy structure [108].

To understand the effects that are typically present for bimetallic catalysts, structure-activity relationships should be considered. A distinction can be made between electronic and geometric effects. The electronic effect concerns the interaction of the molecular orbitals of the reactants and products with the unoccupied d-band of the surface [109]. Sabatier stated that the intermediate compound formed via the interaction between reactant and surface, should be energetically stable for it to form, but not too stable such that it can still transform into products. Alloying of two metals can provide the ideal surface for the formation of this type of intermediate compounds. The geometric effect deals with reactions that can't proceed on one surface atom. Thus, too small particles, or active atoms isolated by another, inactive, type of atoms can't catalyze the reaction. Sometimes, even a special arrangement of atoms is required for the reaction to proceed. These

two effects can, of course, not be separated completely, e.g. the enlargement of an active particle will change the d-band of the surface and facilitate the formation of new active site ensembles. These effects are of utmost importance for active nanoparticles since the addition of 1 atom to that particle more significantly changes the structure-activity relationships of the particle compared to large clusters.

Two groups of alloys have caught the attention for use in ethanol dehydrogenation, i.e., Pd-alloys and NiCu. Iwasa et al. have studied the performance of Pd-alloys and found that PdZn was the most active and selective [110]. Ni and Cu on the other hand, are both active for ethanol dehydrogenation, but both have a disadvantage, i.e., deactivation due to resp. coking and sintering. Via alloying of Ni and Cu, it is aspired that the deactivation effects are canceled and a stable active catalyst remains see section 1.5.2..

1.5.1. PdZn catalysts

Upon mixing Pd and Zn, depending on the composition and temperature, different structures can be formed. In most compositions, an intermetallic compound is formed, see Figure 1- 7. The tetragonal Pd_1Zn_1 structure is stable in a broad range of temperatures and compositions, i.e., from 38.5% to 53% Zn [111, 112]. Up to now, it is unclear how the non-equimolar quantities give rise to the crystal structure. Possibilities are interstitial atoms or defects. This PdZn structure has an AuCu crystal structure, see Figure 1- 8. Every zinc/palladium atom is surrounded by 8 palladium/zinc atoms.

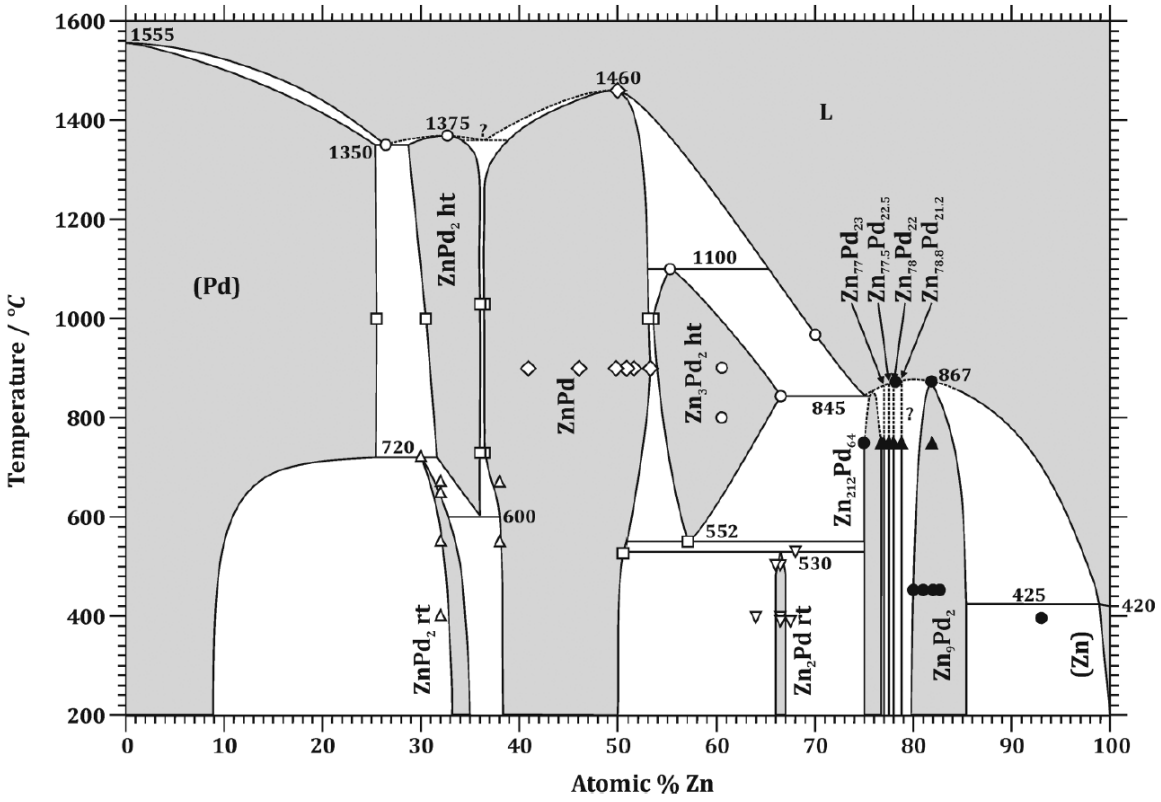

Figure 1- 7: Phase diagram of the binary system Pd-Zn [111].

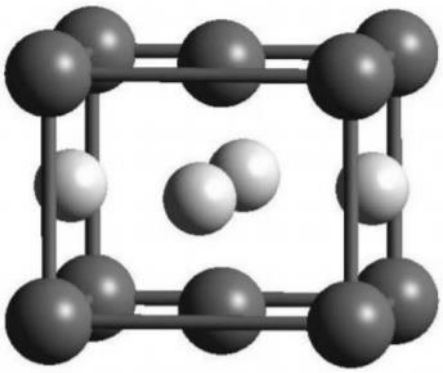

Figure 1- 8: Crystal structure of tetragonal PdZn [111].

Iwasa et al. [113] were the first to investigate Pd/ZnO as a catalyst for methanol steam reforming, a reaction typically catalyzed by Cu. They observed that the catalytic nature of the Pd catalyst was transformed upon addition of Zn. This could be ascribed to the formation of an intermetallic compound PdZn upon reduction. Tsai et al. [114] and Chen et al. [115] have taken interest in why the PdZn catalysts have such similar catalytic properties as Cu. They both

measured the density of states of both structures, see Figure 1- 9, and discovered that the density of states of PdZn closely resembles that of Cu. As mentioned before, in section 1.2.2, Cu-based catalysts are commonly investigated for direct ethanol dehydrogenation. The findings of Tsai et al. and Chen et al. might thus be useful for the synthesis of a more stable, highly active catalyst for ethanol dehydrogenation. This is due to the advantage mentioned earlier, that bimetallic catalysts often are more resistant to sintering, the major drawback of the use of Cu-based catalysts.

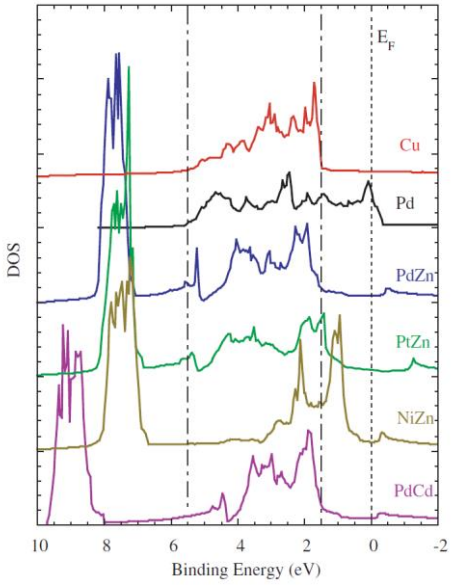

Figure 1- 9: Density of states of Cu and different alloys [114].

Recently, PdZn catalysts have been investigated for a number of reactions, often those that were previously catalyzed by Cu-based catalysts. Mostly investigated is the methanol steam reforming reaction. In this, methanol is converted in the presence of water into CO_2 and H_2.

$$CH_3OH + H_2O \rightleftharpoons CO_2 + 3H_2$$

The reaction is typically carried out at temperatures of 473-573K, pressures of 0.7-3MPa and water to methanol ratios of 0.67-1.5 [112, 116]. The reaction gains current interest from both industry and academia due to its possibility to chemically store hydrogen. Advantages are that methanol is a liquid under ambient conditions which makes it easy to store, transport and handle and it is sulphur-free [117]. It is easily producible at industrial scale from a variety of feedstocks,

i.e., natural gas, biogas, biomass,… [118]. Furthermore, it has a high hydrogen content and due to the presence of only one carbon atom, no carbon-carbon bonds need to be broken, making the reaction less prone to coking [111].

Other reactions investigated for PdZn catalysts are hydrogenation reactions for reactants such as CO_2, acetophenone, … and the water-gas shift reaction.

1.5.2. NiCu catalysts

In contrast with PdZn alloys described above, the phase diagram of NiCu is fairly simple, see Figure 1- 10 [119]. Both elements mix ideally in every composition. The monometallic structures both crystallize in an FCC lattice with lattice parameters of 3.517 and 3.608 Å. Mixing the two metals results in intermediate lattice parameters. At low temperatures however, thermodynamic analysis suggests that the NiCu alloy contains two phases in equilibrium: a copper-rich phase of 80 mol% Cu on the surface and a Ni-rich phase with only 2mol%Cu in the bulk [120].

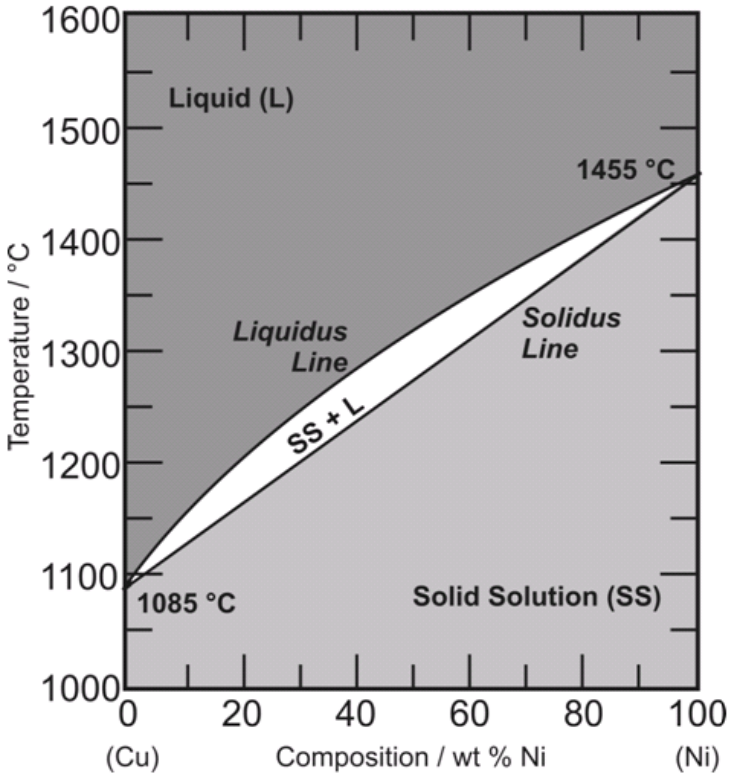

Figure 1- 10: Phase diagram of the binary system Ni-Cu [119].

In contrast with PdZn, the catalytic activity of NiCu is not based on the resemblance with another, monometallic, metal. Both metals retain their original catalytic properties, but exceed these via alloying which makes the catalyst less prone to deactivation, either sintering or coking [121, 122].

The reduction temperature of Ni highly depends on the support. Temperatures between 600K and 1200K have been reported for resp. ZrO_2 supported and hydrotalcite-like compounds supported Ni catalysts [122-125]. Upon the addition of Cu (reduction temperature of ~413K) however, the reduction temperature shifts to significantly lower temperatures, i.e., ~500-600K. This was attributed to hydrogen spillover from reduced Cu to NiO, enhancing the NiO reduction at lower temperature [123]. An advantage of the presence of Ni is that it increases the reduction temperature of the catalyst and thus lowers sintering of the catalyst.

NiCu catalysts are mostly used for alcohol steam reforming, either methanol, ethanol or glycerol was reported [124, 126-132]. In this, the alcohol is transformed into CO_2 and H_2.

$$C_3H_3(OH)_3 + 3H_2O \rightleftharpoons 3\,CO_2 + 7\,H_2$$

$$CH_2CH_3OH + \frac{3}{2}H_2O \rightleftharpoons 2\,CO_2 + 4\,H_2$$

$$CH_3OH + H_2O \rightleftharpoons CO_2 + 3\,H_2$$

Typical conditions used for these reactions are a temperature of 673K to 923K and atmospheric pressure. Ni catalysts are so popular for ethanol and glycerol steam reforming due to their ability to break a C-C bond [124]. However, to further improve the selectivity to H_2, Cu is added. Cu is known for its high activity for the water-gas shift reaction [122]. Thus, all CO produced via ethanol decomposition can be transformed via the water-gas shift reaction into H_2 and CO_2. Cu also improves the Ni dispersion and gives rise to catalysts with a higher BET surface area [124]. Furthermore, less cokes is formed upon addition of Cu [122]. It was also reported that NiCu catalysts are more stable than monometallic Ni catalysts [131].

Another reaction in which NiCu catalysts are commonly investigated is the methane steam reforming to syngas or even to H_2 and cokes [121, 133-137].

$$CH_4 + H_2O \rightleftharpoons CO + 3\,H_2$$

$$CH_4 \rightleftharpoons C + 2H_2$$

This is performed at a temperature of 673K to 1023K, potentially in the presence of CO_2 or H_2O. Here, addition of Cu aids in improving the stability of the catalyst. On Ni catalysts, whiskers of carbon are formed which block the active sites. On NiCu catalysts still those whiskers are formed, but in such a way that the active sites remain accessible.

For both alloy systems discussed above, a general picture is present about the activity and selectivity, but the fundamental understanding of the phenomena occurring during reduction and reaction is missing. Furthermore, the effect that water could play on the catalyst performance is unknown.

1.6. Scope and outline of the thesis

The green production of acetaldehyde, as a platform molecule for the production of chemicals and consumer goods, is a worthy alternative for the use of fossil resources. Direct dehydrogenation seems to be the most valuable route, since no additional reactants are required and hydrogen is a valuable byproduct. Furthermore, the reaction conditions are quite mild.

However, to make this process economically viable, there is a need for innovative catalysts which give rise to a high acetaldehyde selectivity together with a high activity at moderate conditions. Furthermore, stability is of great importance, since irreversible deactivation would be detrimental for the catalyst's use in an industrial plant. Considering the catalysts mentioned in Table 1- 1, none of the catalysts investigated so far were able to fulfill those three requirements. Thus, studying the synthesis of new innovative catalysts on a fundamental level is required to provide an industrially viable candidate for this process.

Besides the activity, selectivity and stability, the catalyst for this process also requires to be easily synthesized industrially and to remain unharmed upon feeding bio-ethanol, i.e., an ethanol-water mixture. As mentioned before, a hydrotalcite-based support seems to be ideal for this purpose, since it is produced via coprecipitation, which is industrially applied, and is hydrothermally stable. As an active site, bimetallic structures are investigated as alternatives for Cu-based catalysts, which have been investigated frequently for ethanol dehydrogenation, but which suffer commonly from deactivation.

First, PdZn catalysts have been pursued since the catalytic properties match those of Cu quite closely. The effects of the activation procedure (Chapter 3) and the synthesis method (Chapter 4) have been investigated. Furthermore, the effect of water on the PdZn catalysts was investigated (Chapter 5), since use of bio-ethanol compared to pure ethanol would be a significant asset for the economic viability of the reaction.

In collaboration with the Institute for Catalysis of Sofia, Bulgaria, also NiCu catalysts have been investigated for ethanol dehydrogenation (Chapter 6). Here, the effect of Ni- and Cu-loading has been assessed as well as the effect of water. Finally, a kinetic model has been constructed to evaluate the performance of the catalyst with the highest industrial potential in a fundamental way (Chapter 7).

1.7.References

[1] W.E. Council, World Energy Resources 2016, in: W.E. Council (Ed.), World Energy Council, United Kingdom, 2016.
[2] M. Bădileanu, M.F.R. Bulearcă, C. Russu, M.-S. Muscalu, C. Neagu, R. Bozga, C. Sima, L.I. Georgescu, D.N. Băleanu, Shale Gas Exploitation– Economic Effects and Risks, Procedia Economics and Finance, 22 (2015) 95-104.
[3] M. Dusselier, P. Van Wouwe, F. de Clippel, J. Dijkmans, D.W. Gammon, B.F. Sels, Mechanistic Insight into the Conversion of Tetrose Sugars to Novel α-Hydroxy Acid Platform Molecules, ChemCatChem, 5 (2013) 569-575.
[4] J. Sun, Y. Wang, Recent Advances in Catalytic Conversion of Ethanol to Chemicals, ACS Catalysis, 4 (2014) 1078-1090.
[5] M. Balat, H. Balat, C. Öz, Progress in bioethanol processing, Progress in Energy and Combustion Science, 34 (2008) 551-573.
[6] C. Manochio, B.R. Andrade, R.P. Rodriguez, B.S. Moraes, Ethanol from biomass: A comparative overview, Renewable and Sustainable Energy Reviews, 80 (2017) 743-755.
[7] R.F. Association, World Fuel Ethanol Production, WWW, 2016.
[8] I.f.e. research, Global Consumption of Fossil Fuels Continues to Increase, 2015.
[9] E.M. Rubin, Genomics of cellulosic biofuels, Nature, 454 (2008) 841-845.
[10] A.W. Bhutto, K. Qureshi, K. Harijan, R. Abro, T. Abbas, A.A. Bazmi, S. Karim, G. Yu, Insight into progress in pre-treatment of lignocellulosic biomass, Energy, 122 (2017) 724-745.
[11] A.D. Moreno, P. Alvira, D. Ibarra, E. Tomás-Pejó, Production of Ethanol from Lignocellulosic Biomass, in: Z. Fang, J.R.L. Smith, X. Qi (Eds.) Production of Platform Chemicals from Sustainable Resources, Springer Singapore, Singapore, 2017, pp. 375-410.
[12] J. Baeyens, Q. Kang, L. Appels, R. Dewil, Y. Lv, T. Tan, Challenges and opportunities in improving the production of bio-ethanol, Progress in Energy and Combustion Science, 47 (2015) 60-88.
[13] A.A. Kiss, D.J.P.C. Suszwalak, Enhanced bioethanol dehydration by extractive and azeotropic distillation in dividing-wall columns, Separation and Purification Technology, 86 (2012) 70-78.
[14] A. Corma, M.E. Domine, S. Valencia, Water-resistant solid Lewis acid catalysts: Meerwein–Ponndorf–Verley and Oppenauer reactions catalyzed by tin-beta zeolite, Journal of Catalysis, 215 (2003) 294-304.
[15] X. Fu, L.A. Clark, W.A. Zeltner, M.A. Anderson, Effects of reaction temperature and water vapor content on the heterogeneous photocatalytic oxidation of ethylene, Journal of Photochemistry and Photobiology A: Chemistry, 97 (1996) 181-186.

[16] A.M. Hilmen, D. Schanke, K.F. Hanssen, A. Holmen, Study of the effect of water on alumina supported cobalt Fischer–Tropsch catalysts, Applied Catalysis A: General, 186 (1999) 169-188.
[17] M. Eckert, G. Fleischmann, R. Jira, H.M. Bolt, K. Golka, Acetaldehyde, Ullmann's Encyclopedia of Industrial Chemistry, Wiley-VCH Verlag GmbH & Co. KGaA2000.
[18] A. News, Global $1.8 Billion Acetaldehyde Market 2018-2022 - Analysis by Process, Derivative, Application and Region - ResearchAndMarkets.com.
[19] M. Intelligence, Acetaldehyde Market - Segmented by Raw Materials, End-use Applications, and Geography - Growth, Trends, and Forecast (2018 - 2023), 2018.
[20] R. Alcala, J.W. Shabaker, G.W. Huber, M.A. Sanchez-Castillo, J.A. Dumesic, Experimental and DFT studies of the conversion of ethanol and acetic acid on PtSn-based catalysts, Journal of Physical Chemistry B, 109 (2005) 2074-2085.
[21] B. Voss, N.C. Schjodt, J.D. Grunwaldt, S.I. Andersen, J.M. Woodley, Kinetics of acetic acid synthesis from ethanol over a Cu/SiO2 catalyst, Applied Catalysis A: General, 402 (2011) 69-79.
[22] J.M. Sun, K.K. Zhu, F. Gao, C.M. Wang, J. Liu, C.H.F. Peden, Y. Wang, Direct Conversion of Bio-ethanol to Isobutene on Nanosized ZnxZryOz Mixed Oxides with Balanced Acid-Base Sites, Journal of the American Chemical Society, 133 (2011) 11096-11099.
[23] M. Leon, E. Diaz, S. Ordonez, Ethanol catalytic condensation over Mg-Al mixed oxides derived from hydrotalcites, Catalysis Today, 164 (2011) 436-442.
[24] C. Angelici, M.E.Z. Velthoen, B.M. Weckhuysen, P.C.A. Bruijnincx, Effect of Preparation Method and CuO Promotion in the Conversion of Ethanol into 1,3-Butadiene over SiO2-MgO Catalysts, Chemsuschem, 7 (2014) 2505-2515.
[25] Y. Nakamura, T. Murayama, W. Ueda, Hydrogen-transfer dehydration between alcohols over V2O3 and MoO2 catalysts for the formation of corresponding alkanes and aldehydes, Journal of Molecular Catalysis A: Chemical, 394 (2014) 137-144.
[26] D.Z. Gao, H.B. Yin, A.L. Wang, L.Q. Shen, S.X. Liu, Gas phase dehydrogenation of ethanol using maleic anhydride as hydrogen acceptor over Cu/hydroxylapatite, Cu/SBA-15, and Cu/MCM-41 catalysts, Journal of Industrial and Engineering Chemistry, 26 (2015) 322-332.
[27] M.X. Gao, Z.Z. Liu, M.H. Zhang, L. Tong, Study on the Mechanism of Butadiene Formation from Ethanol, Catalysis Letters, 144 (2014) 2071-2079.
[28] A.B. Ilin, N.V. Orekhova, M.M. Ermilova, A.B. Yaroslavtsev, Catalytic activity of LiZr2(PO4)(3) nasicon-type phosphates in ethanol conversion process in conventional and membrane reactors, Catalysis Today, 268 (2016) 29-36.
[29] I.C. Freitas, J.M.R. Gallo, J.M.C. Bueno, C.M.P. Marques, The Effect of Ag in the Cu/ZrO2 Performance for the Ethanol Conversion, Topics in Catalysis, 59 (2016) 357-365.
[30] C.R. Ho, S. Shylesh, A.T. Bell, Mechanism and Kinetics of Ethanol Coupling to Butanol over Hydroxyapatite, ACS Catalysis, 6 (2016) 939-948.

[31] S.M. Li, W.P. Wang, X. Liu, X.L. Zeng, W.X. Li, N. Tsubaki, S. Yu, Nitrogen-doped graphene nanosheets as metal-free catalysts for dehydrogenation reaction of ethanol, Rsc Advances, 6 (2016) 13450-13455.
[32] C. Wang, G. Garbarino, L.F. Allard, F. Wilson, G. Busca, M. Flytzani-Stephanopoulos, Low-Temperature Dehydrogenation of Ethanol on Atomically Dispersed Gold Supported on ZnZrOx, ACS Catalysis, 6 (2016) 210-218.
[33] S. Letichevsky, P.C. Zonetti, P.P.P. Reis, J. Celnik, C.R.K. Rabello, A.B. Gaspar, L.G. Appel, The role of m-ZrO2 in the selective oxidation of ethanol to acetic acid employing PdO/m-ZrO2, Journal of Molecular Catalysis A: Chemical, 410 (2015) 177-183.
[34] F. Hosoglu, J. Faye, K. Mareseanu, G. Tesquet, P. Miquel, M. Capron, O. Gardoll, J.-F. Lamonier, C. Lamonier, F. Dumeignil, High resolution NMR unraveling Cu substitution of Mg in hydrotalcites–ethanol reactivity, Applied Catalysis A: General, 504 (2015) 533-541.
[35] D.T. Mai, A.I. Pylinina, Mikhailenko, II, Activity of calcined Ag,Cu,Au/TiO2 catalysts in the dehydrogenation/dehydration of ethanol, Russian Journal of Physical Chemistry A, 89 (2015) 1184-1188.
[36] O.V. Larina, P.I. Kyriienko, S.O. Soloviev, Ethanol Conversion to 1,3-Butadiene on ZnO/MgO-SiO2 Catalysts: Effect of ZnO Content and MgO:SiO2 Ratio, Catalysis Letters, 145 (2015) 1162-1168.
[37] B. Caglar, M. Olus Ozbek, J.W. Niemantsverdriet, C.J. Weststrate, The effect of C-OH functionality on the surface chemistry of biomass-derived molecules: ethanol chemistry on Rh(100), Physical Chemistry Chemical Physics, 18 (2016) 30117-30127.
[38] J.L. Cheong, Y. Shao, S.J.R. Tan, X. Li, Y. Zhang, S.S. Lee, Highly Active and Selective Zr/MCF Catalyst for Production of 1,3-Butadiene from Ethanol in a Dual Fixed Bed Reactor System, ACS Sustainable Chemistry & Engineering, 4 (2016) 4887-4894.
[39] S. Da Ros, M.D. Jones, D. Mattia, M. Schwaab, E. Barbosa-Coutinho, R.C. Rabelo-Neto, F.B. Noronha, J.C. Pinto, Microkinetic analysis of ethanol to 1,3-butadiene reactions over MgO-SiO2 catalysts based on characterization of experimental fluctuations, Chemical Engineering Journal, 308 (2017) 988-1000.
[40] S.G. Chuklina, A.I. Pylinina, L.I. Podzorova, N.A. Mikhailina, I.I. Mikhalenko, Ethanol dehydrogenation on copper catalysts with ytterbium stabilized tetragonal ZrO2 support, Russian Journal of Physical Chemistry A, 90 (2016) 2370-2376.
[41] G.V. Mamontov, M.V. Grabchenko, V.I. Sobolev, V.I. Zaikovskii, O.V. Vodyankina, Ethanol dehydrogenation over Ag-CeO2/SiO2 catalyst: Role of Ag-CeO2 interface, Applied Catalysis A: General, 528 (2016) 161-167.
[42] J. Franckaerts, G.F. Froment, Kinetic study of the dehydrogenation of ethanol, Chemical Engineering Science, 19 (1964) 807-818.

[43] I.C. Freitas, S. Damyanova, D.C. Oliveira, C.M.P. Marques, J.M.C. Bueno, Effect of Cu content on the surface and catalytic properties of Cu/ZrO2 catalyst for ethanol dehydrogenation, Journal of Molecular Catalysis A: Chemical, 381 (2014) 26-37.
[44] N. Kanoun, M.P. Astier, G.M. Pajonk, New vanadium-copper-zinc catalysts, their characterization and use in the catalytic dehydrogenation of ethanol, Applied Catalysis, 70 (1991) 225-236.
[45] Y.-J. Tu, Y.-W. Chen, Effects of Alkaline-Earth Oxide Additives on Silica-Supported Copper Catalysts in Ethanol Dehydrogenation, Industrial & Engineering Chemistry Research, 37 (1998) 2618-2622.
[46] Y.-J. Tu, Y.-W. Chen, C. Li, Characterization of unsupported copper—chromium catalysts for ethanol dehydrogenation, Journal of Molecular Catalysis, 89 (1994) 179-189.
[47] Y.-J. Tu, C. Li, Y.-W. Chen, Effect of chromium promoter on copper catalysts in ethanol dehydrogenation, Journal of Chemical Technology & Biotechnology, 59 (1994) 141-147.
[48] Y.T. Law, W.H. Doh, W. Luo, S. Zafeiratos, A comparative study of ethanol reactivity over Ni, Co and NiCo-ZnO model catalysts, Journal of Molecular Catalysis A: Chemical, 381 (2014) 89-98.
[49] L.V. Mattos, E. Noronha, Hydrogen production for fuel cell applications by ethanol partial oxidation on Pt/CeO2 catalysts: the effect of the reaction conditions and reaction mechanism, Journal of Catalysis, 233 (2005) 453-463.
[50] X.B. Li, E. Iglesia, Selective catalytic oxidation of ethanol to acetic acid on dispersed Mo-V-Nb mixed oxides, Chemistry-a European Journal, 13 (2007) 9324-9330.
[51] B.S. Jiang, R. Chang, Y.C. Lin, Partial Oxidation of Ethanol to Acetaldehyde over LaMnO3-Based Perovskites: A Kinetic Study, Industrial & Engineering Chemistry Research, 52 (2013) 37-42.
[52] A. Ciftci, D.A.J.M. Ligthart, P. Pastorino, E.J.M. Hensen, Nanostructured ceria supported Pt and Au catalysts for the reactions of ethanol and formic acid, Applied Catalysis B: Environmental, 130–131 (2013) 325-335.
[53] J.C. Bauer, G.M. Veith, L.F. Allard, Y. Oyola, S.H. Overbury, S. Dai, Silica-Supported Au-CuOx Hybrid Nanocrystals as Active and Selective Catalysts for the Formation of Acetaldehyde from the Oxidation of Ethanol, ACS Catalysis, 2 (2012) 2537-2546.
[54] A.S. Blokhina, I.A. Kurzina, V.I. Sobolev, K.Y. Koltunov, G.V. Mamontov, O.V. Vodyankina, Selective oxidation of alcohols over Si3N4-supported silver catalysts, Kinetics and Catalysis, 53 (2012) 477-481.
[55] V.I. Sobolev, E.V. Danilevich, K.Y. Koltunov, Role of vanadium species in the selective oxidation of ethanol on V2O5/TiO2 catalysts, Kinetics and Catalysis, 54 (2013) 730-734.
[56] M.C. Holz, K. Tolle, M. Muhler, Gas-phase oxidation of ethanol over Au/TiO2 catalysts to probe metal-support interactions, Catalysis Science & Technology, 4 (2014) 3495-3504.

[57] I. Abdullahi, T.J. Davis, D.M. Yun, J.E. Herrera, Partial oxidation of ethanol to acetaldehyde over surface-modified single-walled carbon nanotubes, Applied Catalysis A: General, 469 (2014) 8-17.
[58] L. Artiglia, S. Agnoli, L. Savio, J. Pal, E. Celasco, M. Rocca, F. Bondino, E. Magnano, C. Castellarin-Cudia, F.P. Netzer, G. Granozzi, From Vanadia Nanoclusters to Ultrathin Films on TiO2(110): Evolution of the Yield and Selectivity in the Ethanol Oxidation Reaction, ACS Catalysis, 4 (2014) 3715-3723.
[59] E.A. Redina, A.A. Greish, I.V. Mishin, G.I. Kapustin, O.P. Tkachenko, O.A. Kirichenko, L.M. Kustov, Selective oxidation of ethanol to acetaldehyde over Au-Cu catalysts prepared by a redox method, Catalysis Today, 241 (2015) 246-254.
[60] J.M. Hidalgo, Z. Tišler, D. Kubička, K. Raabova, R. Bulanek, (V)/Hydrotalcite, (V)/Al2O3, (V)/TiO2 and (V)/SBA-15 catalysts for the partial oxidation of ethanol to acetaldehyde, Journal of Molecular Catalysis A: Chemical, 420 (2016) 178-189.
[61] M.A. Nadeem, G.I.N. Waterhouse, H. Idriss, A study of ethanol reactions on O2-treated Au/TiO2. Effect of support and metal loading on reaction selectivity, Surface Science, 650 (2016) 40-50.
[62] J. Xu, X.-C. Xu, X.-J. Yang, Y.-F. Han, Silver/hydroxyapatite foam as a highly selective catalyst for acetaldehyde production via ethanol oxidation, Catalysis Today, 276 (2016) 19-27.
[63] G.M. Mullen, E.J. Evans, I. Sabzevari, B.E. Long, K. Alhazmi, B.D. Chandler, C.B. Mullins, Water Influences the Activity and Selectivity of Ceria-Supported Gold Catalysts for Oxidative Dehydrogenation and Esterification of Ethanol, ACS Catalysis, 7 (2017) 1216-1226.
[64] J. Wang, R. Huang, Y. Zhang, J. Diao, J. Zhang, H. Liu, D. Su, Nitrogen-doped carbon nanotubes as bifunctional catalysts with enhanced catalytic performance for selective oxidation of ethanol, Carbon, 111 (2017) 519-528.
[65] A.F.F. de Lima, P.C. Zonetti, C.P. Rodrigues, L.G. Appel, The first step of the propylene generation from renewable raw material: Acetone from ethanol employing CeO2 doped by Ag, Catalysis Today, 279, Part 2 (2017) 252-259.
[66] V.V. Dutov, G.V. Mamontov, V.I. Sobolev, O.V. Vodyankina, Silica-supported silver-containing OMS-2 catalysts for ethanol oxidative dehydrogenation, Catalysis Today, 278, Part 1 (2016) 164-173.
[67] W. Zhang, A. Desikan, S.T. Oyama, Effect of Support in Ethanol Oxidation on Molybdenum Oxide, The Journal of Physical Chemistry, 99 (1995) 14468-14476.
[68] H. Idriss, E.G. Seebauer, Reactions of ethanol over metal oxides, Journal of Molecular Catalysis A: Chemical, 152 (2000) 201-212.
[69] Y. Guan, E.J.M. Hensen, Ethanol dehydrogenation by gold catalysts: The effect of the gold particle size and the presence of oxygen, Applied Catalysis A: General, 361 (2009) 49-56.

[70] R.D. Weinstein, A.R. Ferens, R.J. Orange, P. Lemaire, Oxidative dehydrogenation of ethanol to acetaldehyde and ethyl acetate by graphite nanofibers, Carbon, 49 (2011) 701-707.
[71] L. Jelemensky, B.F.M. Kuster, G.B. Marin, Kinetic modelling of multiple steady-states for the oxidation of aqueous ethanol with oxygen on a carbon supported platinum catalyst, Chemical Engineering Science, 51 (1996) 1767-1776.
[72] E. Santacesaria, A. Sorrentino, R. Tesser, M. Di Serio, A. Ruggiero, Oxidative dehydrogenation of ethanol to acetaldehyde on V2O5/TiO2-SiO2 catalysts obtained by grafting vanadium and titanium alkoxides on silica, Journal of Molecular Catalysis A: Chemical, 204–205 (2003) 617-627.
[73] J.A.A. van den Tillaart, B.F.M. Kuster, G.B. Marin, Oxidative dehydrogenation of aqueous ethanol on a carbon supported platinum catalyst, Applied Catalysis A: General, 120 (1994) 127-145.
[74] H. Zhou, J.Y. Wang, X. Chen, C.-L. O'Young, S.L. Suib, Studies of oxidative dehydrogenation of ethanol over manganese oxide octahedral molecular sieve catalysts, Microporous and Mesoporous Materials, 21 (1998) 315-324.
[75] P. Aghaei, R.J. Berger, Reaction kinetics investigation of the selective oxidation of aqueous ethanol solutions with air over a Au/TiO2 catalyst, Applied Catalysis B: Environmental, 132–133 (2013) 195-203.
[76] R. Tesser, V. Maradei, M. Di Serio, E. Santacesaria, Kinetics of the Oxidative Dehydrogenation of Ethanol to Acetaldehyde on V2O5/TiO2−SiO2 Catalysts Prepared by Grafting, Industrial & Engineering Chemistry Research, 43 (2004) 1623-1633.
[77] F.-W. Chang, W.-Y. Kuo, K.-C. Lee, Dehydrogenation of ethanol over copper catalysts on rice husk ash prepared by incipient wetness impregnation, Applied Catalysis A: General, 246 (2003) 253-264.
[78] T. Baskaran, J. Christopher, A. Sakthivel, Progress on layered hydrotalcite (HT) materials as potential support and catalytic materials, Rsc Advances, 5 (2015) 98853-98875.
[79] K. Klemkaite, I. Prosycevas, R. Taraskevicius, A. Khinsky, A. Kareiva, Synthesis and characterization of layered double hydroxides with different cations (Mg, Co, Ni, Al), decomposition and reformation of mixed metal oxides to layered structures, Central European Journal of Chemistry, 9 (2011) 275-282.
[80] W.Y. Hernandez, J. Lauwaert, P. Van Der Voort, A. Verberckmoes, Recent advances on the utilization of layered double hydroxides (LDHs) and related heterogeneous catalysts in a lignocellulosic-feedstock biorefinery scheme, Green Chemistry, 19 (2017) 5269-5302.
[81] T. Selvam, A. Inayat, W. Schwieger, Reactivity and applications of layered silicates and layered double hydroxides, Dalton Transactions, 43 (2014) 10365-10387.

[82] D.P. Debecker, E.M. Gaigneaux, G. Busca, Exploring, Tuning, and Exploiting the Basicity of Hydrotalcites for Applications in Heterogeneous Catalysis, Chemistry – A European Journal, 15 (2009) 3920-3935.
[83] P.P. Sun, G. Siddiqi, M.F. Chi, A.T. Bell, Synthesis and characterization of a new catalyst Pt/Mg(Ga)(Al)O for alkane dehydrogenation, Journal of Catalysis, 274 (2010) 192-199.
[84] A.L. McKenzie, C.T. Fishel, R.J. Davis, Investigation of the surface structure and basic properties of calcined hydrotalcites, Journal of Catalysis, 138 (1992) 547-561.
[85] M. Ogawa, H. Kaiho, Homogeneous Precipitation of Uniform Hydrotalcite Particles, Langmuir, 18 (2002) 4240-4242.
[86] T. Sato, H. Fujita, T. Endo, M. Shimada, A. Tsunashima, Synthesis of hydrotalcite-like compounds and their physico-chemical properties, Reactivity of Solids, 5 (1988) 219-228.
[87] D. Tichit, M.H. Lhouty, A. Guida, B.H. Chiche, F. Figueras, A. Auroux, D. Bartalini, E. Garrone, Textural Properties and Catalytic Activity of Hydrotalcites, Journal of Catalysis, 151 (1995) 50-59.
[88] M. Shiraga, T. Kawabata, D. Li, T. Shishido, K. Komaguchi, T. Sano, K. Takehira, Memory effect-enhanced catalytic ozonation of aqueous phenol and oxalic acid over supported Cu catalysts derived from hydrotalcite, Applied Clay Science, 33 (2006) 247-259.
[89] A.E. Palomares, J.G. Prato, F. Rey, A. Corma, Using the “memory effect” of hydrotalcites for improving the catalytic reduction of nitrates in water, Journal of Catalysis, 221 (2004) 62-66.
[90] InvestMine.
[91] A. Lossin, Copper, Ullmann's Encyclopedia of Industrial Chemistry, Wiley-VCH Verlag GmbH & Co. KGaA2000.
[92] M.V. Twigg, M.S. Spencer, Deactivation of Copper Metal Catalysts for Methanol Decomposition, Methanol Steam Reforming and Methanol Synthesis, Topics in Catalysis, 22 (2003) 191-203.
[93] D.Z. Gao, Y.H. Feng, H.B. Yin, A.L. Wang, T.S. Jiang, Coupling reaction between ethanol dehydrogenation and maleic anhydride hydrogenation catalyzed by Cu/Al2O3, Cu/ZrO2, and Cu/ZnO catalysts, Chemical Engineering Journal, 233 (2013) 349-359.
[94] A.J. Marchi, J.L.G. Fierro, J. Santamaría, A. Monzón, Dehydrogenation of isopropylic alcohol on a Cu/SiO2 catalyst: a study of the activity evolution and reactivation of the catalyst, Applied Catalysis A: General, 142 (1996) 375-386.
[95] N. Iwasa, N. Takezawa, Reforming of ethanol - dehydrogenation to ethyl-acetate and steam reforming to acetic-acid over copper-based catalysts, Bulletin of the Chemical Society of Japan, 64 (1991) 2619-2623.

[96] S. Fujita, N. Iwasa, H. Tani, W. Nomura, M. Arai, N. Takezawa, Dehydrogenation of ethanol over Cu/ZnO catalysts prepared from various coprecipitated precursors, Reaction Kinetics and Catalysis Letters, 73 (2001) 367-372.
[97] E. Santacesaria, G. Carotenuto, R. Tesser, M. Di Serio, Ethanol dehydrogenation to ethyl acetate by using copper and copper chromite catalysts, Chemical Engineering Journal, 179 (2012) 209-220.
[98] S. Zhu, X. Gao, Y. Zhu, Y. Zhu, H. Zheng, Y. Li, Promoting effect of boron oxide on Cu/SiO2 catalyst for glycerol hydrogenolysis to 1,2-propanediol, Journal of Catalysis, 303 (2013) 70-79.
[99] C.K.S. Choong, L. Huang, Z. Zhong, J. Lin, L. Hong, L. Chen, Effect of calcium addition on catalytic ethanol steam reforming of Ni/Al2O3: II. Acidity/basicity, water adsorption and catalytic activity, Applied Catalysis A: General, 407 (2011) 155-162.
[100] J. Wu, Y. Shen, C. Liu, H. Wang, C. Geng, Z. Zhang, Vapor phase hydrogenation of furfural to furfuryl alcohol over environmentally friendly Cu–Ca/SiO2 catalyst, Catalysis Communications, 6 (2005) 633-637.
[101] R. Kam, C. Selomulya, R. Amal, J. Scott, The influence of La-doping on the activity and stability of Cu/ZnO catalyst for the low-temperature water–gas shift reaction, Journal of Catalysis, 273 (2010) 73-81.
[102] C.E.M. Guarido, D.V. Cesar, M. Souza, M. Schmal, Ethanol reforming and partial oxidation with Cu/Nb2O5 catalyst, Catalysis Today, 142 (2009) 252-257.
[103] C.-S. Chen, W.-H. Cheng, S.-S. Lin, Enhanced activity and stability of a Cu/SiO2 catalyst for the reverse water gas shift reaction by an iron promoter, Chemical Communications, (2001) 1770-1771.
[104] B. Coq, F. Figueras, Structure–activity relationships in catalysis by metals: some aspects of particle size, bimetallic and supports effects, Coordination Chemistry Reviews, 178–180, Part 2 (1998) 1753-1783.
[105] A.K. Singh, Q. Xu, Synergistic Catalysis over Bimetallic Alloy Nanoparticles, ChemCatChem, 5 (2013) 652-676.
[106] H.-L. Jiang, Q. Xu, Recent progress in synergistic catalysis over heterometallic nanoparticles, Journal of Materials Chemistry, 21 (2011) 13705-13725.
[107] N. Toshima, T. Yonezawa, Bimetallic nanoparticles-novel materials for chemical and physical applications, New Journal of Chemistry, 22 (1998) 1179-1201.
[108] D. Wang, Y. Li, Bimetallic Nanocrystals: Liquid-Phase Synthesis and Catalytic Applications, Advanced Materials, 23 (2011) 1044-1060.
[109] B. Coq, F. Figueras, Bimetallic palladium catalysts: influence of the co-metal on the catalyst performance, Journal of Molecular Catalysis A: Chemical, 173 (2001) 117-134.

[110] N. Iwasa, O. Yamamoto, R. Tamura, M. Nishikubo, N. Takezawa, Difference in the reactivity of acetaldehyde intermediates in the dehydrogenation of ethanol over supported Pd catalysts, Catalysis Letters, 62 (1999) 179-184.
[111] M. Armbruster, M. Behrens, K. Fottinger, M. Friedrich, E. Gaudry, S.K. Matam, H.R. Sharma, The Intermetallic Compound ZnPd and Its Role in Methanol Steam Reforming, Catalysis Reviews-Science and Engineering, 55 (2013) 289-367.
[112] K. Föttinger, PdZn based catalysts: connecting electronic and geometric structure with catalytic performance, Catalysis, 25 (2013) 77-117.
[113] N. Iwasa, S. Masuda, N. Ogawa, N. Takezawa, Steam reforming of methanol over Pd/ZnO: Effect of the formation of PdZn alloys upon the reaction, Applied Catalysis A: General, 125 (1995) 145-157.
[114] A. Pang Tsai, S. Kameoka, Y. Ishii, PdZn=Cu: Can an Intermetallic Compound Replace an Element?, Journal of the Physical Society of Japan, 73 (2004) 3270-3273.
[115] Z.-X. Chen, K.M. Neyman, A.B. Gordienko, N. Rösch, Surface structure and stability of PdZn and PtZn alloys: Density-functional slab model studies, Physical Review B, 68 (2003) 075417.
[116] P. Häussinger, R. Lohmüller, A.M. Watson, Hydrogen, 2. Production, Ullmann's Encyclopedia of Industrial Chemistry, Wiley-VCH Verlag GmbH & Co. KGaA2000.
[117] T. Conant, A.M. Karim, V. Lebarbier, Y. Wang, F. Girgsdies, R. Schlögl, A. Datye, Stability of bimetallic Pd–Zn catalysts for the steam reforming of methanol, Journal of Catalysis, 257 (2008) 64-70.
[118] Z.-Q. Huang, B. Long, C.-R. Chang, A theoretical study on the catalytic role of water in methanol steam reforming on PdZn(111), Catalysis Science & Technology, 5 (2015) 2935-2944.
[119] W.D. Callister, Materials science and engineering : an introduction, Wiley, New York, 2007.
[120] K.C. Khulbe, R.S. Mann, Nature of Ni-Cu Alloys and Their Role in Chemical Reactions, Catalysis Reviews, 24 (1982) 311-328.
[121] H.-W. Chen, C.-Y. Wang, C.-H. Yu, L.-T. Tseng, P.-H. Liao, Carbon dioxide reforming of methane reaction catalyzed by stable nickel copper catalysts, Catalysis Today, 97 (2004) 173-180.
[122] R.L. Manfro, T.P.M.D. Pires, N.F.P. Ribeiro, M.M.V.M. Souza, Aqueous-phase reforming of glycerol using Ni-Cu catalysts prepared from hydrotalcite-like precursors, Catalysis Science & Technology, 3 (2013) 1278-1287.
[123] R. Pérez-Hernández, G. Mondragón Galicia, D. Mendoza Anaya, J. Palacios, C. Angeles-Chavez, J. Arenas-Alatorre, Synthesis and characterization of bimetallic Cu–Ni/ZrO2 nanocatalysts: H2 production by oxidative steam reforming of methanol, International Journal of Hydrogen Energy, 33 (2008) 4569-4576.

[124] P.V. Tuza, R.L. Manfro, N.F.P. Ribeiro, M.M.V.M. Souza, Production of renewable hydrogen by aqueous-phase reforming of glycerol over Ni–Cu catalysts derived from hydrotalcite precursors, Renewable Energy, 50 (2013) 408-414.
[125] A.A. Smirnov, S.A. Khromova, O.A. Bulavchenko, V.V. Kaichev, A.A. Saraev, S.I. Reshetnikov, M.V. Bykova, L.I. Trusov, V.A. Yakovlev, Effect of the Ni/Cu ratio on the composition and catalytic properties of nickel-copper alloy in anisole hydrodeoxygenation, Kinetics and Catalysis, 55 (2014) 69-78.
[126] A. Carrero, J.A. Calles, A.J. Vizcaíno, Hydrogen production by ethanol steam reforming over Cu-Ni/SBA-15 supported catalysts prepared by direct synthesis and impregnation, Applied Catalysis A: General, 327 (2007) 82-94.
[127] B. Dou, C. Wang, Y. Song, H. Chen, Y. Xu, Activity of Ni–Cu–Al based catalyst for renewable hydrogen production from steam reforming of glycerol, Energy Conversion and Management, 78 (2014) 253-259.
[128] S. Velu, K. Suzuki, M. Vijayaraj, S. Barman, C.S. Gopinath, In situ XPS investigations of Cu1−xNixZnAl-mixed metal oxide catalysts used in the oxidative steam reforming of bio-ethanol, Applied Catalysis B: Environmental, 55 (2005) 287-299.
[129] A.J. Vizcaíno, A. Carrero, J.A. Calles, Hydrogen production by ethanol steam reforming over Cu–Ni supported catalysts, International Journal of Hydrogen Energy, 32 (2007) 1450-1461.
[130] W. Wang, Production of Hydrogen by Steam Reforming of Bio-Ethanol Over Nickel-Copper Bimetallic Catalysts, International Journal of Green Energy, 6 (2009) 92-103.
[131] F. Wang, Y. Li, W. Cai, E. Zhan, X. Mu, W. Shen, Ethanol steam reforming over Ni and Ni–Cu catalysts, Catalysis Today, 146 (2009) 31-36.
[132] C. Wang, B. Dou, H. Chen, Y. Song, Y. Xu, X. Du, L. Zhang, T. Luo, C. Tan, Renewable hydrogen production from steam reforming of glycerol by Ni–Cu–Al, Ni–Cu–Mg, Ni–Mg catalysts, International Journal of Hydrogen Energy, 38 (2013) 3562-3571.
[133] C.A. Bernardo, I. Alstrup, J.R. Rostrup-Nielsen, Carbon deposition and methane steam reforming on silica-supported Ni-Cu catalysts, Journal of Catalysis, 96 (1985) 517-534.
[134] Y. Echegoyen, I. Suelves, M.J. Lázaro, M.L. Sanjuán, R. Moliner, Thermo catalytic decomposition of methane over Ni–Mg and Ni–Cu–Mg catalysts: Effect of catalyst preparation method, Applied Catalysis A: General, 333 (2007) 229-237.
[135] A.C. Lua, H.Y. Wang, Decomposition of methane over unsupported porous nickel and alloy catalyst, Applied Catalysis B: Environmental, 132-133 (2013) 469-478.
[136] T.V. Reshetenko, L.B. Avdeeva, Z.R. Ismagilov, A.L. Chuvilin, V.A. Ushakov, Carbon capacious Ni-Cu-Al2O3 catalysts for high-temperature methane decomposition, Applied Catalysis A: General, 247 (2003) 51-63.

[137] Y. Shen, A.C. Lua, Polyol synthesis of nickel–copper based catalysts for hydrogen production by methane decomposition, International Journal of Hydrogen Energy, 40 (2015) 311-321.

Chapter 2:

Materials and methods

This chapter discusses the material synthesis and all experimental methods used throughout this thesis. First, the different synthesis methods will be discussed, i.e., wet incipient impregnation and coprecipitation. Basic characterization and in situ measurements allowed the determination of the material and catalyst properties. *Material* will be used when referring to the unreduced, thus unactive material. *Catalyst* will be used for the reduced, active material. More advanced characterization methods were also used to support the basic characterization and to determine certain aspects of the material behavior which could not be resolved with basic characterization.

Steady-state activity testing is performed in the HTK-MI set-up to determine the catalyst performance at different conditions and feeds. Also, transient experiments, i.e., TAP, have been performed to assess the reasons for deactivation.

To assess the reaction phenomena in a plug flow reactor, no mass or heat transfer limitations should be present in the reactor, nor complex flow patterns. Data solely depending on reaction phenomena are called intrinsic kinetics. The criteria for it will be listed here.

2.1.Material synthesis

Throughout this thesis, all materials discussed are hydrotalcite-based. This means that they mainly consist of Mg and Al oxides, as explained in Chapter 1. Of course, also other elements can be added during the synthesis of the support, such that a one-pot material synthesis methodology is obtained. *Hydrotalcite* is the material before calcination, which still exists of layers of hydroxides. *Mixed oxide* is the material after calcination, which is also denoted as $Mg(Al)O_x$ if the material only consists of Mg and Al. If other elements are added to the support synthesis, these are mentioned after (Al), also in brackets, representing the replacement of Al by that element. As such, highly active catalysts are aimed for which consist of active nanoparticles. Two synthesis methods were applied, i.e., wet incipient impregnation and coprecipitation. Via wet incipient impregnation, active metals are added to an existing support by addition in a solvent, here, ethanol, and stirring. Coprecipitation requires the addition of all elements into a solution which, in the presence of a base, precipitates.

2.1.1. PdZn materials

The hydrotalcite support Mg(Al)OH was prepared via the coprecipitation of 116.6g $Mg(NO_3)_2.6\ H_2O$ and 17.0g $Al(NO_3)_3.9\ H_2O$ in 400ml deionized water with 2.4g Na_2CO_3 and 22.6g NaOH in 400 ml deionized water. The two solutions were added dropwise under constant stirring at 323K to 100ml deionized water which served as a buffer. After complete addition of the solutions, the mixture remained at this temperature for 30min. The aging of the material was performed at room temperature for 20h. Afterwards, the material was washed to remove all $NaNO_3$ and Na_2CO_3 and subsequently filtered and dried at 393K. Calcination in air was done by heating to 873K at a rate of 2.5K min^{-1}, after which it was maintained at this temperature for 2h. This concludes the formation of the mixed oxide $Mg(Al)O_x$.

Wet incipient impregnation of 1wt%Pd and 1.2wt%Zn was performed on the prepared hydrotalcite-based support in ethanol in a porcelain cup of 50ml for 5g of material under constant

stirring at 400rpm at 313K, leading to PdO,ZnO/Mg(Al)O_x. After reduction, its activated form is achieved which will be denoted as PdZn/Mg(Al)O_x throughout the thesis. First Pd in ethanol solution was added to the support, afterwards Zn in ethanol solution was added. Drying and calcination of the material was performed as mentioned above.

The Mg(Al)(Pd)(Zn)O_x material was prepared via a similar procedure as mentioned above, but now $Pd(NO_3)_2.2\ H_2O$ and $Zn(NO_3)_2.6\ H_2O$ were already added to the first solution at the expense of $Al(NO_3).9\ H_2O$. Thus, the complete material was prepared in one step. Again a loading of 1wt% Pd and 1.2wt% Zn was aimed at.

PdZn/ZnO was prepared as a reference catalyst. ZnO was first synthesized via addition of NH_4OH to $Zn(NO_3)_2.6H_2O$ dissolved in H_2O. Thereby ZnO is precipitated and subsequently filtered off and dried. It is then calcined with the same procedure as mentioned before for the Mg(Al)O_x material. Subsequently, 1wt% Pd is added to ZnO via wet incipient impregnation via the addition of a solution of $Pd(NO_3)_2.2H_2O$ in ethanol to the ZnO support under constant stirring. Afterwards, the material is again dried and calcined via the procedures as mentioned above.

2.1.2. *NiCu materials*

Ni-Cu-Mg-Al samples were synthesized in a five-neck 5-liter glass reactor equipped with a steam jacket, stirrer, pH electrode, thermocouple and reflux condenser. The carbonate forms of hydrotalcite-based support were obtained by coprecipitation at 333K and constant pH = 9.5–10, using '*pro analyze*' purity grade nitrate salts of the corresponding metals and Na_2CO_3 as a precipitating agent. A certain volume of distilled water was placed in the reactor, heated to 333K, and adjusted with 0.9M Na_2CO_3 solution to reach pH = 9.5. The mixed Ni-Cu-Mg-Al solution [total metal concentration of 0.5M and Mg^{2+}/Al^{3+} ratio of 5/1] and the precipitant were introduced simultaneously drop-wise to the reactor controlled by two peristaltic pumps under vigorous stirring. The resulting slurry was aged for 60 min in the mother liquor under stirring at 333K and pH = 9.5–10. Then it was filtered off, washed thoroughly with distilled water up to absence of

$NaNO_3$ ions in the filtrate; the presence of $NaNO_3$ ions was verified by solution of diphenylamine in H_2SO_4. The as-synthesized hydrotalcite was dried at 378K for 20 h. Calcination in air was done by heating to 873K at a rate of 2.5K min^{-1}, after which it was maintained at this temperature for 2h.

2.2. *Catalyst characterization*

2.2.1. *Elemental analysis*

The bulk chemical composition of the materials was determined by means of inductively coupled plasma optical emission spectrometry (ICP-OES) (ICAP 6500 system, Thermo Scientific). The calcined and spent samples of all materials were analyzed.

The samples were mineralized by fusion with sodium peroxide and dissolution in a mixture of HNO_3, HF and $HClO_4$. In the spectrometer, the sample is vaporized and conducted via an argon gas flow to the argon plasma. There, ions are formed which are excited by the thermal energy. When they return to their ground state, photons are emitted which are characteristic for the element. As such, the concentrations of the elements in the sample are measured.

2.2.2. *N_2 adsorption*

To determine the surface area and the pore properties, N_2 adsorption at 77K was performed in a Gemini V Micromeritics set-up. As such the surface area is calculated via the Brunauer – Emmett – Teller equation which requires measuring 5 points. The pore volume and pore diameter are determined via the method described by Barrett – Joyner - Halenda which needs 15 points. The pore size distribution is based on 40 points as described by Harkins and Jura. Of course, all these methods are related with each other, i.e., if the pore volume increases, also the surface area should increase. Thus, in the following chapters, only the BET surface area of all catalysts is mentioned. These properties were measured for the calcined, reduced and used samples.

The samples were first degassed for 12h at 473K to remove any volatile adsorbates from the surface. Then, they are placed in the Micromeritics set-up where they are being suspended in liquid nitrogen, such that a constant temperature of 77K is reached.

2.2.3. *STEM*

To determine the active particle size, support topology and the location of the active metals in the catalyst, STEM-EDX was performed. Via impacting an electron beam onto the sample, different signals are produced, such as secondary electrons, backscattered electrons, … . Combining these signals allows for the determination of the topology of the structure, which is represented as a picture.

2.2.3.1. *PdZn catalysts*

Dark field scanning transmission electron microscopy (STEM) was used for structural analysis. Energy dispersive X-ray spectrometry (EDX) was used for local chemical analysis. These techniques were implemented using a JEOL JEM-2200FS, Cs-corrected microscope operated at 200 kV, which was equipped with a Schottky-type field-emission gun (FEG) and EDX JEOL JED-2300D.

All samples were deposited by immersion onto a lacey carbon film on a Cu support grid. The particle size distribution could be determined with the SimpleMeasure program.

2.2.3.2. *NiCu catalysts*

To prepare the specimens for TEM analysis, the materials were mixed with ethanol using an ultrasonic bath. A few drops of the obtained suspensions were deposited onto Au TEM grid covered with carbon. High angle annular dark field scanning transmission electron microscopy images and energy dispersive X-ray (EDX) maps were acquired on the FEI Osiris microscope equipped with a Super-X detector and operated at 200 kV. On the EDX spectra, the Cu-K line is at 8.04 keV and the Ni-K line is at 7.47 keV.

2.2.4. *TPR & TPO*

Other important catalyst properties are the reduction and oxidation temperature of the materials as well as the determination of the amount of cokes which accumulated on the catalyst during reaction. These properties were determined via temperature programmed reduction (TPR) and oxidation (TPO) in an Autochem II 2920 of Micromeritics equipped with a TCD detector and an OmniStar mass spectrometer of Pfeiffer.

For TPR, the calcined material was placed in a quartz tube with an internal diameter of 10mm diameter and prevented from blow through via quartz wool. The reduction was performed with 5wt% H_2/He, employing a temperature ramp of 10K min^{-1} starting from room temperature to 873K and dwelling there for 600s. The same method was used for the PdZn and the NiCu catalysts.

Figure 2- 1 represents the TPR profile of the impregnated PdZn/Mg(Al)O_x and incorporated PdZn/Mg(Al)(Pd)(Zn)O_x catalyst. The profile was corrected for the catalyst mass. Several contributions in the profile could be attributed to different phase transformations, e.g. the small shoulder in the peak of PdZn/Mg(Al)(Pd)(Zn)O_x might be related with reduction of PdO to Pd whereas the big peak takes into account the reduction of PdO and ZnO with the formation of PdZn.

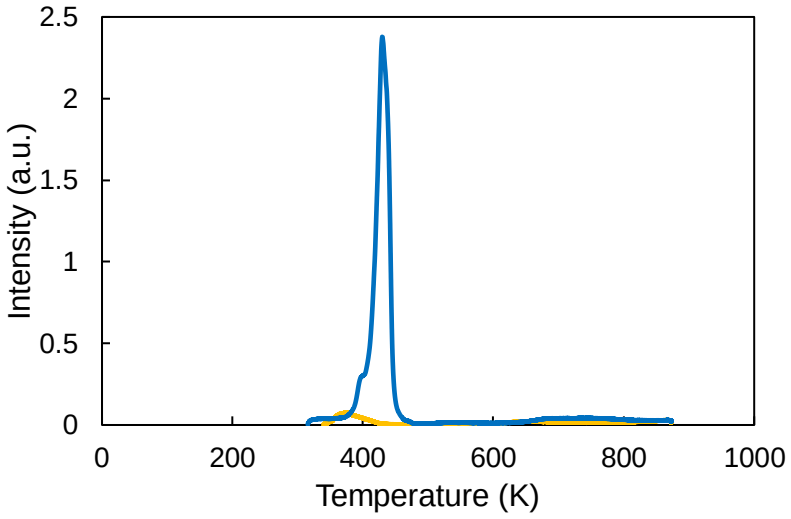

Figure 2- 1: H_2-TPR profile of impregnated PdZn/Mg(Al)O_x (orange) and incorporated PdZn/Mg(Al)(Pd)(Zn)O_x (blue) at a ramp of 10K min^{-1}.

For TPO, the catalysts after reaction were used and installed as mentioned above. The oxidation was performed with 10mol% O_2/He at a temperature ramp of 5K min^{-1} starting from room temperature to 873K and dwelling there for 600s. To analyze the results, the MS data are coupled with the TCD data to determine the temperature at which cokes were burnt off. The amount of cokes burnt off is determined via calibration of the MS signal with a CO_2 pulse containing 1ml of CO_2. For all PdZn and NiCu catalysts, this method was used.

2.2.5. CO chemisorption

To determine the number of active sites of the PdZn catalysts, CO chemisorption was performed in an Autochem II 2920. The measurement was performed on PdZn/ZnO and PdZn/Mg(Al)(Pd)(Zn)O_x in a quartz tube with an internal diameter of 10 mm. Prior to CO chemisorption, in-situ reduction and oxidation treatments, i.e., H_2-O_2-H_2-O_2-H_2, on PdZn/Mg(Al)(Pd)(Zn)O_x and only reduction on Pd/ZnO were performed at 823K with resp. 5 vol% H_2 in He atmosphere and 100% O_2. At a temperature of 200K, achieved via immersion of the tube in isopropanol ice, 1wt% CO in He atmosphere was pulsed with a pulse loop of 1ml onto the catalyst. After 10 pulses no significant change was observed in the surface area of the measured peak, hence, it could be assumed that the catalyst surface was saturated with CO.

2.2.6. N_2O oxidation

To determine the number of active sites of the NiCu catalysts, also CO (and H_2) chemisorption was attempted, but this did not lead to satisfactory results. Therefore, oxidation by N_2O was performed via the method described by Gervasini et al. [1] in an Autochem II 2920. This is done in a three step procedure. First, the material was fully reduced via H_2-TPR. Secondly, oxidation by N_2O at fixed temperature was performed, which oxidized only the outer layer of every active particle. Thirdly, H_2-TPR was repeated, reducing again the CuO and NiO layer. Thereby, titration of the amount of H_2 needed for reduction was performed. Since reduction of CuO and NiO proceeds via the following reaction, one hydrogen molecule is needed per Cu and Ni atom.

$$CuO + H_2 \rightleftharpoons Cu + H_2O$$

$$NiO + H_2 \rightleftharpoons Ni + H_2O$$

Thus, the number of active sites equals the amount of H_2 consumed. The average particle size can be determined from the number of active sites:

$$\emptyset_{av} = \frac{10^7 * SK * C_M * W_{Cu}}{SF * N_A * mol_{H_2} * \rho_{Cu}} \qquad \textbf{Equation 1}$$

With:

$\emptyset_{av}$ average diameter (nm);

SK constant depending on shape of Cu (6);

C_M amount of Cu atoms in one m^2 of metal Cu ($1.47\ 10^{19}$ atoms m^{-2});

W_{Cu} Cu loading (wt%);

SF Stoichiometric factor (2);

N_A Constante of Avogadro ($6.02\ 10^{23}$ atoms mol^{-1});

Mol_{H2} Number of mol H_2 adsorbed;

P_{Cu} Density of Cu (8.92 g cm^{-3}).

For the first H_2-TPR, 5wt%H_2/He was sent on the sample while applying a temperature ramp of 8K min^{-1} starting from room temperature to 873K. Isothermal N_2O oxidation was performed with a 1vol%N_2O/He at a temperature of 303K. The second H_2-TPR was performed with a heating rate of 20K min^{-1} to 1073K.

The H_2-TPR measured for all NiCu catalysts after N_2O oxidation are represented in Figure 2-2. These curves correspond with the typical curve obtained for TPR after N_2O oxidation, i.e., a high peak which corresponds with the number of active sites at low temperatures, i.e., 300 to 500K, and a small peak at higher temperatures, i.e., 900 to 1100K, which is the deep reduction of the support [1].

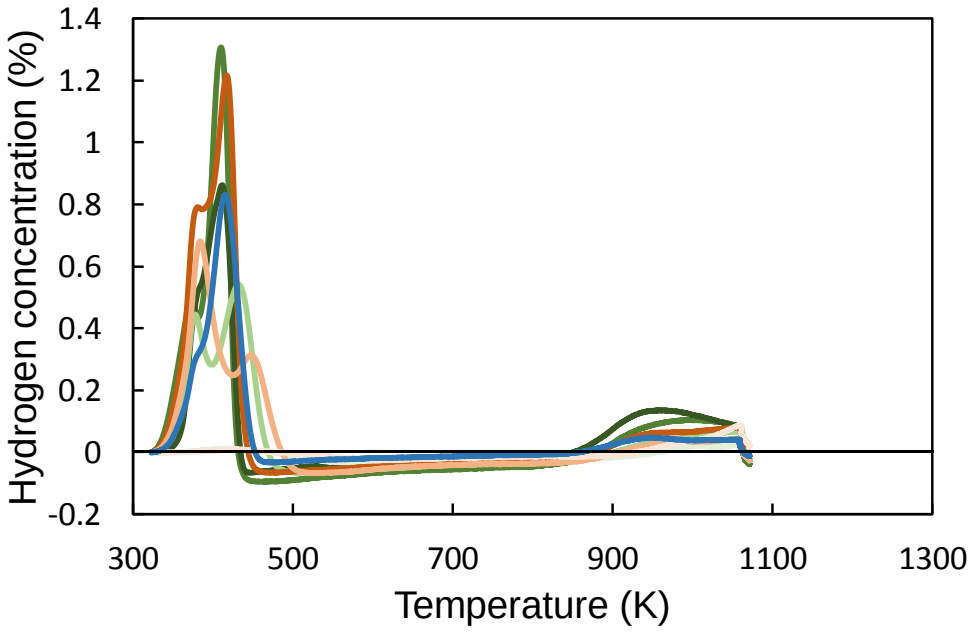

Figure 2- 2: TPR profiles after N_2O oxidation of 10wt%Cu/Mg(Al)(Cu)O_x (blue), 0.5wt%Ni-Xwt%Cu/Mg(Al)(Ni)(Cu)O_x (X=0, 5, 10) (green, darker=higher loading) and 1wt%Ni-Xwt%Cu/Mg(Al)(Ni)(Cu)O_x (X= 0, 5, 10, 20) (orange, darker=higher loading).

2.2.7. *(in-situ) XRD*

To determine the different phases that are present on the materials and the changes upon reduction, oxidation or reaction, in-situ X-ray diffraction (XRD) measurements were performed. Full XRD scans were measured on calcined or used samples and prior to and after each in-situ

measurement. They have been acquired in a Bruker-AXS D8 Discover which emits a Cu Kα radiation with a wavelength of 0.154nm, see Figure 2- 3.

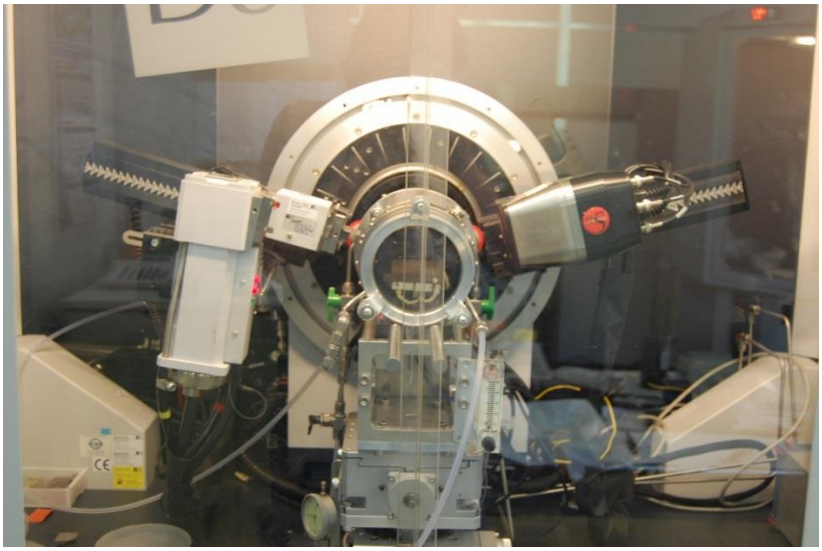

Figure 2- 3:Picture of the in-situ XRD set-up with the Cu Kα source on the left and the detector on the right.

For the in-situ measurements, an in-house built reaction chamber with a Kapton foil for X-ray transmission was used. A linear detector covers an angular range of 20° with a resolution of 0.1° and an acquisition time of 10s. 10mg of sample was evenly spread on a Si wafer. No interaction between the sample and the wafer was observed. Prior to the analysis, the chamber was evacuated to 4Pa and flushed. For the redox cycles, a temperature ramp of 50K min^{-1} was applied to 823K at which the cycles were performed. Reduction was performed with 10% H_2/He and oxidation with pure oxygen. The O_2-TPO was performed with a temperature ramp of 10K min^{-1} to 873K. The data have been compared with standardized XRD maps of the different elements to determine the phases present on the materials.

For the PdZn catalysts, the results are described in the next chapters. For the NiCu catalysts, XRD measurements were performed but no Ni, Cu or NiCu was detected. Probably, the particles are too small to be detectable.

2.2.8. XPS

To determine the composition at the surface of the PdZn catalysts, X-ray photoelectron spectroscopy (XPS) was performed. As such, segregation or depletion of the surface could be determined. This is especially important for the catalysts used in this work, since the active metals need to diffuse from the support to the surface. A S-Probe Monochromatized XPS spectrometer from Surface Science Instruments (VG) with a monochromatic 1486.6eV AlKα X-ray source was used. The spectra were recorded with a source power of 200W. The samples were tilted 45° relative to the analyzer. The base pressure at measurement was 5 10^{-7}Pa. Detailed windows of C1s, Al2s, Mg2s, Pd3d, Zn2p and O1s were recorded with a pass energy of 107.8eV and a step of 0.1eV. Energy calibration was performed by alignment of the C1s signal to 284.6eV.

2.2.9. XAS

In order to investigate the PdZn alloy formation in both impregnated and incorporated materials, X-ray absorption spectroscopy (XAS) experiments were performed at the DUBBLE beamline of the 6GeV European Synchrotron Radiation Facility (ESRF) in Grenoble (France) in 16 bunch mode, see Figure 2- 4. Via XAS, detailed measurements on the oxidation state of Pd and Zn were performed which allows to determine more precisely how the formation of the active catalyst proceeds.

Figure 2- 4: Picture of the DUBBLE XAS set-up.

Both the Pd K-edge, at 24365eV, and the Zn K-edge, at 9673eV, were measured in transmission mode. For both edges, pellets where prepared with a mass of about 150mg. No dilution was used. The optics alignment and energy referencing were performed using a Pd and Zn foil, respectively. The XANES (X-ray absorption near edge structure) scans took ± 2 minutes, while EXAFS (extended X-ray absorption fine structure) scans were recorded in ± 6 minutes. Gas flows were delivered via the DUBBLE gas rig system [2]. An in-house built Microtomo Furnace was used with a Ni sample holder and a clamp hole of 3mm. It was heated by a Thermocoax 40W Temp. An EXAFS scan of the as prepared sample was taken under He flow of 20.46 µmol s^{-1}. The calcination was performed in 8.87 µmol s^{-1} 20wt% O_2/He with a temperature ramp of 20K min^{-1} to 873K. The sample was then cooled in 20wt% O_2/He and an EXAFS scan was measured. Subsequent reduction was performed in 20.46 µmol s^{-1} 5wt% H_2/N_2 also at a temperature ramp of 20K min^{-1} to 823K. After cooling in 5wt% H_2/N_2, an EXAFS measurement was performed. To finalize the program, the sample was heated to 823K and 2 oxidation-reduction cycles were performed. Oxidation with 8.87 µmol s^{-1} 20wt% O_2/He and reduction with 20.46 µmol s^{-1} 5wt% H_2/N_2 took 5 minutes each per cycle with 2.5 minutes intermediate flushing with 1.23mol s^{-1} He. In total the procedure thus took

25 minutes. Experiments were repeated at both edges. At the Zn-edge, an extra experiment was performed on both catalysts to elucidate the effect of redox cycling on the formation of the catalyst. The calcined material was subjected to 12 redox cycles with 5 minutes of oxidation, 5 minutes of reduction and 2.5 minutes flushing with He in between. XAS data processing was performed with Athena of the Demeter 0.9.24 software package [3].

2.2.10. *CO-DRIFTS*

In order to have some indication on the formation of a NiCu alloy, CO-DRIFTS was performed on a Tensor 27 of Bruker with a MCT detector. With this technique, the vibration frequency of CO on the active metals, in this case Ni and Cu, can be determined and compared with literature to determine the adsorption configuration, i.e., linear, bridged, threefold,… Furthermore, the exact vibration frequency is indicative for the nature of the atom, e.g. alloyed or pure monometallic. The in-situ DRIFTS cell is mounted in a Selector™ accessory. All measurements were performed in absorbance mode between 600 cm^{-1} and 4000 cm^{-1} with 1000 scans with a resolution of 4 cm^{-1}. The data analysis has been performed using the OPUS 7.2 software of Bruker. The spectra have been converted to Kubelka-Munk units and the background was subtracted. The calcined material was mixed with KBr, i.e., the inert material for FTIR, in a material/KBr-ratio of 1/10. This was done to assure a good resolution of the spectra. The diluted material was put in the in-situ cell and all remaining gas molecules were removed with a vacuum pump. Then, a flow of 100% H_2 at a rate of 99µmol s^{-1} was added and the sample was heated to 773K and kept at that temperature for 30min. Then, the sample was cooled down in H_2 and the flow was switched to 100% He at a rate of 99 µmol s^{-1}. A background sample was measured. 99µmol s^{-1} 1wt%CO/He was then sent onto the sample while performing 5 measurements of 1000 scans. The measurement was performed in the presence of CO because CO is easily removed from the surface [4].

2.3. *Activity testing*

Activity testing of the investigated catalysts is of utmost importance to assess its industrial potential. High activity, acetaldehyde selectivity and stability are desired, with turn-over frequencies ranging from 10^{-2} – 10^{2} s^{-1}. In the HTK-MI, an almost complete automation of the set-up control aids in providing reliable data. It is always aimed to measure intrinsic kinetics, i.e., only the reaction kinetics are probed and no heat or mass transfer limitations are present. Here, the requirements to satisfy intrinsic kinetics will be mentioned and in the section 2.4, the criteria for intrinsic kinetics will be discussed. Next to the investigation to assess the steady-state, transient experiments were performed in the TAP-3 set-up to determine the phenomena occurring during the start-up of the reaction. This can be performed in the TAP-3 set-up.

2.3.1. HTK-MI

The activity measurements were performed in a high-throughput kinetics mechanistic investigation (HTK-MI) set-up comprising 8 plug flow reactors with an internal diameter of 0.011m and a length of 0.9m [5, 6]. Figure 2- 5 represents one reactor block in the HTK-MI.

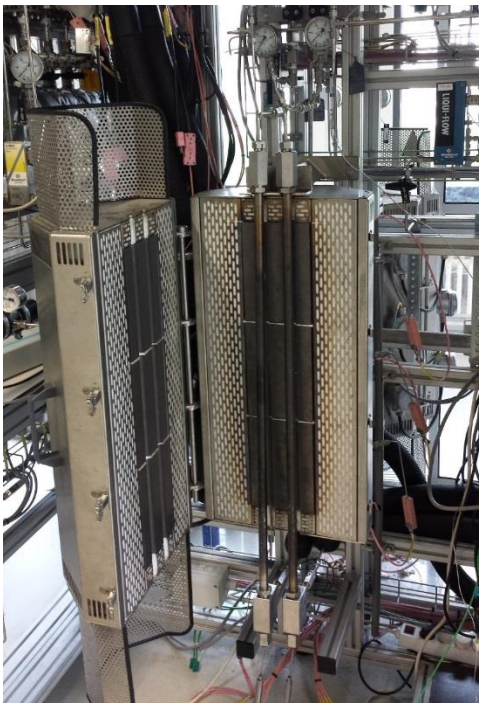

Figure 2- 5: Picture of a reactor block of HTK-MI with two plug flow reactors in one oven.

The online product analysis was conducted with a 3000 microGC of Agilent equipped with four complementary columns and thermal conductivity detectors. The product composition was calculated via response factors determined from the analysis of a known reference mixture and validated by comparison with the response factors as determined by Dietz [7].

The reaction was carried out at a temperature of 533K, an ethanol partial pressure of 23kPa, a total pressure of 0.5MPa and a space time of 36kg_{cat} s mol^{-1} as a reference experiment and these are the conditions used unless stated otherwise. Ethanol was fed as a liquid and mixed with N_2 in a molar N_2/ethanol-ratio of 20 before entering the reactor. As such, the reactant mixture was vaporized and condensation was avoided throughout the reactor and analysis section.

For all catalysts investigated, the occurrence of intrinsic kinetics has been assured. The experimental settings required for intrinsic kinetics differ per catalyst type. By adjusting them, excessive pressure drop and internal mass transfer limitations have been avoided. Non-porous sintered α-Al_2O_3 was used as inert material in the catalyst bed to avoid heat transfer limitations. It was also placed upfront of the catalyst bed to ensure a homogeneous distribution of the reactant

mixture. The absence of external mass and heat transfer limitations, as well as the establishment of the ideal plug flow regime, was verified via the corresponding correlations [8]. The carbon balance was measured for all experiments and was within 5%.

The conversion was defined as the amount of reacted moles of ethanol, i.e., $F_{EtOH,0}$-F_{EtOH}, to the initial number of moles, i.e., $F_{EtOH,0}$.

$$X = \frac{F_{EtOH,0} - F_{EtOH}}{F_{EtOH,0}} \quad \textbf{Equation 2}$$

Product selectivities, S_i, are determined on an atomic carbon basis towards product i and, hence, are defined by the ratio of the number of moles of i produced, i.e., F_i, corrected for the number of carbon atoms in the compound, a_i, to the number of reacted moles of ethanol, i.e., $F_{EtOH,0}$-F_{EtOH}, also corrected for the number of carbon atoms in ethanol, i.e., 2:

$$S_i = \frac{a_i F_i}{2(F_{EtOH,0} - F_{EtOH})} \quad \textbf{Equation 3}$$

The space time yield of acetaldehyde, STY_{AcH}, is defined as the ratio of the molar outlet flow rate of acetaldehyde, F_{AcH}, and the mass of the catalyst, W.

$$STY_{AcH} = \frac{F_{AcH}}{W} \quad \textbf{Equation 4}$$

The average turnover frequency is defined as the ratio of the molar flow rate of converted ethanol $F^0_{EtOH} - F_{EtOH}$ to the number of active sites N_{AC}.

$$TOF = \frac{F^0_{EtOH} - F_{EtOH}}{N_{AC}} \quad (s^{-1}) \quad \textbf{Equation 5}$$

2.3.1.1. PdZn catalysts

2g of catalyst was required per run, which was pelletized into flakes and crushed into pellets of 250-600μm. Prior to reaction, an in-situ activation procedure was applied consisting of a H_2 reduction at 823K for 30min using a flow rate of 5.7 10^{-4}mol s^{-1}, further denoted as 'single

reduction', or by alternating a pure H_2 and air flow rate of 5.7 10^{-4}mol s^{-1}, i.e., H_2-air-H_2-air-H_2, further denoted as 'cycled reduction'. In between the H_2 and air flows, the reactor was flushed with N_2 to avoid the simultaneous presence of H_2 and O_2 in the reactor. Catalyst regeneration was performed via oxidation with air and subsequent reduction with H_2 at 823K with a flow rate amounting to 5.7 10^{-4}mol s^{-1} for the singly reduced sample and by alternating H_2 and air with a flow rate of 5.7 10^{-4}mol s^{-1} for the cycled reduced sample, i.e., the same procedure as for the activation.

The Pd/ZnO catalyst was reduced with single reduction at 823K by sending a pure H_2 flow with a flow rate of 5.7 10^{-4} mol s^{-1}.

The impact of water on the catalyst performance after cycled reduction was assessed via the following sequence of operating conditions. First, as liquid part of the feed, pure ethanol was used. These conditions are denoted as '100wt%ethanol'. Subsequently, 30wt%H_2O/ethanol was employed, thereby keeping the ethanol partial pressure and space time constant, i.e., the amount of water is compensated by lowering the N_2 dilution. These conditions are denoted as '30wt%H_2O/ethanol'. Afterwards, the liquid feed was switched back to pure ethanol, denoted as '100wt%ethanol after water feed'. Finally, the previously mentioned activation procedure was repeated to 'regenerate' the catalyst and 100wt%ethanol was again used as liquid feed to the reactor. These conditions are denoted as '100wt%ethanol after regeneration'.

2.3.1.2. *NiCu catalysts*

Pellets with a diameter of 100-250µm were required to assure intrinsic kinetics. 0.1g or 0.2g was loaded in the reactor depending on the required space times. As an activation treatment, H_2 reduction was performed. Here, cycled reduction was avoided, because oxidation might cause sintering of the Cu particles. At room temperature and atmospheric pressure, 5.7 10^{-4}mol s^{-1} of 100% H_2 was sent to the reactor. Then, the reactor was heated to 773K in approximately 30min. The reactor was kept at that temperature for 30min and then cooled down to reaction temperature, i.e., 533K. Next to testing the deactivation behavior, the effect of water was tested

on the catalysts. For this, the feed was changed from a pure ethanol feed to a 30wt%H_2O/ethanol feed. Again, the ethanol partial pressure was unchanged by accounting for the presence of water in the N_2 dilution.

For the NiCu catalysts, the influence of temperature, pressure and space time on the catalyst behavior has been tested. The conditions vary with temperatures from 453 to 533K, pressures of 0.5-1.5MPa and space time from 0.9 to 27 kg_{cat} s mol^{-1}.

2.3.2. *TAP-3*

To determine the coking phenomena occurring on the PdZn catalyst in the first instances of reaction, transient experiments were performed. These were performed in a TAP-3 reactor set-up originally described by Gleaves [9], see Figure 2- 6. TAP is short for Temporal Analysis of Products. The methodology is based on short pulses at low pressures to determine the different steps that occur initially on a catalytic system. This technique might also be used for more thorough understanding of the reaction network, but this was not the purpose of the experiments performed here.

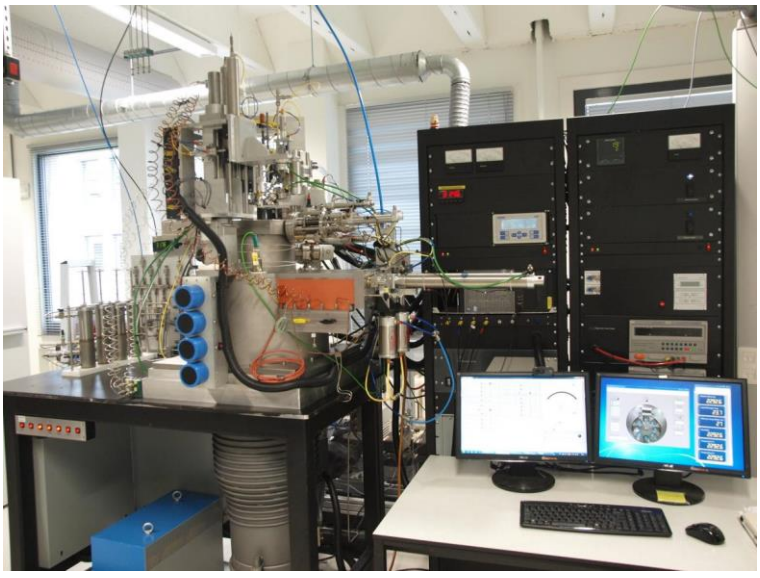

Figure 2- 6: Picture of the TAP-3 set-up.

The reactor is kept at a high vacuum of 10^{-5}-10^{-6}Pa, created via a turbomolecular and a diffusion pump. A quartz micro-reactor of 47.5 mm length with an internal diameter of 4mm is packed in the so-called thin zone reactor model. In this configuration, 15 mg of catalyst is sandwiched between layers of inert material. This thin zone reactor implementation is required since this assures the changes in the catalyst to occur uniformly, whereas a more thick catalyst bed would have differences throughout the catalyst bed which could influence the measurements. The experiments were conducted on the incorporated catalyst, both on the one activated by single reduction and on the one activated by cycled reduction. Ethanol feed was prepared via the injection of 850µl ethanol in a liquid vaporizing chamber filled with He and heated to 423K. The reactant feeding lines and the pulse valves were heated to 423K. Single-pulse experiments of ethanol were performed at 533K. Each pulse train in an experiment contains 210 pulses. The number of moles of ethanol in each injected pulse amounted to 9.3 10^{-8}mol and 2.7 10^{-8}mol for the single reduction and cycled reduction, respectively. Data acquisition was done via an Extrel 150QC quadrupole mass spectrometer. A collection time of 3s was used to record the entire pulse response.

2.4. *Intrinsic kinetics*

For all experiments performed at the HTK-MI, it was verified whether intrinsic kinetics were measured. An experiment is called intrinsic if only reaction phenomena are measured. Hence, ideal plug flow and lack of heat and mass flow phenomena can be considered. Intrinsic kinetics are obtained if the observed rate of formation doesn't deviate more than 5% from the intrinsic rate of formation:

$$\left|\frac{R^{obs} - R^{ins}}{R^{ins}}\right| < 0.05 \qquad \textbf{Equation 6}$$

with:

R^{obs} the observed rate of formation (mol kg^{-1}_{cat} s^{-1});

R^{ins} the intrinsic rate of formation (mol kg^{-1}_{cat} s^{-1}).

All equations or restrictions were obtained from Berger et al. [8]. The criteria used for the different catalysts were mentioned in section 2.3.

2.4.1. Restrictions at the reactor scale

2.4.1.1. Ideal plug flow regime

For ideal plug flow, the flow through the reactor should be uniform in both the radial and axial direction. No short cuts might be present due to, e.g., loose packing of the catalyst. For radial dispersion, a rule of thumb is chosen:

$$\frac{d_t}{d_p} > 8 \qquad \textbf{Equation 7}$$

with:

d_t the reactor (tube) diameter (m);

d_p the pellet diameter (m).

For the axial dispersion, the following equation should be satisfied:

$$\frac{L}{d_p} > \frac{20}{Pe'_a} \ln\left(\frac{1}{1 - X_A}\right) \qquad \textbf{Equation 8}$$

with:

L length of the reactor (m);

X_A conversion (-);

Pe'_a Peclet number defined as $\frac{u d_p}{D_{er}}$ (-);

u velocity (m s^{-1});

D_{er} radial diffusion coefficient.

However, Gierman has concluded that this criterion could be relaxed by using a factor 8 instead of 20 [10]. For an *n*-th order reaction, the right-hand side of expression Equation 8 should be multiplied with n.

2.4.1.2. *Axial isothermicity or maximum dilution degree*

In order to achieve axial isothermicity, the heat generated should be removed at a rate that equals the production rate. By adding inert material to the catalyst bed, the surface area of heat transfer increases and hence the axial isothermicity is attained. However, diluting the catalyst bed can affect the conversion and hence a maximum ratio exists given by:

$$b < \frac{1}{1 + 10X_{dil}\left(\frac{d_p}{L}\right)} \qquad \textbf{Equation 9}$$

with:

b the maximum dilution degree ($m^3_{inert}\ m^{-3}_{inert+cat}$);

X_{dil} conversion obtained with diluted bed (-).

2.4.1.3. *Radial isothermicity*

In order to prevent the occurrence of a radial temperature profile throughout the reactor, the ratio of the surface area to the volume should be high thereby resulting in an efficient removal of the heat generated. Several criteria have been proposed, but here the two parameter model is chosen to determine the temperature profile in the reactor. In the two parameter model, both the effective radial heat conductivity of the catalyst bed λ_{er} and the heat transfer coefficient between the catalyst bed and the reactor wall α_w should be known. For these parameters, correlations can be found in literature. In order to obtain a maximum deviation of 5% from the intrinsic rate of formation, the following criterion should be satisfied:

$$\frac{|\Delta_r H| r_v^{obs} (1-\varepsilon_B)(1-b) d_t^2}{\lambda_{er} T_{wi}} < \frac{1.6 \frac{R T_{wi}}{E_a}}{1 + 8 \frac{\lambda_{er}}{\alpha_w d_t}}$$ **Equation 10**

with:

λ_{er} effective radial heat conductivity of the catalyst bed ($Wm_r^{-2}K^{-1}$)

α_w heat transfer coefficient between bed and reactor wall ($Wm_r^{-2}K^{-1}$)

$|\Delta_r H|$ the reaction enthalpy ($J\ mol^{-1}$);

r_v^{obs} observed volumetric rate of formation ($mol\ m^{-3}_{cat}\ s^{-1}$);

$(1-\varepsilon_B)$ the fraction of the reactor volume occupied by the catalyst bed ($m_B^3\ m_r^{-3}$);

$(1-b)$ the fraction of the catalyst bed occupied by the catalyst ($m_p^3\ m_B^{-3}$);

T_{wi} the internal wall temperature (K);

E_a activation energy ($kJ\ mol^{-1}$);

R universal gas constant ($8.31\ J\ K^{-1}\ mol^{-1}$).

2.4.1.4. Pressure drop gradient

When considering the pressure in a tubular reactor, a pressure drop might occur due to friction with the catalyst bed. The pressure drop should be minimized in order to obtain the same reaction conditions throughout the reactor. The following criterion should be valid for intrinsic kinetics:

$$\Delta p < 0.2\ p_{tot}$$ **Equation 11**

with:

Δp pressure drop (Pa)

P_{tot} total pressure (Pa)

2.4.2. *Restrictions at the pellet scale*

On the pellet scale, both internal and external mass and heat transport limitations can be encountered. However, for the acquirement of an intrinsic kinetics dataset, these transport limitations should be minimized. These internal and external transport phenomena result in , see also Figure 2- 8:

1. Internal temperature gradients
2. Internal concentration gradients
3. External concentration gradients
4. External temperature gradients

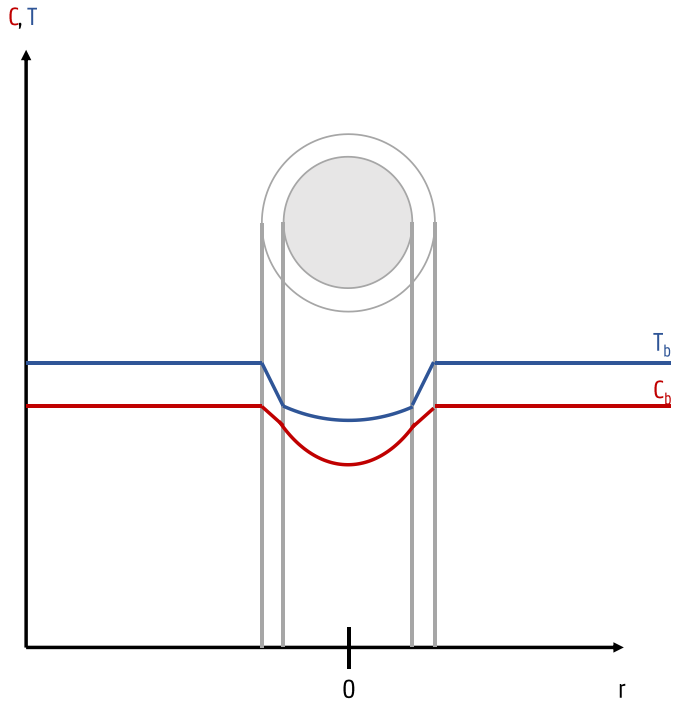

Figure 2- 7: Representation of the temperature and concentration profile in and along the pellet. Around the pellet, the boundary layer is illustrated via a grey circle. Red: concentration profile; blue: temperature profile.

In lab scale experimental set-ups, the absence of external temperature gradients is the first criterion that is not fulfilled, whereas internal temperature gradients are seldom present.

2.4.2.1. *External concentration gradients*

External concentration gradients occur in the boundary layer around the pellet due to the faster diffusion into the pellet and reaction in the pellet. It can be represented by the film model, as depicted in Figure 2- 8.

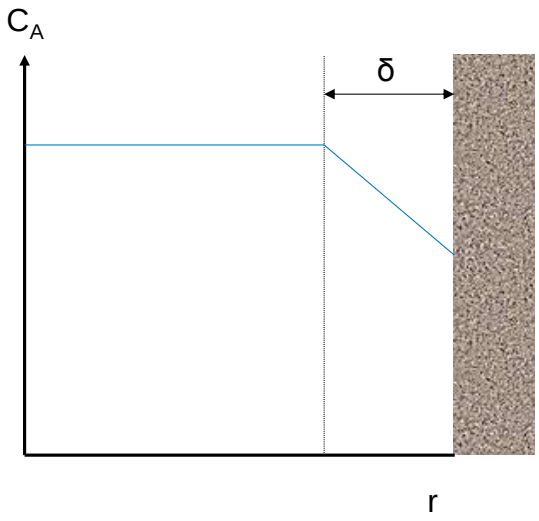

Figure 2- 8: Concentration profile according to the film model. δ is the width of the boundary layer.

The criterion to avoid external concentration limitations is:

$$\frac{\left|R_{w,A}^{obs}\right|}{k_{fA}a_s C_{A,b}} < 0.03 \qquad \textbf{Equation 12}$$

with:

k_{fA} mass transfer coefficient ($m_f^{-3}\ m_i^{-2}\ s^{-1}$)

a_s specific external surface area ($m_i^2\ kg_{cat}^{-1}$)

$C_{A,b}$ concentration of A in the bulk ($mol\ m_f^{-3}$)

The k_{fA} coefficient can be easily calculated from the j_D factor according to Chilton-Colburn:

$$j_D = \frac{k_{fA} y_{fA} \rho}{\phi_m} Sc^{\frac{2}{3}}$$ **Equation 13**

With:

Sc the Schmidt number defined as $\mu (\rho D_A)^{-1}$.

y_{fA} film factor (mol fraction)

D_A molecular diffusion coefficient ($m_f^2 s^{-1}$)

ρ density of the gas phase (kg m_f^{-3})

ϕ_m total mass flux (kg $m_r^{-2} s^{-1}$)

μ dynamic viscosity (kg $m_r^{-1} s^{-1}$)

For packed bed reactors with gas phase conditions, the correlation of Gupta and Thodos can be used [11]:

$$j_D = 0.01 + \frac{0.863}{Re_p^{0.58} - 0.483} \quad for\ Re_p > 1$$ **Equation 14**

With:

j_D j factor of Chilton and Colburn (-);

Re_p Reynolds number of particle (-).

2.4.2.2. *External temperature gradients*

As already stated, a deviation in observed rate of formation relative to the intrinsic rate of formation is easily achieved due to external temperature gradients. This is due to the difficulty to remove the generated heat. The criterion to assess the absence of external temperature gradients is:

$$\frac{\rho_p d_p |-\Delta_r H| r_w^{obs}}{\alpha T_b} < \frac{0.3 R T_b}{E_a}$$ **Equation 15**

With:

ρ_p the density of the pellet (kg m^{-3});

d_p pellet diameter (m);

$\Delta_r H$ the reaction enthalpy (J mol^{-1});

r_w^{obs} the rate of consumption of A per mass of catalyst (mol kg_{cat}^{-1} s^{-1});

α the heat transfer coefficient (W m_i^{-2} K^{-1});

T_b the bulk temperature (K).

2.4.2.3. Internal concentration gradients

In the pellet, transport by diffusion and reaction occur simultaneously. The criterion to neglect the occurrence of internal concentration gradients is:

$$\frac{(n+1)\rho_p r_w^{obs}}{2 a_v^2 D_{eA} C_{A,s}} \ll 1$$ **Equation 16**

with:

n the reaction order (-);

D_{eA} the effective diffusion coefficient, corrected with the porosity and tortuosity of the pellet (m^2 s^{-1});

$C_{A,s}$ the concentration of A at the external surface (mol m^{-3});

a_v volumetric interface surface area (m^2_i m^{-3}).

2.4.2.4. *Internal temperature gradients*

As already stated, inside the pellet, temperature gradients are encountered exceptionally on lab scale. However, it is necessary to derive a criterion in order to assure the intrinsic nature of the kinetic dataset acquired. Via the application of the conservation of energy, the following equation is obtained:

$$\frac{d_p r_w^{obs} \rho_p |\Delta_r H|}{\lambda_p T_s} < \frac{3.0 R T_s}{E_a} \qquad \textbf{Equation 17}$$

with:

λ_p the heat conductivity of the catalyst pellet (W m^{-1} K^{-1}).

2.4.3. *Restrictions applied to 1wt%Ni-10wt%Cu/Mg(Al)(Ni)(Cu)O_x*

Before measuring a kinetic dataset, the restrictions on the intrinsic kinetics should be assessed with the previously described correlations. In Table 2- 1, the minimum and maximum restrictions for 1wt%Ni-10wt%Cu/Mg(Al)(Ni)(Cu)O_x are presented. The reaction conditions differ from these because of practical reasons. One example for this is that the pellet size should be higher than 100µm to prevent blow out from the reactor. When investigating the effect of temperature, a minimum temperature of 473K was chosen because almost no conversion was observed at lower temperatures. The maximum was there because at higher temperatures, internal mass transfer limitations start to appear. For the pressure, a too high pressure drop was encountered when going to pressures lower than 325Pa, but no real maximum could be set, based on the intrinsic kinetic correlations. Of course, the highest pressure the HTK-MI can handle is 15MPa and performing ethanol dehydrogenation at such high pressures is not desired. The minimum space time is set due to internal mass transfer limitations, the maximum space time is limited due to too high conversion , thus the Berger criterion is no longer valid. The pellet size is determined to the lower side due to pressure drop and to the higher side due to internal mass transfer limitations.

When putting too little dilution material as compared to catalyst, radial heat gradients are present. The upper limit is set because of the presence of a too high pressure drop.

Table 2- 1: Restrictions for intrinsic kinetics for 1wt%Ni-10wt%Cu/Mg(Al)(Ni)(Cu)O_x.

	Minimum	Maximum
Temperature (K)	473	533
Total pressure (Pa)	325	∞
Space time (kg_{cat} s mol^{-1})	0.076	10.92
Pellet size (μm)	11	250
Dilution ratio (-)	40	7700

2.5. References

[1] A. Gervasini, S. Bennici, Dispersion and surface states of copper catalysts by temperature-programmed-reduction of oxidized surfaces (s-TPR), Applied Catalysis A: General, 281 (2005) 199-205.
[2] V. Martis, A.M. Beale, D. Detollenaere, D. Banerjee, M. Moroni, F. Gosselin, W. Bras, A high-pressure and controlled-flow gas system for catalysis research, Journal of Synchrotron Radiation, 21 (2014) 462-463.
[3] B. Ravel, M. Newville, ATHENA, ARTEMIS, HEPHAESTUS: data analysis for X-ray absorption spectroscopy using IFEFFIT, Journal of Synchrotron Radiation, 12 (2005) 537-541.
[4] K. Föttinger, PdZn based catalysts: connecting electronic and geometric structure with catalytic performance, Catalysis, 25 (2013) 77-117.
[5] K. Van der Borght, K. Toch, V. Galvita, J. Thybaut, G. Marin, Information-Driven Catalyst Design Based on High-Throughput Intrinsic Kinetics, Catalysts, 5 (2015) 1948.
[6] N. Navidi, J.W. Thybaut, G.B. Marin, Experimental investigation of ethylene hydroformylation to propanal on Rh and Co based catalysts, Applied Catalysis A: General, 469 (2014) 357-366.
[7] W. Dietz, Response factors for gas chromatographic analyses, Journal of Chromatographic Science, 5 (1967) 68-71.
[8] R.J. Berger, E.H. Stitt, G.B. Marin, F. Kapteijn, J.A. Moulijn, EUROKIN. Chemical reaction kinetics in practice, Cattech, 5 (2001) 36-60.
[9] J.T. Gleaves, G. Yablonsky, X. Zheng, R. Fushimi, P.L. Mills, Temporal analysis of products (TAP)—Recent advances in technology for kinetic analysis of multi-component catalysts, Journal of Molecular Catalysis A: Chemical, 315 (2010) 108-134.
[10] H. Gierman, Design of laboratory hydrotreating reactors: Scaling Down of Trickle-flow Reactors, Applied Catalysis, 43 (1988) 277-286.
[11] A.S. Gupta, G. Thodos, Mass and heat transfer in the flow of fluids through fixed and fluidized beds of spherical particles, AIChE Journal, 8 (1962) 608-610.

Chapter 3:

Formation and stability of an active PdZn nanoparticle catalyst on a hydrotalcite-based support for ethanol dehydrogenation*

A one-pot method has been used to synthesize a hydrotalcite-based PdZn nanoparticle catalyst, PdZn/Mg(Al)(Pd)(Zn)O_x. The activation procedure, comprising H_2 and air treatment(s) allows tuning the nanoparticle formation and, hence, the catalyst performance. Elaborate catalyst characterization via EXAFS, in-situ XRD, STEM and CO chemisorption demonstrated that single reduction leads to the formation of Pd-rich alloy nanoparticles, i.e., a PdZn shell with a Pd core. On the other hand, cycled reduction, i.e., 3 subsequent hydrogen and air treatments, ensures the formation of more homogeneously mixed PdZn nanoparticles. Compared with a PdZn/ZnO reference catalyst, the nanoparticles obtained after cycled reduction exhibit a higher initial average turnover frequency in ethanol dehydrogenation, i.e., 7.0 s^{-1} rather than 3.2 s^{-1}. An activity loss is observed during the first hours on stream. It is attributed to coking of the Pd sites, which are also deemed responsible for acetaldehyde decomposition. Hence, the acetaldehyde selectivity steadily increases during the first hours on stream. Subsequently, the acetaldehyde space time yield and selectivity stabilize at 0.7 10^{-4} mol s^{-1} kg^{-1}_{Pd} and 98%, respectively.

* A modified version of this chapter has been published as: J. De Waele, V.V. Galvita, H. Poelman, C. Detavernier, J.W. Thybaut, Formation and stability of an active PdZn nanoparticle catalyst on a hydrotalcite-based support for ethanol dehydrogenation, Catal. Sci. Technol., 7 (2017) 3715-3727.

3.1.Introduction

Bimetallic nanoparticles typically exhibit interesting catalytic properties, distinct from those of the respective bulk metals [1]. Quite often higher activities and selectivities are obtained [2-4]. The catalyst particle size may play a determining role in the ultimate performance as a result of a geometric effect. For certain reactions to occur, a well-defined configuration of atoms is required. The correspondingly available number of such active sites then depends on the particle size. Furthermore, bimetallic nanoparticles often exhibit electronic effects which differentiate their catalytic properties from those of their monometallic counterparts. Due to alloying of the atoms, a change in the interaction of reactants and products with the electronic levels of the surface sites frequently occurs, as stated by Sabatier [5-8]. Thanks to the tunable ratio of active metals, bimetallic catalyst performance can be optimized [9-11].

Bimetallic catalysts are extensively studied since they can mimic the catalytic behavior of a monometallic catalyst offering the benefit of an improved stability [12]. An example for this are PdZn catalysts as an alternative for Cu in ethanol dehydrogenation to acetaldehyde.

$$CH_3CH_2OH \rightleftharpoons CH_3CHO + H_2$$

As already mentioned in Chapter 1, the stability of the Cu catalyst in ethanol dehydrogenation is a matter of concern because of its sintering [13-16]. In view of industrial applications, irreversible deactivation should be avoided and, in this respect, PdZn could provide a solution. Intermetallic PdZn catalysts exhibit similar electronic properties as Cu, but the presence of Zn prevents Pd from sintering and, hence, the catalyst retains an activity close to its initial one [17-19]. Also, for methanol steam reforming, a reaction similar to ethanol dehydrogenation, intermetallic PdZn catalysts have been reported to outperform Cu-based ones [17].

The synthesis of bimetallic nanoparticles typically entails a complicated procedure at the laboratory scale, not to mention the industrial one. Several lab scale techniques such as seeded growth method, atomic layer deposition (ALD),… have recently been reported [20-25]. Wet

incipient impregnation and incorporation of the active metals in the support appear to offer promising perspectives for implementation at a larger scale [2, 26, 27]. Indeed, incorporation of the active metals within the support via a one pot synthesis method is an easy and reproducible route for bimetallic catalyst synthesis. For propane dehydrogenation into propene, incorporation of the active metals in a hydrotalcite-based support has already proven to yield superior catalysts when compared with wet incipient impregnation [28]. Via the incorporation of the active materials in a single-phase hydrotalcite-based precursor, stable nanoparticle catalysts are obtained after calcination and reduction [26-34].

Deactivation due to coking on metal clusters is often reported as the cause of activity decline of hydrotalcite-based bimetallic catalysts [30, 32, 35]. Hence, the development of activation or regeneration procedures is of significant importance for enhancing the catalyst lifetime and its potential commercial exploitation. Akporiaye et al. [35] investigated the effect of a single reduction as activation procedure for a PtSnCs on hydrotalcite catalyst for propane dehydrogenation, compared to a reduction-oxidation-reduction cycle before the start of the reaction. These authors observed a higher initial activity and improved stability after such a reduction-oxidation-reduction cycle. Siddiqi et al. [32] investigated the fundamental cause for the initial activity loss and increase in selectivity to the desired alkenes during ethane and propane dehydrogenation over Pt. They found that coke is first formed on the very reactive unalloyed Pt particles and subsequently partially transferred from the Pt particles to the support. This effect is most pronounced for ethane dehydrogenation and results in a less pronounced activity loss due to the migration of coke to the support. Sun et al. [30] support this statement by proving that, for propane dehydrogenation, a small increase in selectivity to propene is observed within the first hour, after which the selectivity becomes stable. This corresponds to a switch from propane conversion into methane and coke on unalloyed Pt particles to conversion into propene on intermetallic PtIn particles [30]. More recently, Redekop et al. proved the migration of coke from the Pt particles to the support by means of TAP [36].

In this chapter, the one-pot synthesis of an intermetallic PdZn catalyst is pursued. Via incorporation of the active metals in a hydrotalcite material, with subsequent calcination and reduction, PdZn nanoparticles are obtained on a mixed oxide. The activity of this catalyst is tested for ethanol dehydrogenation and compared with a benchmark PdZn/ZnO catalyst which has already been described in literature for the same reaction [37-41]. The activation procedure is of key importance for the ultimate catalyst performance and, more particularly, its stability. Therefore, single reduction, i.e., hydrogen treatment, and cycled reduction, i.e., alternating hydrogen and air treatments, are compared to clarify the impact of the activation procedure on the catalyst performance and stability.

3.2. Results

3.2.1. PdZn nanoparticle characterization

The Pd and Zn loading as measured via ICP-OES as well as the resulting molar Pd/Zn-ratio are reported in Table 3- 1. The actual loading of the calcined catalyst corresponds well with the nominal one. The loadings aren't altered considerably upon reduction and reaction. The active metals are, hence, stable against leaching. It is also evident from Table 3- 1 that the catalyst surface area slightly decreases upon reduction. This is attributed to the diffusion of Pd and Zn from the support to the surface thereby blocking the smallest pores.

Table 3- 1: BET surface area and weight percentages of Pd and Zn on PdZn/Mg(Al)(Pd)(Zn)O_x, determined via ICP-OES.

Treatment	BET surface area ($m^2\ g_{cat}^{-1}$)	Pd-loading (wt%)	Zn-loading (wt%)	Zn/Pd-ratio (mol/mol)
Calcined	29 ± 3.0	1.03	1.42	2.24
Singly reduced, after reaction	23 ± 5.2	0.93	1.26	2.22
Cycled reduced, after reaction	17 ± 2.0	1.12	1.55	2.21

Pd and Zn were incorporated in the support of this catalyst. However, upon calcination and reduction, bulk depletion or segregation can occur. This can lead to changes in the concentration of available active metals at the surface and, hence, also in the relative amounts of Pd and Zn available for reaction. To probe the surface composition, XPS has been performed. The surface concentrations of Pd and Zn are reported in Table 3- 2. Zn and Pd diffuse from the support to the surface upon single reduction, but the presence of Pd at the surface can be enhanced by applying cycled reduction. The overall higher values for Zn can be attributed to easier diffusion of Zn from the support as compared to Pd [42]. To determine the chemical nature of Pd and Zn, the position of the peaks relative to the reference C1s was determined, see Table 3- 2. It is evident from the values reported in this table that both the singly and cycled reduced catalyst tend towards the chemical nature of metallic Pd and Zn which have a binding energy of resp. 335.5 eV for $Pd3d_{5/2}$ and 1021.5 eV for $Zn2p_{3/2}$ and a kinetic energy of 988 eV for $Zn_{L3M45M45}$. The discrepancies between the reported values in Table 3- 2 and the values for metallic Pd and Zn suggest the formation of a different state, such as an alloy. Additional characterization techniques will be used further to confirm that an alloy is actually formed.

Table 3- 2: Metal surface mol fraction $C_{surf,Pd}$ and $C_{surf,Zn}$ and binding and kinetic energies as determined from XPS, after activation.

Activation procedure	$C_{surf,Pd}$ (mol%)	$C_{surf,Zn}$ (mol%)	Binding Energy $Pd3d_{5/2}$ (eV)	Binding Energy $Zn2p_{3/2}$ (eV)	Kinetic Energy Zn $L_3M_{45}M_{45}$ (eV)
Singly reduced	0.94 ± 0.31	3.16 ± 0.31	336.73	1021.38	989.7
Cycled reduced	1.61 ± 0.27	2.21 ± 0.45	336.76	1021.32	989.9

Ex-situ XRD has been performed on the sample, calcined as well as reduced, see Figure 3- 1. MgO, i.e., the main contributor of the support, is clearly present in both samples with major peaks at 42.9° and 62.3° and a smaller peak at 36.9° (PDF 00-045-0946). No traces of hydrotalcite are present in the spectra, indicating the full transformation of the hydrotalcite-based support upon

calcination. Diffraction peaks originating from PdO at 33.8° (PDF 00-041-1107) and ZnO at 31.8°, 34.4° (PDF 00-036-1451) are only slightly visible due to the low loading of these metals and peak overlap with those from the support. They disappear completely for both samples after reduction at 873K and a clear PdZn diffraction appears at 41.2° (PDF 00-006-0620). An accurate size of the PdZn particles could not be determined due to overlap with the MgO peak.

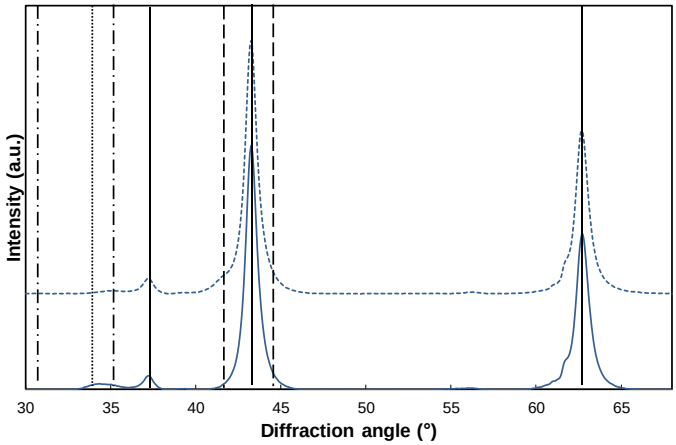

Figure 3- 1: Full XRD scans before (full line) and after (dashed line) reduction at 873K of PdZn/Mg(Al)(Pd)(Zn)O_x. full line: MgO, dotted line: PdO, dash-dotted line: ZnO, dashed line: PdZn.

3.2.1.1. Effect of redox cycling on the nanoparticle formation

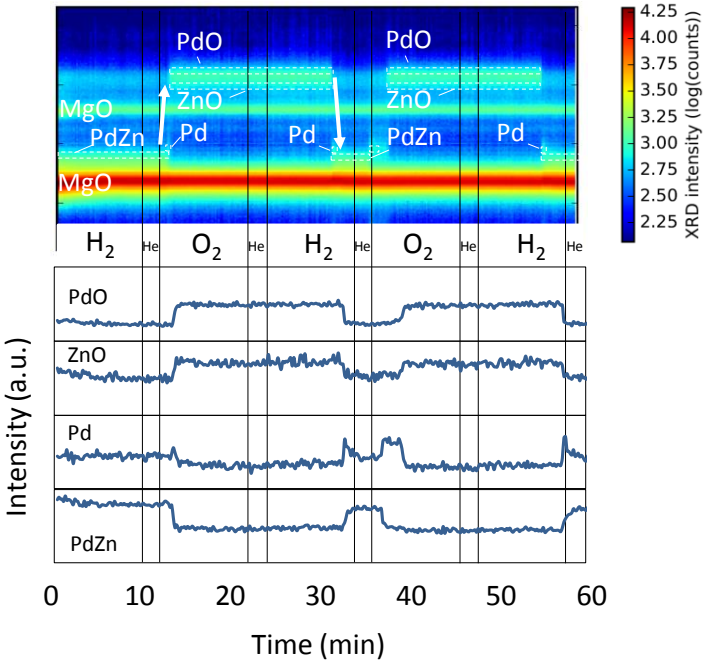

Figure 3- 2: in-situ XRD during redox cycles at 873K. 2D XRD map on top and intensities of PdO, i.e., 34.01°, ZnO, i.e., 35.16°, Pd, i.e., 40.09° and PdZn, i.e., 41.58° at the bottom. The arrows indicate the transformation of PdO and ZnO to PdZn and vice versa. The vertical black lines delineate the reduction and oxidation stages.

When performing redox cycles at 873K in in-situ XRD, the formation and decomposition of the PdZn intermetallic phase can be directly observed, see Figure 3- 2. Diffraction peaks at 36.94° and 42.92° (PDF 00-045-0946) are characteristic for MgO, i.e., the support. These peaks remain present during oxidation and reduction. Between 33° and 35°, diffraction peaks corresponding to PdO (PDF 00-041-1107) and ZnO (PDF 00-036-1451) are observed during oxidation, see Figure 3- 2. These disappear when subjecting the sample to hydrogen. A peak attributable to PdZn (PDF 00-006-0620) appears at 41.19°, as indicated with the downward arrow on Figure 3- 2 and visualized by the intensities of PdO, ZnO and PdZn. An induction period is observed before this PdZn phase develops during reduction. Upon oxidation, the changes occur practically instantaneously. The different kinetics stem from the dilution of H_2 in He compared to the use of pure O_2 for oxidation.

For both reduction and oxidation treatments, the transformation of PdZn to PdO and vice versa, occurs via an intermediate monometallic Pd state, as can be seen in Figure 3- 2. PdO is, hence, fully reduced prior to the intermetallic compound formation. Furthermore, upon oxidation, Zn is extracted and oxidized first from the intermetallic particle before Pd oxidation occurs. It can be noted that the peaks corresponding with PdO and ZnO disappear completely upon reduction, indicating that all active material is transformed into PdZn particles.

3.2.1.2. *Oxidation state determination*

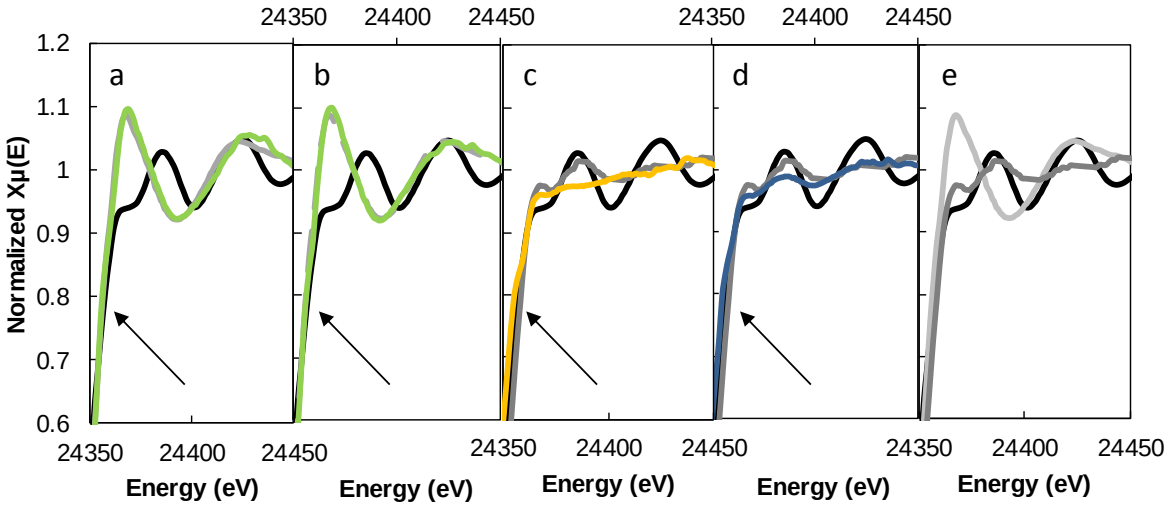

Figure 3- 3: Comparison of the XANES spectra for PdZn/Mg(Al)(Pd)(Zn)O_x at the Pd K-edge with PdO (light grey), PdZn (dark grey) and Pd foil (black) as reference.
The arrow points to a small shoulder in the spectra indicating a good interaction with the support. a: as prepared (green), b: after calcination at 873K (green),
c: after single reduction at 823K (orange), d: after cycled reduction at 823K (blue), e: reference spectra: PdO (light grey), PdZn (dark grey) and Pd foil (black).

To further validate the XRD results and investigate the formation of the PdZn intermetallic phase, XAS experiments have been performed. Figure 3- 3 illustrates the spectra at the Pd K-edge at different stages of catalyst formation: as prepared, calcined, singly reduced and cycled reduced. The spectra of Pd foil, PdZn and PdO have been added for comparison. The 'as prepared' catalyst, see Figure 3- 3a, exhibits a spectrum that closely resembles the one of PdO. This can be attributed

to the incorporation of Pd in the hydrotalcite layers, thus surrounding Pd with oxygen atoms. Less clear on the figure, indicated with an arrow, is a small shoulder in the Pd edge which suggests a good interaction with the support. This feature can be related to an atomic distribution of Pd within the layers. Empty states appear in small metal clusters arising from the interaction with the support. This enables the transition of electrons to these empty states which gives rise to a shoulder. This is also reported by Longo et al. [43]. The spectrum of the calcined sample, see Figure 3- 3b, also corresponds with PdO. After single reduction, see Figure 3- 3c, the spectrum is clearly distinct from the one of PdO but doesn't resemble that of the Pd foil either. It rather retraces that reported by Tew et al. and Ota et al. as PdZn [44, 45]. Given the distinct difference between the obtained spectrum and that of the Pd foil, it is indicative of the formation of an intermetallic phase in this sample. Upon cycled reduction, no further significant change is observed in the spectrum.

Table 3- 3: Chemical nature of Pd and Zn determined by least square regression of reference spectra.

Activation procedure	Pd as PdZn (%)	Pd as PdO (%)	Pd as Pd (%)	Zn as PdZn (%)	Zn as $ZnAl_2O_4$ (%)	Zn as ZnO (%)	Zn as Zn (%)
Calcined	0	100	0	0	61.06	38.94	0
Singly reduced	88.73	11.27	0	26.07	40.22	22.04	11.67
Cycled reduced	87.81	9.43	2.76	39.26	46.23	14.51	0

To determine the amount of Pd as PdO, PdZn and free Pd, the XANES spectra of the calcined, singly reduced and cycled reduced sample were fitted using a linear combination of the reference spectra PdO, Pd foil and PdZn [46]. The fits can be found in Figure 3- 4. Their resulting contributions in the catalysts are reported in Table 3- 3. For the calcined catalyst, Pd is mainly present as PdO. For the singly and cycled reduced sample almost 90% of Pd is present as PdZn, indicating that the formation of the catalyst via extraction of Pd and Zn from the support to the surface strongly aids in the alloying of most of the Pd into PdZn intermetallic particles.

When looking for differences at the Zn K-edge between single and cycled reduction, little difference can be found in the XANES spectra. Again, a linear combination was performed, now using Zn, ZnO, PdZn and $ZnAl_2O_4$ as reference spectra (see Figure 3- 4) [47, 48]. The contributions of the reference spectra are also reported in Table 3- 3. Particularly the presence of $ZnAl_2O_4$ in the calcined and reduced spectra is remarkable and can be explained from the interaction of Zn with the support. Furthermore, Zn is present as metal upon single reduction, but is included into PdZn after cycled reduction.

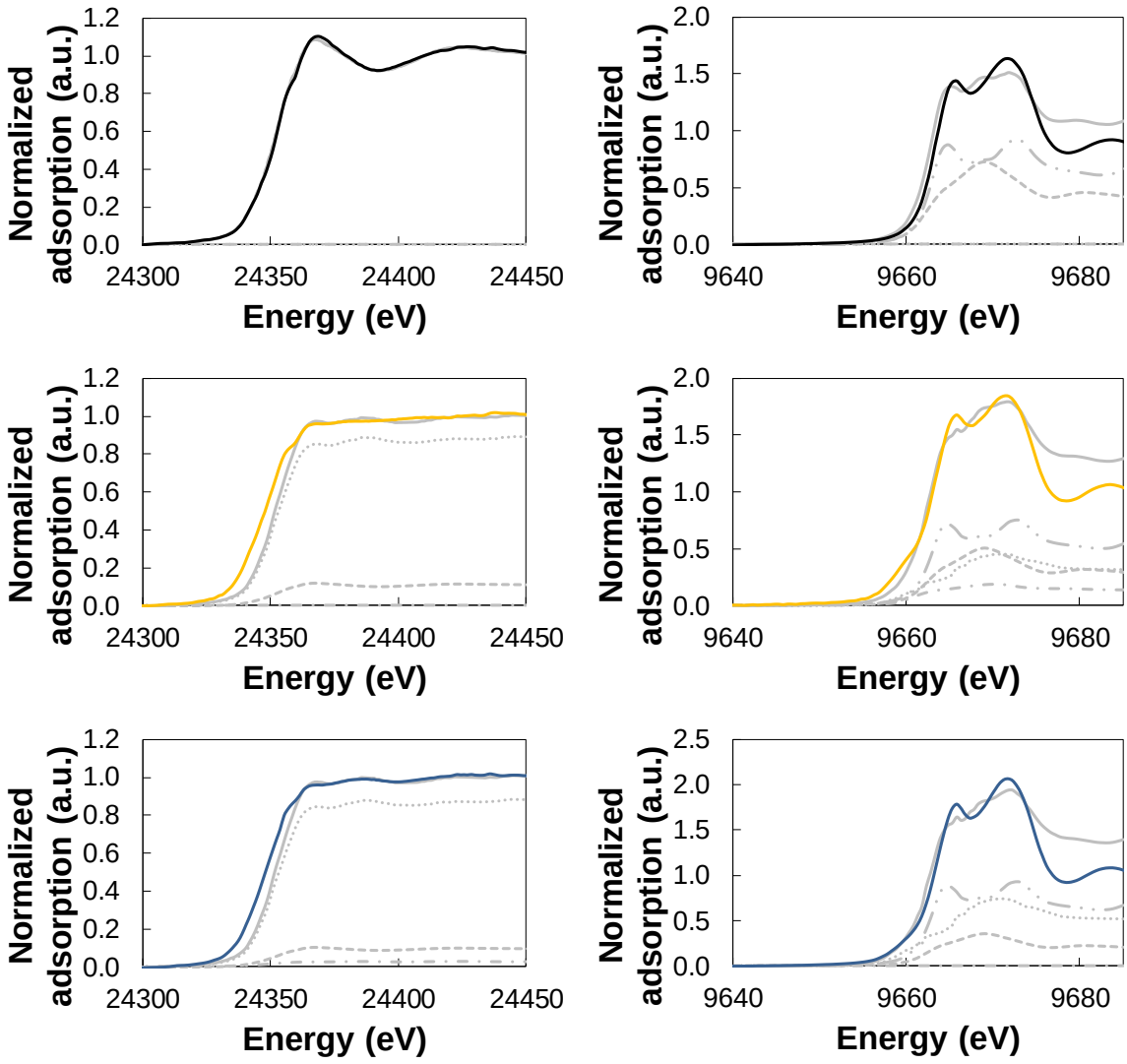

Figure 3- 4: Least square regression of XANES energy spectra of calcined (top, black), singly (middle, orange) and cycled (bottom, blue) reduced PdZn/Mg(Al)(Pd)(Zn)O_x to the reference spectra of PdZn (dotted

line), PdO (dashed line) and Pd-foil (dash-dotted line) on Pd K-edge (left) and of PdZn (dotted line), ZnO (dashed line), Zn-foil (dash-dotted line), $ZnAl_2O_4$ (dash-dot-dotted line) on Zn K-edge (right).

3.2.1.3. Particle size and number of active sites

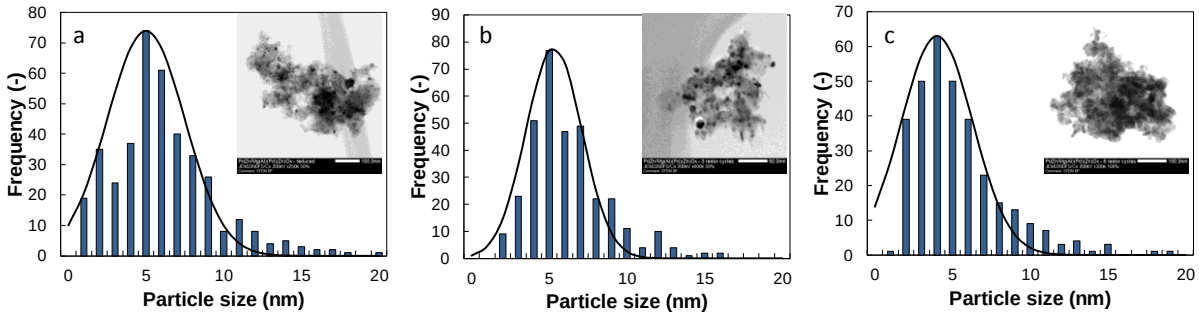

Figure 3- 5: STEM images of the singly reduced catalyst (a), cycled reduced catalyst (b) and two times cycled reduced catalyst (c).

The particle size was determined by means of STEM. The analysis was performed on a singly reduced sample at 873K, a cycled reduced one and a sample that was subjected to a second cycled reduction, i.e., 6 reduction-oxidation treatments, see Figure 3- 5. The catalyst always exhibits a close to unimodal distribution and the average particle size remains constant throughout the treatments, with 5.0 ± 2.5nm for the singly reduced sample, 5.3 ± 1.8nm after cycled reduction and 4 ± 2.3nm after a second cycled reduction. The size of the nanoparticles formed is determined by the synthesis method, i.e., the incorporation of Pd and Zn in the support entails their uniform dispersion in the support such that the metal atoms can remain finely distributed after diffusion towards the surface. This results in a homogeneous distribution of the metal atoms over the hydrotalcite and, hence, in the correspondingly obtained nanoparticles. The particle size of both the singly and cycled reduced sample was found not to change after reaction for the investigated catalyst (see Table 3- 4).

Table 3- 4: Evolution of the average particle size determined via TEM.

Activation procedure	Particle size before reaction (nm)	Particle size after reaction (nm)
Singly reduced	5.0 ± 2.5	6.0 ± 2.3
Cycled reduced	5.3 ± 2.0	5.8 ± 1.5

Since different amounts of active metals diffuse from the support to the surface depending on the reduction procedure, see Table 3- 2, the particle size of the PdZn particles doesn't correlate directly with the number of active sites. Therefore, the number of active sites was determined via CO chemisorption. PdZn sites are not active for H_2 chemisorption due to the dissociative nature of H_2 on Pd and the absence of two adjacent Pd atoms [49-51]. CO pulse chemisorption was performed at 200K since at room temperature, CO desorbs instantaneously [51]. To eliminate the adsorption of CO on the support, CO chemisorption was also performed on $Mg(Al)O_x$, but none was observed. It can be seen that the number of active sites increases after cycled reduction compared to single reduction. This is in agreement with the observation from XPS that more Pd and Zn atoms have diffused to the surface after cycled reduction, resulting in a higher number of nanoparticles and, hence, more active sites. The number of active sites was also determined for a PdZn/ZnO reference catalyst in view of comparison.

Table 3- 5: Number of active sites determined by means of CO pulse chemisorption, and TOF and acetaldehyde selectivity at time on stream 0h and 3h.

Catalyst	Activation procedure	Number of active sites (mol kg_{cat}^{-1})	TOF (TOS=0h) (s^{-1})	Acetaldehyde selectivity (%)	
				TOS=0h	TOS=3h
PdZn/ZnO		$0.88\ 10^{-3}$	3.2	95	96
PdZn/Mg(Al)(Pd)(Zn)O_x	Singly reduced	$1.19\ 10^{-3}$	2.2	89	98
	Cycled reduced	$1.80\ 10^{-3}$	7.0	93	98

3.2.2. Activated catalyst performance

The initial average turnover frequency and acetaldehyde selectivity exhibited by the PdZn/Mg(Al)(Pd)(Zn)O_x catalyst activated via single or cycled reduction and the PdZn/ZnO reference catalyst are reported in Table 3- 5. It can be seen that the initial TOF obtained on the singly reduced PdZn/Mg(Al)(Pd)(Zn)O_x is lower than the one on the PdZn/ZnO reference catalyst, but the TOF after cycled reduction doubles that exhibited by the reference catalyst. The acetaldehyde selectivity obtained when using the PdZn/Mg(Al)(Pd)(Zn)O_x catalyst, i.e., 98% after 3h, is slightly higher than that of the PdZn/ZnO reference catalyst. Other reaction products were methane and carbon monoxide, with selectivities always below 1%.

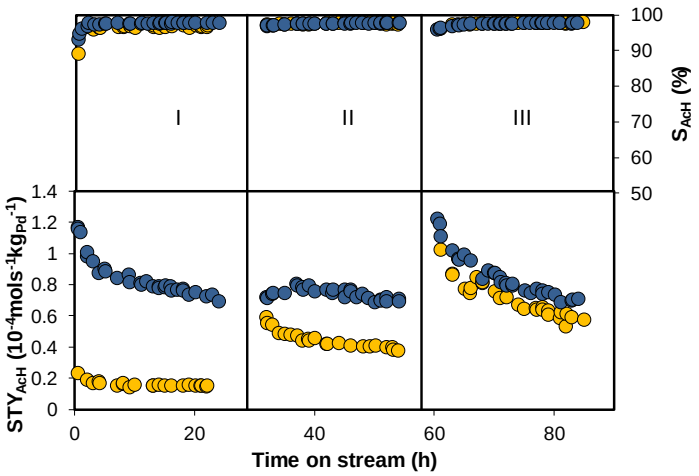

Figure 3- 6: Performance curves of PdZn/Mg(Al)(Pd)(Zn)O_x activated with single reduction (orange) and cycled reduction (blue).I: freshly activated catalyst, II: catalyst after 1 regeneration, III: catalyst after 2 regenerations.

The evolution of the activity with time on stream of the catalyst activated via single or cycled reduction, has been assessed for freshly activated as well as regenerated samples. To represent the activity of the catalyst as a function of time on stream, see Figure 3- 6, the acetaldehyde space time yield (STY_{AcH}) has been used, rather than the turnover frequency. Indeed, some ambiguity cannot be avoided after a change in TOF as it can originate from an actual change in activity of each site, or from a change in the number of active sites. The space time yield decreases within the first hours on stream and subsequently stabilizes at resp. 0.15 10^{-4} mol (s kg_{Pd})$^{-1}$ and 0.7 10^{-4} mol (s kg_{Pd})$^{-1}$ for the singly and cycled reduced samples. As mentioned above, see Section 3.2.1 and 3.2.1.3, neither leaching, sintering nor pore collapse could be invoked to explain this decrease in activity, leaving coke formation as the most likely reason for this behavior. Temperature programmed oxidation of the spent samples has been performed to verify this possibility. In-situ XRD was also performed, but it was impossible to distinguish between cokes and the intermetallic compound PdZn. From the TPO measurements, a broad CO_2-peak was observed at temperatures between 450K and 700K, indicating that, indeed, coke had been formed. The amount of coke burnt from the surface was resp. 9.85 10^{-3} ± 6.95 10^{-3} mol g^{-1} and 6.19 10^{-4} ± 3.8 10^{-5} mol g^{-1} for the singly and cycled reduced catalyst.

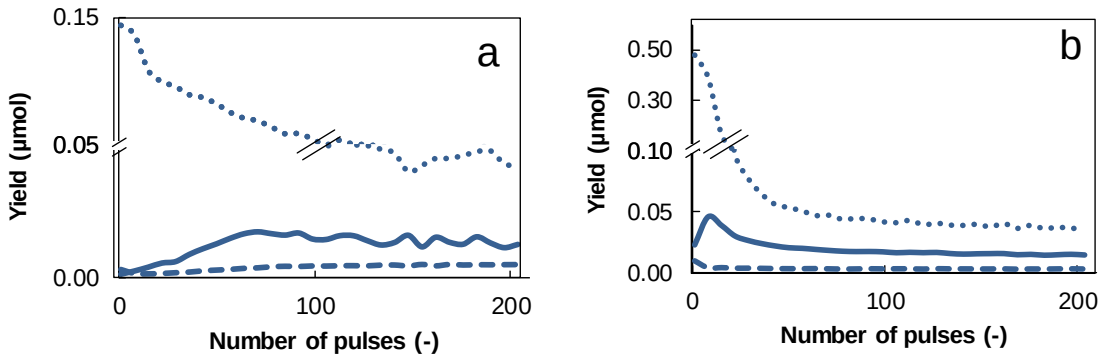

Figure 3- 7: Evolution of the hydrogen (dotted line), acetaldehyde (full line) and methane and carbon monoxide (coinciding, dashed line) production as a function of pulse number at 533K for PdZn/Mg(Al)(Pd)(Zn)O_x after single reduction (a) and cycled reduction (b) in TAP.

To identify the origin of coke formation, a transient technique, i.e., Temporal Analysis of Products (TAP), was employed. This technique aids in investigating the initial stages of the reaction. Single pulse experiments were performed on the samples activated by single and cycled reduction. The integrated yield of hydrogen, methane, carbon monoxide and acetaldehyde has been plotted against the number of pulses, see Figure 3- 7. In the first pulses, the hydrogen response amounts to 0.15 10^{-6} mol and 0.5 10^{-6} mol for the singly and cycled reduced catalyst respectively, but decreases significantly during the first 50 pulses. The acetaldehyde production by the cycled reduced sample exceeds that of the singly reduced sample, i.e., 1.5 10^{-8} mol for the cycled reduced compared to 1.2 10^{-8} mol for the singly reduced sample. The differences in acetaldehyde production between singly and cycled reduced samples can be related to the presence of more PdZn intermetallic particles after cycled reduction. The methane and carbon monoxide responses coincide, indicating that both are stoichiometrically formed via the same reaction.

3.3. Discussion

It is clear that the PdZn/Mg(Al)(Pd)(Zn)O_x catalyst activated via cycled reduction exhibits a more interesting ethanol dehydrogenation performance than the PdZn/ZnO reference catalyst, both in terms of activity and acetaldehyde selectivity, see Table 3- 5. In what follows, three questions are addressed in more detail: Which phenomenon is at the origin of the high acetaldehyde selectivity on the PdZn nanoparticles? What renders the PdZn nanoparticle catalyst obtained after cycled reduction so active, compared to the singly reduced one? Which phenomena cause the initial activity loss and simultaneous increase of acetaldehyde selectivity?

3.3.1. Acetaldehyde selectivity

Only acetaldehyde, methane and carbon monoxide are observed as reaction products. Mavrikakis et al. reported that acetaldehyde decomposition requires two adjacent Pd sites [52]. Li et al. have indeed found that the removal of the first H atom from ethanol proceeds on a single site and that this atom subsequently moves to another Pd site [53]. The migration of H to this other Pd site doesn't require the concerned Pd sites to be adjacent whereas this is imperative for acetaldehyde decomposition [54]. The low selectivity to methane and carbon monoxide thus suggests that practically no adjacent Pd sites are present on the investigated catalysts. The characterization discussed in the previous sections allows constructing a schematic representation of the nanoparticle catalysts obtained after single and cycled reduction, see Figure 3- 8.

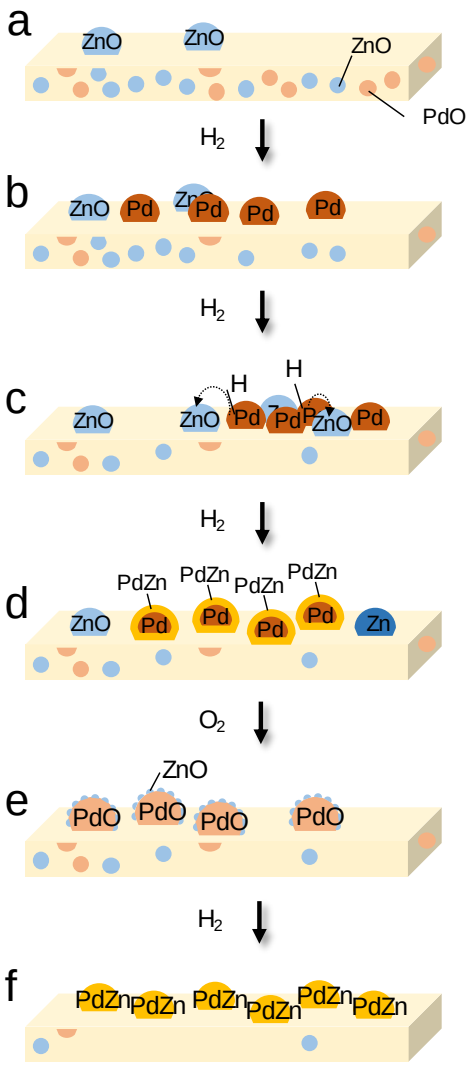

Figure 3- 8: Representation of the formation of the intermetallic compound during single reduction (a-d) and cycled reduction (e-f) at 823K for PdZn/Mg(Al)(Pd)(Zn)O_x. dark orange: Pd, light blue: ZnO or ZnAl2O4, light orange: PdO, gold: intermetallic compound PdZn.

Figure 3- 8 frame a, starts from the calcined material. Pd and Zn are atomically dispersed in the support and some small ZnO clusters are already present on the surface, as confirmed by STEM, see Figure 3- 9. Pd and Zn are present in oxide form, i.e., PdO for Pd and ZnO or $ZnAl_2O_4$ for Zn, see Table 3- 3.

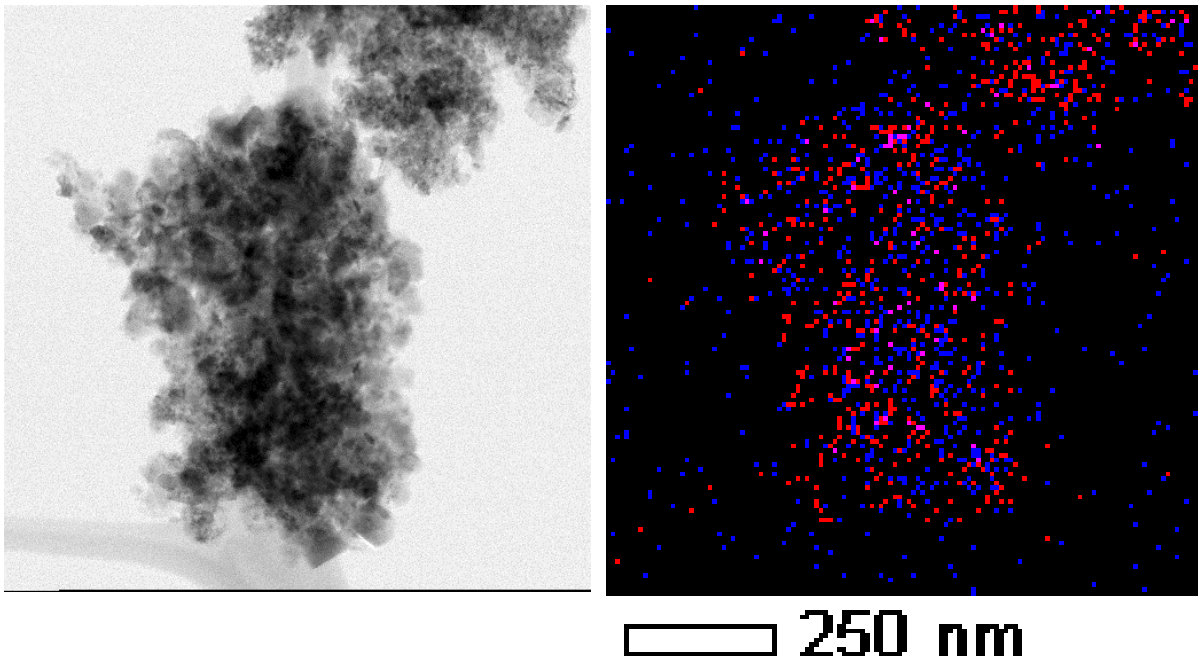

Figure 3- 9: TEM-EDX of calcined PdZn/Mg(Al)(Pd)(Zn)O_x. red: Pd, blue: Zn.

Upon H_2 treatment at 823K, Pd and Zn diffuse from the support towards the surface, Pd being more easily reduced, Figure 3- 8, frame b. It results in the presence of ZnO on the surface, since the reduction temperature of ZnO exceeds 873K, together with metallic Pd. Later in the hydrogen treatment, excess hydrogen spills over from the Pd particles to ZnO, aiding its reduction to Zn, see Figure 3- 8, frame c. ZnO can only be reduced in the presence of another metal, such as Cu or Pd, which is able to form an alloy with Zn. ZnO itself only becomes active for H_2 adsorption at temperatures exceeding 873K [55, 56]. Thus, spillover of hydrogen from Pd is necessary for the reduction of ZnO [57] and the subsequent formation of the PdZn intermetallic compound. Zn diffuses into the Pd particle as the employed reduction temperature exceeds its migration temperature, i.e., 823K vs. 583K. However, some Zn remains, together with unreduced ZnO, present on the surface of the support, being reduced but unable to diffuse into the Pd particle at that moment in the procedure. It results in Pd-rich alloy nanoparticles, i.e., a Pd core with PdZn shell, see Figure 3- 8, frame d [39, 58]. The XANES fitting after single reduction confirms the Zn excess on the surface, see Table 3- 1 [44, 45]. Moreover, the presence of Zn in the PdZn layer limits the Pd availability for further H_2 activation, since two adjacent Pd sites are required for H_2

dissociation. As a result, complete ZnO reduction cannot be achieved after a single reduction [39]. This is also reported by Araña et al., who demonstrated that H_2 chemisorption experiments did not exhibit any adsorption on PdZn [50]. Tamtögl et al. generated additional proof for this more difficult H_2 activation by Zn by comparing pure Pd with PdZn via TPD [51]. Alloying Pd with Zn does not cause any energetic differences, but the number of adsorption sites decreases. Similar phenomena were also observed by Föttinger et al. and Ota et al. for PdZn and by Filez et al. for PtGa [39, 44, 59].

Upon subjecting the reduced material to oxidation, the intermetallic phase decomposes into PdO and ZnO, according to in-situ XRD (Section 3.2.1.1), see Figure 3- 8, frame e. In-situ XRD shows that Zn is first removed from the PdZn particle and subsequently undergoes oxidation, while the particle remains as metallic Pd. Afterwards, also Pd is oxidized to PdO. A second reduction re-establishes the PdZn particles with Zn now being more homogeneously distributed throughout the particles, thereby obtaining homogeneous PdZn particles, as confirmed by XAS, see Table 3- 3 and Figure 3- 8 frame f. When comparing the surface concentrations of both catalysts after single and cycled reduction, see Table 3- 2, it can be seen that the Pd concentration increases, indicating that subsequent oxidation/reduction treatments allow extracting additional Pd from the support. The particle size remains the same, irrespective of the number of cycles, see Figure 3- 5, but the number of active sites increases. Thus, the decomposition and re-establishment of the intermetallic compound leaves the clusters intact indicating a good stability of the particles on the support.

For the reference catalyst PdZn/ZnO, Bahruji et al. and Föttinger et al. have already investigated the appearance of the catalyst [37-39]. These authors concluded that PdZn nanoparticles are formed, but overall, larger particles, i.e., in the range of 10-20nm, are reported for PdZn/ZnO than for the PdZn/Mg(Al)(Pd)(Zn)O_x catalyst discussed in our work. This causes an incomplete diffusion of Zn into the Pd particle, leading to a PdZn shell over a Pd core.

Concluding, both single and cycled reduction give rise to PdZn nanoparticles. These particles are composed of Pd atoms which are surrounded by Zn atoms, as reported by Neyman et al. [54]. This explains the high acetaldehyde selectivity. Initially, the singly reduced sample gave a lower selectivity due to the Pd-rich nature of the active sites. After 3h, however, the selectivity is the same for both activation procedures, since the adjacent Pd sites have been blocked by coke formed in the initial stage of the reaction, see also Section 3.3.3. The acetaldehyde selectivity slightly exceeds that from the reference PdZn/ZnO catalyst after 3h. This could indicate a better homogeneity of the PdZn particles and, hence, the presence of less adjacent Pd sites, after incorporation.

3.3.2. Activity

In contrast with the selectivity, the activity of the catalyst does depend on the activation procedure. Overall, the catalyst initial average turnover frequency is high, i.e., 2.2 mol_{EtOH} $(mol_{Pd}\ s)^{-1}$ for singly reduced and 7.0 mol_{EtOH} $(mol_{Pd}\ s)^{-1}$ for the cycled reduced catalyst, see Table 3- 5. This is related to the presence of active nanoparticles on the catalysts. The difference in initial average turnover frequency can be explained with the catalyst formation scheme, Figure 3- 8. Upon reduction by excess H_2 spilled over from Pd, Zn diffuses towards and into these Pd metal particles. By doing so, it decreases the number of Pd atoms accessible for H_2 and, hence, further ZnO reduction is hindered. This results in Pd-rich alloy nanoparticles with an outer PdZn layer and a Pd core. As described above, only upon cycled reduction, PdZn nanoparticles with a homogeneous composition are formed. Towards the first experimental point, at 0.5h, rapid coking is taking place, leading to lower catalyst activity. This also explains why the singly reduced sample is initially less active than the reference catalyst. For the PdZn/ZnO catalyst, the abundant availability of Zn may result in Pd sites being covered by Zn, thereby reducing the coking. However, it does not allow the establishment of the homogeneity that is achieved by the cycled reduction [37-39].

Furthermore, it should be taken into account that, initially, the acetaldehyde selectivity is slightly lower for the singly reduced sample. This indicates a more frequent occurrence of two adjacent Pd atoms since more methane and carbon monoxide is produced. The transition state for acetaldehyde decomposition requires the occupancy of two sites whereas ethanol dehydrogenation proceeds on a single site and the removed H-atom moves toward a free Pd site that is situated in the neighborhood, but not necessarily adjacent [52-54]. Since TOF is defined as number of molecules reacting per site per second, the requirement of two sites biases the calculation of the TOF.

Catalyst regeneration has subsequently been assessed, see Figure 3- 6, frame II and III. For the singly reduced sample, an oxidation treatment is performed to burn off the coke and consecutive reduction restores the intermetallic nanoparticles. For the cycled reduced catalyst, again a cycled regeneration is performed after the coke burn off. The cycled reduced catalyst maintains its original activity, see the blue circles in Figure 3- 6, frame II. It can, hence, be concluded that this catalyst is restored after stabilization to the same active state as the freshly activated catalyst. The singly reduced sample exhibits an enhanced performance after regeneration, see Figure 3- 6, frame II. The additional redox cycle to which the catalyst has been exposed during the regeneration procedure resulted in the extraction of more Pd and Zn from the support, thereby increasing the number of active sites and improving the homogeneity of the PdZn particle. This explains why, after two regenerations, i.e., subsequent air and hydrogen treatment, the average turnover frequency of acetaldehyde is comparable for the singly and the cycled reduced sample. After the 2nd regeneration, the singly reduced catalyst, in fact, behaves like the cycled reduced catalyst. When taking into account the chemical nature of Pd and Zn present on the surface before and after reaction, see Figure 3- 10 and Figure 3- 11, it can be seen that Pd and Zn both evolve towards the metallic state. It can, hence, be assumed that all Pd and Zn have indeed been extracted from the support and homogeneously distributed throughout the particle. Since they don't reach the metallic state, it can be assumed that Pd and Zn are in the intermetallic state.

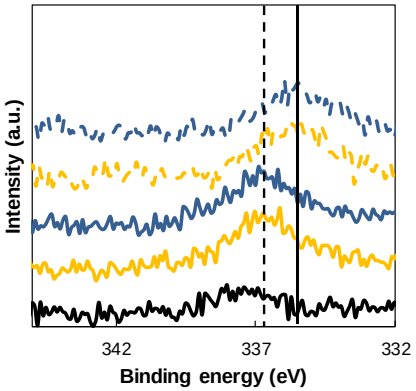

Figure 3- 10: Determination of chemical nature of Pd in the PdZn/Mg(Al)(Pd)(Zn)O_x catalyst. full black line: calcined, full orange line: single reduced, full blue line: cycled reduced, dashed orange line: single reduced after reaction, dashed blue line: cycled reduced after reaction. The dashed vertical line indicates the position of PdO and the full vertical line corresponds with the peak position of Pd.

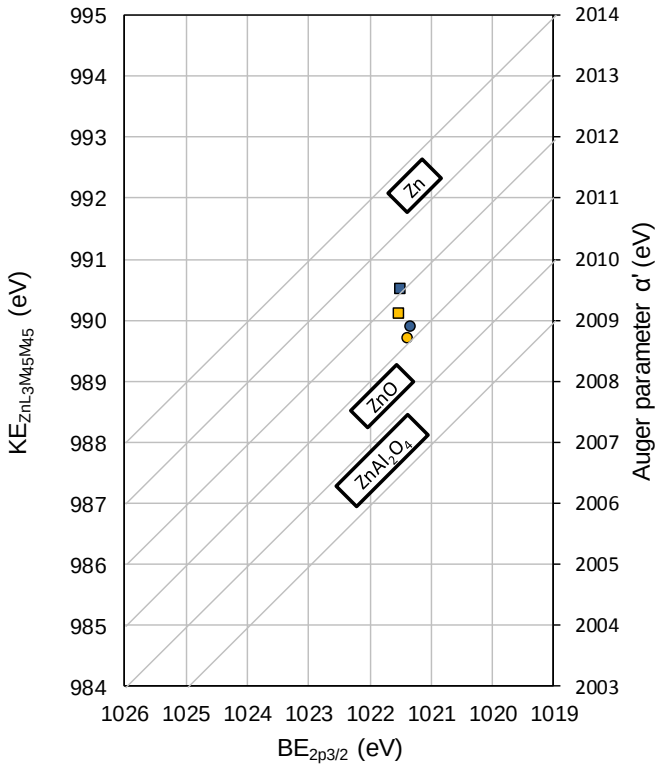

Figure 3- 11: Determination of chemical nature of Zn in the PdZn/Mg(Al)(Pd)(Zn)O_x catalyst. Black ●: calcined, orange●: single reduced reduced, blue ●: cycled reduced, orange ■: single reduced after reaction, blue ■: cycled reduced after reaction.

It can be concluded that performing a cycled reduction is beneficial for the catalyst performance and stability. A single reduction treatment doesn't suffice to convert all ZnO to Zn and let it diffuse into Pd. Furthermore, synthesis of the catalyst via incorporation of the active metals and cycled reduction gives rise to a more active catalyst compared to the PdZn/ZnO reference catalyst. Furthermore, regeneration with the same cycled reduction restores the initial activity, indicating that the catalyst composition is not altered upon regeneration.

3.3.3. Initial activity loss

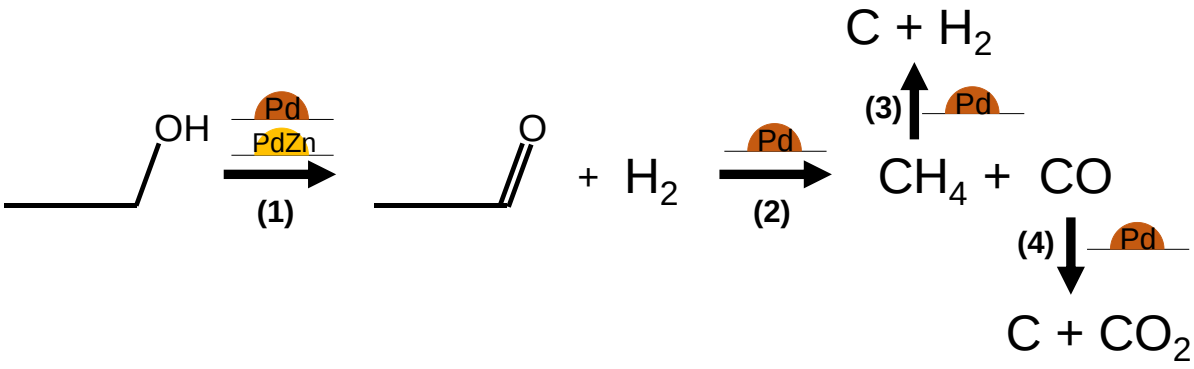

Figure 3- 12: Schematic representation of the reaction mechanism on a PdZn catalyst.

Gold: PdZn particles, orange: Pd-rich particles.

The catalyst experiences an initial activity loss irrespective of the activation procedure. The methane selectivity decreases simultaneously with this activity loss (see Figure 3- 13), while that of acetaldehyde increases to close to 100%, see Figure 3- 6. Based on the results in Table 3- 1, it can be concluded that the catalyst's surface area doesn't change significantly, such that an explanation for the activity loss will not be situated in this direction. Also sintering and leaching could be excluded as potential causes for the activity loss, since the particle size and metal loading remain the same after reaction, see Table 3- 5 and Table 3- 1. This represents a considerable improvement compared with commercial Cu catalysts where irreversible deactivation due to sintering has been proven to be a major drawback [13-16].

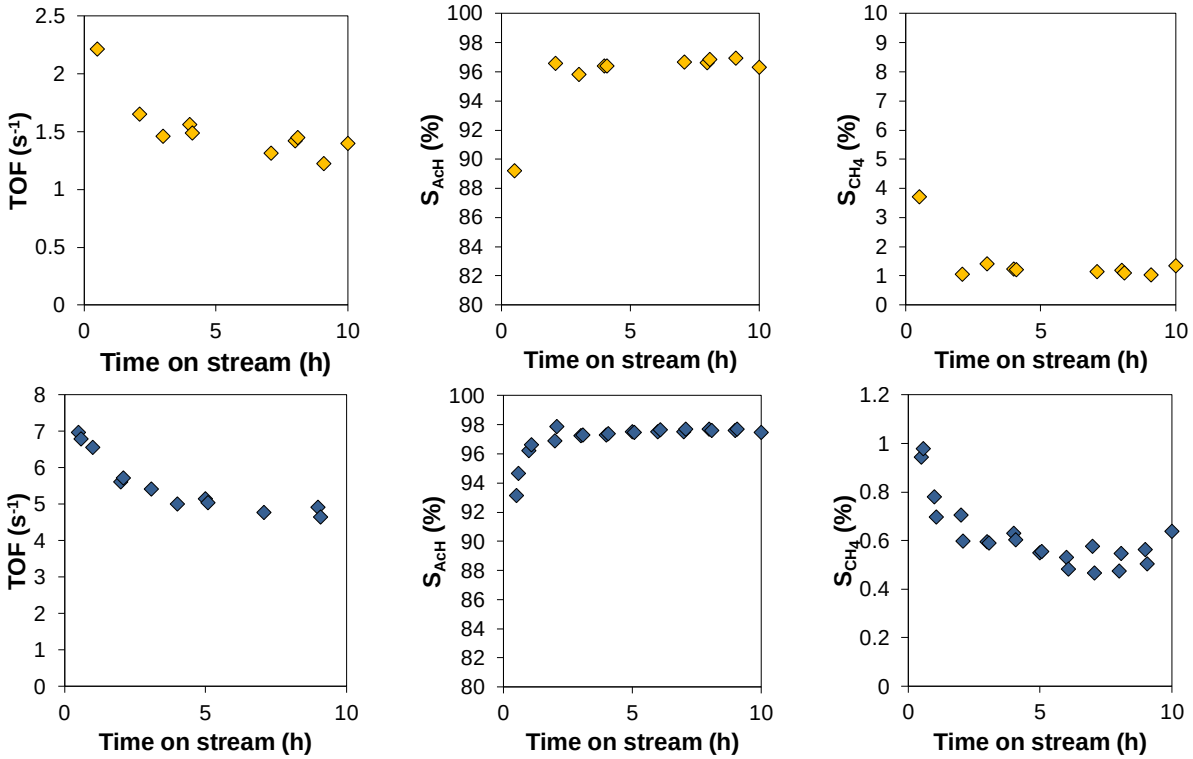

Figure 3- 13: zoom on the deactivation curves of PdZn/Mg(Al)(Pd)(Zn)O_x after single reduction (top, orange) and after cycled reduction (bottom, blue). Fresh activated catalyst with resp. 30 min H_2 and H_2-O_2-H_2-O_2-H_2 for 30 min each at 823 K .

TPO and TAP results indicate that coke formation is at the origin of the activity loss. Based on the reactions represented in Figure 3- 12, it can be seen that, if only reactions (1) and (2) would occur, the hydrogen production, in Figure 3- 7, should equal the sum of the acetaldehyde and methane production. A higher hydrogen production than expected from the stoichiometry of those two reactions, hence, indicates the occurrence of an additional reaction such as reaction (3) in Figure 3- 12. Indeed, when methane decomposes into coke, more hydrogen is produced, explaining the initial pulse responses observed in the TAP measurements. In subsequent pulses, the hydrogen production per pulse decreases, but still exceeds the amount expected based on reactions (1) and (2). During the first pulses, a rapid blockage of adjacent Pd sites occurs by coke via reactions (1) to (4). Afterwards, a slower activity loss occurs, possibly related to the migration of cokes towards the support and the recoking of adjacent Pd sites. This coking behavior

eventually disappears and leaves the PdZn sites intact, resulting in a stable and selective conversion to acetaldehyde.

When combining all results discussed above, the stable space time yield of the activated samples, i.e., Figure 3- 6, can be explained. The lower STY of the singly reduced catalyst compared to the cycled reduced, is attributed to a lower amount of active sites and to rapid coking of the adjacent Pd sites. Upon cycled reduction, more active sites are formed with a homogeneously mixed composition of the PdZn particle which reduces the coking. It can be noted that, for both catalysts, coking blocks adjacent neighboring Pd-sites, improving the selectivity towards acetaldehyde. After the initial activity changes, the catalyst, activated by single or cycled reduction, remains stable which opens up perspectives for commercial applications in the production of acetaldehyde.

The best catalyst discussed in this work, i.e., the cycled reduced PdZn/Mg(Al)(Pd)(Zn)O_x catalyst, exhibits an improved selectivity compared to PdZn/ZnO and a stable activity after a few hours, allowing for a long term use of this catalyst in a potential industrial application.

3.4. Conclusions

PdZn/Mg(Al)(Pd)(Zn)O_x, a PdZn nanoparticle catalyst prepared via a one-pot synthesis of a hydrotalcite-based support, exhibits promising features as an alternative catalyst to Cu for ethanol dehydrogenation. Its activity can be tuned via the adopted activation procedure. After single reduction an initial average TOF of 2.2 s^{-1} is achieved whereas cycled reduction, i.e., a sequence of hydrogen and air treatments, enhances this initial average TOF to 7.0 s^{-1}. After 3h, the acetaldehyde selectivity is independent of the activation procedure. Overall, the cycled reduced PdZn/Mg(Al)(Pd)(Zn)O_x catalyst exhibits both a superior activity and selectivity compared to the reference PdZn/ZnO catalyst.

The high acetaldehyde selectivity was achieved via the presence of Zn isolating the Pd sites. As a result, acetaldehyde adsorption on two adjacent Pd sites, as necessary for its decomposition into methane and carbon monoxide, is hindered. The main difference between the singly and cycled reduced catalyst is the remaining Pd core after a single reduction. A cycled reduction comprising 3 successive oxidation-reduction treatments is required to entirely convert the Pd core into a mixed PdZn phase.

The initial activity loss and simultaneous, increasing acetaldehyde selectivity are attributed to the coking and, hence, blocking of adjacent Pd sites, i.e., those required for acetaldehyde decomposition. Subsequently, an up to 20h stable catalyst activity with close to 100% selective acetaldehyde formation on PdZn is observed.

3.5. References

[1] B.C. Gates, Supported Metal Cluster Catalysts, Preparation of Solid Catalysts, Wiley-VCH Verlag GmbH2008, pp. 371-388.
[2] M. Armbrüster, G. Wowsnick, M. Friedrich, M. Heggen, R. Cardoso-Gil, Synthesis and Catalytic Properties of Nanoparticulate Intermetallic Ga–Pd Compounds, Journal of the American Chemical Society, 133 (2011) 9112-9118.
[3] D. Wang, Y. Li, Bimetallic Nanocrystals: Liquid-Phase Synthesis and Catalytic Applications, Advanced Materials, 23 (2011) 1044-1060.
[4] H.-L. Jiang, Q. Xu, Recent progress in synergistic catalysis over heterometallic nanoparticles, Journal of Materials Chemistry, 21 (2011) 13705-13725.
[5] A.K. Singh, Q. Xu, Synergistic Catalysis over Bimetallic Alloy Nanoparticles, ChemCatChem, 5 (2013) 652-676.
[6] N. Toshima, T. Yonezawa, Bimetallic nanoparticles-novel materials for chemical and physical applications, New Journal of Chemistry, 22 (1998) 1179-1201.
[7] Z. Wei, J. Sun, Y. Li, A.K. Datye, Y. Wang, Bimetallic catalysts for hydrogen generation, Chemical Society Reviews, 41 (2012) 7994-8008.
[8] B. Coq, F. Figueras, Structure–activity relationships in catalysis by metals: some aspects of particle size, bimetallic and supports effects, Coordination Chemistry Reviews, 178–180, Part 2 (1998) 1753-1783.
[9] X. Mao, L. Yang, J. Yang, J. Key, S. Ji, H. Wang, R. Wang, A Volcano Curve: Optimizing Activity of Shell-Core PtxRuy@PdCu/C Catalysts for Methanol Oxidation by Tuning Pt/Ru Ratio, Journal of the Electrochemical Society, 160 (2013) H219-H223.
[10] W. An, D. Gatewood, B. Dunlap, C.H. Turner, Catalytic activity of bimetallic nickel alloys for solid-oxide fuel cell anode reactions from density-functional theory, Journal of Power Sources, 196 (2011) 4724-4728.
[11] I.E.L. Stephens, A.S. Bondarenko, F.J. Perez-Alonso, F. Calle-Vallejo, L. Bech, T.P. Johansson, A.K. Jepsen, R. Frydendal, B.P. Knudsen, J. Rossmeisl, I. Chorkendorff, Tuning the Activity of Pt(111) for Oxygen Electroreduction by Subsurface Alloying, Journal of the American Chemical Society, 133 (2011) 5485-5491.
[12] A. Pang Tsai, S. Kameoka, Y. Ishii, PdZn=Cu: Can an Intermetallic Compound Replace an Element?, Journal of the Physical Society of Japan, 73 (2004) 3270-3273.
[13] F.-W. Chang, W.-Y. Kuo, K.-C. Lee, Dehydrogenation of ethanol over copper catalysts on rice husk ash prepared by incipient wetness impregnation, Applied Catalysis A: General, 246 (2003) 253-264.

[14] N. Kanoun, M.P. Astier, G.M. Pajonk, New vanadium-copper-zinc catalysts, their characterization and use in the catalytic dehydrogenation of ethanol, Applied Catalysis, 70 (1991) 225-236.
[15] Y.-J. Tu, C. Li, Y.-W. Chen, Effect of chromium promoter on copper catalysts in ethanol dehydrogenation, Journal of Chemical Technology & Biotechnology, 59 (1994) 141-147.
[16] E. Santacesaria, G. Carotenuto, R. Tesser, M. Di Serio, Ethanol dehydrogenation to ethyl acetate by using copper and copper chromite catalysts, Chemical Engineering Journal, 179 (2012) 209-220.
[17] N. Iwasa, T. Mayanagi, W. Nomura, M. Arai, N. Takezawa, Effect of Zn addition to supported Pd catalysts in the steam reforming of methanol, Applied Catalysis A: General, 248 (2003) 153-160.
[18] N. Takezawa, N. Iwasa, Steam reforming and dehydrogenation of methanol: Difference in the catalytic functions of copper and group VIII metals, Catalysis Today, 36 (1997) 45-56.
[19] K. Föttinger, PdZn based catalysts: connecting electronic and geometric structure with catalytic performance, Catalysis, 25 (2013) 77-117.
[20] J. Zhu, M.-L. Yang, Y. Yu, Y.-A. Zhu, Z.-J. Sui, X.-G. Zhou, A. Holmen, D. Chen, Size-Dependent Reaction Mechanism and Kinetics for Propane Dehydrogenation over Pt Catalysts, ACS Catalysis, 5 (2015) 6310-6319.
[21] D. Astruc, F. Lu, J.R. Aranzaes, Nanoparticles as Recyclable Catalysts: The Frontier between Homogeneous and Heterogeneous Catalysis, Angewandte Chemie International Edition, 44 (2005) 7852-7872.
[22] M.A. El-Sayed, Some Interesting Properties of Metals Confined in Time and Nanometer Space of Different Shapes, Accounts of Chemical Research, 34 (2001) 257-264.
[23] H. Bönnemann, Ryan M. Richards, Nanoscopic Metal Particles − Synthetic Methods and Potential Applications, European Journal of Inorganic Chemistry, 2001 (2001) 2455-2480.
[24] J. Dendooven, R.K. Ramachandran, K. Devloo-Casier, G. Rampelberg, M. Filez, H. Poelman, G.B. Marin, E. Fonda, C. Detavernier, Low-Temperature Atomic Layer Deposition of Platinum Using (Methylcyclopentadienyl)trimethylplatinum and Ozone, The Journal of Physical Chemistry C, 117 (2013) 20557-20561.
[25] R.K. Ramachandran, J. Dendooven, M. Filez, V.V. Galvita, H. Poelman, E. Solano, M.M. Minjauw, K. Devloo-Casier, E. Fonda, D. Hermida-Merino, W. Bras, G.B. Marin, C. Detavernier, Atomic Layer Deposition Route To Tailor Nanoalloys of Noble and Non-noble Metals, ACS Nano, 10 (2016) 8770-8777.
[26] P.P. Sun, G. Siddiqi, M.F. Chi, A.T. Bell, Synthesis and characterization of a new catalyst Pt/Mg(Ga)(Al)O for alkane dehydrogenation, Journal of Catalysis, 274 (2010) 192-199.

[27] V. Galvita, G. Siddiqi, P. Sun, A.T. Bell, Ethane dehydrogenation on Pt/Mg(Al)O and PtSn/Mg(Al)O catalysts, Journal of Catalysis, 271 (2010) 209-219.
[28] M. Filez, E.A. Redekop, H. Poelman, V.V. Galvita, M. Meledina, S. Turner, G. Van Tendeloo, C. Detavernier, G.B. Marin, One-pot synthesis of Pt catalysts based on layered double hydroxides: an application in propane dehydrogenation, Catalysis Science & Technology, (2016).
[29] A. Ota, J. Kröhnert, G. Weinberg, I. Kasatkin, E.L. Kunkes, D. Ferri, F. Girgsdies, N. Hamilton, M. Armbrüster, R. Schlögl, M. Behrens, Dynamic Surface Processes of Nanostructured Pd2Ga Catalysts Derived from Hydrotalcite-Like Precursors, ACS Catalysis, 4 (2014) 2048-2059.
[30] P. Sun, G. Siddiqi, W.C. Vining, M. Chi, A.T. Bell, Novel Pt/Mg(In)(Al)O catalysts for ethane and propane dehydrogenation, Journal of Catalysis, 282 (2011) 165-174.
[31] E.A. Redekop, V.V. Galvita, H. Poelman, V. Bliznuk, C. Detavernier, G.B. Marin, Delivering a Modifying Element to Metal Nanoparticles via Support: Pt–Ga Alloying during the Reduction of Pt/Mg(Al,Ga)Ox Catalysts and Its Effects on Propane Dehydrogenation, ACS Catalysis, 4 (2014) 1812-1824.
[32] G. Siddiqi, P. Sun, V. Galvita, A.T. Bell, Catalyst performance of novel Pt/Mg(Ga)(Al)O catalysts for alkane dehydrogenation, Journal of Catalysis, 274 (2010) 200-206.
[33] K. Takehira, "Intelligent" reforming catalysts: Trace noble metal-doped Ni/Mg(Al)O derived from hydrotalcites, Journal of Natural Gas Chemistry, 18 (2009) 237-259.
[34] P. Li, C. He, J. Cheng, C.Y. Ma, B.J. Dou, Z.P. Hao, Catalytic oxidation of toluene over Pd/Co3AlO catalysts derived from hydrotalcite-like compounds: Effects of preparation methods, Applied Catalysis B: Environmental, 101 (2011) 570-579.
[35] D. Akporiaye, S.F. Jensen, U. Olsbye, F. Rohr, E. Rytter, M. Rønnekleiv, A.I. Spjelkavik, A Novel, Highly Efficient Catalyst for Propane Dehydrogenation, Industrial & Engineering Chemistry Research, 40 (2001) 4741-4748.
[36] E.A. Redekop, S. Saerens, V.V. Galvita, I.P. González, M. Sabbe, V. Bliznuk, M.-F. Reyniers, G.B. Marin, Early stages in the formation and burning of graphene on a Pt/Mg(Al)Ox dehydrogenation catalyst: A temperature- and time-resolved study, Journal of Catalysis, 344 (2016) 482-495.
[37] H. Bahruji, M. Bowker, G. Hutchings, N. Dimitratos, P. Wells, E. Gibson, W. Jones, C. Brookes, D. Morgan, G. Lalev, Pd/ZnO catalysts for direct CO2 hydrogenation to methanol, Journal of Catalysis, 343 (2016) 133-146.
[38] K. Föttinger, The effect of CO on intermetallic PdZn/ZnO and Pd2Ga/Ga2O3 methanol steam reforming catalysts: A comparative study, Catalysis Today, 208 (2013) 106-112.
[39] K. Föttinger, J.A. van Bokhoven, M. Nachtegaal, G.n. Rupprechter, Dynamic Structure of a Working Methanol Steam Reforming Catalyst: In Situ Quick-EXAFS on Pd/ZnO Nanoparticles, The Journal of Physical Chemistry Letters, 2 (2011) 428-433.

[40] A. Karim, T. Conant, A. Datye, The role of PdZn alloy formation and particle size on the selectivity for steam reforming of methanol, Journal of Catalysis, 243 (2006) 420-427.
[41] N. Iwasa, O. Yamamoto, R. Tamura, M. Nishikubo, N. Takezawa, Difference in the reactivity of acetaldehyde intermediates in the dehydrogenation of ethanol over supported Pd catalysts, Catalysis Letters, 62 (1999) 179-184.
[42] J. Pelleg, Diffusion in MgO (Magnesia or Periclase), Diffusion in Ceramics, Springer International Publishing, Cham, 2016, pp. 237-299.
[43] A. Longo, L.F. Liotta, G. Pantaleo, F. Giannici, A.M. Venezia, A. Martorana, Structure of the Metal–Support Interface and Oxidation State of Gold Nanoparticles Supported on Ceria, The Journal of Physical Chemistry C, 116 (2012) 2960-2966.
[44] A. Ota, E.L. Kunkes, I. Kasatkin, E. Groppo, D. Ferri, B. Poceiro, R.M. Navarro Yerga, M. Behrens, Comparative study of hydrotalcite-derived supported Pd2Ga and PdZn intermetallic nanoparticles as methanol synthesis and methanol steam reforming catalysts, Journal of Catalysis, 293 (2012) 27-38.
[45] M.W. Tew, H. Emerich, J.A. van Bokhoven, Formation and Characterization of PdZn Alloy: A Very Selective Catalyst for Alkyne Semihydrogenation, The Journal of Physical Chemistry C, 115 (2011) 8457-8465.
[46] A.V. Chistyakov, V.Y. Murzin, G.M. A., M.V. Tsodikov, Pd-Zn Containing Catalysts for Ethanol Conversion Towards Hydrocarbons, Chemical Engineering Transactions, 32 (2013) 619-624.
[47] B.G. Ershov, A.V. Anan'ev, E.V. Abkhalimov, D.I. Kochubei, V.V. Kriventsov, L.M. Plyasova, I.Y. Molina, N.Y. Kozitsyna, S.E. Nefedov, M.N. Vargaftik, I.I. Moiseev, Bimetallic Pd-M (M = Co, Ni, Zn, Ag) nanoparticles containing transition metals: Synthesis, characterization, and catalytic performance, Nanotechnologies in Russia, 6 (2011) 323-329.
[48] S. Pin, M. Suardelli, F. D'Acapito, G. Spinolo, M. Zema, S.C. Tarantino, P. Ghigna, Role of Interfacial Energy and Crystallographic Orientation on the Mechanism of the ZnO + Al2O3 → ZnAl2O4 Solid-State Reaction: I. Reactivity of Films Deposited onto the Sapphire (110) and (012) Faces, The Journal of Physical Chemistry C, 117 (2013) 6105-6112.
[49] H. Xiong, A. DeLaRiva, Y. Wang, A.K. Datye, Low-temperature aqueous-phase reforming of ethanol on bimetallic PdZn catalysts, Catalysis Science & Technology, 5 (2015) 254-263.
[50] J. Araña, N. Homs, J. Sales, J.L.G. Fierro, P. Ramirez de la Piscina, CO/CO2 hydrogenation and ethylene hydroformylation over silica-supported PdZn catalysts, Catalysis Letters, 72 (2001) 183-189.
[51] A. Tamtögl, M. Kratzer, J. Killman, A. Winkler, Adsorption/desorption of H2 and CO on Zn-modified Pd(111), The Journal of Chemical Physics, 129 (2008) 224706.
[52] M. Mavrikakis, M.A. Barteau, Oxygenate reaction pathways on transition metal surfaces, Journal of Molecular Catalysis A: Chemical, 131 (1998) 135-147.

[53] M. Li, W. Guo, R. Jiang, L. Zhao, H. Shan, Decomposition of Ethanol on Pd(111): A Density Functional Theory Study, Langmuir, 26 (2009) 1879-1888.
[54] K.M. Neyman, K.H. Lim, Z.-X. Chen, L.V. Moskaleva, A. Bayer, A. Reindl, D. Borgmann, R. Denecke, H.-P. Steinruck, N. Rosch, Microscopic models of PdZn alloy catalysts: structure and reactivity in methanol decomposition, Physical Chemistry Chemical Physics, 9 (2007) 3470-3482.
[55] K.-D. Jung, O.-S. Joo, S.-H. Han, Structural change of Cu/ZnO by reduction of ZnO in Cu/ZnO with methanol, Catalysis Letters, 68 (2000) 49-54.
[56] L. Lloyd, Handbook of Industrial Catalysts, Springer US2011.
[57] W. Karim, C. Spreafico, A. Kleibert, J. Gobrecht, J. VandeVondele, Y. Ekinci, J.A. van Bokhoven, Catalyst support effects on hydrogen spillover, Nature, 541 (2017) 68-71.
[58] B. Schwab, A. Ruh, J. Manthey, M. Drosik, Zinc, Ullmann's Encyclopedia of Industrial Chemistry, Wiley-VCH Verlag GmbH & Co. KGaA2000.
[59] M. Filez, E.A. Redekop, V.V. Galvita, H. Poelman, M. Meledina, S. Turner, G. Van Tendeloo, A.T. Bell, G.B. Marin, The role of hydrogen during Pt-Ga nanocatalyst formation, Physical Chemistry Chemical Physics, 18 (2016) 3234-3243.

Chapter 4:

PdZn nanoparticle catalyst formation for ethanol dehydrogenation: active metal impregnation vs incorporation*

Two hydrotalcite-based catalysts have been prepared to investigate the effect of synthesis methods on the catalyst behavior in ethanol dehydrogenation to acetaldehyde. On the first one, PdZn/Mg(Al)O_x, Pd and Zn were impregnated on the hydrotalcite support while on the second one, PdZn/Mg(Al)(Pd)(Zn)O_x, Pd and Zn were both incorporated during the support synthesis. Elaborate catalyst characterization including EXAFS, XPS, STEM, XRD,… indicated that impregnation of the active metals gives rise to larger nanoparticles as compared to incorporation. Impregnation provokes incomplete reduction, yielding nanoparticles with a PdZn shell and a Pd core. More homogeneously alloyed nanoparticles were obtained after incorporation. The higher methane selectivity on the impregnated catalyst is in agreement with the less uniformly alloyed nanoparticles, which more likely exhibit adjacent Pd-sites promoting product acetaldehyde decomposition. Overall, incorporation gave rise to the most active and selective catalyst to acetaldehyde for ethanol dehydrogenation to acetaldehyde.

* A modified version of this chapter has been published as: J. De Waele, V.V. Galvita, H. Poelman, C. Detavernier, J.W. Thybaut, PdZn nanoparticle catalyst formation for ethanol dehydrogenation: active metal impregnation vs incorporation , Appl. Catal. A, 555 (2018) 12-19.

4.1. Introduction

The chemical industry is always thriving towards more efficient and waste-free processes. Catalyst research plays an important role in this endeavor by pursuing materials improving activity and selectivity to the desired product such that, among others, the need for further product purification is reduced. Metal catalysts are commonly used for this purpose. Quite often, the catalytic behavior of a single metal is further tuned by adding a second one [1]. The synergistic properties typically exhibited by such bimetallic catalysts have been exploited already in various conventional petroleum converting processes and are currently investigated for use in the bio-based chemical industry [2].

The ultimate properties exhibited by bimetallic catalysts very much depend on the exact preparation method that has been adopted. Bimetallic catalysts are often synthesized via more complex techniques such as chemical vapor deposition, flame spray pyrolysis, etc. [3-6]. The advantage of such techniques being that they typically result in more finely dispersed metal nanoparticles as compared to the ones that are obtained via bulk techniques, their major challenge is their scale up to produce commercially relevant quantities. As a result, industrially employed catalysts are often produced via wet incipient impregnation or coprecipitation, i.e., techniques that are more easily applicable at a larger scale, yet typically not allowing the same fine control of metal nanoparticle formation as the above-cited, more complex techniques [3]. Recently, significant advances have been made towards the controlled synthesis of nanoparticles via so-called bulk techniques via the incorporation of active metals in a hydrotalcite-based support [7-11]. Key to this is that upon reduction, the active metals diffuse to the support surface and form well-dispersed nanoparticles.

The introduction of an active phase onto a hydrotalcite-based support via different synthesis techniques, i.e., from wet incipient impregnation of the active metals to incorporation in the support upon its synthesis, has been reported recently [7, 12-14]. Ota et al. used the latter technique for the formation of alloy particles [13]. Sun et al. investigated the effect of

incorporating different amounts of In while impregnating Pt on the support [15]. These authors found that an optimal amount of alloying material should be added, depending on the targeted stoichiometry of the alloy. Li et al. have compared Pd impregnation versus incorporation in a Co_3AlO hydrotalcite-like support [14]. These authors have found that for their reaction and catalyst, i.e., total oxidation of toluene on a metal oxide catalyst, the incorporated sample was more active compared to the impregnated one. They have attributed this to a higher Pd dispersion and reducibility, which maximized the interaction between the PdO and Co_3O_4 sites. However, no real alloy particle was formed.

Investigating the effect of the synthesis method on the formation of an alloy catalyst can be performed on PdZn catalysts as this is a relevant alternative catalyst to Cu catalysts typically used for dehydrogenation reactions [16]. The effect of the activation treatment on the catalyst behavior for PdZn/Mg(Al)(Pd)(Zn)O_x, i.e., the incorporated version of this catalyst, was investigated in the previous chapter. Cycled reduction, i.e., subsequent H_2-air-H_2-air-H_2 treatments, was demonstrated to improve the stability and activity of the catalyst as compared to the singly reduced variant, i.e., only having undergone single H_2 treatment. In the present chapter, two synthesis methods for the PdZn alloy catalyst are compared: the previously used direct incorporation of Pd and Zn into the support, and the synthesis of the support with subsequent addition of Pd and Zn via incipient wet impregnation. As such, the effect of the synthesis method on the alloy formation and catalyst performance for ethanol dehydrogenation is investigated. We obtain more insight in what conditions are needed for homogeneous alloy nanoparticle formation.

4.2. Results

4.2.1. PdZn nanoparticle characterization

The Pd and Zn loading as measured via ICP-OES as well as the resulting molar Pd/Zn-ratio on the synthesized catalysts are reported in Table 4- 1. The actual loading of the calcined catalysts corresponds well with the nominal one.

However, after activation and reaction for 6 days the loading of the impregnated catalyst has decreased with one third. In contrast, the incorporated catalyst does not lose any of its active metals. The loss in Zn and Pd loading after reaction and regeneration could be attributed either to evaporation or to migration. Zn is known for easy evaporation due to its relatively low boiling point, i.e., 1180K, which is even further reduced by the nanosize of the Zn particles [17, 18]. For Pd, evaporation is less evident. However, the oxidation sequences in the regeneration will not only burn off possible coke deposits, but also oxidize the Pd particles, reducing the melting point from 1828K to 1023K. Additionally, this process will locally generate heat. Based on the removal of all potentially formed coke and oxidation of Pd and Zn and assuming that no heat dissipation occurs, a temperature rise of more than 600K was calculated. Even in the presence of heat losses, it can reasonably be assumed that sufficient heat is generated to increase the Pd mobility and have it migrating towards the inert diluent material, if not evaporating. During the reduction sequences, Pd hydrides can be formed for which Di Vece et al. reported that the evaporation temperature severely decreases as compared to Pd [19]. The latter hydrides can indeed be formed during reduction [19]. The evaporation temperature could, hence, even decrease to 600K. These phenomena only occur when the interaction of the active metals with the support is weak. It thus seems that the stability of the active metals is improved upon incorporation in the support compared to impregnation. The surface area of the impregnated catalyst exceeds that of the incorporated catalyst, see Table 4- 1, which is attributed to the hydrotalcite structure formation being disturbed by the introduction of larger Pd and Zn atoms compared to the Mg and Al atoms

in the incorporated variant. Upon activation, the surface area decreases for both catalysts, although for the impregnated catalyst, the change is more significant. This is attributed to the diffusion of Pd and Zn towards each other, thereby blocking the catalyst pores.

Table 4- 1: BET surface area and weight percentages of Pd and Zn on PdZn/Mg(Al)O_x and PdZn/Mg(Al)(Pd)(Zn)O_x, determined via ICP-OES.

Catalyst	Treatment	BET surface area ($m^2\ g_{cat}^{-1}$)	Pd-loading (wt%)	Zn-loading (wt%)	Zn/Pd-ratio (mol/m
PdZn/Mg(Al)O_x	Calcined	158 ± 9.3	1.0 ± 0.008	1.1 ± 0.008	1.8
	Activated, after reaction	34 ± 5.0	0.3 ± 0.0005	0.3 ±0.0005	1.5
PdZn/Mg(Al)(Pd)(Zn)O	Calcined	28 ± 3.0	1.0 ± 0.008	1.4 ± 0.008	2.2
	Activated, after reaction	17 ± 2.0	1.1 ± 0.005	1.6 ± 0.005	2.2

Table 4- 2: Metal surface mol fraction $C_{surf,Pd}$ and $C_{surf,Zn}$ as determined from XPS, after activation.

Catalyst	$C_{surf,Pd}$ (mol%)	$C_{surf,Zn}$ (mol%)	Binding Energy $Pd3d_{5/2}$ (eV)	Binding Energy $Zn2p_{3/2}$ (eV)	Kinetic Energy Zn $L_3M_{45}M_{45}$ (eV)
PdZn/Mg(Al)O_x	1.7 ± 0.3	0.4 ± 0.4	336.9	1021.8	989.6
PdZn/Mg(Al)(Pd)(Zn)O_x	1.6 ± 0.3	2.2 ± 0.5	336.8	1021.3	989.9

Following the different synthesis methods, the active metals are either deposited on the surface or incorporated in the support. To determine the surface composition, XPS has been performed . The surface concentrations of Pd and Zn are listed in Table 4- 2. For the impregnated sample, a higher Pd surface concentration than the nominal one, i.e., 1 wt% or 0.6 mol%, was measured. Since wet incipient impregnation deposits the active metals on the surface or in the pores of the catalyst, the catalyst surface is rich in Pd and Zn before calcination and activation.

Upon these treatments, Zn and Pd can diffuse into the support or remain at the surface. It seems that Pd prefers to stay at the surface rather than diffusing into the support. The Zn surface concentration on the impregnated catalyst is lower than the bulk concentration, as determined by ICP. Several reasons can be at the origin of this observation, e.g., Zn may have diffused into the support, leading to surface depletion or Pd may have partially covered Zn. On the incorporated sample, Zn and Pd diffuse both from the support to the surface, see Table 4- 2, resulting in active metal enrichment on the surface for both Pd and Zn and, hence, the formation of easily accessible nanoparticles. To determine the chemical state of Pd and Zn, the position of the peaks relative to the reference C1s was determined, see Table 4- 2 . For the impregnated sample, the chemical nature of Pd and Zn present in the calcined and the activated sample is always close to metallic Pd and ZnO. For the incorporated catalyst, Pd and Zn are in the metallic state after activation.

4.2.1.1.Effect of redox cycling on the nanoparticle formation

When performing redox cycles at 823K during in-situ XRD measurements on both catalysts, the formation and decomposition of the PdZn intermetallic phase can be directly observed, see Figure 4- 1. MgO remains present throughout the cycles with diffraction peaks at 36.9° and 42.9° (PDF 00-045-0946). At angles between 33° and 35°, diffraction peaks of PdO (PDF 00-041-1107) and ZnO (PDF 00-036-1451) are observed during oxidation, see Figure 4- 1a-b. These disappear upon reduction when the peak of PdZn (PDF 00-006-0620) appears at 41.2°, as indicated with the downward arrow on Figure 4- 1 and visualized in the integrated intensities of PdO, ZnO and PdZn.

For the impregnated PdZn/Mg(Al)O_x catalyst, peaks of PdO and ZnO remain present upon reduction, even when the PdZn phase is already formed, see Figure 4- 1a. This indicates the presence of larger PdO and ZnO clusters, that require more time for full reduction. Peaks corresponding to remaining PdO and ZnO were not observed for the incorporated catalyst PdZn/Mg(Al)(Pd)(Zn)O_x.

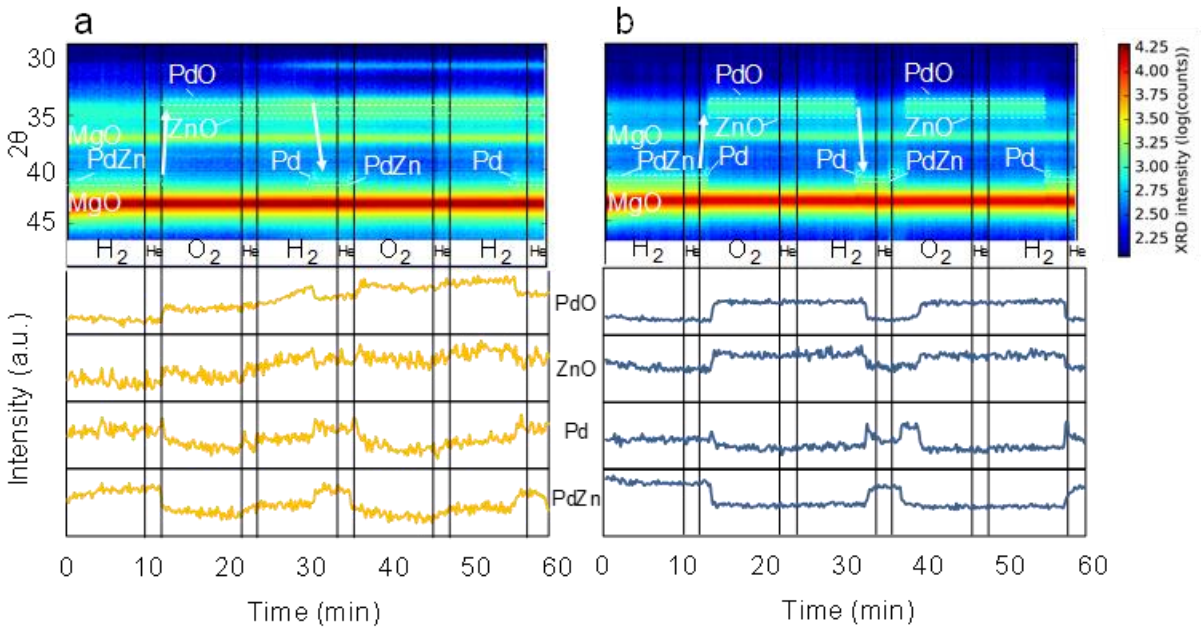

Figure 4- 1: in-situ XRD during redox cycles at 823K for PdZn/Mg(Al)O_x (a, orange) and PdZn/Mg(Al)(Pd)(Zn)O_x (b, blue). 2D XRD map on top and intensities of PdO, i.e., 34.0°, ZnO, i.e., 35.2°, Pd, i.e., 40.1° and PdZn, i.e., 41.6° at the bottom.

The arrows indicate the transformation of PdO and ZnO to PdZn. The vertical black lines delineate the reduction and oxidation stages.

4.2.1.2. Oxidation state determination

To further validate the XRD results and investigate the formation of the PdZn intermetallic phase, XAS experiments have been performed. Figure 4- 2 illustrates the spectra at the Pd K-edge at different stages of catalyst formation: as prepared, calcined and activated. The spectra of Pd foil, PdO and PdZn have been added as a reference in Figure 4- 2d for the interpretation of the results. Figure 4- 2a nicely shows how, for the as prepared catalysts, the XANES spectrum of the incorporated catalyst retraces PdO, while the one of the impregnated catalyst approaches that of a Pd foil. Interaction of Pd with NO_3 could be expected from the preparation of this latter catalyst, however, when comparing its spectrum with the reference spectra, it is clear that this does not occur and Pd takes up a metallic state.

The spectra of the calcined samples, see Figure 4- 2b, are very similar to each other and correspond with PdO. Upon activation, both XANES spectra change towards a PdZn reference spectrum [20], with the incorporated sample having a more pronounced resemblance.

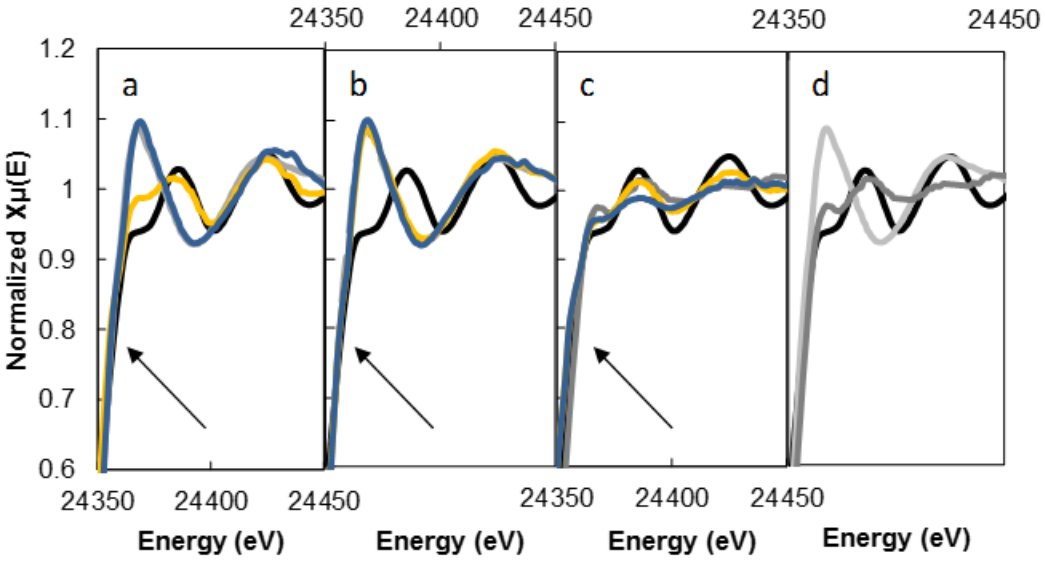

Figure 4- 2: Comparison of the XANES-WL for PdZn/Mg(Al)O_x (orange) and PdZn/Mg(Al)(Pd)(Zn)O_x (blue) at the Pd K-edge with PdO (light grey), PdZn (dark grey) and Pd foil (black) as references. The arrow points to a small shoulder in the spectra indicating a good interaction with the support.
a: as prepared, b: after calcination at 873K, c: after activation at 823K, d: references.

Also here, linear combinations are fitted to the reference spectra, as explained in Chapter 3. The resulting contributions of Pd, PdO and PdZn in the catalysts are reported in Table 4- 3. For the calcined catalysts, Pd is mainly present as PdO. When applying activation on the impregnated catalyst, the contribution of PdZn changes significantly to 55%. This is even more pronounced for the incorporated catalyst, where almost 90% of Pd is present as PdZn. This indicates that the formation of the catalyst via the extraction of Pd and Zn from the support to the surface strongly aids the formation of a homogeneous stoichiometric intermetallic particle.

Table 4- 3: Chemical nature of Pd and Zn in PdZn/Mg(Al)O_x and PdZn/Mg(Al)(Pd)(Zn)O_x determined by least square regression of reference spectra.

Catalyst	Activation procedure	Pd as PdZn (%)	Pd as PdO (%)	Pd as Pd (%)	Zn as PdZn (%)	Zn as $ZnAl_2O_4$ (%)	Zn as ZnO (%)	Zn as Zn (%)
PdZn/Mg(Al)O_x	Calcined	0.0	93.7	6.3	0.0	71.2	28.8	0.0
	Activated	55.0	3.6	41.4	44.1	55.9	0.0	0.0
PdZn/Mg(Al)(Pd)(Zn)O_x	Calcined	0.0	100.0	0.0	0.0	61.1	38.9	0.0
	Activated	87.8	9.4	2.8	39.3	46.2	14.5	0.0

When looking at the Zn K-edge in the XANES spectra, little difference between the impregnated and incorporated sample can be found. Again, a linear combination was performed, now using Zn, ZnO, PdZn and $ZnAl_2O_4$ as reference spectra [21, 22]. The contributions of the reference spectra are mentioned in Table 4- 3. Even for the impregnated catalyst, Zn has a strong interaction with the support, thus indicating that Zn is stabilized in the support as $ZnAl_2O_4$ rather than forming ZnO clusters on the surface. This explains the XPS result that, for the impregnated catalyst, Zn is less present on the surface than expected. Upon activation, Zn is partially incorporated in PdZn and is less present at the surface as ZnO or Zn, for both samples. Still, the contribution of $ZnAl_2O_4$ remains considerable.

The R-space spectra obtained from full Zn K-edge EXAFS scans indicate a deeper reduction of the incorporated sample as compared to the impregnated sample, see Figure 4- 3. This is evident from the intensity ratio of the two major peaks in the spectra, at 1.5Å and 2.6Å. In the ZnO reference, the peak at 1.5Å represents Zn-O bonds, while the second peak, appearing at ~2.9Å, originates from second neighbors. Both peaks have a similar intensity for this reference ZnO material. For metallic Zn, a single peak is obtained at 2.2Å. The peak at 2.6Å obtained for the

impregnated and incorporated catalysts can, hence, be seen as a superposition of the oxide peak with the metal peak. Therefore, the relative intensity of the 1.5Å peak compared to the peak at 2.6Å is interpreted as a qualitative indication of the degree of oxidation or reduction. For the incorporated catalyst, the relative intensity of the oxide peak is lower than for the impregnated catalyst, thus indicating a higher reduction of the nanoparticles on the incorporated catalyst.

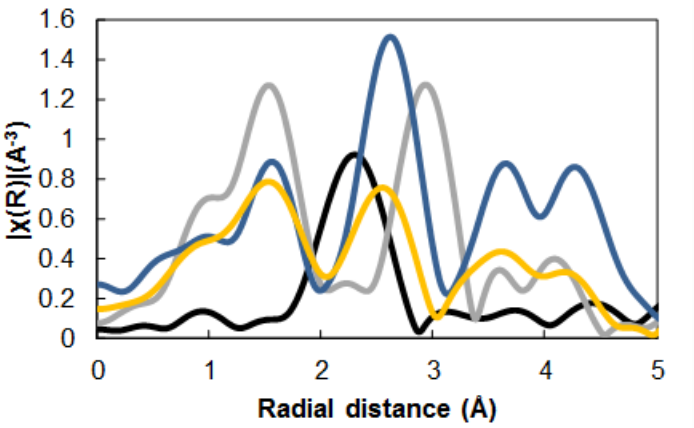

Figure 4- 3: Comparison of PdZn/Mg(Al)O_x (orange) and PdZn/Mg(Al)(Pd)(Zn)O_x (blue) after activation at 823K in R-space at the Zn K-edge with ZnO (grey) and Zn foil (black) as reference.

4.2.1.3. Particle size

The particle size was determined by means of STEM, see Figure 4- 4. The analysis was performed on samples that were subjected to the activation procedure. The average particle size is 7 ± 2.3nm for the impregnated catalyst and 5.3 ± 1.8nm for the incorporated one. These results are in line with the synthesis methods used, i.e., somewhat larger clusters are formed on the surface after impregnation, the incorporation of Pd and Zn in the support entails a more uniform dispersion, which pertains after diffusion of both metals to the surface. This results in a more homogeneous distribution of the metal atoms over the catalyst surface and, hence, in smaller particles. When being subjected to several redox cycles, these clusters decompose and reform, as observed during in-situ XRD measurements (see Figure 4- 1). It has to be noted that both synthesis methods give rise to nanosize intermetallic particles, which is beneficial for the fraction exposed and, hence, for the activity of the catalysts in comparison with conventional Pd catalysts impregnated on ZnO which typically have a diameter in the range from 10 to 20nm [23].

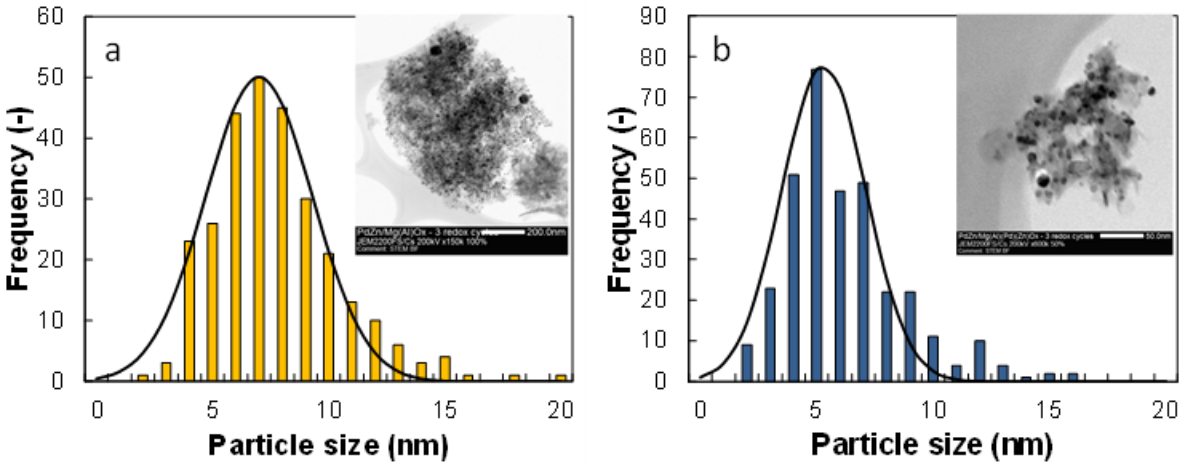

Figure 4- 4: Particle size distribution of activated PdZn/Mg(Al)O_x (a) and PdZn/Mg(Al)(Pd)(Zn)O_x (b), based on STEM images (see insets).

4.2.2. Performance testing

The evolution of the activity with time on stream for the activated impregnated and incorporated catalysts has been assessed in continuous flow experiments. As seen in Figure 4- 5, the activity is lower for the impregnated catalyst as compared to the incorporated catalyst, i.e., resp. 0.14 mol $(s\ kg_{Pd})^{-1}$ and 0.8 mol $(s\ kg_{Pd})^{-1}$. Here, the nominal Pd content was used to calculate the STY. Doing so, we can compare the catalyst performance irrespective of the metal loading [24]. The acetaldehyde selectivity is also lower for the impregnated sample, i.e., 93% compared to 97.5%. This effect is even more pronounced in the first hours on stream.

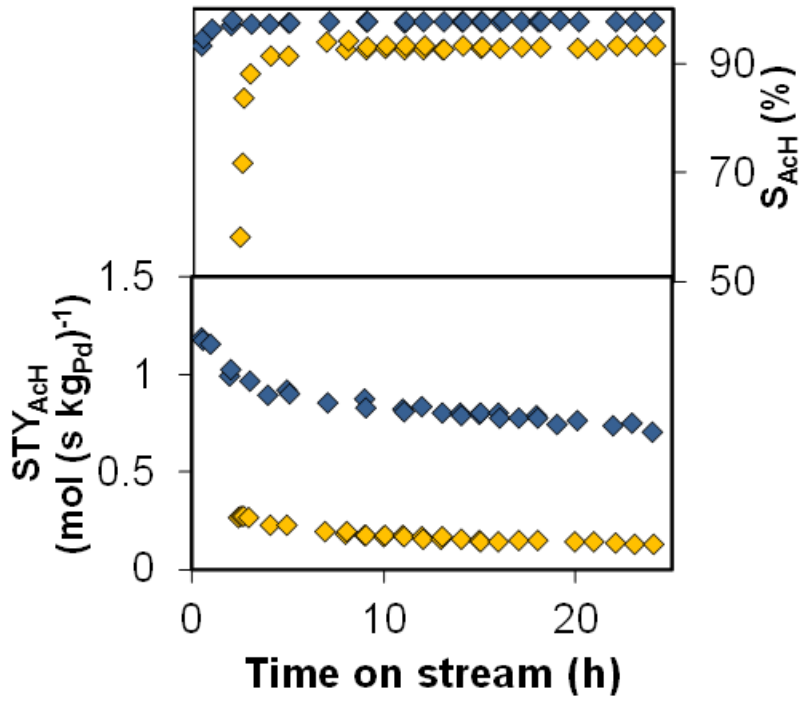

Figure 4- 5: Performance curves of the activated PdZn/Mg(Al)O_x (orange) and PdZn/Mg(Al)(Pd)(Zn)O_x (blue) catalysts.

4.3. Discussion

Based on the results presented in the previous sections, it is evident that the structure of the impregnated and incorporated catalyst is different. It results in distinct differences in activity and selectivity. In what follows, first the structure of the catalysts will be discussed and, subsequently, this interpretation will be employed in the assessment of the catalyst performance.

4.3.1. Formation of the active PdZn nanoparticles

A schematic representation of the formation of both catalysts is given in Figure 4- 7. The main difference between the two catalysts after calcination is that Pd and Zn are present on the surface for the impregnated catalyst, whereas they are embedded in the support for the incorporated catalyst. This is confirmed by STEM, see Figure 4- 6. As expected, both elements are present in an oxide state, i.e., PdO for Pd and ZnO and $ZnAl_2O_4$ for Zn, for both catalysts, see Table 4- 3.

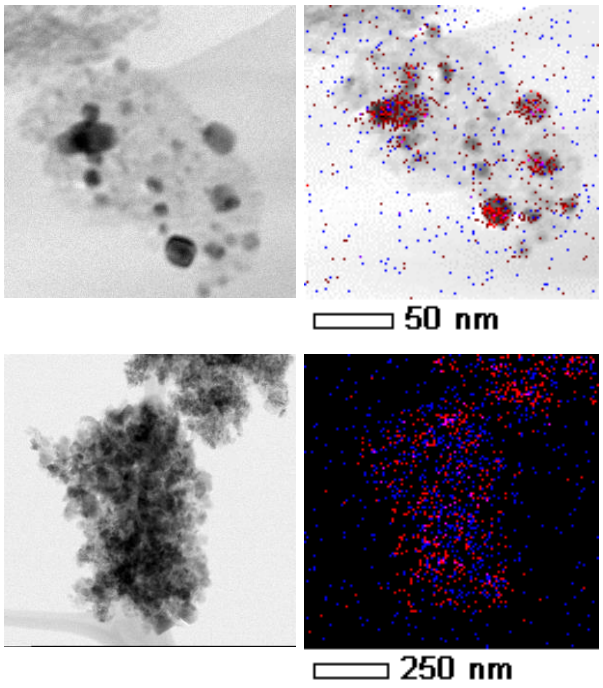

Figure 4- 6: STEM-EDX of calcined PdZn/Mg(Al)O_x (top) and PdZn/Mg(Al)(Pd)(Zn)O_x (bottom). red: Pd, blue: Zn.

Upon H_2 reduction at 823K, Pd is reduced first for both catalysts. As mentioned in Chapter 3, hydrogen spillover from Pd to ZnO is required for the reduction of the latter and Pd-Zn alloy formation. In the previous chapter, it was proven that upon reduction and alloy formation, the presence in and diffusion of Zn towards the Pd surface stops the H_2 dissociative adsorption on Pd and, hence, also the further ZnO reduction, resulting in particles with a PdZn shell and a Pd core [24]. The cyclic nature of the activation procedure is specifically required for the formation of fully alloyed particles.

When considering the results obtained for the impregnated sample, XAS results indicate the presence of only 55% Pd as PdZn, see Table 4- 3. This is also clear when looking at Figure 4- 2, the XANES and first EXAFS region do not correspond fully with the PdZn reference spectrum for the impregnated catalyst, whereas they do correspond better for the incorporated catalyst. The XAS results on the Zn edge, see Table 4- 3, also indicate the presence of Zn as $ZnAl_2O_4$ for the impregnated catalyst which suggest diffusion of Zn into the support. This is remarkable, since Zn is indeed present as ZnO on the incorporated catalyst. This most likely corresponds with remaining Zn which did not get incorporated in the PdZn particle but that stayed in the neighborhood on the surface of the support. Figure 4- 4 shows that the nanoparticles on the impregnated sample are slightly larger than for the incorporated one. This renders their entire reduction more difficult by hindering Zn diffusion in the Pd nanoparticles. The nanoparticles on the incorporated catalyst are sufficiently small to ensure Zn diffusion throughout the entire Pd nanoparticle. Combining these results indicates that a PdZn shell with a Pd core is formed for the impregnated catalyst, even after activation, while for the incorporated sample, the PdZn particles are uniform.

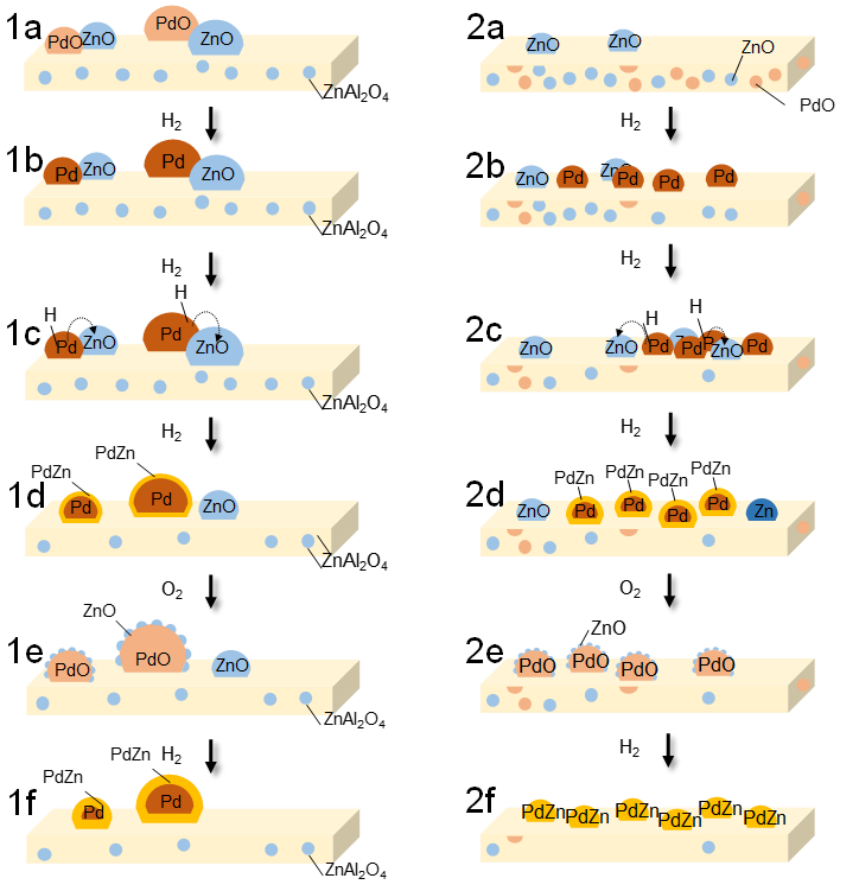

Figure 4- 7: Representation of the formation of the intermetallic compound during activation at 823K. 1: PdZn/Mg(Al)O_x, 2: PdZn/Mg(Al)(Pd)(Zn)O_x. dark orange: Pd, light blue: ZnO or $ZnAl_2O_4$, light orange: PdO, gold: intermetallic compound PdZn.

4.3.2. Catalyst performance evaluation

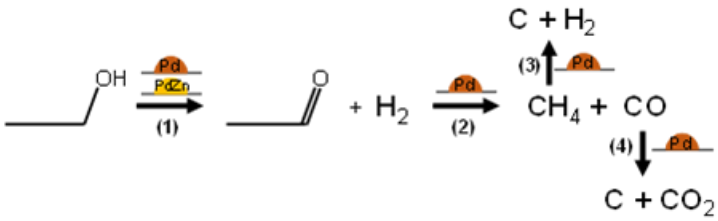

Figure 4- 8: Schematic representation of the reaction mechanism on a PdZn catalyst.

Gold: PdZn particles, orange: Pd-rich particles.

As discussed in the previous chapter, the occurring reactions actually take place on two different types of sites. On PdZn sites, only the desired ethanol conversion into acetaldehyde proceeds. This reaction can also occur on adjacent Pd sites, which, however, also catalyze the subsequent transformation of the product acetaldehyde to methane and carbon monoxide, and further to coke [24]. This explains the activity loss and enhancement of acetaldehyde selectivity during the first hours on stream for both catalysts, albeit more pronounced for the impregnated sample. A less uniform alloy catalyst nanoparticle, as present on the impregnated sample will exhibit more adjacent Pd sites and, hence, result in a higher methane selectivity, see Figure 4- 8. Metal losses are found after reaction for six days with 4 regenerations. Metal evaporation was, probably, caused due to a local hotspot when burning coke from the catalyst. Small nanoparticles can be formed via partial evaporation of a particle, thereby reducing its size or due to the re-condensation of the evaporated material on the catalyst surface. Of course, also part of the material will effectively be removed from the catalyst due to these phenomena. Enhanced alloy formation compensates for the metal losses via regeneration cycles. Even after accounting for the active metal losses, see Table 4- 1, the activity of the incorporated catalyst remains higher than of the impregnated catalyst. This might be due to the coking of the Pd sites, thereby also blocking active PdZn sites [24]. Furthermore, the impregnated catalyst has bigger particles, leading to less available active sites.

4.4. Conclusions

The effect of impregnation versus incorporation in bimetallic PdZn nanoparticle synthesis on a hydrotalcite-based mixed oxide support has been investigated. Impregnation of the active metals on the support was found to result in comparatively larger particles, whereas incorporation atomically disperses the active metals Pd and Zn throughout the support which, upon activation, give rise to smaller particles, i.e., 5nm compared to 7nm for the impregnated catalyst. Upon reduction, alloying is observed for both catalysts. Due to the smaller particles formed on the incorporated catalyst, entirely reduced and homogeneously alloyed nanoparticles are more easily obtained on this catalyst as compared to the impregnated one. Activation improves the intermetallic particle formation for the impregnated catalyst and increases the active site concentration on the incorporated one. Active metal losses were determined after activation and reaction for the impregnated catalyst, whereas they are maintained properly on the incorporated variant.

The impregnated catalyst is less active than the incorporated one. Also, the selectivity towards acetaldehyde exhibited by the incorporated catalyst exceeds that of the impregnated catalyst. This is attributed to the higher concentrations of Pd-Pd sites on the impregnated catalyst, which are more prone to acetaldehyde decomposition and methane decomposition to cokes. Furthermore, the active site concentration on the impregnated catalyst is lower than on the incorporated catalyst due to the bigger particle size.

Overall, active metal impregnation versus incorporation has been proven to exert a great impact on the formation of the active sites and their activity. The activated incorporated PdZn/Mg(Al)(Pd)(Zn)O_x catalyst turns out to be superior in activity compared to the impregnated variant.

4.5. References

[1] B.C. Gates, Supported Metal Cluster Catalysts, Preparation of Solid Catalysts, Wiley-VCH Verlag GmbH2008, pp. 371-388.
[2] M. Sankar, N. Dimitratos, P.J. Miedziak, P.P. Wells, C.J. Kiely, G.J. Hutchings, Designing bimetallic catalysts for a green and sustainable future, Chemical Society Reviews, 41 (2012) 8099-8139.
[3] R.J. White, R. Luque, V.L. Budarin, J.H. Clark, D.J. Macquarrie, Supported metal nanoparticles on porous materials. Methods and applications, Chemical Society Reviews, 38 (2009) 481-494.
[4] J.D. Aiken, R.G. Finke, A review of modern transition-metal nanoclusters: their synthesis, characterization, and applications in catalysis, Journal of Molecular Catalysis A: Chemical, 145 (1999) 1-44.
[5] H. Bönnemann, Ryan M. Richards, Nanoscopic Metal Particles − Synthetic Methods and Potential Applications, European Journal of Inorganic Chemistry, 2001 (2001) 2455-2480.
[6] D. Astruc, F. Lu, J.R. Aranzaes, Nanoparticles as Recyclable Catalysts: The Frontier between Homogeneous and Heterogeneous Catalysis, Angewandte Chemie International Edition, 44 (2005) 7852-7872.
[7] V. Galvita, G. Siddiqi, P. Sun, A.T. Bell, Ethane dehydrogenation on Pt/Mg(Al)O and PtSn/Mg(Al)O catalysts, Journal of Catalysis, 271 (2010) 209-219.
[8] A. Ota, J. Kröhnert, G. Weinberg, I. Kasatkin, E.L. Kunkes, D. Ferri, F. Girgsdies, N. Hamilton, M. Armbrüster, R. Schlögl, M. Behrens, Dynamic Surface Processes of Nanostructured Pd2Ga Catalysts Derived from Hydrotalcite-Like Precursors, ACS Catalysis, 4 (2014) 2048-2059.
[9] E.A. Redekop, V.V. Galvita, H. Poelman, V. Bliznuk, C. Detavernier, G.B. Marin, Delivering a Modifying Element to Metal Nanoparticles via Support: Pt–Ga Alloying during the Reduction of Pt/Mg(Al,Ga)Ox Catalysts and Its Effects on Propane Dehydrogenation, ACS Catalysis, 4 (2014) 1812-1824.
[10] S. Narayanan, K. Krishna, Structure activity relationship in Pd/hydrotalcite: effect of calcination of hydrotalcite on palladium dispersion and phenol hydrogenation, Catalysis Today, 49 (1999) 57-63.
[11] K. Takehira, "Intelligent" reforming catalysts: Trace noble metal-doped Ni/Mg(Al)O derived from hydrotalcites, Journal of Natural Gas Chemistry, 18 (2009) 237-259.
[12] M. Filez, E.A. Redekop, H. Poelman, V.V. Galvita, M. Meledina, S. Turner, G. Van Tendeloo, C. Detavernier, G.B. Marin, One-pot synthesis of Pt catalysts based on layered double hydroxides: an application in propane dehydrogenation, Catalysis Science & Technology, (2016).
[13] A. Ota, M. Armbrüster, M. Behrens, D. Rosenthal, M. Friedrich, I. Kasatkin, F. Girgsdies, W. Zhang, R. Wagner, R. Schlögl, Intermetallic Compound Pd2Ga as a Selective Catalyst for the Semi-

Hydrogenation of Acetylene: From Model to High Performance Systems†, The Journal of Physical Chemistry C, 115 (2010) 1368-1374.
[14] P. Li, C. He, J. Cheng, C.Y. Ma, B.J. Dou, Z.P. Hao, Catalytic oxidation of toluene over Pd/Co3AlO catalysts derived from hydrotalcite-like compounds: Effects of preparation methods, Applied Catalysis B: Environmental, 101 (2011) 570-579.
[15] P. Sun, G. Siddiqi, W.C. Vining, M. Chi, A.T. Bell, Novel Pt/Mg(In)(Al)O catalysts for ethane and propane dehydrogenation, Journal of Catalysis, 282 (2011) 165-174.
[16] A. Pang Tsai, S. Kameoka, Y. Ishii, PdZn=Cu: Can an Intermetallic Compound Replace an Element?, Journal of the Physical Society of Japan, 73 (2004) 3270-3273.
[17] B. Schwab, A. Ruh, J. Manthey, M. Drosik, Zinc, Ullmann's Encyclopedia of Industrial Chemistry, Wiley-VCH Verlag GmbH & Co. KGaA2000.
[18] K.K. Nanda, A. Maisels, F.E. Kruis, H. Fissan, S. Stappert, Higher Surface Energy of Free Nanoparticles, Physical Review Letters, 91 (2003) 106102.
[19] M. Di Vece, D. Grandjean, M.J. Van Bael, C.P. Romero, X. Wang, S. Decoster, A. Vantomme, P. Lievens, Hydrogen-Induced Ostwald Ripening at Room Temperature in a Pd Nanocluster Film, Physical Review Letters, 100 (2008) 236105.
[20] M.W. Tew, H. Emerich, J.A. van Bokhoven, Formation and Characterization of PdZn Alloy: A Very Selective Catalyst for Alkyne Semihydrogenation, The Journal of Physical Chemistry C, 115 (2011) 8457-8465.
[21] B.G. Ershov, A.V. Anan'ev, E.V. Abkhalimov, D.I. Kochubei, V.V. Kriventsov, L.M. Plyasova, I.Y. Molina, N.Y. Kozitsyna, S.E. Nefedov, M.N. Vargaftik, I.I. Moiseev, Bimetallic Pd-M (M = Co, Ni, Zn, Ag) nanoparticles containing transition metals: Synthesis, characterization, and catalytic performance, Nanotechnologies in Russia, 6 (2011) 323-329.
[22] S. Pin, M. Suardelli, F. D'Acapito, G. Spinolo, M. Zema, S.C. Tarantino, P. Ghigna, Role of Interfacial Energy and Crystallographic Orientation on the Mechanism of the ZnO + Al2O3 → ZnAl2O4 Solid-State Reaction: I. Reactivity of Films Deposited onto the Sapphire (110) and (012) Faces, The Journal of Physical Chemistry C, 117 (2013) 6105-6112.
[23] K. Föttinger, PdZn based catalysts: connecting electronic and geometric structure with catalytic performance, Catalysis, 25 (2013) 77-117.
[24] J. De Waele, V.V. Galvita, H. Poelman, C. Detavernier, J.W. Thybaut, Formation and stability of an active PdZn nanoparticle catalyst on a hydrotalcite-based support for ethanol dehydrogenation, Catalysis Science & Technology, 7 (2017) 3715-3727.

Chapter 5:

Effect of water on the ethanol dehydrogenation performance of PdZn/Mg(Al)(Pd)(Zn)O_x

---

PdZn intermetallic catalysts demonstrate high activity and acetaldehyde selectivity in ethanol dehydrogenation. The use of bio-ethanol and, hence, the concomitant presence of water in the feed, typically renders its catalytic conversion more challenging. Kinetic measurements demonstrate that water reversibly decreases the activity of a PdZn/Mg(Al)(Pd)(Zn)O_x catalyst during ethanol dehydrogenation, and shifts the selectivity from acetaldehyde to methane. Via a combination of catalyst characterization and computational catalysis, the water effect on the catalyst performance is attributed to the partial removal of Zn from the PdZn intermetallic particle and its oxidation into ZnO patches. The latter occurs on a Pd-rich surface resulting in an increased methane selectivity. Eliminating water from the feed partially restores the catalyst activity and acetaldehyde selectivity. Both can be fully restored by consecutive hydrogen and air treatments, which allow regenerating the PdZn intermetallic particles.

5.1. Introduction

In the previous chapters, the formation of a highly active and selective PdZn/Mg(Al)(Pd)(Zn)O_x catalyst was investigated. To be able to use this catalyst in an industrial environment, its behavior with respect to a water-containing feed should be investigated, see Chapter 1.

The presence of water in the feed, however, often dramatically impacts on the catalyst performance [1-3], e.g., by oxidation of the metallic dehydrogenation catalyst or by competitive adsorption of water on the active sites [2-8]. For the PdZn catalyst system, Friedrich et al. have investigated a PdZn/ZnO catalyst for methanol steam reforming [9]. They have proven that ZnO patches are formed on the PdZn intermetallic particle under reaction conditions. The employed catalyst particles had a diameter of ~20 nm. These authors found that, for methanol steam reforming, the ZnO/PdZn interface is key for an active and selective catalyst.

As mentioned before, hydrotalcite-based supports, which are composed of layers of hydroxides, are used for their basic nature and hydrothermal stability [10]. Upon calcination, a mixed oxide is formed which has a 3D structure rather than a layered one. A remarkable phenomenon of mixed oxides originating from hydrotalcites is the memory effect. Via this, the mixed oxide reconstructs into the layered hydrotalcite structure upon addition of water [11]. This is often detrimental for the catalyst performance, but this effect has also been used recently as an advantage [12].

In this chapter, PdZn/Mg(Al)(Pd)(Zn)Ox is tested for bio-ethanol dehydrogenation and the effect of the water content on the activity, selectivity and catalyst properties is assessed. This is performed via an experiment subjecting the catalyst to consecutively pure ethanol, 30wt%H_2O/ethanol and again pure ethanol. Also regeneration and reaction with pure ethanol on this sample is investigated. Via detailed characterization of the intermediate catalyst samples,

fundamental insight is obtained in the effects occurring during water presence. DFT calculations describing the thermodynamics have been performed to validate the experimental observations.

5.2. *DFT thermodynamic calculations*

Gibbs free energies were determined using the vdW-DF2 [13, 14] functional as implemented in the Vienna Ab initio Simulation Package (VASP)[15, 16]. A plane-wave basis set with a cut-off kinetic energy of 450 eV was applied. Benchmark calculations performed for the reduction of ZnO motivated the use of the VdW-DF2 functional. The Brillouin zone was sampled with a 3 x 3 x 1 Monkhorst-Pack grid in the case of gas phase and surface calculations. For the calculation of the bulk structures, the size of the grid was varied to keep an approximately equal number of points per unit of reciprocal distance. Therefore, an 11 x 11 x 11 grid was applied for bulk Pd and for Pd_2Zn, an 11 x 11 x 13 grid for PdZn and a 9 x 9 x 10 grid for bulk ZnO. An overview of the optimized lattice constants and a comparison to the experimental values is presented in Table 5- 1. The VdW-DF2 functional slightly overestimates the lattice constants. No experimental values were available for the lattice constant(s) of Pd_2Zn.

Table 5- 1: Optimized lattice constants for bulk Pd, PdZn and ZnO using the VdW-DF2 functional and comparison to experimental data.

Structure	a_{calc} [Å]	a_{exp} [Å]	b_{calc} [Å]	b_{exp} [Å]
Pd	4.07	3.89 [17]	-	-
PdZn	4.27	4.10 [18]	3.49	3.35 [18]
ZnO	3.30	3.20 [19]	5.34	5.12 [19]

5.3. Results

5.3.1. Effect of water on the activity

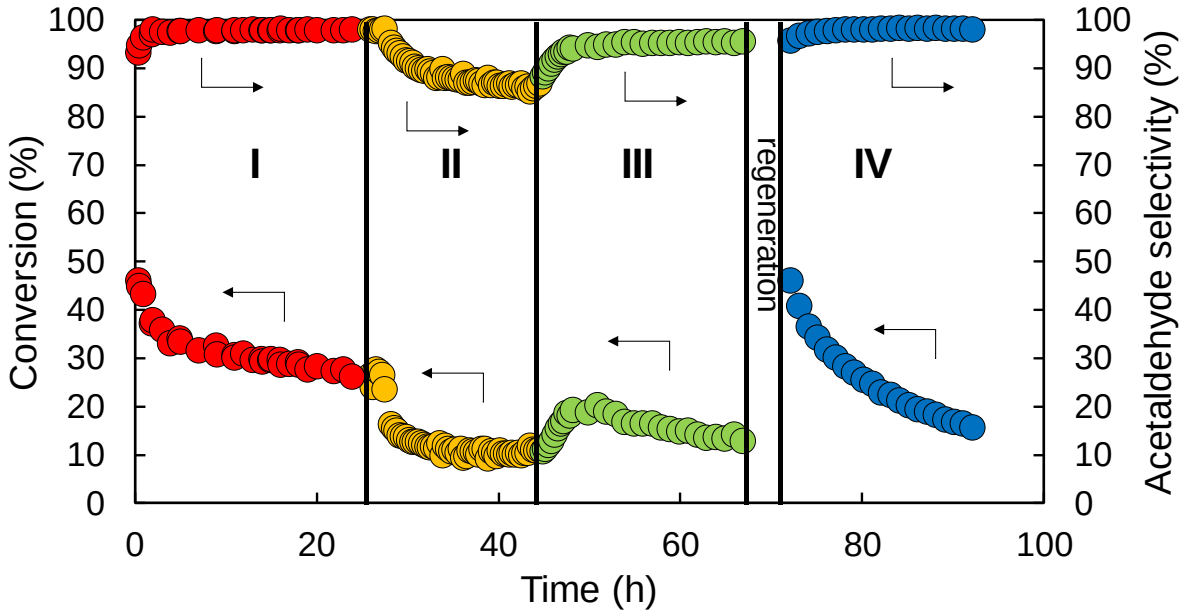

Figure 5- 1: Performance curves of PdZn/Mg(Al)(Pd)(Zn)O_x for subsequently 100wt% ethanol (I, red), 30wt% H_2O/ethanol (II, yellow), 100wt% ethanol after water feed (III, green), 100wt% ethanol after regeneration (IV, blue).

Figure 5- 1 represents the cycled reduced PdZn catalyst activity and selectivity as a function of the time on stream under the following sequence of operating conditions:

- pure ethanol, i.e., the sample '100wt% ethanol'
- 30wt% H_2O/ethanol, i.e., the sample '30wt% ethanol'
- pure ethanol , i.e., the sample '100wt% ethanol after water feed'
- again pure ethanol after an intermediate regeneration, i.e., the sample '100wt% ethanol after regeneration'.

When using pure ethanol as liquid part of the feed, frame I and red dots, the initial activity decreases in the first hours to a stable level together with an increasing acetaldehyde selectivity. This behavior has been discussed in detail in Chapter 3 [20]. The decreasing activity was attributed to the coking of adjacent Pd sites on the catalyst surface, leaving the selective PdZn sites intact, simultaneously explaining the increased acetaldehyde selectivity. In frame II, indicated by the yellow dots, it can be observed that at '30wt% H_2O/ethanol', the ethanol conversion and acetaldehyde selectivity both drop to a new stable regime, i.e., to 10% instead of 26% with an acetaldehyde selectivity of 85%. If merely a change in reaction mechanism would be at the origin of this behavior, the activity and selectivity can be expected to recover after switching back to a '100wt%ethanol' feed. As can be observed in frame III of Figure 5- 1, i.e., with the green dots, this is clearly not the case. This thus indicates that other phenomena cause the activity and selectivity losses when adding water to the feed. Only upon regeneration and feeding a pure ethanol feed, the original acetaldehyde selectivity is restored. Also the activity recovers to its original level, but subsequently decreases to a lower level than the original one, i.e., to 16% conversion rather than 26% conversion.

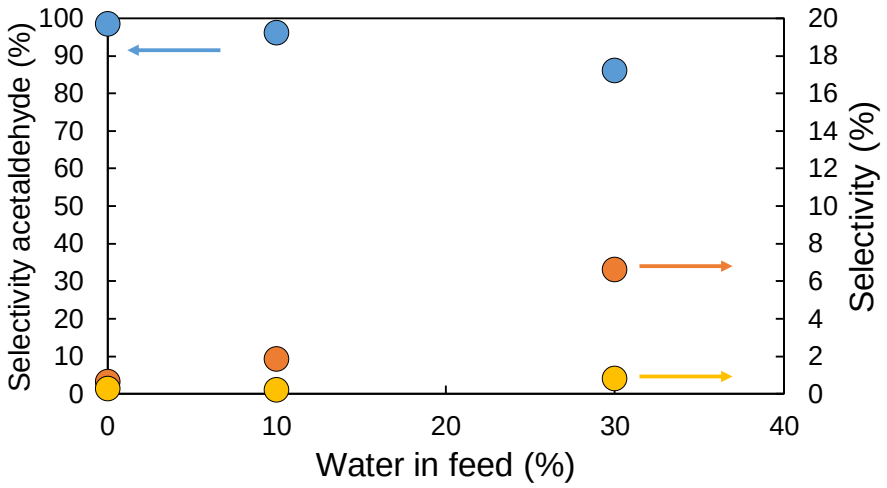

Figure 5- 2: Product selectivities at isoconversion exhibited by PdZn/Mg(Al)(Pd)(Zn)O_x at T=533K, P_{tot}=0.5MPa, N_2/Ethanol=20, X=10% for different amounts of water in ethanol. Blue: acetaldehyde, orange: methane, yellow: ethyl acetate.

Figure 5- 2 shows that the water content in the feed effectively impacts on the acetaldehyde selectivity, i.e., the observed changes in selectivity cannot be attributed to a conversion effect only. By manipulating the space time such that an ethanol conversion of approximately 10% is achieved, it becomes evident how the selectivity towards acetaldehyde drops in favor of methane, mostly, and ethyl acetate to a lesser extent by increasing the presence of water in the feed.

5.3.2. Spent catalyst characterization

To better understand the behavior during reaction, catalyst samples have been recovered and characterized after each of the previously mentioned sets of operating conditions applied.

Table 5- 2: Surface area measured by N_2 adsorption, metal loading determined by ICP-OES and particle size determined by STEM.

	BET surface area ($m^2\ g^{-1}$)	Metal loading (wt%)		STEM particle size (nm)
		Pd	Zn	
activated catalyst	95.0 ± 1.67	1.03	1.42	5.0 ± 2.0
100wt% ethanol	71.4 ± 1.66	1.25	1.62	5.0 ± 2.0
30wt% H_2O/ethanol	45.9 ± 2.15	1.16	1.66	2.0 ± 1.0
100wt% ethanol after water feed	44.9 ± 1.17	1.08	1.57	2.5 ± 1.2 & 8.0 ± 3.0
100wt% ethanol after regeneration	90.6 ± 0.82	0.76	0.95	5.5 ± 2.0

ICP analysis of the catalysts reveals that the active metal loading on the catalyst remains constant throughout the reaction, even with 30wt% H_2O/ethanol feed, see Table 5- 2. Upon regeneration however, the metal loading has dropped significantly for both Pd and Zn.

The BET surface of the spent samples decreases significantly upon feeding a water/ethanol mixture, see Table 5- 2, and remains at this lower value when switching back to pure ethanol. This can be explained by the memory effect of hydrotalcite-based materials [12]. Since the catalyst was prepared via calcination of a hydrotalcite-like material upon which it restructures into a mixed oxide, addition of water to the support might partially restore the hydrotalcite layers, i.e., the so-called memory effect [21]. This changes the surface area of the catalyst and can't be restored until calcination is repeated, as during the regeneration procedure.

The particle size is determined via STEM and doesn't change significantly upon reaction with pure ethanol from the value reported for the activated catalyst, see Table 5- 2. When feeding 30wt% H_2O/ethanol, the particle size decreases significantly, i.e., to 2 ± 1 nm. For the sample '100wt%ethanol after water', 2nm particles remain present, but a bi-modal distribution develops comprising also particles of 8 ± 3 nm. Only after regeneration, the original particle size is restored.

Two remarkable features were observed thanks to the STEM measurements. The first one is that all samples contain a fraction of hollow particles, see also Figure 5- 3 for the catalyst that was subjected to 30wt% H_2O/ethanol. This is only observed in the largest nanoparticles, i.e., particles larger than 20nm. Wang et al. and Liu et al. reviewed on the occurrence and formation of hollow nanoparticles [22, 23]. These authors describe the Kirkendall effect. Because of a difference in atomic diffusivities, the element entering the particle diffuses more slowly from the surface to the center than the element diffusing outward, i.e., in opposite direction. Thus hollow particles are formed. Here, Zn is diffusing inwards and Pd is diffusing outwards to form a hollow PdZn intermetallic particle upon reduction.

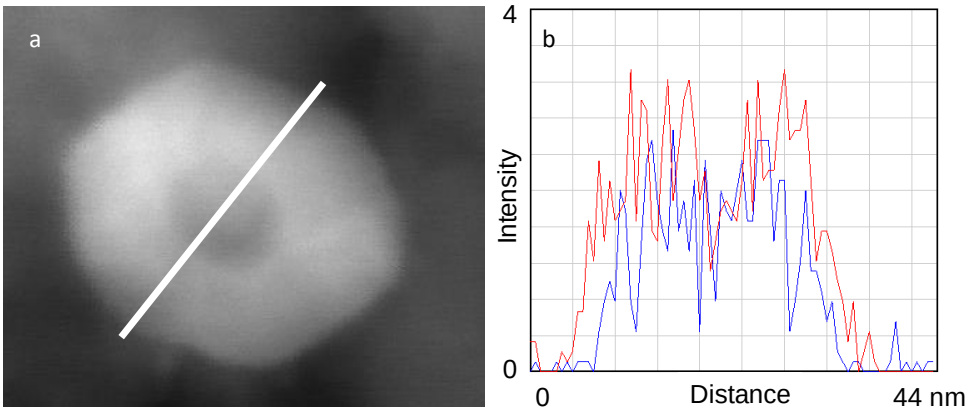

Figure 5- 3: a. STEM image of a particle of PdZn/Mg(Al)(Pd)(Zn)O_x after reaction with 30wt% H_2O/ethanol. b. Line scan through the particle in the direction of the white line on the figure left (a) with Pd (red) and Zn (blue).

Secondly, on the catalysts '30wt%H_2/ethanol' and '100wt%ethanol after water feed', Zn rich spots seem to be present on the surface of a PdZn particle, see Figure 5- 4. It, hence, seems that Zn has segregated to the surface of the PdZn particle. More line scans were performed at that surface and all showed a higher presence of Zn at the surface. Furthermore, dark spots appear in the dark field STEM images. These dark spots should be from a material which has a lower atomic mass than Pd. ZnO spots on the surface of that particle might provide an answer to this, since Zn has a lower atomic radius and won't light up as Pd in the dark field image.

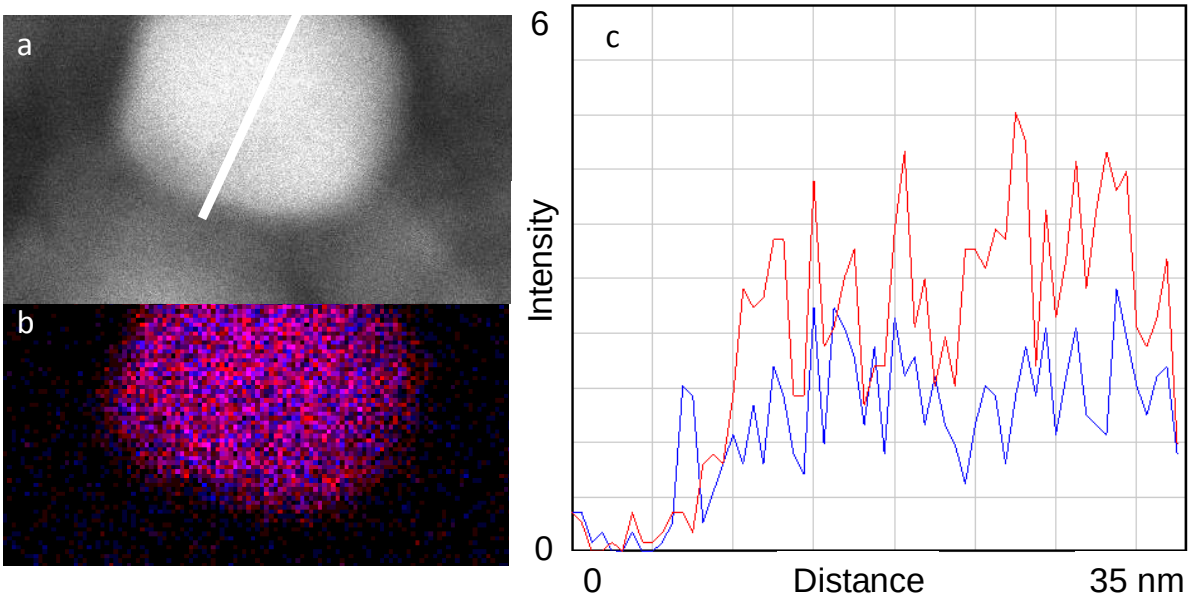

Figure 5- 4: a. STEM image of particle of PdZn/Mg(Al)(Pd)(Zn)O_x after reaction with 100wt% ethanol after water. b. Elemental mapping of the particle of the figure left (a) with Pd (red) and Zn (blue). c. Line scan through the particle in the direction of the white line on the figure left (a) with Pd (red) and Zn (blue).

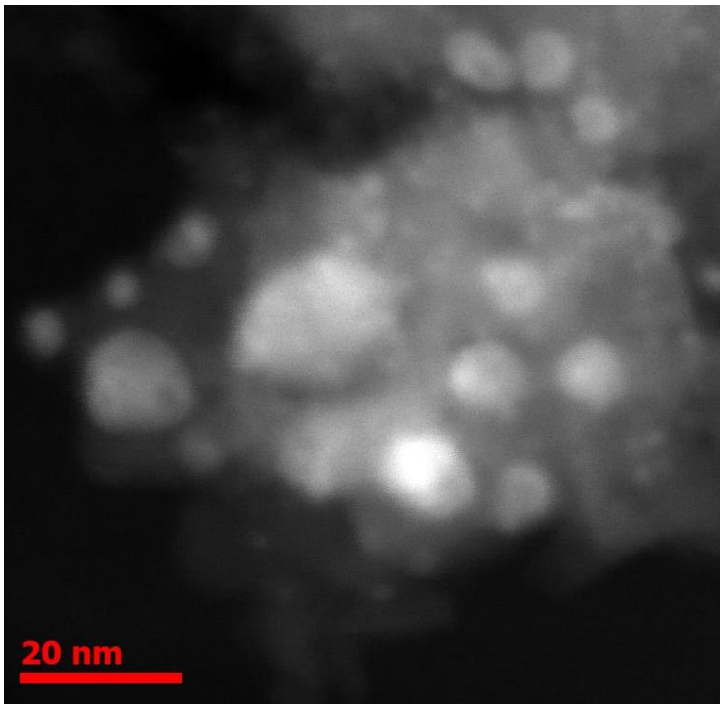

Figure 5- 5: Dark field STEM image of PdZn/Mg(Al)(Pd)(Zn)O_x after reaction with 30wt%H_2O/ethanol.

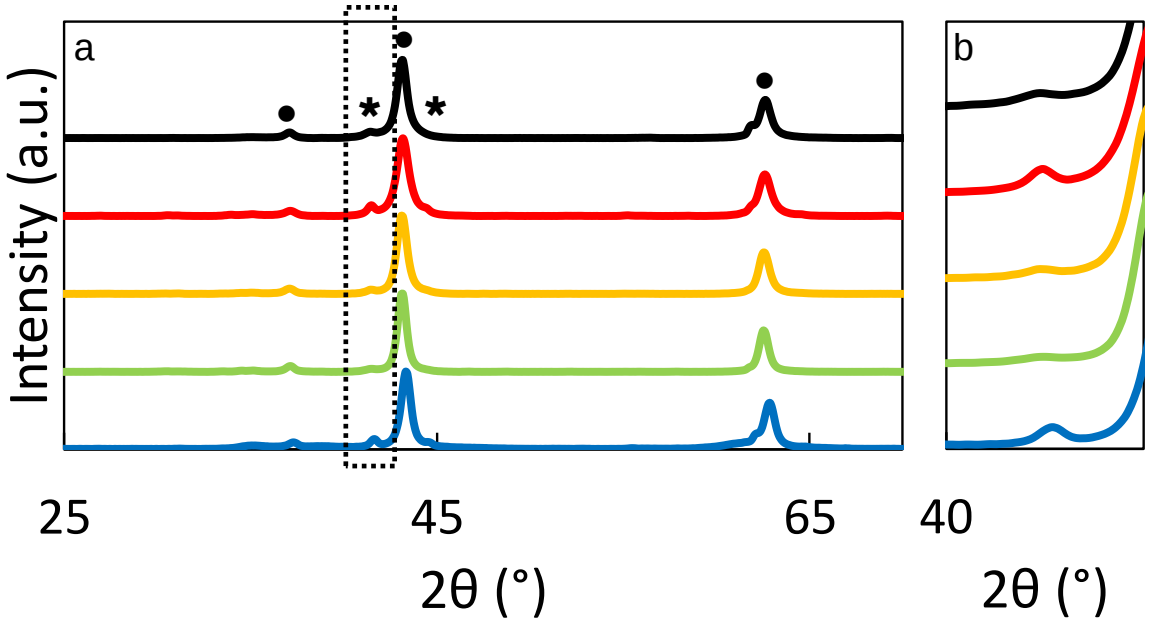

Figure 5- 6: a: XRD patterns of fresh (black) and spent PdZn/Mg(Al)(Pd)(Zn)O_x after subsequently 100wt% ethanol (red), 30wt%H_2O/ethanol (yellow), 100wt% ethanol after water feed (green), 100wt%ethanol (blue) after regeneration. MgO: ●, PdZn: ✱. b: a zoom on the PdZn peak, also denoted with a dotted box in a.

An XRD full scan is performed on each catalyst sample, see Figure 5- 6. For the sample subjected to pure ethanol, peaks of MgO are clearly present at resp. 36.9°, 42.9° and 62.3° (PDF 00-045-0946). At 41.2° and 44.1°, a small peak is also visible from PdZn (PDF 00-006-0620). For the sample '30wt%H2O/ethanol' and '100wt%ethanol after water feed', the MgO peaks remain unchanged, whereas the PdZn peaks drop in intensity. Upon regeneration, the PdZn peaks regain their original intensity. It thus seems that the PdZn intermetallic is present to a lesser extent or, at least, some of the crystallinity is lost upon feeding a water containing feed, but that it can be regained upon regeneration.

The number of active sites was determined via CO chemisorption, see Table 5- 3. After use, this number changed quite severely, which could possibly be assigned to both coking of the active sites as well as the reduction in surface area, which might point to blockage of pores and thus also making the active sites inaccessible. The number of active sites was found to be halved upon feeding 30wt%H_2O/ethanol, which is in line with the decrease in surface area of the support. The

reconstruction of the hydrotalcite material thus encapsulates the active sites. The number of active sites doesn't recover upon feeding pure ethanol again, but only after regeneration.

Table 5- 3: Number of active sites measured via CO chemisorption at 300K and cokes production as determined by temperature programmed oxidation with 10mol% O_2/He.

	Number of active sites (mmol kg^{-1}_{cat})	Cokes production (mol g^{-1})
activated catalyst	1.80 ± 0.025	-
100wt% ethanol	0.59 ± 0.149	0.097 ± 0.042
30wt% H_2O/ethanol	0.33 ± 0.194	0.018 ± 0.005
100wt% ethanol after water feed	0.30 ± 0.091	0.024 ± 0.002
100wt% ethanol after regeneration	0.40 ± 0.693	0.092 ± 0.069

Via temperature programmed oxidation, the amount of cokes remaining on the catalyst was determined via measurement of the CO_2 signal. This amount is significantly lower upon feeding 30wt%H_2O/ethanol. Restoring the pure ethanol feed doesn't affect the amount of cokes found on the catalyst. It thus seems that the catalyst has changed into a state which is less prone to coking. Only upon regeneration, the amount of cokes as determined on the catalyst surface was similar to the one found after the first test with pure ethanol.

5.3.3. Phase stability

Ab initio thermodynamic calculations were performed to construct a PdZn phase diagram, see Figure 5- 7, allowing to determine the thermodynamic stability of different Pd-Zn phases under reaction conditions. At low oxygen chemical potential, i.e., low water partial pressures, the PdZn 1:1 intermetallic compound is stable and no segregation is expected. However when the water partial pressure is increased, Zn atoms tend to be oxidized and removed from the intermetallic compound, resulting in a PdZn 2:1 alloy as most stable configuration. When the oxygen chemical potential is increased even further by increasing the water partial pressure, the most stable PdZn

configuration systematically contains less Zn in the bulk of the catalyst particles, resulting in a Pd particle with a PdZn 2:1 surface alloy. When the water partial pressure has increased such that all Zn has been removed from the bulk, it will gradually start being removed from the surface. As a result, going up along the vertical line from the PdZn intermetallic zone into the surface alloy zone, which is a higher water partial pressure as compared to the hydrogen partial pressure, represents a depletion of the surface alloy from a Pd:Zn surface ratio of 2 to isolated zinc atoms at infinite distance. At very high oxygen chemical potential, the surface contains no Zn at all and the catalyst has entirely segregated into ZnO and Pd. It is clear from Figure 5- 7 that complete removal of Zn from the Pd particles does not occur under reaction conditions, i.e., represented via the blue dashed box.

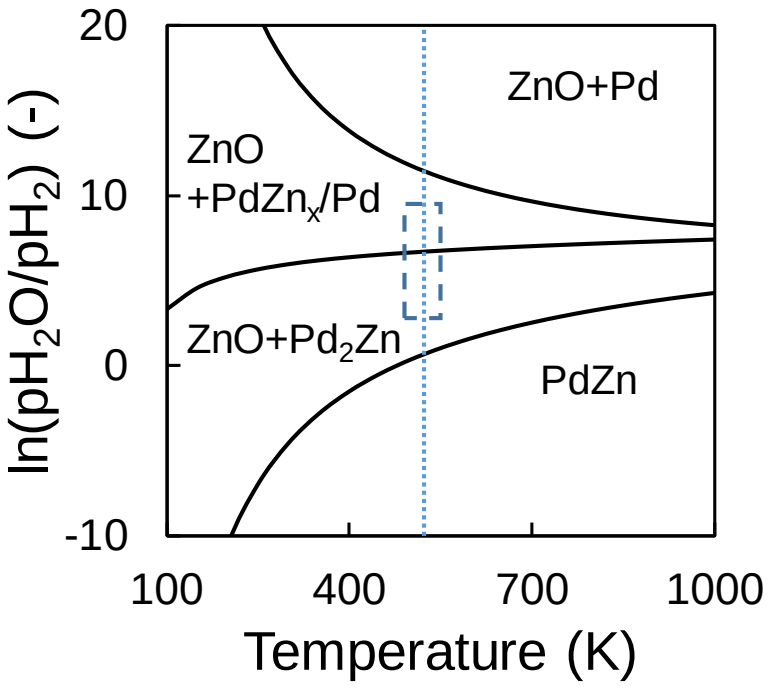

Figure 5- 7: Phase diagram for the Pd-Zn system under a water atmosphere. X <<1. The blue dotted line is the reaction temperature, the blue dashed box is the region of H_2O/H_2 ratios which was achieved during reaction.

5.4. Discussion

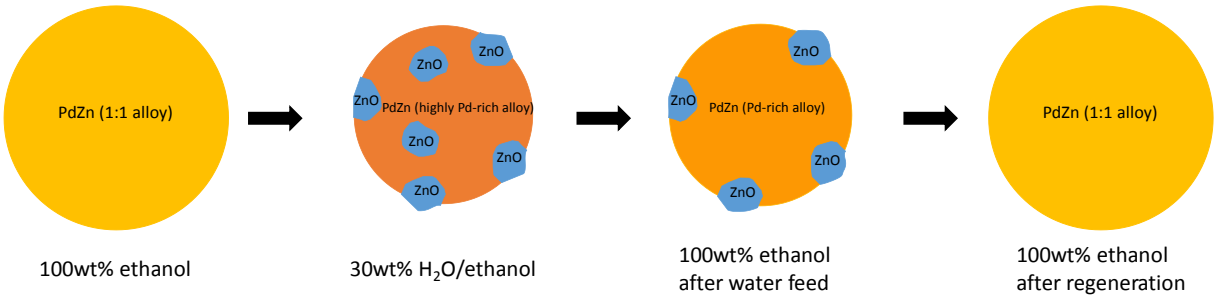

Figure 5- 8: Schematic representation of the PdZn particles on the PdZn/Mg(Al)(Pd)(Zn)O_x upon the activity tests.

With the information obtained by catalyst characterization and DFT calculations, an explanation for the behavior observed during the performance tests presented in Figure 5- 1 can be put forward. Incorporating 30wt%water into the feed decreases the ethanol conversion and

acetaldehyde selectivity from resp. 26 to 10% and 98 to 85%, see Figure 5- 1. The decrease in acetaldehyde selectivity stems from an enhanced formation of methane and carbon monoxide. Taking into account the results of Chapter 3, the formation of methane and carbon monoxide suggests the presence of adjacent Pd sites [20]. Catalyst characterization showed that the addition of 30wt%water into the feed results in a decreased intensity of the PdZn peak during XRD, see Figure 5- 6, a drop in the number of active sites from 5.9 ± 1.49 10^{-4} mol kg^{-1}_{cat} to 3.3 ± 1.94 10^{-4} mol kg^{-1}_{cat}, see Table 5- 2, and a lower amount of cokes, i.e., 0.018 ± 0.005 mol g^{-1} compared to 0.097 ± 0.042 mol g^{-1}. Furthermore, STEM-EDX indicates that Zn-rich clusters appear on the surface after incorporating 30wt%water into the feed, see Figure 5- 4. Combining all these catalyst characterization and performance results with the insight acquired from the DFT thermodynamic calculations, it can be reasonably proposed that upon feeding 30wt%H_2O/ethanol, Zn is partially removed from the PdZn nanoparticles and transformed into ZnO, see Figure 5- 8. This reduces the accessibility of the PdZn nanoparticle surface, explaining the decreased activity. Moreover, this particle has become richer in Pd, leading to more Pd-Pd neighboring sites and, hence, the product aldehyde will be more prone to decomposition. Coking of these sites is prevented due to the presence of water [24]. It is clear from Figure 5- 7 that Zn is removed gradually from the active particle. However, the partial pressure present during reaction does not suffice to extract all Zn from the PdZn. If doing so, the selectivity towards methane and carbon monoxide would even be higher. As mentioned in the introduction, Friedrich et al. [9] have investigated PdZn/ZnO for methanol steam reforming and also concluded that during methanol steam reforming conditions, the catalyst changes from PdZn particles to ZnO patches on the PdZn particle. We observed furthermore that the particle size dropped from 5 ± 2 to 2 ± 1 nm. Having an oxidant, H_2O, and a reductant, H_2, simultaneously available in the reactor, the alloy particles decompose and reform into smaller ones.

For the sample '100% EtOH after water', the driving force for oxidation is no longer present, rendering coalescence of the particles possible. Furthermore, H_2 is still produced, so ZnO on the

surface of the Pd-rich alloy particle can again partially reduce, see Figure 5- 7 and Figure 5- 8. Full reduction seems unreachable via the amount of H_2 produced during reaction.

Of course, when regeneration is performed, the PdZn particles are fully oxidized and again reduced, leading to homogeneous intermetallic particles as present after fresh activation, see Figure 5- 8. However, ICP results indicated that some active metals are lost upon regeneration. As already mentioned in Chapter 4, this can be attributed to a local hotspot on the catalyst via the burning of cokes [25]. Furthermore, Zn is known for its high volatility due to a relatively low boiling point, i.e., 1180K, and also PdH, formed during reduction, has an evaporation temperature that could become as low as 600K. These phenomena only occur when the interaction between the active metals and the support is weakened. It thus seems that feeding water weakens this interaction and that, subsequently, the high temperatures during regeneration cause some metal losses.

5.5. Conclusions

Feeding a water containing ethanol mixture over a PdZn/Mg(Al)(Pd)(Zn)O_x nanoparticle catalyst leads to a reconstruction of the active PdZn particles. After activation, a homogeneous intermetallic particle is present which, under water containing reaction conditions, transforms into a Pd-rich PdZn particle with ZnO patches on its surface. DFT thermodynamic calculations made clear that the amount of Zn which is extracted from the PdZn particle depends on the $\frac{p_{H_2O}}{p_{H_2}}$ ratio. This restructured PdZn particle with ZnO patches results in a reduced catalyst activity as well as acetaldehyde selectivity in favor of methane and CO. Upon feeding again pure ethanol, the particle is only partially restored, i.e., ZnO patches still remain. The catalyst has, hence, not recovered completely, resulting in, still, a lower activity and selectivity. Only upon regeneration, the catalyst is fully restored, although some metal losses are observed. Other phenomena which were caused by the water presence in the feed are the reconstruction of the hydrotalcite structure

from the mixed oxide via the memory effect and the weakened interaction of the active metals with the support.

A PdZn/Mg(Al)(Pd)(Zn)O_x catalyst reversibly adapts itself when exposed to a water containing feed. Because of the formation of ZnO patches on the PdZn surface, the acetaldehyde selectivity drops in favor of methane, but still an acetaldehyde selectivity of 80% remains. It can be restored into the original performance, however, at the expense of some metal losses.

5.6. References

[1] A. Corma, M.E. Domine, S. Valencia, Water-resistant solid Lewis acid catalysts: Meerwein–Ponndorf–Verley and Oppenauer reactions catalyzed by tin-beta zeolite, Journal of Catalysis, 215 (2003) 294-304.
[2] X. Fu, L.A. Clark, W.A. Zeltner, M.A. Anderson, Effects of reaction temperature and water vapor content on the heterogeneous photocatalytic oxidation of ethylene, Journal of Photochemistry and Photobiology A: Chemistry, 97 (1996) 181-186.
[3] A.M. Hilmen, D. Schanke, K.F. Hanssen, A. Holmen, Study of the effect of water on alumina supported cobalt Fischer–Tropsch catalysts, Applied Catalysis A: General, 186 (1999) 169-188.
[4] J.C. van Giezen, F.R. van den Berg, J.L. Kleinen, A.J. van Dillen, J.W. Geus, The effect of water on the activity of supported palladium catalysts in the catalytic combustion of methane, Catalysis Today, 47 (1999) 287-293.
[5] X. Li, L. Wang, Q. Xia, Z. Liu, Z. Li, Catalytic oxidation of toluene over copper and manganese based catalysts: Effect of water vapor, Catalysis Communications, 14 (2011) 15-19.
[6] H. Pan, M. Xu, Z. Li, S. Huang, C. He, Catalytic combustion of styrene over copper based catalyst: Inhibitory effect of water vapor, Chemosphere, 76 (2009) 721-726.
[7] R. Kikuchi, S. Maeda, K. Sasaki, S. Wennerström, K. Eguchi, Low-temperature methane oxidation over oxide-supported Pd catalysts: inhibitory effect of water vapor, Applied Catalysis A: General, 232 (2002) 23-28.
[8] D. Ciuparu, L. Pfefferle, Support and water effects on palladium based methane combustion catalysts, Applied Catalysis A: General, 209 (2001) 415-428.
[9] M. Friedrich, S. Penner, M. Heggen, M. Armbrüster, High CO2 Selectivity in Methanol Steam Reforming through ZnPd/ZnO Teamwork, Angewandte Chemie International Edition, 52 (2013) 4389-4392.
[10] D. Tichit, M.H. Lhouty, A. Guida, B.H. Chiche, F. Figueras, A. Auroux, D. Bartalini, E. Garrone, Textural Properties and Catalytic Activity of Hydrotalcites, Journal of Catalysis, 151 (1995) 50-59.
[11] T. Baskaran, J. Christopher, A. Sakthivel, Progress on layered hydrotalcite (HT) materials as potential support and catalytic materials, Rsc Advances, 5 (2015) 98853-98875.
[12] K. Takehira, T. Shishido, Preparation of supported metal catalysts starting from hydrotalcites as the precursors and their improvements by adopting “memory effect”, Catalysis Surveys from Asia, 11 (2007) 1-30.
[13] K. Lee, É.D. Murray, L. Kong, B.I. Lundqvist, D.C. Langreth, Higher-accuracy van der Waals density functional, Physical Review B, 82 (2010) 081101.

[14] J. Klimeš, D.R. Bowler, A. Michaelides, Van der Waals density functionals applied to solids, Physical Review B, 83 (2011) 195131.
[15] G. Kresse, J. Hafner, Ab initio, Physical Review B, 47 (1993) 558-561.
[16] G. Kresse, J. Hafner, Ab initio, Physical Review B, 48 (1993) 13115-13118.
[17] R.W.C. Structures, Vol. 1, Interscience, New York, (1963) 360.
[18] H. Nowotny, H. Bittner, Die Kristallstruktur von PdZn, Monatshefte für Chemie/Chemical Monthly, 81 (1950) 679-680.
[19] H. Sowa, H. Ahsbahs, High-pressure X-ray investigation of zincite ZnO single crystals using diamond anvils with an improved shape, Journal of Applied Crystallography, 39 (2006) 169-175.
[20] J. De Waele, V.V. Galvita, H. Poelman, C. Detavernier, J.W. Thybaut, Formation and stability of an active PdZn nanoparticle catalyst on a hydrotalcite-based support for ethanol dehydrogenation, Catalysis Science & Technology, 7 (2017) 3715-3727.
[21] D. Tichit, B. Coq, Catalysis by Hydrotalcites and Related Materials, CATTECH, 7 (2003) 206-217.
[22] X. Wang, J. Feng, Y. Bai, Q. Zhang, Y. Yin, Synthesis, Properties, and Applications of Hollow Micro-/Nanostructures, Chemical Reviews, 116 (2016) 10983-11060.
[23] B. Liu, H.C. Zeng, Fabrication of ZnO “Dandelions” via a Modified Kirkendall Process, Journal of the American Chemical Society, 126 (2004) 16744-16746.
[24] S.K. Goud, W.A. Whittenberger, S. Chattopadhyay, M.A. Abraham, Steam reforming of n-hexadecane using a Pd/ZrO2 catalyst: Kinetics of catalyst deactivation, International Journal of Hydrogen Energy, 32 (2007) 2868-2874.
[25] J. De Waele, V.V. Galvita, H. Poelman, C. Detavernier, J.W. Thybaut, PdZn nanoparticle catalyst formation for ethanol dehydrogenation: Active metal impregnation vs incorporation, Applied Catalysis A: General, 555 (2018) 12-19.

Chapter 6:

Promotion of Cu catalysts with Ni via NiCu alloy formation for (bio-)ethanol dehydrogenation

---

Ni alloying of Cu-based catalysts is investigated for ethanol dehydrogenation. Two Xwt%Ni/Mg(Al)(Ni)O_x catalysts, five Xwt%Ni-Ywt%Cu/Mg(Al)(Ni)(Cu)O_x and one 10wt%Cu/Mg(Al)(Cu)O_x catalyst were investigated with X being 0.5 or 1 and Y being 5, 10 or 20. It was found that Ni promotion increases the turn-over frequency of the Cu-based catalysts. Two deactivation regimes were observed on the catalysts, i.e., a fast deactivation with improved acetaldehyde selectivity within the first hours on stream and a slower deactivation afterwards. Via TPO and STEM, it was determined that in the first regime probably coking was at the origin of deactivation and in the second one sintering. On the best performing catalyst, i.e., 1wt%Ni-10wt%Cu/Mg(Al)(Ni)(Cu)O_x, no fast deactivation regime is observed. For this catalyst also the least cokes was produced compared to the other catalysts. Upon feeding 30wt%H_2O/ethanol, the activity of all NiCu catalysts increases. This was attributed to activation of water on Cu with the formation of H_2. This then removes the cokes on the catalyst surface. Overall 1wt%Ni-10wt%Cu/Mg(Al)(Ni)(Cu)O_x was the best performing catalyst with a TOF of 0.90s^{-1} and a selectivity of 99%.

6.1. Introduction

Taking into account the information obtained for the PdZn catalysts in the previous chapters, it has become clear that Zn is inactive for ethanol dehydrogenation and only participates to change the nature of the Pd sites and as a buffer to isolate Pd sites. If, however, two metals can be found which are both active for ethanol dehydrogenation and can be alloyed with each other, then, a more active catalyst can be synthesized. Furthermore, the use of Pd for an industrial catalyst gives rise to a high material cost. The use of cheaper metals would hence improve the potential for industrial use.

As already mentioned in Chapter 1, Cu-based catalysts have a low material cost, but are sensitive to deactivation by sintering. Alloying of Cu with another metal with a higher melting point could provide a possible solution for this problem. The mobility of metal particles on a support is relative to its melting point, thus a higher melting point decreases the potential for sintering [1]. Ni is a viable candidate for this, since it is also active for ethanol dehydrogenation.

However, when using Ni as a monometallic catalyst, it is subject to fast deactivation due to coking [2]. Cu has been used as a promoter for Ni-based catalysts in CO_2 reforming of methane to prevent cokes formation [3]. Thus, the alloying of Ni and Cu might prevent both deactivation phenomena or at least lower the deactivation rates.

As previously mentioned in Chapter 1, Ni and Cu can be mixed in every concentration with subsequent alloy formation due to their similar atomic radius and their FCC lattice structure [4]. In contrast with Cu, Ni has, apart from a high activity for (de)hydrogenation reaction, also the ability for C-C rupture [5]. Depending on the investigated reaction, alloys are synthesized with more or less Ni to tune for this C-C rupture.

In this chapter, the effect of the atomic Ni/Cu-ratio and total metal loading on the catalytic activity, selectivity and stability in ethanol dehydrogenation is assessed. Taking into account the

activity of Ni for C-C rupture, rather low Ni/Cu ratios will be tested. A pure Cu/Mg(Al)(Cu)O_x has also been tested as a bench mark.

6.2. *Procedures*

The procedure for catalyst synthesis has been described in Chapter 2. All catalysts have been prepared via incorporation of the active metals in a hydrotalcite-based support. The notation of the catalysts will be shortened throughout the text, see Table 6- 1. All characterization procedures and steady-state testing methods were discussed in Chapter 2.

Table 6- 1: Notation of the investigated catalysts

Catalyst	Abbreviation
10wt%Cu/Mg(Al)(Cu)O_x	10Cu
0.5wt%Ni/Mg(Al)(Ni)O_x	0.5Ni
0.5wt%Ni-5wt%Cu/Mg(Al)(Ni)(Cu)O_x	0.5Ni – 5Cu
0.5wt%Ni-10wt%Cu/Mg(Al)(Ni)(Cu)O_x	0.5Ni – 10Cu
1wt%Ni/Mg(Al)(Ni)O_x	1Ni
1wt%Ni-5wt%Cu/Mg(Al)(Ni)(Cu)O_x	1Ni – 5Cu
1wt%Ni-10wt%Cu/Mg(Al)(Ni)(Cu)O_x	1Ni – 10Cu
1wt%Ni-20wt%Cu/Mg(Al)(Ni)(Cu)O_x	1Ni – 20Cu

6.3. Catalyst characterization

Table 6- 2 represents the metal loadings of the catalysts as determined via ICP-OES. During synthesis of the catalysts, the desired metal loading was reached, with only small deviations. After use with a pure ethanol feed, the nominal metal loadings are still present on the catalysts, which reveals the stability of the metals upon incorporation in the support. The surface areas of the materials were determined via N_2 adsorption after calcination, after reduction and after use with a pure ethanol feed, see Table 6- 3. It can be seen that after calcination, the materials show a trend with higher Ni loading. Upon addition of Ni, the surface area decreases. This might be attributed to the blockage of the hydrotalcite layer formation, which also impacts the mixed oxide formation. For the Cu loading, no trend could be observed. This is remarkable since the Cu loading is changed more drastically than the Ni loading. Upon reduction at 873K, some changes can be noticed to the surface area. First of all, the surface area of the 10Cu catalyst decreased significantly. For the other materials, the surface area changes slightly, but the values remain in the same order of magnitude. A more significant change was encountered for the surface area after use. It rose for all catalysts to values all exceeding $100 m^2 g^{-1}$. Only based on these values, no explanation can be given for this drastic change. However, it can be suggested that during use, the structure of the catalyst or active site changed. When comparing the pore size mean, see Table 6- 4, it can be seen that the pore size of the catalysts reduces with activation via reduction and with reaction. This can be understood when considering the diffusion of active metals to the surface and thus lowering the pore size. Furthermore, upon reaction, deactivation mechanisms such as coking, poisoning or sintering might take place which can also lead to a reduction in pore size.

Table 6- 2: Metal loading of calcined and spent NiCu catalysts as determined via ICP-OES.

Catalyst	Metal loading after calcination (wt%)		Ni/Cu-ratio (mol mol^{-1})	Metal loading spent catalyst (wt%)		Ni/Cu-ratio (mol mol^{-1})
	Ni	Cu		Ni	Cu	
10Cu	-	9.3	-	-	10.7	-
0.5Ni	0.55	-	-	0.55	-	-
0.5Ni – 5Cu	0.48	4.8	0.11	0.49	4.7	0.11
0.5Ni – 10Cu	0.54	10.3	0.06	0.56	10.6	0.06
1Ni	0.92	-	-	1.16		
1Ni – 5Cu	0.72	3.4	0.23	1.02	4.5	0.24
1Ni – 10Cu	1.14	9.9	0.12	1.32	11.4	0.13
1Ni – 20Cu	1.12	23.3	0.05	1.1	22.8	0.05

Table 6- 3: BET surface area of calcined, reduced and used NiCu catalysts as determined by N_2 adsorption.

BET surface area (m^2 g^{-1})	Catalyst	0wt%Ni	0.5wt%Ni	1wt%Ni
After calcination	0wt%Cu	-	83.2 ± 1.7	19.0 ± 2.3
	5wt%Cu	-	109.9 ± 3.2	31.6 ± 1.0
	10wt%Cu	147.7 ± 8.8	75.1 ± 5.1	8.8 ± 0.2
	20wt%Cu	-	-	131.3 ± 2.8
After reduction	0wt%Cu	-	52.1 ± 0.09	47.6 ± 2.3
	5wt%Cu	-	53.0 ± 3.2	95.7 ± 1.0
	10wt%Cu	52.4 ± 8.8	117.5 ± 5.1	19.5 ± 0.2
	20wt%Cu		-	229.1 ± 2.8
After use	0wt%Cu		120.0 ± 12.4	115.0 ± 1.6
	5wt%Cu	-	174.7 ± 13.2	152.2 ± 3.5
	10wt%Cu	183.1 ± 31.3	101.9 ± 51.6	155.0 ± 3.2
	20wt%Cu	-	-	149.3 ± 8.78

Table 6- 4: Pore size mean of calcined, reduced and used NiCu catalysts as determined by N_2 adsorption.

Pore size mean (nm)	Catalyst	0wt%Ni	0.5wt%Ni	1wt%Ni
After calcination	0wt%Cu	-	230.3 ± 12.88	266.3 ± 16.39
	5wt%Cu	-	269.9 ± 9.81	273.43 ± 9.46
	10wt%Cu	287.2 ± 8.71	176.1 ± 10.11	270.0 ± 40.59
	20wt%Cu	-	-	292.2 ± 6.50
After reduction	0wt%Cu		241.4 ± 7.68	152.5 ± 16.39
	5wt%Cu	-	240.4 ± 9.81	162.6 ± 9.46
	10wt%Cu	444.3 ± 8.71	170.4 ± 14.35	231.7 ± 40.59
	20wt%Cu	-	-	198.6 ± 6.75
After use	0wt%Cu		130.5 ± 12.5	101.2 ± 1.8
	5wt%Cu	-	122.6 ± 2.01	143.4 ± 12.08
	10wt%Cu	225.3 ± 19.69	110.8 ± 14.35	94.5 ± 1.79
	20wt%Cu	-	-	131.8 ± 6.75

6.3.1. Reducibility

TPR was performed on the catalysts to determine the required reduction temperature to ensure full reduction of the catalyst, as can be seen in Figure 6- 1. Reduction of the materials with a low Ni/Cu-ratio, i.e., a ratio of 1/10 or without Ni, starts at 400K. Increasing the Ni/Cu-ratio, increases the reduction temperature. At the maximum reduction temperature, i.e., 873K, the catalysts without Cu, i.e., 0.5Ni and 1Ni, were only reduced for 12%. This suggests that alloying Cu with Ni shifts the reduction temperature to higher temperatures as compared to pure Cu catalysts. CuO has a reduction temperature of ~413K and reduction of NiO occurs partially from 540K on, but full reduction only takes place at 1173K-1593K [6, 7]. Because of spill-over of hydrogen from Cu to NiO, NiO is more easily reduced in the presence of Cu, with potential alloy formation as a consequence. $NiAl_2O_4$ spinel formation with support elements has a reduction temperature of 1073K [8]. Most likely, the 0.5Ni and 1Ni catalysts thus rather form a spinel with Al than to be removed from the support with the formation of Ni active sites. The presence of the spinel can

however only be determined via XPS or XAS. For XRD, the presence of the phase is too small to be detectable. Only when Cu is present on the catalyst, NiO reduction becomes favorable. Via the calculation of the amount of consumed H_2, it was found that 12% Ni is reduced on the 0.5Ni and 1Ni materials. It can be assumed that slightly more will be reduced in the presence of Cu. A temperature of 773K was chosen as reduction temperature for the steady-state activity testing of the catalyst.

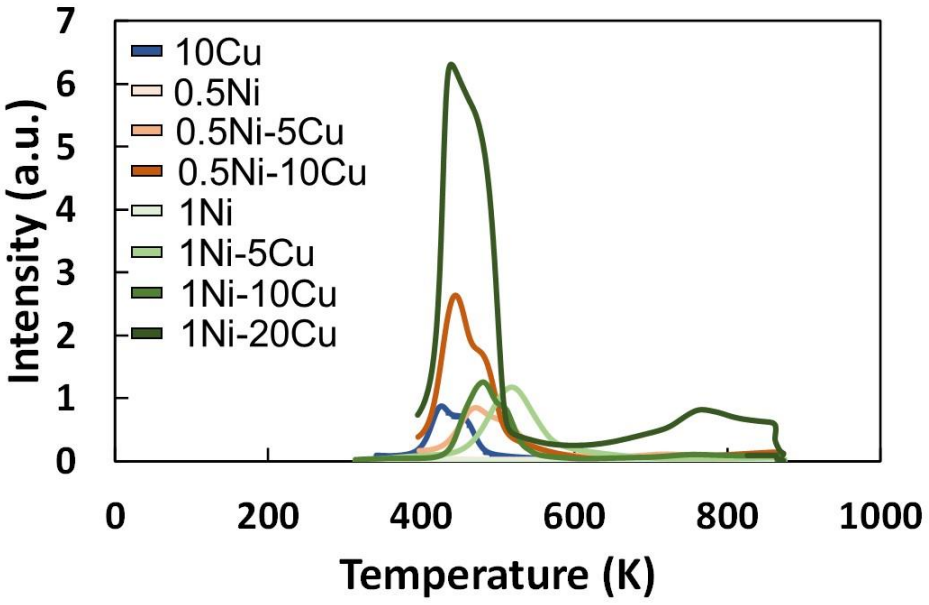

Figure 6- 1: Temperature programmed reduction with 10mol%H_2/Ar for 10Cu (blue), 0.5Ni-XCu (X=0,5,10) (red, light->dark=higher Cu loading), 1Ni-XCu (X=0,5,10,20) (green, light->dark=higher Cu loading).

6.3.2. Alloy formation

Figure 6- 2 represents the FTIR spectra of CO adsorption on the catalysts. On the pure 10Cu catalyst, peaks are visible at 2104cm^{-1}, 1672cm^{-1}, 1514cm^{-1}, 1375cm^{-1} and 1120cm^{-1}, see Figure 6-2a. These can be considered to be representative for Cu-CO vibration frequencies, since these peaks were not observed for the pure 0.5Ni and 1Ni catalysts. Thus they can't be a result of CO interacting with the support. On all NiCu catalysts, no Ni-CO peaks were observed which is probably due to the low loading, thereby being undetectable. The peaks at 1672cm^{-1}, 1514cm^{-1},

1375cm^{-1} and 1120cm^{-1} were also observed for the 0.5Ni10Cu catalyst and for the 1Ni5Cu catalyst and not for the other catalysts. This is remarkable, because it could be assumed that CO would interact with Cu in the same configurations on all NiCu catalysts. The peak at 2104cm^{-1} was present for all Cu-containing catalysts, see Figure 6- 2b. It can be seen that, for all NiCu catalysts, the peak maximum shifts and also the peak broadens as compared to the pure 10Cu catalyst. This suggests the formation of a NiCu alloy. Dalmon et al. reported that higher vibrational frequencies were reported upon alloying Cu with Ni [9]. This is also visible here; the catalysts with more Ni have a shoulder at higher wavenumbers. For the 1Ni-5Cu and 0.5Ni10Cu catalysts, peaks were present at 1672cm^{-1} to 1120cm^{-1}. These catalysts also exhibit the least broadening of the peak at 2104cm^{-1}. This suggests that for the other catalysts, i.e., 0.5Ni5Cu, 1Ni10Cu and 1Ni20Cu, an alloy is formed. For the 1Ni10Cu catalyst, the broadening is the biggest, which might indicate the formation of the most uniform alloy.

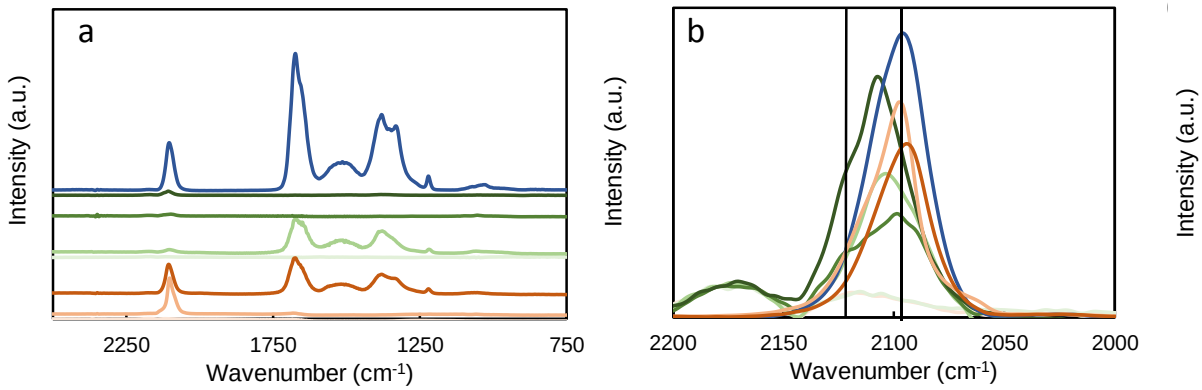

Figure 6- 2: FTIR spectra of CO adsorption (2 kPa, 298K) on 10Cu (blue), 0.5Ni-XCu (X=0,5,10) (orange, darker= more loading) and 1Ni-XCu (X=0,5,10,20) (green, darker= more loading). a: full spectra; b: zoom on Cu-CO peak at 2104cm^{-1}. The vertical lines represent the shift in peak wavenumber.

When investigating the presence of a NiCu alloy on the investigated catalysts via XRD, no Ni, Cu or NiCu phases could be detected due to the small particle size of the active metals. However, to assess the presence of a NiCu alloy upon reduction, in-situ XRD during TPR was performed on a 7wt%Ni-4.3wt%Cu/Mg(Al)(Ni)(Cu)O_x catalyst, see Figure 6- 3. It can be seen in Figure 6- 3a that upon reduction a phase appears at 51.26° which is representative for a NiCu alloy. This of course

doesn't prove the existence of a NiCu alloy in the investigated catalysts, but it does support the believe that a NiCu alloy can form on these catalysts under the activation conditions.

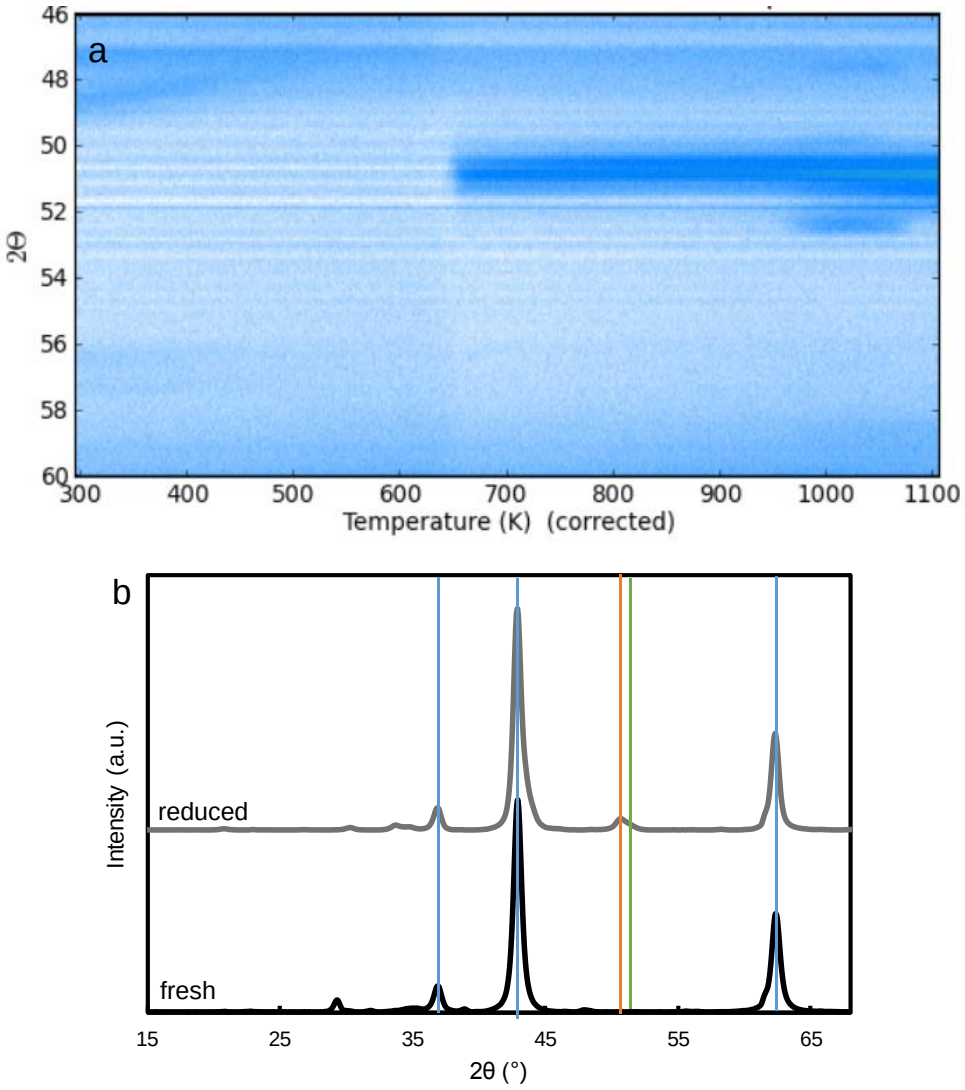

Figure 6- 3: a) in-situ XRD during TPR at a temperature ramp of 10K min^{-1}. b) full XRD scan of fresh calcined (black) and reduced (grey) catalyst. The characteristic reflections of MgO (blue), Ni (green) and NiCu (orange) were mentioned via full lines.

6.3.3. Number of active sites

The number of active sites has been determined via N_2O oxidation with the method proposed by Gervasini et al., see also Chapter 2 [10]. When taking into account the number of sites, see Table 6- 5, it can be seen that, evidently, the number of active sites increases with increasing metal

loading. This, however, is not the case for the 1Ni-10Cu catalyst. This indicates that with the addition of Cu, bigger particles are formed rather than more particles. Addition of Ni doesn't influence the number of active sites significantly, which can be understood with the low loading of Ni as compared to Cu.

Table 6- 5: Number of active sites as determined via N_2O oxidation. ND= not detectable.

Number of Cu active sites (mmol g_{cat}^{-1})	0wt%Ni	0.5wt%Ni	1wt%Ni
0wt%Cu	-	ND	ND
5wt%Cu	-	0.12	0.10
10wt%Cu	0.22	0.16	0.11
20wt%Cu	-	-	0.20

6.4. Performance testing

6.4.1. Catalyst stability assessment and Turn-Over Frequency determination

Figure 6- 4 represents the conversion and selectivity exhibited by the various catalyst samples. It can be observed that the catalysts without Cu, i.e., 0.5Ni and 1Ni, deactivate completely within a relatively short time, i.e., after only 3h on stream. Also the acetaldehyde selectivity is low for these catalysts. Furthermore, for almost every catalyst, two regimes are present as function of time-on-stream. Within the first five hours on stream, the conversion decreases with an acetaldehyde selectivity increase. Afterwards, the selectivity remains constant, but the conversion still decreases, although at a slower rate. Overall, the acetaldehyde selectivity exceeds 95% for all but the 0.5Ni catalyst. It can be seen that the conversion of the catalysts increases with an increasing metal loading. To unambiguously determine the best performing catalyst, turn-over frequencies are calculated, see Figure 6- 5. The best performing catalyst is the 1Ni-10Cu catalyst.

The catalyst containing only Cu was as stable as that catalyst, but the turn-over frequency of the 1Ni-10Cu catalyst was almost double of the activity of the pure Cu catalyst. This proves that alloying with Ni does improve the turn-over frequency of the Cu catalyst for ethanol dehydrogenation.

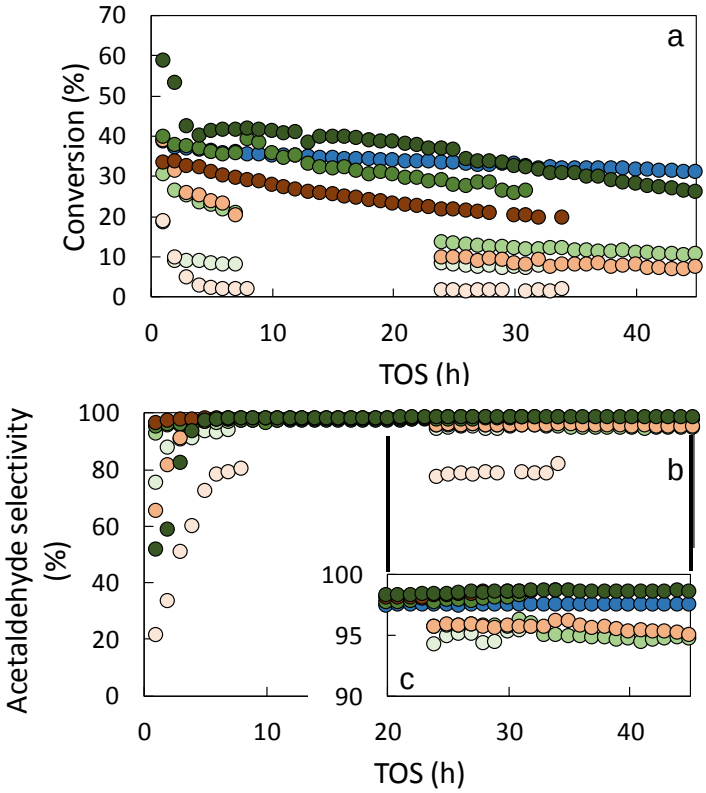

Figure 6- 4: Performance curves for 10Cu (blue), 0.5Ni-XCu (X=0,5,10) (red, light->dark=higher Cu loading), 1Ni-XCu (X=0,5,10,20) (green, light->dark=higher Cu loading). a: conversion, b: acetaldehyde selectivity, c: zoom on acetaldehyde selectivity.

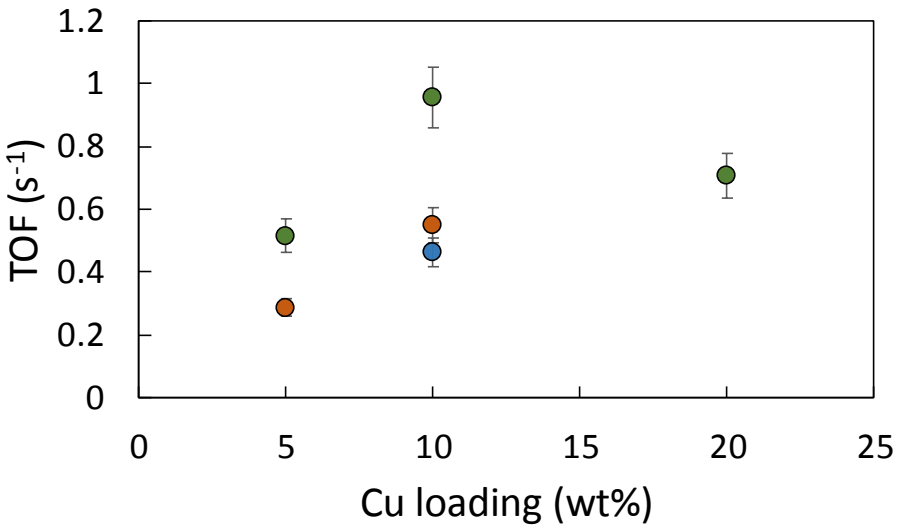

Figure 6- 5: Effect of Cu loading on the turn-over frequencies for 10Cu (blue), 0.5Ni-XCu (X=5,10) (red), 1Ni-XCu (X=5,10,20) (green).

6.4.2. Effect of water

Since ethanol produced from bio-based resources always contains some water and complete removal of water from (bio)-ethanol is highly energy intensive, the effect of the presence of water in the feed on the catalyst performance has been assessed by feeding 30wt%H_2O/ethanol. First, the original activity is measured for a pure ethanol feed and afterwards, the feed is changed to 30wt%H_2O/ethanol. The acetaldehyde selectivity was unchanged when switching to another feed. The conversion and selectivity were stable for all catalysts. To compare the conversion of both measurements, the ratio of the conversion upon feeding 30wt%H_2O/ethanol to the original conversion with pure ethanol is represented, see Table 6- 6. It can be seen that depending on the Ni and Cu loading, water has a detrimental, advantageous or no effect at all. Overall, it can be seen that all catalysts with both Cu and Ni have a higher conversion upon feeding 30wt%H_2O/ethanol. Since water can't reverse the sintering behavior, it seems that water removes cokes from the surface, even if it is already formed. Koryabkina et al. have reported that for the water-gas shift reaction, water can be adsorbed on a Cu surface with the formation of H_2, even at 473K [11]. H_2 can then help in the removal of cokes from the surface.

Table 6- 6: Ratio of the conversion upon feeding 30wt%H_2O/EtOH to the original conversion with pure ethanol. T= 533K, P_{tot}=0.5MPa, W/F_{EtOH}=3.6kg_{cat}s mol^{-1}.

Ratio (-)	0wt%Ni	0.5wt%Ni	0wt%Ni
0wt%Cu	-	1.00	0.26
5wt%Cu	-	1.89	1.53
10wt%Cu	0.65	1.10	1.20
20wt%Cu	-	-	1.52

6.5. *Deactivation phenomena*

As already mentioned in section 6.4.1, two deactivation regimes can be observed, i.e., a fast deactivation within the first hours on stream and afterwards, a slower deactivation. In general, many deactivation phenomena can occur on catalytic systems. However, with the knowledge on Ni and Cu for dehydrogenation reactions, it could be suggested that coking and sintering are the reasons for deactivation. To evaluate this, TPO and STEM have been performed.

The TPO experiment was performed as described in Chapter 2. The CO_2 production during TPO is represented in Figure 6- 6 for all catalysts and is considered representative for the amount of cokes produced during reaction. It is seen that for the catalysts with only Ni the highest amount of cokes was burnt off. For the best performing catalysts, i.e., the 1Ni-10Cu and the 1Ni-20Cu catalysts, the amount of cokes was the lowest. Furthermore, cokes formed on the catalysts containing Cu is easier to burnt off than for the 0.5Ni and 1Ni catalyst. When comparing the cokes production with the conversion curve in Figure 6- 4a, it can be seen that the behavior of the first hours on stream corresponds well with the cokes production. The catalysts with the highest cokes production, i.e., 0.5Ni and 1Ni, had the fastest deactivation. 1Ni-10Cu had the lowest cokes production and, indeed, no fast deactivation was observed. We can thus assume that the fast deactivation is due to coking of the active sites. To be able to explain the coking phenomena, the occurring reactions on Ni and Cu should be taken into account. Mariño et al. reported that Ni is

also active for acetaldehyde decomposition reactions [5]. Thus, the phenomena that were discussed before for ethanol dehydrogenation on Pd in PdZn, see Chapter 3, apply here as well. When the active site catalyzes acetaldehyde decomposition to methane and CO, it is also capable of catalyzing the decomposition of methane and CO to cokes. This part of the reaction network requires the presence of 2 adjacent Ni sites [12]. Alloying of Ni with Cu, thus reduces the number of adjacent sites and consequently the rapid deactivation.

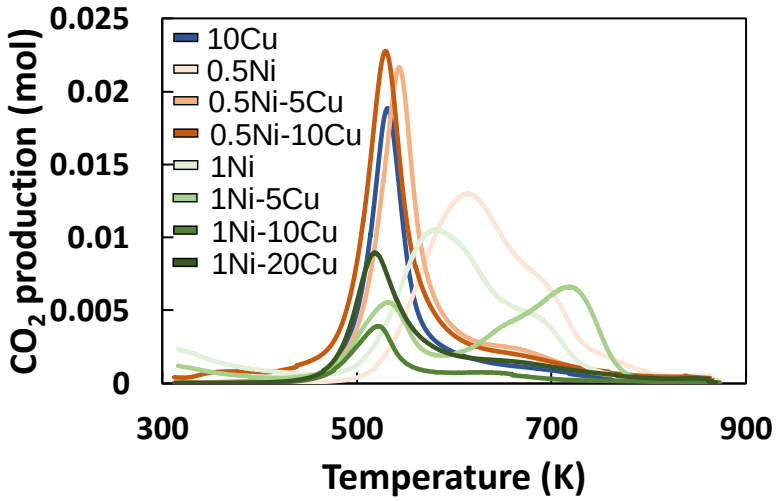

Figure 6- 6: CO_2 intensity with 10mol%O_2/He for 10Cu (blue), 0.5Ni-XCu (X=0,5,10) (red, light->dark=higher Cu loading), 1Ni-XCu (X=0,5,10,20) (green, light->dark=higher Cu loading) used with a pure ethanol feed.

In the second regime, i.e., after five hours on stream, the catalyst conversion still decreases, but to a lesser extent than before. To determine which phenomena were at the origin of this, STEM-EDX was performed on the best performing sample, i.e., the 1Ni-10Cu. It can be seen, in Figure 6- 7, that upon reduction, a highly disperse catalyst is present. Cu and Ni were finely dispersed in the catalyst particle and the particle size was estimated at 3-8nm. Upon use, some sintering of active particles was visible, see Figure 6- 7. Furthermore, the number of active sites after reaction was also determined for this catalyst. The number of active sites dropped from 0.23 to 0.18 mmol g^{-1}. Thus, it can be assumed that sintering is at the origin of the slow decrease in conversion after five hours on stream for all catalysts.

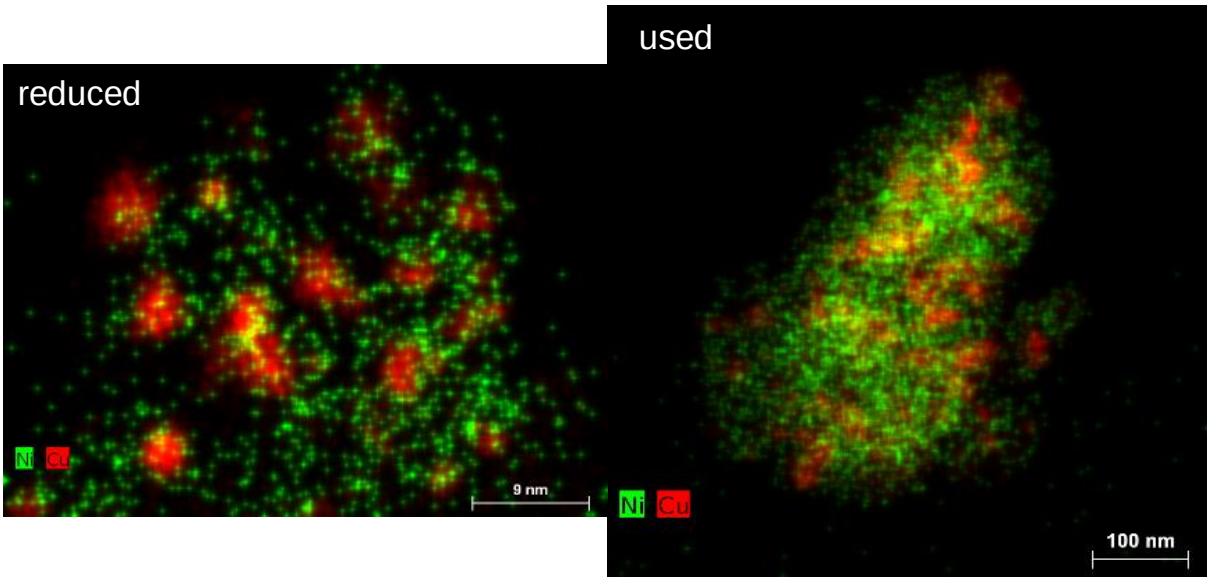

Figure 6- 7: STEM-EDX images of the reduced and used 1Ni-10Cu.

6.6. *Comparison of NiCu with PdZn catalysts*

The PdZn catalysts described in the previous chapters can now be compared with the NiCu catalysts, see Table 6- 7. The two best performing catalysts have been compared which are the 1wt%Pd-1.2wt%Zn/ Mg(Al)(Pd)(Zn)O_x activated via cycled reduction and the 1wt%Ni-10wt%Cu/ Mg(Al)(Ni)(Cu)O_x activated with single reduction. It was found that the turn-over frequency of the PdZn catalysts exceeds that of the NiCu catalysts. This doesn't mean that the NiCu catalysts are less active than the PdZn catalysts, since for the NiCu catalysts both Ni and Cu are active for the reaction and both metals are accounted for in the number of active sites. For the PdZn catalysts, it is considered that only the Pd sites can activate ethanol thus resulting in a lower number of active sites. The acetaldehyde selectivity, not reported in the table, was similar for both catalysts and amounted for 97%. Furthermore, at the same space time, i.e., 36kg_{cat} s mol^{-1}, the NiCu catalyst reached the maximum thermodynamic conversion of 60% whereas conversion of the PdZn catalyst was only 26%. When checking the industrial potential of the catalysts, it must furthermore be noted that the price of the NiCu catalyst is 400 times lower than of the PdZn catalyst, even with a higher metal loading of the NiCu catalysts. Thus taking into account the

conversion and selectivity per gram of catalyst, the NiCu catalyst seems to have the highest potential. When considering the possibility to feed bio-ethanol, i.e., an ethanol-water mixture, also the NiCu catalysts seem to be the most promising, since they remain unchanged upon feeding water and the activity is even slightly increased due to less cokes formation. Overall, both PdZn and NiCu catalysts have promising properties, but the NiCu catalysts seem to have a higher industrial potential.

Table 6- 7:Comparison of the NiCu catalysts with the PdZn catalysts

Best performing catalyst	1wt%Pd-1.2wt%Zn/ $Mg(Al)(Pd)(Zn)O_x$ – cycled reduced	1wt%Ni-10wt%Cu/ $Mg(Al)(Ni)(Cu)O_x$ – single reduced
Structure	Intermetallic compound	Alloy
TOF (s^{-1})	7.0	1.0
Particle size (nm)	5.3 ± 1.8	~3
Number of active sites (mmol g^{-1}_{cat})	$1.8\ 10^{-3}$	0.11
Effect of water	X ↓, S ↓	X ≈, S =
Price active metals (€/kg_{cat})	277	0.7

6.7. Conclusions

Cu-based catalysts promoted and alloyed with Ni were tested for ethanol dehydrogenation and the effect of Ni and Cu loading was investigated. As a benchmark, a $Cu/Mg(Al)(Cu)O_x$ catalyst was also investigated. The catalysts seem to be a promising alternative catalyst for the production of acetaldehyde from ethanol, especially because of their ability to cope with the presence of water in the ethanol feed. Upon alloying of Cu with Ni, a higher turn-over frequency is observed than compared to the benchmark catalyst. It can be suggested that the higher turn-over frequency is due to lowering of the reduction temperature of Ni via spillover from Cu, rendering the Ni sites active and incorporated in the Cu particle. An advantage of this for the Cu sites is that via alloying

a higher melting point is achieved than for pure Cu, thereby increasing also the migration temperature and thus lowering sintering. The acetaldehyde selectivity exceeds 95% for all NiCu catalysts. This suggests that only a limited number of adjacent Ni sites are present, since this would make the catalyst more selective for acetaldehyde decomposition to methane and carbon monoxide.

Upon reaction, two deactivation regimes were observed, i.e., a fast deactivation within the first hours on stream and a more slow deactivation afterwards. The first regime was attributed to coking on the adjacent Ni sites whereas the second was, probably, due to sintering of the active particles.

Via FTIR, an indication was given that alloying of Ni and Cu occurred and more specifically, that on the 1Ni-10Cu catalyst, the most homogeneously mixed alloy is present. This is also suggested since on this catalyst, fast deactivation was not encountered, which points to only a small fraction of adjacent Ni sites. When adding water to the ethanol feed, after measurement of the original activity with pure ethanol, the conversion on all NiCu catalysts increases. This might be due to the activation of water on Cu with the formation of H_2, even at 473K. This then aids in the removal of cokes from the surface.

Overall, the best performing catalyst is the 1wt%Ni-10wt%Cu/Mg(Al)(Ni)(Cu)O_x catalyst with an activity of 0.9 s^{-1}, an acetaldehyde selectivity of 99% and a relatively high stability.

6.8. References

[1] M. Baerns, Basic Principles in Applied Catalysis, Springer2004.
[2] A.J. Vizcaíno, A. Carrero, J.A. Calles, Hydrogen production by ethanol steam reforming over Cu–Ni supported catalysts, International Journal of Hydrogen Energy, 32 (2007) 1450-1461.
[3] J.-H. Lee, E.-G. Lee, O.-S. Joo, K.-D. Jung, Stabilization of Ni/Al2O3 catalyst by Cu addition for CO2 reforming of methane, Applied Catalysis A: General, 269 (2004) 1-6.
[4] K.C. Khulbe, R.S. Mann, Nature of Ni-Cu Alloys and Their Role in Chemical Reactions, Catalysis Reviews, 24 (1982) 311-328.
[5] F.J. Mariño, E.G. Cerrella, S. Duhalde, M. Jobbagy, M.A. Laborde, Hydrogen from steam reforming of ethanol. characterization and performance of copper-nickel supported catalysts, International Journal of Hydrogen Energy, 23 (1998) 1095-1101.
[6] H.P. Wang, C.T. Yeh, On the Reduction of Copper Oxide, Journal of the Chinese Chemical Society, 30 (1983) 139-143.
[7] K.V. Manukyan, A.G. Avetisyan, C.E. Shuck, H.A. Chatilyan, S. Rouvimov, S.L. Kharatyan, A.S. Mukasyan, Nickel Oxide Reduction by Hydrogen: Kinetics and Structural Transformations, The Journal of Physical Chemistry C, 119 (2015) 16131-16138.
[8] C. Jiménez-González, Z. Boukha, B. de Rivas, J.R. González-Velasco, J.I. Gutiérrez-Ortiz, R. López-Fonseca, Behavior of Coprecipitated NiAl2O4/Al2O3 Catalysts for Low-Temperature Methane Steam Reforming, Energy & Fuels, 28 (2014) 7109-7121.
[9] J.-A. Dalmon, M. Primet, G.-A. Martin, B. Imelik, Magnetic and infrared study of CO chemisorption on silica supported nickel-copper alloys, Surface Science, 50 (1975) 95-108.
[10] A. Gervasini, S. Bennici, Dispersion and surface states of copper catalysts by temperature-programmed-reduction of oxidized surfaces (s-TPR), Applied Catalysis A: General, 281 (2005) 199-205.
[11] N.A. Koryabkina, A.A. Phatak, W.F. Ruettinger, R.J. Farrauto, F.H. Ribeiro, Determination of kinetic parameters for the water–gas shift reaction on copper catalysts under realistic conditions for fuel cell applications, Journal of Catalysis, 217 (2003) 233-239.
[12] M. Mavrikakis, M.A. Barteau, Oxygenate reaction pathways on transition metal surfaces, Journal of Molecular Catalysis A: Chemical, 131 (1998) 135-147.

Chapter 7:

A comprehensive kinetic model for ethanol dehydrogenation on bimetallic catalysts: validation for NiCu

---

A generic kinetic model for ethanol dehydrogenation on metal-based catalysts was constructed. For validation purposes, the 1wt%Ni-10wt%Cu/Mg(Al)(Ni)(Cu)O_x was employed. The employed reaction conditions varied in temperature from 473K to 533K, a total pressure of 0.5MPa to 1.5MPa and a space time of 0.9kg_{cat} s mol^{-1} to 27kg_{cat} s mol^{-1}. Two types of sites were accounted for in the model, i.e., dehydrogenation and decomposition sites. As the major and desired route in this thesis, ethanol dehydrogenation was expressed in terms of elementary steps. Decomposition reactions were accounted for via global reactions with reaction orders. The parameters are estimated by non-linear regression of the model to an experimental data set comprising 41 experiments including 13 repeat experiments. The estimates were physically meaningful and statistically significant. The reaction path analysis revealed that the ethanol dehydrogenation reactions to acetaldehyde on the dehydrogenation sites are fast. Methane and carbon monoxide production occurred via adsorption of acetaldehyde on the decomposition sites.

7.1. Introduction

Insight in chemical reactions and the effect of a catalyst composition on the reaction performance can be obtained via a thorough experimental investigation [1]. Such experimental campaigns are necessary when little is known on the reaction and a broad range of operating conditions and catalysts are still to be tested. Nowadays, with the improvement of computing capacity, this qualitative experimental understanding can be translated into a more quantitative one via the construction of a kinetic model. With this, improvements with respect to operating conditions and catalyst composition can be identified in a more rational manner, reducing the time consuming and expensive data collection.

The construction of a kinetic model is never a purpose in itself [2]. It is rather to be used as a tool for defining guidelines for catalyst design and to simulate the performance of a commercial-scale reactor based on laboratory-scale kinetics. The latter is of interest in industry, where a thorough understanding of how varying operating conditions impact on the product distribution, allows a better production planning and, hence, overall process reliability and revenue. The former can be applied in research to predict the performance of a catalyst before its synthesis. In this respect, the model should include two types of parameters which are independent of each other, i.e., kinetic and catalyst descriptors. Kinetic descriptors, on the one hand, purely relate to the kinetics of a given chemical reaction, irrespective of the catalyst used. Catalyst descriptors, on the other hand, capture the effect of the catalyst composition on the reaction performance. As such, the catalyst descriptors which optimize the performance can be identified in silico, bringing their more rational design within reach. Thus, with these catalyst descriptors, the performance of different catalysts can be simulated, which, due to thermodynamic differences, might be completely different from the base catalyst. This is because the thermodynamic importance of reactions in the network might change significantly upon changing these catalyst descriptors.

For major industrially exploited reactions such as Fischer-Tropsch [3], hydrocracking [4], catalytic cracking [5], methanol-to-olefins [6], etc. , detailed kinetic models have already been

constructed. With the increasing interest in bio-based processes, a corresponding need for modelling them in a more fundamental manner has emerged. The specific reaction of interest in this work is ethanol dehydrogenation to acetaldehyde.

Ethanol dehydrogenation is to become an important reaction in the production of chemicals from bio-based resources. The product, i.e., acetaldehyde, can serve as a platform molecule for the production of a wide range of chemicals, from pesticides to car parts. Ethanol dehydrogenation can proceed via a direct dehydrogenation or via an oxidative route. Since the direct dehydrogenation simultaneously yields hydrogen as a byproduct, this route has been selected in this thesis. Ethanol dehydrogenation is activated by metal catalysts such as Cu, PdZn or NiCu as discussed in the previous chapters.

In this chapter, data acquired on 1wt%Ni-10wt%Cu/Mg(Al)(Ni)(Cu)O_x, i.e., the catalyst with the highest industrial potential among all those tested in this thesis, will be employed for regression and validation purposes. By doing so, specific insight can be obtained in the contribution of different types of active sites to the ethanol conversion and their nature simultaneously with a more generic insight in the reaction behavior. The model accounts for the various elementary phenomena relevant during intrinsic kinetic data acquisition. Given the intrinsic kinetics character of the data, no mass or heat transfer limitations need to be considered, nor the occurrence of complex, non-ideal reactor hydrodynamics.

7.2. Kinetic model construction

7.2.1. Reaction network

A literature review on the reactions proceeding on the catalysts indicated that two types of sites are available for all investigated catalysts in this thesis. One type of sites is capable of realizing C-C bond scissions, such as Pd and Ni, while the other type of sites selectively impacts on C-H bonds, such as Cu, NiCu and PdZn [7, 8]. Therefore, a two-site model has been constructed.

The elementary steps, as represented in Table 7- 1, to produce acetaldehyde from ethanol occur on the so-called *dehydrogenation sites*. Table 7- 2 reports the steps occurring on the *decomposition sites*. In addition to the desired transformation of ethanol to acetaldehyde, also its further conversion into methane and CO occurs on this type of sites [9-11].

Table 7- 1: Reaction network on dehydrogenation sites (DH=dehydrogenation).

Adsorption	$CH_3CH_2OH + * \rightleftharpoons CH_3CH_2OH^*$	**Reaction DH-1**
Reaction	$CH_3CH_2OH^* + * \rightleftharpoons CH_3CH_2O^* + H^*$	**Reaction DH-2**
	$CH_3CH_2O^* + * \rightleftharpoons CH_3CHO^* + H^*$	**Reaction DH-3**
	$CH_3CHO^* + * \rightleftharpoons CH_3CO^* + H^*$	**Reaction DH-4**
	$CH_3CO^* + CH_3CH_2O^* \rightleftharpoons CH_3COOC_2H_5^*$	**Reaction DH-5**
Desorption	$2H^* \rightleftharpoons H_2 + 2*$	**Reaction DH-6**
	$CH_3CHO^* \rightleftharpoons CH_3CHO + *$	**Reaction DH-7**
	$CH_3COOC_2H_5^* \rightleftharpoons CH_3COOC_2H_5 + *$	**Reaction DH-8**

Table 7- 2: Reaction network on decomposition sites (DC=decomposition).

Adsorption	$CH_3CH_2OH + * \rightleftharpoons CH_3CH_2OH^*$	**Reaction DC-1**
Reaction	$CH_3CH_2OH^* + * \rightleftharpoons CH_3CH_2O^* + H^*$	**Reaction DC-2**
	$CH_3CH_2O^* + * \rightleftharpoons CH_3CHO^* + H^*$	**Reaction DC-3**
	$CH_3CHO^* + * \rightleftharpoons CH_3CO^* + H^*$	**Reaction DC-4**
	$CH_3CO^* + * \rightleftharpoons CH_2CO^* + H^*$	**Reaction DC-5**
	$CH_2CO^* + * \rightleftharpoons CHCO^* + H^*$	**Reaction DC-6**
	$CHCO^* + * \rightleftharpoons CH^* + CO^*$	**Reaction DC-7**
	$CH^* + H^* \rightleftharpoons CH_2^* + *$	**Reaction DC-8**
	$CH_2^* + H^* \rightleftharpoons CH_3^* + *$	**Reaction DC-9**
Desorption	$2H^* \rightleftharpoons H_2 + 2*$	**Reaction DC-10**
	$CH_3CHO^* \rightleftharpoons CH_3CHO + *$	**Reaction DC-11**
	$CO^* \rightleftharpoons CO + *$	**Reaction DC-12**
	$CH_3^* + H^* \rightleftharpoons CH_4 + 2*$	**Reaction DC-13**

The methane selectivity observed during experimentation was so low and the description in elementary reactions on the decomposition sites includes so many steps that it would be highly challenging to significantly estimate all parameters for the elementary steps on the decomposition sites. Furthermore, owing to the low selectivity, omitting this will not significantly affect the obtained results. Hence, a more simple reaction network is considered which describes the formation of acetaldehyde, methane and CO in a global manner, rather than via elementary steps, see Table 7- 3. These reactions were considered irreversible after the calculation of the equilibrium coefficient of the global reaction.

Table 7- 3: Simplified reaction network on decomposition sites.

Adsorption	$CH_3CH_2OH + * \rightleftharpoons CH_3CH_2OH^*$	**Reaction DC-1**
Reaction	$CH_3CH_2OH^* + 2\ * \rightarrow CH_3CHO^* + 2\ H^*$	**Reaction DC-2**
	$CH_3CH_2O^* + * \rightarrow CH_4^* + CO^*$	**Reaction DC-3**
Desorption	$2H^* \rightleftharpoons H_2 + 2\ *$	**Reaction DC-4**
	$CH_3CHO^* \rightleftharpoons CH_3CHO + *$	**Reaction DC-5**
	$CO^* \rightleftharpoons CO + *$	**Reaction DC-6**
	$CH_4^* \rightleftharpoons CH_4 + *$	**Reaction DC-7**

The rate coefficients of a reaction i will be represented as $k_{DH,i,+}$ for the forward reaction and $k_{DH,i,-}$ for the reverse reaction for the dehydrogenation steps and $k_{DC,I,+}$ and $k_{DC,I,-}$ for the decomposition ones. The rate expressions of all reactions can be found in Appendix.

7.2.2. Analytical determination of initial intermediate concentration

The adsorption of gas phase species on the catalyst is considered to be quasi-equilibrated. Hence, the only intermediates which cannot directly be related to a corresponding gas phase species are the following ones occurring on the dehydrogenation sites, i.e., the ethoxyl species, $CH_2CH_3O^*$, and the acetyl species, CH_3CO^*. Their concentration is calculated by applying the pseudo-steady state approximation. Given the model assumptions made so far, it is impossible to have an acetyl species concentration different from zero at time zero when employing ethanol as the only reactant. The initial concentration of the ethoxyl species can, a priori, be calculated from

a set of algebraic equations, see Appendix. This yields an analytical expression for the initial ethoxyl and free dehydrogenation site fraction, see Equation 1 and Equation 2.

$$\theta_{EtO,DH} = \frac{k_{DH,2,+} K_{EtOH} p_{EtOH}}{k_{DH,3,+}(1 + K_{EtOH} p_{EtOH}) + k_{DH,2,+} K_{EtOH} p_{EtOH}} \quad \textbf{Equation 1}$$

$$\theta_{*,DH} = \frac{1}{1 + K_{EtOH} p_{EtOH} + \frac{k_{DH,2,+} K_{EtOH} p_{EtOH}}{k_{DH,3,+}}} \quad \textbf{Equation 2}$$

7.2.3. Determination of the kinetic and equilibrium coefficients

Due to the partially elementary description of the reactions, 38 model parameters are present in the model. To facilitate the regression of the parameters, the model parameters which could be calculated based on thermodynamic considerations will be determined a priori. The thermodynamic properties such as the enthalpy of formation and the heat capacity of the reactants and products were used as available in the literature [12]. Standard molar entropies have been calculated by Paraskevas et al. [13] and validated in this thesis by comparison of the heat capacity reported by Paraskevas with the values in *The properties of gases and liquids* [12]. For the ethoxyl and acetyl intermediates the values as reported by Paraskevas et al. have been used directly.

7.2.3.1. Pre-exponential factors and reaction entropies

To determine the absolute entropy of an adsorbed species, the adsorption entropy is subtracted from the entropy of the gas phase species. The adsorption entropy is calculated by employing the Sackur-Tetrode equation, thereby assuming that the amount of entropy lost can be quantified as a fraction of the translational entropy, irrespective of the actual degrees of freedom which are lost, i.e., translational, rotational and/or vibrational.

$$S_{trans} = \frac{3}{2} R\ ln(M) + \frac{5}{2} R\ ln(T) - R\ ln(p) + Rln\left(\frac{(2\pi k_B)^{\frac{3}{2}}}{h^3 N_A^{\frac{5}{2}}}\right) + \frac{5}{2} R + R\ ln(R) \qquad \textbf{Equation 3}$$

With:

S_{trans}	Translational entropy (J K^{-1} mol^{-1})
R	Universal gas constant (8.314 J K^{-1} mol^{-1})
M	Molar mass (kg mol^{-1})
T	Temperature (K)
p	Pressure (Pa)
k_B	Boltzmann constant (1.38 10^{-23} m^2 kg s^{-2} K^{-1})
h	Planck's constant (6.626 10^{-34} m^2 kg s^{-1})
N_A	Avogadro constant (6.022 10^{23} mol^{-1})

In general, it is assumed that an amount equivalent with two thirds of the translational entropy is lost upon chemisorption. For carbon monoxide however, it is expected that no translational entropy remains, thus thereby, all degrees of freedom are considered lost [14].

The pre-exponential factor is determined a priori via transition state theory to reduce the number of parameters that need to be estimated [15].

$$A = \frac{k_B T}{h} exp\left(\frac{\Delta S^{\ddagger}}{R}\right) \qquad \textbf{Equation 4}$$

With:

A	Pre-exponential factor (s^{-1})
$\Delta S^{\ddagger}$	Activation entropy (J K^{-1} mol^{-1})

The entropy change $\Delta S^{\ddagger}$ is calculated by the entropy difference between the transition state and the reactants. The entropy of the transition state was calculated, assuming that the transition state has lost one degree of freedom less than the product, since the transition state can still move between the reactant and the product. To calculate the equilibrium coefficient of a reaction or the

adsorption of a species, the reaction entropy $\Delta_r S$ is calculated by the entropy difference between the products and the reactants.

7.2.3.2. Reaction enthalpies

The reaction enthalpy is calculated by the enthalpy difference between the products and reactants. It should be noted that the activation energy of a forward reaction cannot be negative but also not smaller than the reaction enthalpy, because otherwise, the reverse reaction would have a negative activation energy. The enthalpy of formation of an adsorbed species is determined via subtracting the adsorption enthalpy from the enthalpy of formation of the gas phase species. The adsorption enthalpy is determined via the Unity Bond Index-Quadratic Exponential Potential (UBI-QEP) method developed by Shustorovich et al. [16].

7.2.3.3. UBI-QEP

In UBI-QEP, the chemisorption enthalpy of a species on a transition metal surface is related to the atomic chemisorption enthalpy of the constituting atoms, Q_A, and the gas phase molecular bond energy between the atoms in the molecule, D_{AB}. The latter can be determined from what is reported in open databases or from group additivity values [13, 17, 18]. The former can be determined from experimental values or from ab initio calculations. However, these values can often only be used as initial guesses and need fine tuning by model regression to experimental data. This is because coverage effects, surface defects, … can significantly affect the interaction between atoms and/or molecules. Q_A (A=C,H,O) are, hence, adjustable parameters in the kinetic model.

The UBI-QEP relates the atomic chemisorption enthalpy of a *n* fold coordination site, Q_A (kJ mol^{-1}), with the atomic chemisorption enthalpy of a top site, Q_{0A} (kJ mol^{-1}).

$$\boldsymbol{Q_A = Q_{0A}\left(2 - \frac{1}{n}\right)} \qquad \textbf{Equation 5}$$

That way, knowing the atomic chemisorption enthalpy of an element on a top site results in knowing the atomic chemisorption enthalpy on all coordination sites. Here, it is assumed that the coordination sites for C and O are threefold (n=3).

The method differentiates between weak, intermediate and strong chemisorption of molecules to the surface. Depending on this, different formulas need to be applied to correctly describe the adsorption enthalpy of a molecule. The reader is referred to Shustorovich et al. for a more detailed description [16].

7.2.4. Parameter estimation

7.2.4.1. Regression methodology

In a kinetic model, a variety of parameters are incorporated, i.e., activation energies of the occurring reactions, chemisorption enthalpies, … In order to obtain a good estimate for these parameters, a regression is performed. The regression is based on the minimization of the weighted differences between the model simulated and experimentally observed values of the responses:

$$S(\beta) = \sum_{j=1}^{n_{exp}} \sum_{i=1}^{n_{resp}} w_i \left(F_{i,j} - \widehat{F_{i,J}}\right)^2 \qquad \textbf{Equation 6}$$

With:

$F_{i,j}$ the experimentally measured response

$\widehat{F_{i,J}}$ the calculated response.

w weight factor

In practice, the outlet molar flow rates of the components are employed as responses. *w* is the weight factor that is accounted for in this minimization such that the objective function equally depends on the different responses. This is necessary since the values of the different responses may vary by several orders of magnitude, i.e., the variance of the responses is not constant. The

weight factors are obtained as the elements of the inverse of the covariance matrix σ_{ii}^2 of the experimental errors on the responses:

$$w_i = \frac{1}{\sigma_{ii}^2} \qquad \textbf{Equation 7}$$

In the kinetic model, the regression is performed via the Rosenbrock algorithm followed by the Levenberg-Marquardt method [19, 20]. In both methods, the sum-of-squares area is scanned in the search for an absolute minimum.

7.2.4.2. Statistical evaluation of the model, regression and parameters

In kinetic modeling, not only the physical meaning but also the statistical significance of the model, regression and estimated parameters is important. Several tests can be performed to verify this statistical significance. Depending on the desired severity of the tests, the probability that the test gives a correct representation can be selected. Here, as typically performed, a probability of 95% is used for all statistical tests.

Global significance of the regression

In this test, the parameters are tested whether they simultaneously differ significantly from zero, i.e., whether performing the regression was useful or whether the experimental values can simply be approximated by their average values. In this test, the regression sum of squares is compared with the sum of squares of the residuals:

$$F_{sign} = \frac{\frac{\hat{y}^T \hat{y}}{p}}{\frac{y^T y - b^T X^T y}{n - p}} \qquad \textbf{Equation 8}$$

With:

n	Number of experiments
p	Number of unknown parameters
$\hat{y}$	Calculated dependent variable matrix
y	Observed dependent variable matrix
b	Parameter estimation matrix

X Independent variable matrix

T matrix transposition operator

When the value of F_{sign} exceeds the tabulated F value with n and n-p degrees of freedom, the regression is deemed globally significant with the corresponding probability.

Individual significance of the parameters

Apart from the global significance of the regression, the parameters estimates should also be tested on their individual significance. To do so, the difference between the calculated value and the tested value, here zero, is compared with the standard deviation on the estimated value:

$$\boldsymbol{t = \frac{b_i - 0}{s(b_i)}} \qquad \textbf{Equation 9}$$

With:

b_i Estimated parameter of β_i

$s(b_i)$ Estimated standard deviation on b_i

When the calculated t value exceeds the tabulated t value with n-p degrees of freedom, the estimate is considered to significantly differ from zero.

Individual confidence interval

The same information can be obtained determining the individual confidence interval of the parameter. This interval represents the range in which the true value of the parameter can be expected with a probability of 1-α. The procedure for determining the individual confidence interval is based on the t test for the individual significance:

$$\boldsymbol{P\left(\frac{|b_i - \beta_i|}{s(b_i)} < t\left(n - p; 1 - \frac{\alpha}{2}\right)\right) = 1 - \alpha} \qquad \textbf{Equation 10}$$

The confidence interval hence, becomes:

$$b_i - t\left(n-p; 1-\frac{\alpha}{2}\right)s(b_i) \leq \beta_i \leq b_i + t\left(n-p; 1-\frac{\alpha}{2}\right)s(b_i) \quad \textbf{Equation 11}$$

Binary correlation coefficient

The binary correlation coefficient $\rho_{i,j}$ describes the impact two parameters have on each other. The correlation coefficient is calculated via:

$$\rho_{i,j} = \frac{\sigma_{ij}^2}{\sigma_i \sigma_j} \quad \textbf{Equation 12}$$

With:

σ_{ij} Covariance of i and j

σ_i Variance of i

7.3. Results and discussion

7.3.1. Data analysis

A dataset of 41 experiments has been acquired on 1wt%Ni-10wt%Cu/Mg(Al)(Ni)(Cu)O_x, including 13 repeat experiments, see also Chapter 6. The operating conditions have been varied in a temperature range from 493 to 533K, a total pressure range from 0.5 to 1.5MPa at space times between 0.9 and 3.6 kg_{cat} s mol^{-1}. All data meet the requirements for intrinsic kinetics.

At 533K and 0.5MPa the most extended space time range was employed, see Figure 7- 1. It can be seen that for space times exceeding 3.6kg_{cat} s mol^{-1}, the integral regime of operation is achieved. It thus seems that a conversion of 60% is the highest that can be achieved in these conditions, which was verified by calculating the maximum thermodynamic conversion. For space times below 3.6 kg_{cat} s mol^{-1}, a linear relationship between conversion and space time is found, corresponding to the differential region. In order to retrieve a maximum of kinetic information from the experimental data, all measurements have been performed with a maximum space time of 3.6kg_{cat} s mol^{-1}. Figure 7- 2 represents the conversion as function of the space time for three temperatures. All data were clearly measured in the differential regime here.

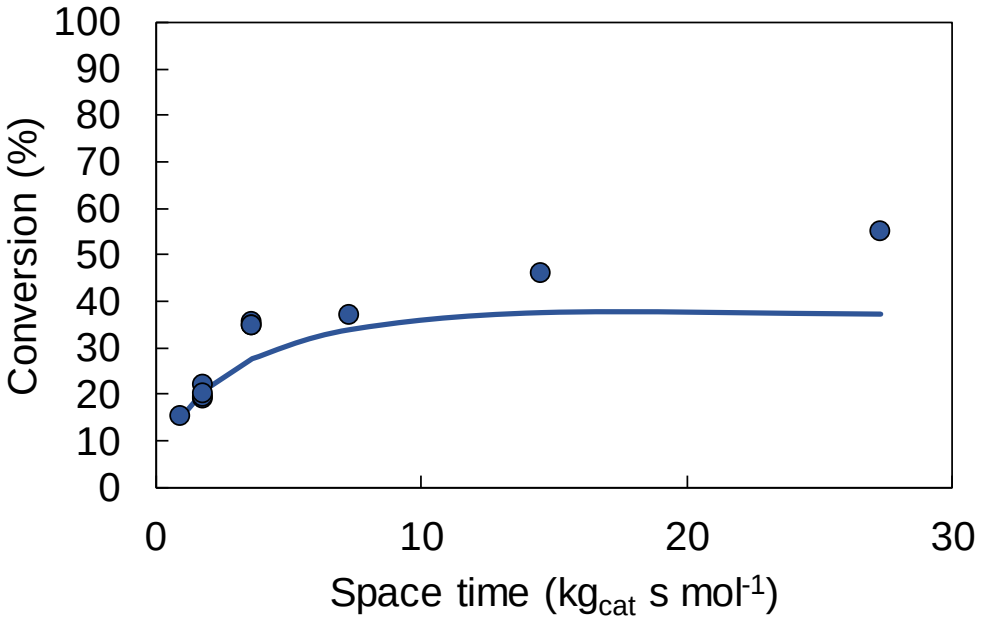

Figure 7- 1: Effect of space time on the conversion for 1wt%Ni-10wt%Cu/Mg(Al)(Ni)(Cu)O_x at T=533K, P_{tot}=0.5MPa and N_2/EtOH=20. Dots: experimental, line: model performance.

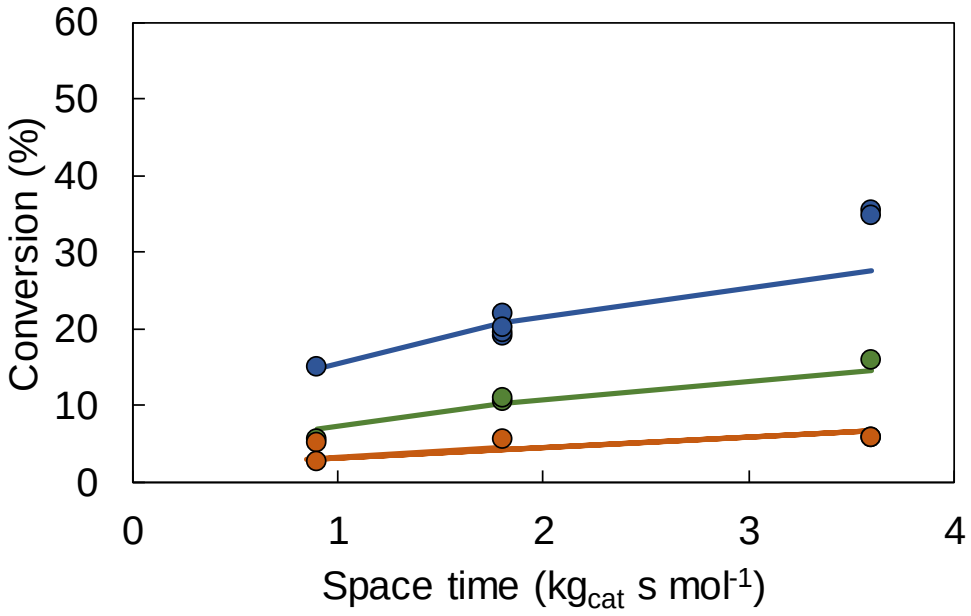

Figure 7- 2: Ethanol conversion as a function of the space time on 1wt%Ni-10wt%Cu/Mg(Al)(Ni)(Cu)O_x at P_{tot}=0.5MPa, N_2/EtOH=20 and T=493K (orange), T=513K (green) and T=533 (blue). Dots: experimental, line: model performance.

To assess the temperature effect on the acetaldehyde selectivity, the space time was manipulated such that approximately 10% conversion was achieved in all experiments, see Figure

7- 3. Such isoconversion data are necessary to allow an interpretation not biased by conversion effects. It can be seen that with increasing temperature, also the acetaldehyde selectivity increases: a rise in selectivity of 10% for a difference in temperature of 60K. This can be understood if the activation energy of $k_{DC,2,+}$ is lower than the activation energy of $k_{DH,2,+}$.

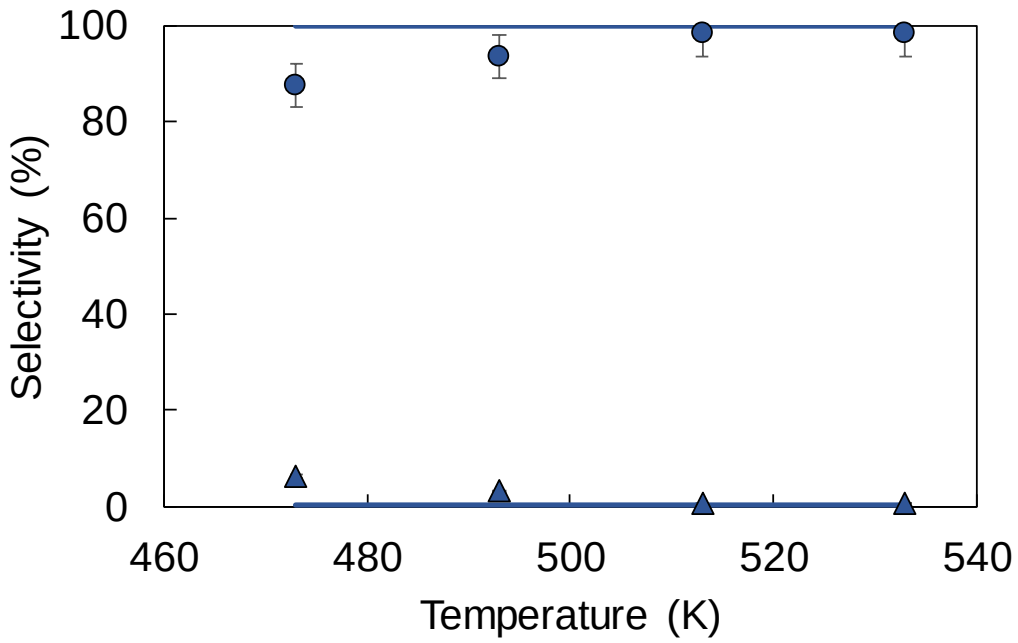

Figure 7- 3: Effect of temperature on the acetaldehyde (dots) and methane (triangle) selectivity on 1wt%Ni-10wt%Cu/Mg(Al)(Ni)(Cu)O_x for P_{tot}=0.5MPa, X=10wt% and N_2/EtOH=20. Symbols: experimental, line: model performance.

It can be seen in Figure 7- 4 that, upon increase of the total pressure, the conversion decreases, especially from 0.8MPa onwards. The selectivity, see Figure 7- 5, isn't altered upon a change in total pressure. The change in conversion as function of total pressure can't be a result of thermodynamic constrains because the conversion is too low, so it seems that inhibition of the reaction due to strong adsorption of the products is present.

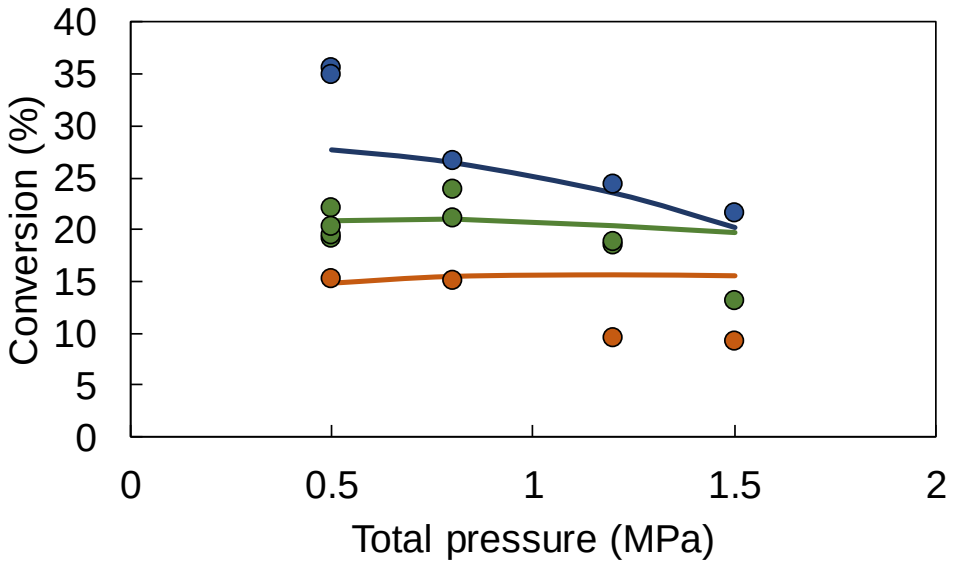

Figure 7- 4: Effect of pressure on the conversion for T=533K, N_2/EtOH=20 and $W/F_{EtOH,0}$=0.9 kg_{cat} s mol^{-1} (orange), 1.8 kg_{cat} s mol^{-1} (green) and 3.6 kg_{cat} s mol^{-1}). Symbols: experimental, line: model performance.

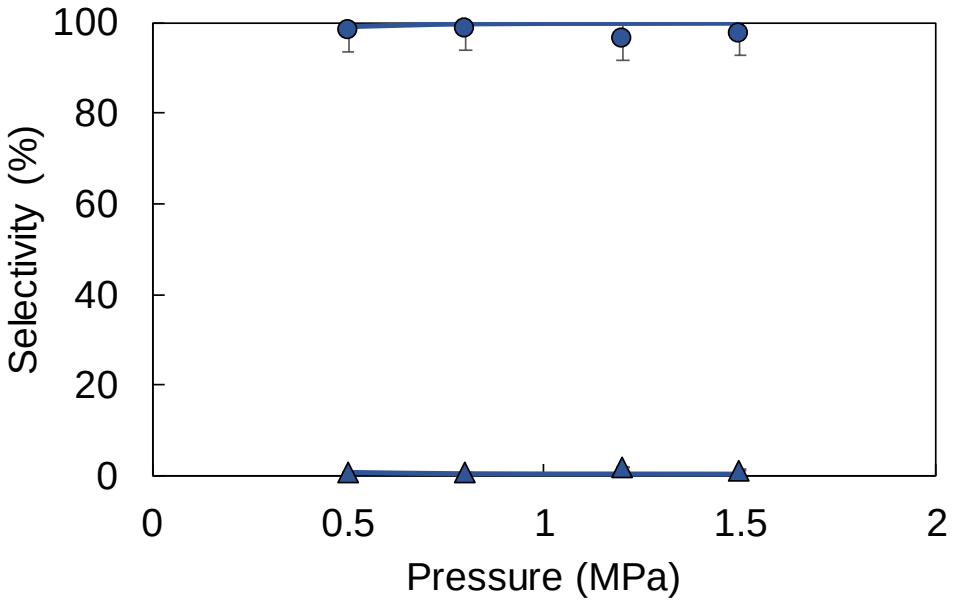

Figure 7- 5: Effect of pressure on the acetaldehyde (dots) and methane (triangles) selectivity for T=533K, X=10% and N_2/EtOH=20. Symbols: experimental, line: model performance.

7.3.2. Apparent reaction order, activation energy

The apparent reaction order and activation energy can be determined from the kinetic data. When simplifying the reaction scheme to only ethanol being converted to acetaldehyde, the reaction rate is described as:

$$r_{AcH} = -r_{EtOH} = k * p_{EtOH}^{a}$$

Taking a logarithm of this then results in:

$$\log(r_{AcH}) = \log(k) + a * \log(p_{EtOH})$$

The data have been presented as such in Figure 7- 6a. It can be concluded from this that the apparent reaction order is -0.76.

The same procedure can be applied to determine the apparent activation energy, with the equation being transformed into:

$$\log(r_{AcH}) = \log(A * p_{EtOH}^{a}) - \frac{E_a}{RT}$$

It results from Figure 7- 6b that the activation energy is 40.6kJ mol^{-1}.

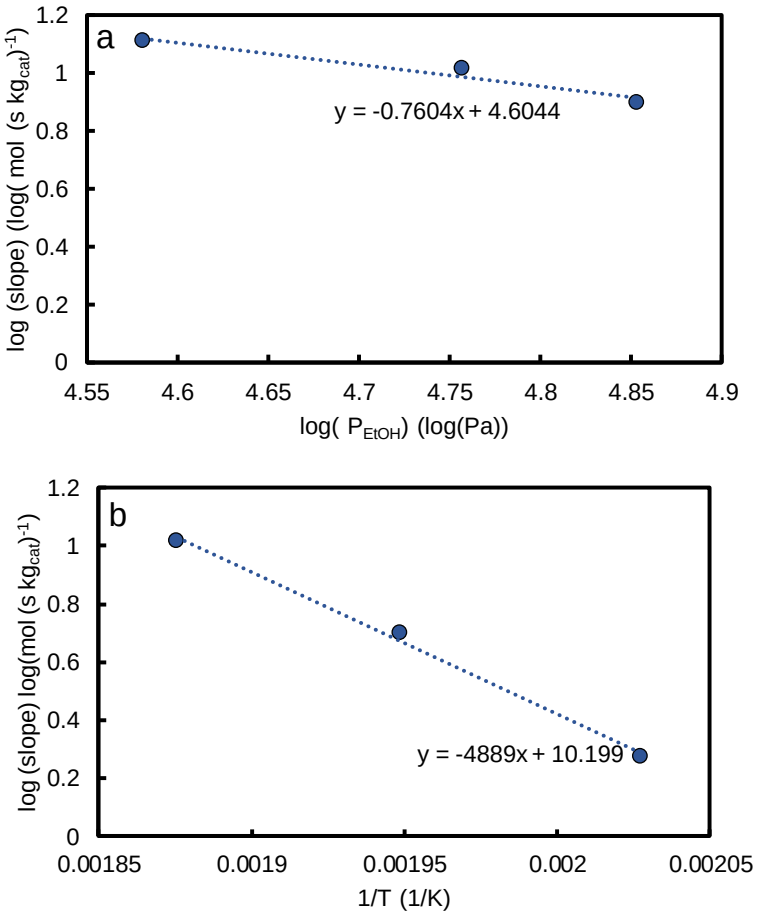

Figure 7- 6: Determination of the apparent reaction order (a) and activation energy (b)

7.3.3. Regression results and model performance

The generic model comprised 19 parameters, i.e., 3 atomic chemisorption enthalpies corresponding to the dehydrogenation sites, 3 atomic chemisorption enthalpies corresponding to the decomposition sites, 6 activation energies, the fraction of dehydrogenation sites and 6 reaction orders for the decomposition reactions. Of these, 2 parameters were fixed. Since for this catalyst, no ethyl acetate production was encountered, the activation energies couldn't be estimated and they thus were set at a high value and fixed. They were not excluded from the model reactions to allow the description of the performance of the other catalysts used in this thesis. As such 17 parameters remain to be estimated via non-linear regression from 41 experiments. The estimated activation energies are tabulated in bold in Table 7- 4. The pre-exponential factors and reaction entropies were calculated a priori via use of statistical thermodynamic considerations and are

included in Table 7- 4. The reaction enthalpies are calculated from the estimates for the atomic chemisorption enthalpies and are reported in italic in Table 7- 4. Table 7- 5 then tabulates the remaining parameter estimates, i.e., the fraction of dehydrogenation sites, the atomic chemisorption enthalpies and the reaction orders. No reaction orders were estimated for the reaction from methane and carbon monoxide to acetaldehyde since the calculated equilibrium coefficient of that reaction favored the formation of methane and carbon monoxide greatly. All parameters were estimated significantly, i.e., this value is sufficiently different from zero to contribute to the kinetics. Furthermore, all parameters are physico-chemically meaningful. The F value for the global significance of the model, see section 7.2.4.2, amounts to 3100 whereas the tabulated value is only 2.79. The model, hence, significantly represents the experimental observations. The binary correlation coefficients are reported in Table 7- 6 and show that the correlation between the parameters estimates is limited. The parity diagrams for ethanol, acetaldehyde and methane, see resp. Figure 7- 7a, b and c, indicate that the conversion is accurately described. For the acetaldehyde response, the model captures the experiments quite well, i.e. the experimental points are nicely spread around the first bisector, see Figure 7- 7b. The methane responses are also nicely spread around the first bisector, but could still be improved. This would require a more detailed model which also describes the formation of methane and carbon monoxide via elementary steps. In Figure 7- 1, Figure 7- 2, Figure 7- 3 and Figure 7- 5, the simulated model performance is depicted via the full lines. It can be seen in Figure 7- 1 and Figure 7- 2 that the effect of space time and temperature on the conversion was very accurately reproduced by the model. The effect of pressure on the conversion was not completely captured by the model, see Figure 7- 4, but the trend is correct.

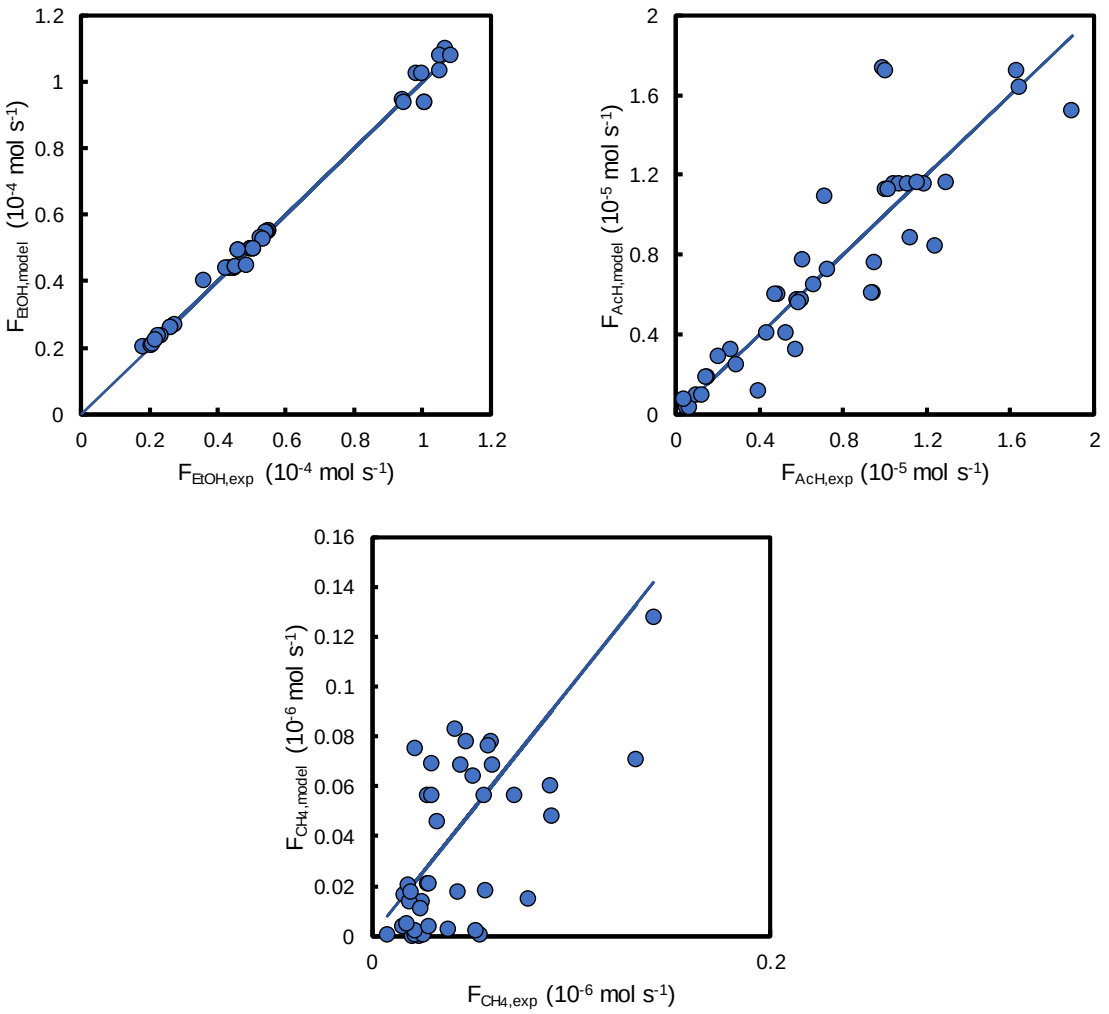

Figure 7- 7: Parity diagrams for ethanol (a), acetaldehyde (b) and methane (c). All data (blue) but the data points at 533K at 1.2MPa and 1.5MPa (orange).

Table 7- 4: Pre-exponential factors A^f, activation energies E_a^f for the forward reactions, surface reaction enthalpies $H_r°$ and surface reaction entropies $S_r°$ at 533K. The parameters in bold are estimated via non-linear regression. The parameters in italic are calculated from parameters estimates.

Reactions	A^f (s^{-1} or MPa s^{-1})	E_a^f (kJ mol^{-1})	$\Delta H_r°$ (kJ mol^{-1})	$\Delta S_r°$ (J (K $mol)^{-1}$)
Dehydrogenation sites				
Adsorption				
$CH_3CH_2OH + * \rightleftharpoons CH_3CH_2OH^*$			*67.7*	*-112.5*
Reaction				
$CH_3CH_2OH^* + * \rightleftharpoons CH_3CH_2O^* + H^*$	$6.9\ 10^{14}$	**60.3 ± 6.99**	*41.8*	*111.3*
$CH_3CH_2O^* + * \rightleftharpoons CH_3CHO^* + H^*$	$2.9\ 10^{12}$	**60.7 ± 0.07**	*37.3*	*67.7*
$CH_3CHO^* + * \rightleftharpoons CH_3CO^* + H^*$	$2.5\ 10^{16}$	309.7	*309.7*	*140.8*
$CH_3CO^* + CH_3CH_2O^* \rightleftharpoons CH_3COOC_2H_5^*$	$3.7\ 10^{3}$	180.4	*-364.5*	*-183.0*
Desorption				
$2H^* \rightleftharpoons H_2 + 2*$			*-7.7*	*61.2*
$CH_3CHO^* \rightleftharpoons CH_3CHO + *$			*-50.2*	*112.1*
$CH_3COOC_2H_5^* \rightleftharpoons CH_3COOC_2H_5 + *$			*-79.0*	*117.9*
Decomposition sites				
Adsorption				
$CH_3CH_2OH + * \rightleftharpoons CH_3CH_2OH^*$			*78.6*	*-112.5*
Reaction				
$CH_3CH_2OH^* + 2 * \rightarrow CH_3CHO^* + 2\,H^*$	$7.5\ 10^{16}$	**58.3 ± 20.06**	*56.5*	*120.3*
$CH_3CH_2O^* + 2 * \rightarrow CH_4^* + CO^*$	$6.7\ 10^{13}$	**39.2 ± 3.52**	*-147.7*	*-35.9*
Desorption				
$2H^* \rightleftharpoons H_2 + 2*$			*-0.78*	*61.2*
$CH_3CHO^* \rightleftharpoons CH_3CHO + *$			*-90.7*	*112.1*
$CO^* \rightleftharpoons CO + *$			*-83.3*	*162.5*
$CH_4^* + H^* \rightleftharpoons CH_4 + 2*$			*-134.9*	*103.7*

Table 7- 5: Fraction of dehydrogenation active sites Θ_{DH}, atomic chemisorption enthalpies Q of C, H and O for the dehydrogenation sites ($Q_{C,DH}$, $Q_{H,DH}$, $Q_{O,DH}$) and for the decomposition sites ($Q_{C,DC}$, $Q_{H,DC}$, $Q_{O,DC}$) and reaction orders on the decomposition reactions a, b, c, d, e and f.

Θ_{DH}	**0.92 ± 0.003**
Dehydrogenation sites	
Atomic chemisorption enthalpy (kJ mol^{-1})	
$Q_{C,DH}$	**500.3 ± 11.78**
$Q_{H,DH}$	**215.6 ± 0.79**
$Q_{O,DH}$	**453.7 ± 1.08**
Decomposition sites	
Atomic chemisorption enthalpy (kJ mol^{-1})	
$Q_{C,DC}$	**693.8 ± 13.27**
$Q_{H,DC}$	**219.1 ± 0.01**
$Q_{O,DC}$	**494.4 ± 14.46**
Reaction order (-)	
$CH_3CH_2OH^{*a} + 2\ *^b \rightarrow CH_3CHO^{*c} + 2\ H^{*d}$	
a	**1.43 ± 0.004**
b	**1.01 ± 0.003**
c	**1.01 ± 0.027**
d	**1.00 ± 0.004**
$CH_3CH_2O^{*e} + 2\ *^f \rightarrow CH_4^* + +CO^*$	
e	**0.96 ± 0.024**
f	**1.01 ± 0.005**

Table 7- 6: Binary correlation coefficients of the dehydrogenation atomic chemisorption enthalpies (1,2,3), activation energies on the dehydrogenation sites (4), the decomposition atomic chemisorption enthalpies (5,6,7), activation energies on the decomposition sites (10,11), fraction of dehydrogenation sites (10), reaction orders of the forwards decomposition reactions (11,12,13,14).

	1	2	3	4	5	8	9	10	11	12	13	14	15	16	17	18	19
1	1.00																
2	-0.35	1.00															
3	0.76	-0.07	1.00														
4	0.69	-0.54	0.81	1.00													
5	0.70	-0.02	0.24	-0.02	1.00												
8	0.87	-0.15	0.47	0.27	0.94	1.00											
9	-0.09	0.14	0.11	0.16	-0.31	-0.37	1.00										
10	0.49	0.12	-0.01	-0.27	0.94	0.81	-0.20	1.00									
11	-0.26	-0.09	0.14	0.39	-0.75	-0.68	0.80	-0.73	1.00								
12	-0.68	0.54	-0.80	-1.00	0.04	-0.25	-0.16	0.29	-0.40	1.00							
13	-0.71	0.01	-0.25	0.01	-1.00	-0.94	0.30	-0.94	0.74	-0.03	1.00						
14	0.06	0.26	-0.33	-0.62	0.70	0.54	-0.65	0.77	-0.96	0.63	-0.69	1.00					
15	0.59	-0.54	0.76	0.99	-0.15	0.13	0.20	-0.40	0.49	-0.99	0.15	-0.71	1.00				
16	-0.29	-0.19	0.14	0.44	-0.84	-0.72	0.62	-0.86	0.97	-0.46	0.83	-0.97	0.55	1.00			
17	0.17	0.22	-0.24	-0.54	0.77	0.63	-0.66	0.81	-0.97	0.55	-0.76	0.99	-0.63	-0.99	1.00		
18	-0.69	-0.09	-0.36	-0.11	-0.81	-0.75	-0.28	-0.83	0.28	0.10	0.82	-0.30	0.00	0.47	-0.37	1.00	
19	-0.21	-0.30	0.23	0.56	-0.83	-0.65	0.39	-0.92	0.86	-0.58	0.83	-0.94	0.67	0.96	-0.95	0.59	1.00

7.3.4. Assessment of the model parameters

For the atomic chemisorption enthalpies on the dehydrogenation and the decomposition sites on 1wt%Ni-10wt%Cu/Mg(Al)(Ni)(Cu)O_x, it was assumed that the decomposition sites corresponded with Ni, whereas the dehydrogenation sites are rather NiCu alloy sites. Both for Ni and Cu, Shustorovich reported atomic chemisorption enthalpies, see Table 7- 7 [16]. The estimated atomic chemisorption enthalpies for carbon and hydrogen are all higher than these values. The estimated values rather correspond nicely with those reported by Appari et al. for Ni and Mirzanejad et al. for Cu, see Table 7- 7 [21, 22]. When calculating the apparent Gibbs free energy of formation based on Figure 7- 1 and comparing it to the Gibbs free energy of formation estimated for the dehydrogenation reaction, these values are in line, i.e., 6.6kJ mol^{-1} and 1.1kJ mol^{-1} resp. calculated and estimated.

Table 7- 7: Literature reported values for the atomic chemisorption enthalpy of C, H and O.

Atomic chemisorption enthalpy (kJ mol^{-1})	Shustorovich et al. – Cu [16]	Shustorovich et al. – Ni [16]	Mirzanejad et al. – Cu [22]	Appari et al. – Ni [21]
Q_C	301.4	429.56	502.4	715.9
Q_H	140.7	158.3	234.5	263.8
Q_O	258.7	288.9	431.2	481.5

The number of kinetic models constructed for ethanol dehydrogenation or decomposition is limited. Carotenuto et al. have constructed a kinetic model for the production of ethyl acetate from ethanol on a Cu-based catalyst [23]. However, the considered reactions were not elementary ones. Therefore, it is difficult to compare the activation energies with the estimates in this chapter. Li et al. have performed DFT calculations to determine the activation energies of the elementary reactions. The reported activation energies are all in the range of 100kJ or more, which is rather high. Overall, the estimated parameters, tabulated in Table 7- 4, seem to be physically meaningful.

The fraction of dehydrogenation sites is 0.92 which supports the result from Chapter 6 in which we suggested that Ni is almost fully incorporated in Cu.

7.3.5. Reaction path analysis

The combination of the reaction rates and the surface coverages gives more insight in how the reactions occur, at least according to the model. Figure 7- 8 depicts the surface coverages of all compounds on the dehydrogenation sites, i.e., Figure 7- 8a, and the decomposition sites, Figure 7- 8b. Figure 7- 10 represents the reaction mechanism indicating the rates of the various considered steps. Adsorption and desorption of the gas compounds were assumed to be in quasi-equilibrium and are indicated in black. For the reaction steps, a color code is employed to indicate the corresponding rate.

It is evident from Figure 7- 8 that only hydrogen occupies the catalyst surface. No other molecules occupy the surface. In Figure 7- 9, the hydrogen coverage is depicted as function of pressure. It can be seen that the hydrogen occupancy increases with pressure. The coverages of the other reactants, intermediates or products are still non-existing with increasing pressure. It is clear from Figure 7- 10 that the acetaldehyde formation reactions on the dehydrogenation sites proceed very fast. The acetaldehyde formation on the decomposition sites has a very low rate. It can thus safely be assumed that methane and carbon monoxide are only produced from acetaldehyde formation on the dehydrogenation sites and readsorption on the decomposition sites.

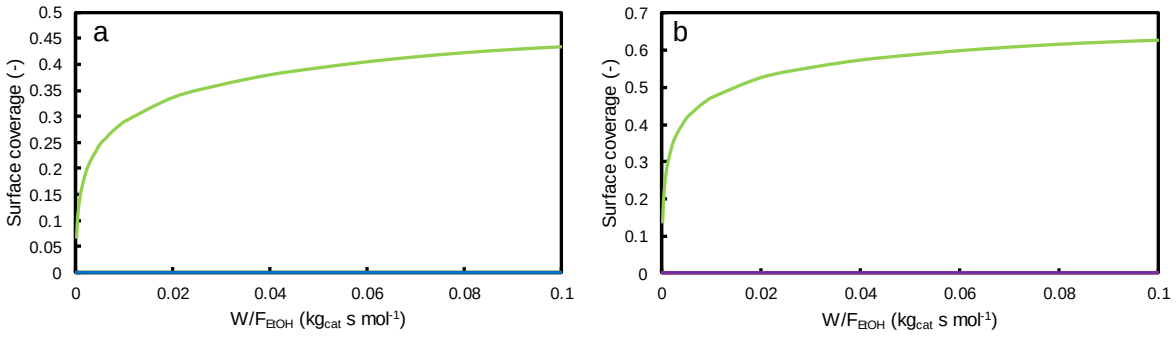

Figure 7- 8: Surface coverage of ethanol (red), acetaldehyde (orange), ethyl acetate (yellow), hydrogen (green), etoxy (light blue), acetyl (dark blue), methane (light purple), carbon monoxide (dark purple) at T=533K, P_{tot}=5bar, N_2/EtOH=20.

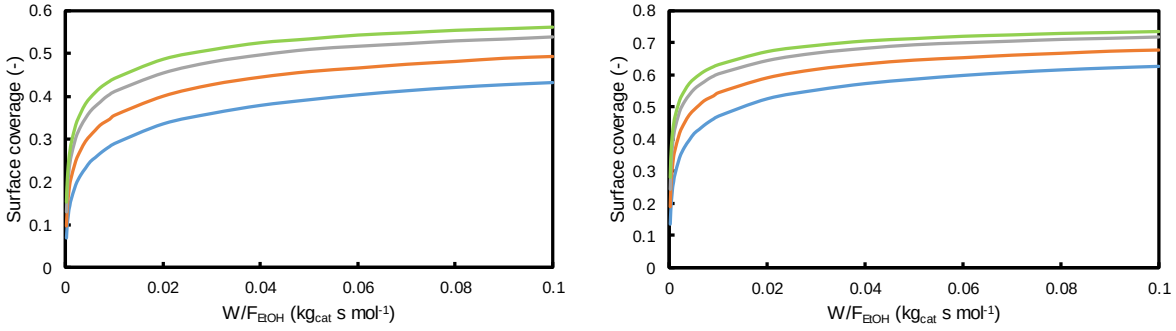

Figure 7- 9: Surface coverage of hydrogen for total reaction pressure of 0.5MPa (blue), 0.8MPa (orange), 1.2MPa (grey) and 1.5MPa (green).

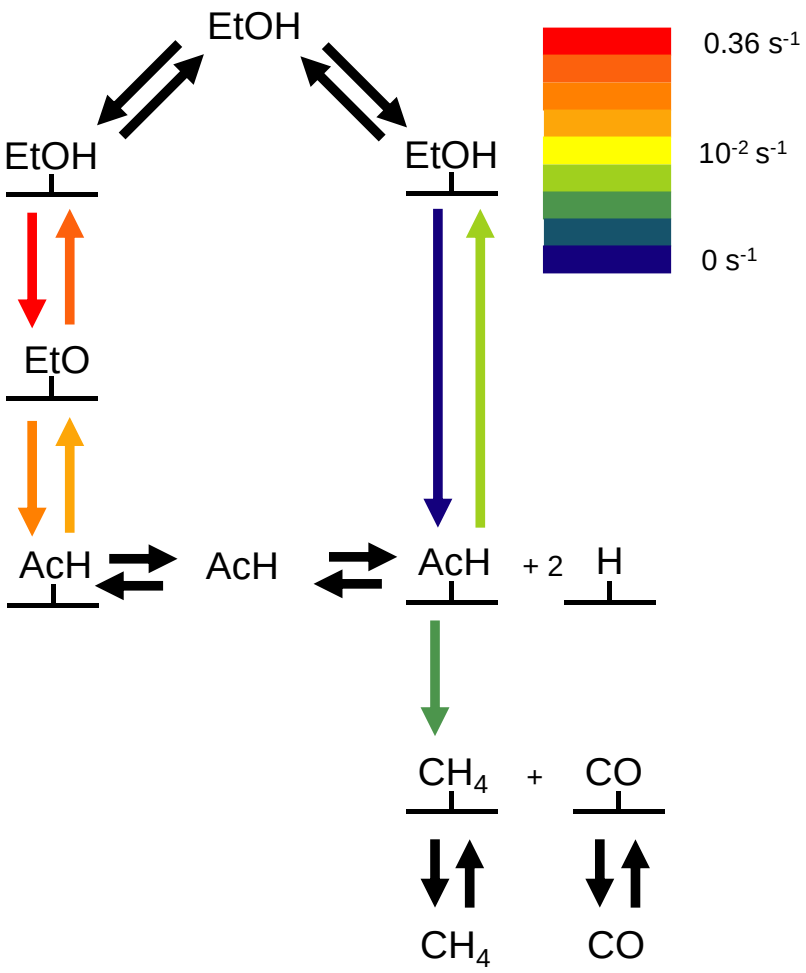

Figure 7- 10: Reaction path analysis at T=533K, P_{tot}=0.5MPa, W/F_{EtOH}=3.6kg_{cat} s mol^{-1}. The colors represent the relative rates, i.e., dark red=high rate → dark blue=low rate.

7.4. Conclusions

A kinetic model was constructed for ethanol dehydrogenation. For the main route, i.e., ethanol dehydrogenation, elementary reactions were considered. For the decomposition route, global reactions with reaction orders were considered, since the response of methane and carbon monoxide was low and too many parameters should be estimated when expressing also this route in terms of elementary steps. The pre-exponential factors and reaction entropies were calculated a priori by thermodynamic considerations. The reaction enthalpy was calculated based on the UBI-QEP method developed by Shustorovich. For this the atomic chemisorption enthalpies of H,

O and C were estimated for the dehydrogenation and the decomposition sites. Furthermore, the activation energies and fraction of dehydrogenation sites were estimated via non-linear regression. The Rosenbrock and Levenberg-Marquardt algorithms were used for the non-linear regression.

All parameter estimates were physically meaningful and statistically significant. The activation energy of the ethyl acetate production was not estimated since no ethyl acetate was produced on this catalyst. Comparison of the estimated chemisorption enthalpies with literature values was performed and the reported values correspond well with the estimated ones.

The reaction path analysis revealed that the formation of acetaldehyde occurs mainly on the dehydrogenation sites and adsorption on the decomposition sites results in the formation of methane and carbon monoxide. The formation of acetaldehyde from ethanol on the dehydrogenation is also really fast. This results in a low coverage of reactants or products.

7.5. References

[1] K. Van der Borght, K. Toch, V. Galvita, J. Thybaut, G. Marin, Information-Driven Catalyst Design Based on High-Throughput Intrinsic Kinetics, Catalysts, 5 (2015) 1948.
[2] J.W. Thybaut, G.B. Marin, Single-Event MicroKinetics: Catalyst design for complex reaction networks, Journal of Catalysis, 308 (2013) 352-362.
[3] J. Van Belleghem, C. Ledesma, J. Yang, K. Toch, D. Chen, J.W. Thybaut, G.B. Marin, A Single-Event MicroKinetic model for the cobalt catalyzed Fischer-Tropsch Synthesis, Applied Catalysis A: General, 524 (2016) 149-162.
[4] B.D. Vandegehuchte, J.W. Thybaut, A. Martínez, M.A. Arribas, G.B. Marin, n-Hexadecane hydrocracking Single-Event MicroKinetics on Pt/H-beta, Applied Catalysis A: General, 441-442 (2012) 10-20.
[5] R. Quintana-Solórzano, J.W. Thybaut, G.B. Marin, R. Lødeng, A. Holmen, Single-Event MicroKinetics for coke formation in catalytic cracking, Catalysis Today, 107-108 (2005) 619-629.
[6] P. Kumar, J.W. Thybaut, S. Svelle, U. Olsbye, G.B. Marin, Single-event microkinetics for methanol to olefins on H-ZSM-5, Industrial & Engineering Chemistry Research, 52 (2013) 1491-1507.
[7] M. Mavrikakis, M.A. Barteau, Oxygenate reaction pathways on transition metal surfaces, Journal of Molecular Catalysis A: Chemical, 131 (1998) 135-147.
[8] P.D. Vaidya, A.E. Rodrigues, Glycerol Reforming for Hydrogen Production: A Review, Chemical Engineering & Technology, 32 (2009) 1463-1469.
[9] M. Li, W. Guo, R. Jiang, L. Zhao, H. Shan, Decomposition of Ethanol on Pd(111): A Density Functional Theory Study, Langmuir, 26 (2009) 1879-1888.
[10] R.Z. Li, M.H. Zhang, Y.Z. Yu, A DFT study on the Cu (111) surface for ethyl acetate synthesis from ethanol dehydrogenation, Applied Surface Science, 258 (2012) 6777-6784.
[11] Y. Huang, Z.-X. Chen, Density Functional Investigations of Methanol Dehydrogenation on Pd−Zn Surface Alloy, Langmuir, 26 (2010) 10796-10802.
[12] R.C. Reid, J.M. Prausnitz, B.E. Poling, The Properties of Gases and Liquids, McGraw-Hill1987.
[13] P.D. Paraskevas, M.K. Sabbe, M.-F. Reyniers, N. Papayannakos, G.B. Marin, Group Additive Values for the Gas-Phase Standard Enthalpy of Formation, Entropy and Heat Capacity of Oxygenates, Chemistry – A European Journal, 19 (2013) 16431-16452.
[14] V.P. Zhdanov, J. Pavlíček, Z. Knor, Preexponential Factors for Elementary Surface Processes, Catalysis Reviews, 30 (1988) 501-517.
[15] J.A. Dumesic, D.F. Rudd, L.M. Aparicio, J.E. Rekoske, A.A. Treviño, The microkinetics of heterogeneous catalysis, American Chemical Society Washington, DC1993.

[16] E. Shustorovich, H. Sellers, The UBI-QEP method: A practical theoretical approach to understanding chemistry on transition metal surfaces, Surface Science Reports, 31 (1998) 1-119.
[17] N.I.o.S.a. Technology, NIST Standard Reference Database Number 69, U.S. Department of Commerce, 2017.
[18] N. Cohen, Revised Group Additivity Values for Enthalpies of Formation (at 298 K) of Carbon–Hydrogen and Carbon–Hydrogen–Oxygen Compounds, Journal of Physical and Chemical Reference Data, 25 (1996) 1411-1481.
[19] H.H. Rosenbrock, An Automatic Method for Finding the Greatest or Least Value of a Function, The Computer Journal, 3 (1960) 175-184.
[20] J. Moré, The Levenberg-Marquardt algorithm: Implementation and theory, in: G.A. Watson (Ed.) Numerical Analysis, Springer Berlin Heidelberg1978, pp. 105-116.
[21] S. Appari, V.M. Janardhanan, R. Bauri, S. Jayanti, O. Deutschmann, A detailed kinetic model for biogas steam reforming on Ni and catalyst deactivation due to sulfur poisoning, Applied Catalysis A: General, 471 (2014) 118-125.
[22] A. Mirzanejad, Thermal chemistry of 2-halo-1-propanols on Ni(111) and Cu(111) surfaces: A UBI-QEP energetic modeling, Applied Surface Science, 359 (2015) 576-588.
[23] G. Carotenuto, R. Tesser, M. Di Serio, E. Santacesaria, Kinetic study of ethanol dehydrogenation to ethyl acetate promoted by a copper/copper-chromite based catalyst, Catalysis Today, 203 (2013) 202-210.

Chapter 8.

General conclusions and outlook

8.1. General conclusions

Bio-ethanol has been recognized as a promising alternative base chemical in a more sustainable chemical industry. It is already employed as a fuel, blended up to 10% in gasoline, but it can also serve for the production of chemicals. A challenge in this respect is that, without specific purification steps, bio-ethanol contains significant amounts of water and complete water removal is highly energy intensive due to the azeotrope around 95% ethanol. To mitigate this issue, ethanol could be converted to acetaldehyde, since acetaldehyde and water do not exhibit such an azeotrope. For this transformation, two routes are available, i.e., a direct dehydrogenation in which hydrogen is produced as a byproduct and an oxidative dehydrogenation in which water is produced. Since hydrogen is a valuable byproduct, the direct dehydrogenation was preferred.

For this direct hydrogenation route, Cu-based catalysts are typically employed, but they experience pronounced deactivation due to sintering. Alternative catalysts should, hence, be found which are not subject to such irreversible deactivation. Furthermore, the presence of acid sites may result in the production of undesired byproducts such as diethyl ether. To avoid this, basic hydrotalcite-based mixed oxides can be recurred to. Apart from their basicity, a major advantage of such hydrotalcites as support is that active metals can be *incorporated* during synthesis. Upon calcination and reduction these active metals diffuse to the surface and form well controlled (nano)particles. As alternatives for the Cu-based catalysts, bimetallic catalysts were explored. Since Cu and PdZn are reported to exhibit a similar density of states, it's a logic assumption that their catalytic properties would also be similar. This appeared to be the case

indeed. Moreover, the presence of Zn prevented sintering of the active particles, such that the negative property of pure Cu is resolved.

First, the effect of the activation procedure on the activity and stability of the catalyst was investigated. It was found that a cycled reduction, i.e., consecutive hydrogen and oxygen treatments, improved the catalyst activity thanks to a higher number of active sites which were segregated from the support to the surface and a better alloy formation.

Secondly, the effect of synthesis method on the catalyst performance was assessed. Wet incipient impregnation on a presynthesized support was compared with the direct incorporation of the active metals in the support. It was found that incorporation of the active metals gave rise to a more active catalyst due to the smaller diameter of the particles on this incorporated catalyst. Owing to this smaller diameter, the alloy formation was complete on the incorporated catalyst, whereas for the impregnated one, a core-shell structure of the particles remained.

The presence of water in the feed was found to induce PdZn particle decomposition into ZnO patches on a Pd-rich PdZn particle. This reduces both the activity and acetaldehyde selectivity of the catalyst. Upon regeneration, the original PdZn particles are restored, but the interaction between the active metals with the support appeared to be weakened resulting in Pd and Zn losses via evaporation.

The above-discussed results clearly indicated that the dehydrogenation reaction proceeds only on Pd and isolated Pd sites are required for the selective formation of acetaldehyde. Adjacent Pd sites catalyze acetaldehyde decomposition into methane and carbon monoxide. No activity is attributed to Zn. A more active catalyst might be obtained if the two alloying metals would both be active for ethanol dehydrogenation, e.g., Ni and Cu. It can be assumed that a NiCu alloy was formed. The highest activity, selectivity and stability was found for 1wt%Ni-10wt%Cu/Mg(Al)(Ni)(Cu)O_x. This catalyst also had the highest level of alloying, as evident from FTIR measurements. In case of the presence of water in the feed, the activity of the catalyst even improved. This NiCu-based catalyst,

hence, really presents itself as promising candidate for industrial acetaldehyde production from bio-ethanol.

A generic kinetic model was constructed to obtain insight in the bio-ethanol conversion into acetaldehyde. Most of the model parameters were determined a priori via thermodynamic considerations. The remaining model parameters were estimated via non-linear regression to a kinetic dataset acquired on 1wt%Ni-10wt%Cu/Mg(Al)(Ni)(Cu)O_x, i.e., the best performing of all investigated catalysts in this thesis. All parameter estimates were physically meaningful and statistically significant. A reaction path analysis indicated that after adsorption, ethanol practically instantaneously reacts into acetaldehyde. The latter subsequently desorbs or moves towards decomposition sites for the production of methane and carbon monoxide.

In general, from this thesis, fundamental insight has been obtained for the synthesis of new highly active catalysts for bio-ethanol dehydrogenation. The fundamental effect of synthesis method and activation procedure on the catalyst performance have been determined as well as the effect of water. Two bimetallic systems have been under investigation to give initial insight in the effect of different active metals and to determine which phenomena are common for all catalysts. Via kinetic modelling of the 1wt%Ni-10wt%Cu/Mg(Al)(Ni)(Cu)O_x first insights are also obtained in the reaction behavior.

8.2. Outlook

While bimetallic nanoparticle synthesis had already been investigated, this PhD thesis was the first to employ them for bio-ethanol dehydrogenation. Future activities may be developed along two lines, i.e., the experimental catalyst synthesis and characterization part and in-silico catalyst design via kinetic modelling.

When taking into account the experimental part, the PdZn catalysts can be optimized for their stability for water by adding less zinc upon synthesis, such that thermodynamically, zinc will

rather stay in the core of the PdZn particle than become oxidized on the PdZn particle. For both the PdZn or NiCu system, the effect of particle size on the catalyst performance is worth the investigation. The challenges here will be to vary only the particle size and no other catalyst properties. Apart from PdZn and NiCu catalysts, also other bimetallic systems would seem good candidates for ethanol dehydrogenation catalysts, such as PdCu, PdSn, PdGa,… . These could be investigated with the knowledge acquired above.

Taking into account the in-silico catalyst development, the model can be validated with all investigated catalysts to prove the existence of true catalyst and kinetic descriptors. Furthermore, guidelines can be put forward to synthesize the optimal catalyst based on an optimization analysis on the kinetic descriptors.

When fundamental insight in the catalyst systems is acquired, it can be validated for other alcohols. Bio-butanol acquired from bio-based resources can be converted in butanal, for example, which can be used for the synthesis of aspirin and vitamin E. In the assessment of the dehydrogenation kinetics of another feedstock, the Single-Event MicroKinetic (SEMK) methodology could be used. This methodology classifies similar reactions into so-called reaction families, e.g., the removal of hydrogen from ethanol to form an ethoxyl species and the removal of hydrogen from butanol to form a butoxyl species. Within such a reaction family, a single kinetic coefficient suffices to describe the reaction rate, after a potential correction for the number of single events. This number specifically accounts for symmetry effects on the rate coefficient. Via this methodology, an experimental data set obtained on butanol to butanal should be described by the model by solely changing the number of single events, leaving all catalyst and kinetic descriptors unaltered.

The intrinsic kinetics model can be embedded in a reactor model accounting for potential heat and mass transport limitations and complex flow patterns which may be unavoidable in industrial reactors. A fixed bed reactor design can be investigated since the catalysts are sufficiently stable to avoid continuous removal and regeneration of the catalyst. Potentially, a membrane reactor

could be employed to overcome the thermodynamic constraints imposed by the reaction by the removal of hydrogen from the reactor.

Appendix A:

Activity and stability of Pd/ZnO and Pd/Mg(Al)(Pd)O_x

1. *Pd/ZnO*

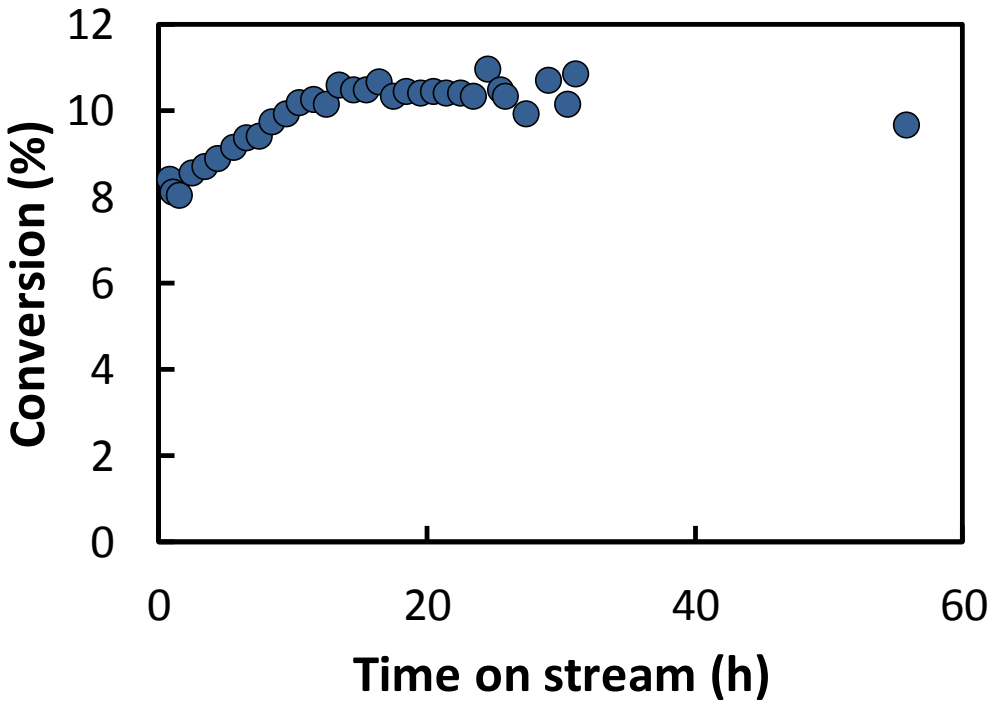

Figure S 1: Conversion profile as function of time on stream for Pd/ZnO after reduction at 823K.

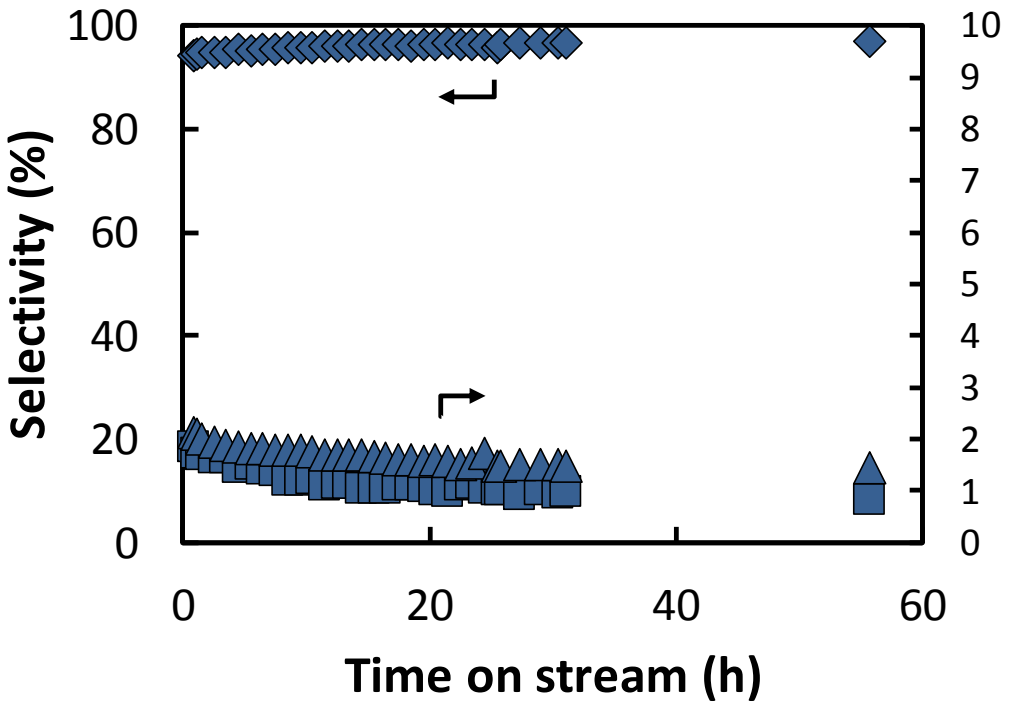

Figure S 2: Selectivity profile of acetaldehyde (◆), methane (■) and di-ethyl ether (▲) as function of time on stream for Pd/ZnO after reduction at 823K.

2. *Pd/Mg(Al)(Pd)O_x*

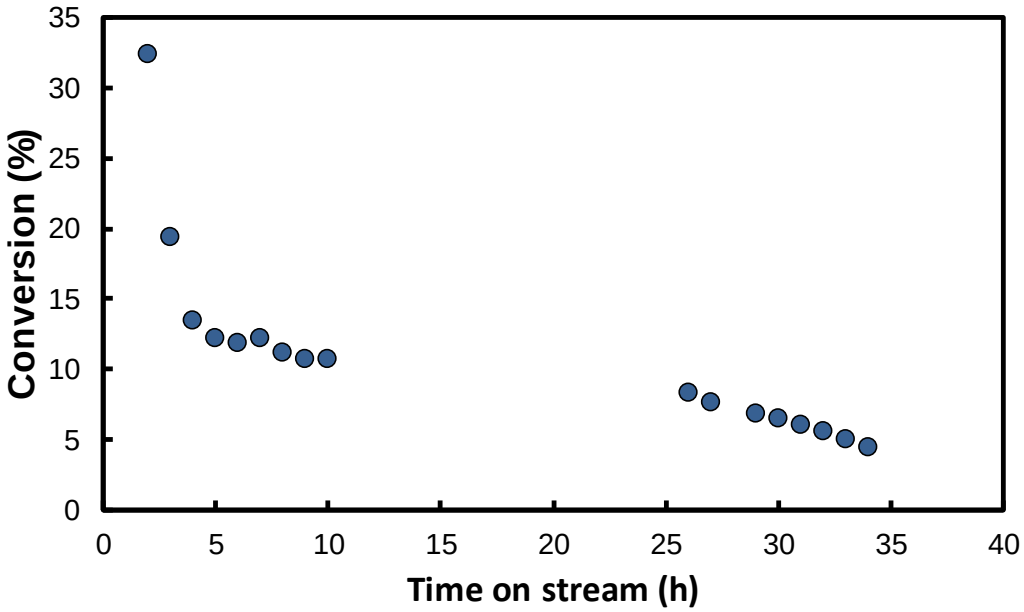

Figure S 3: Conversion profile as function of time on stream for Pd/Mg(Al)(Pd)O_x after cycled reduction at 823K.

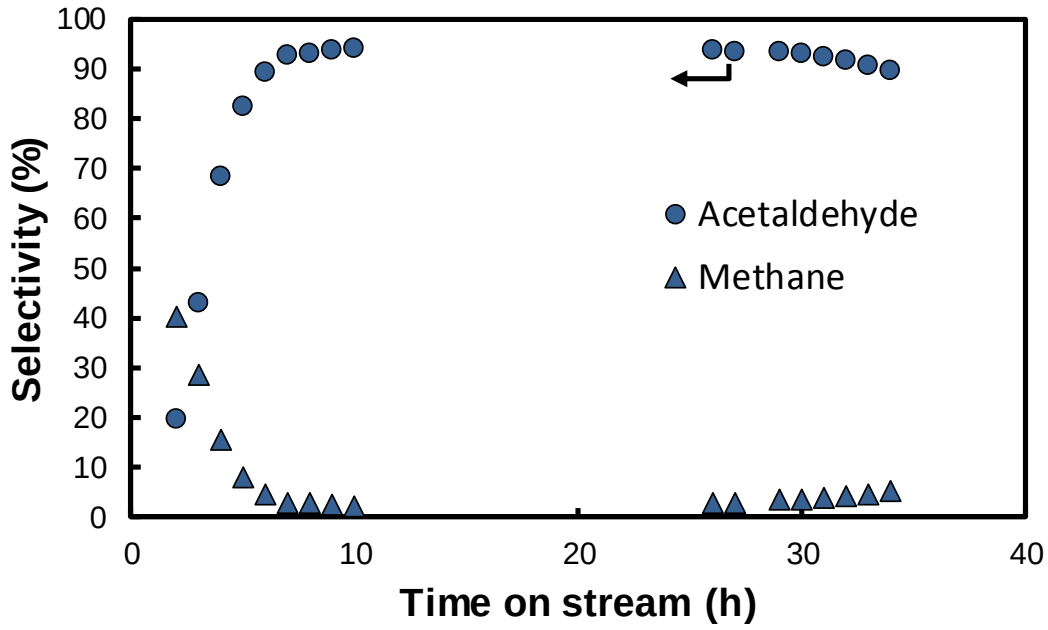

Figure S 4: Selectivity profile of acetaldehyde (●), methane (▲) as function of time on stream for Pd/Mg(Al)(Pd)O_x after cycled reduction at 823K.

The strong deactivation of this catalyst in the first hours could be related to coking of the active sites. A cokes production of 3.46 mol g^{-1}_{cat} is observed as compared to only 0.097 mol g^{-1}_{cat} for the PdZn/Mg(Al)(Pd)(Zn)O_x. This of course also affects the acetaldehyde selectivity.

Appendix B:

Kinetic model

1. Kinetic rate expressions

$$\frac{\partial F_{EtOH}}{\partial W} = -k_{DH,2,+}\theta_{EtOH,DH}\theta_{*,DH}z_{DH}C_{tot,DH} + k_{DH,2,-}\theta_{EtO,DH}\theta_{H,DH}z_{DH}C_{tot,DH} - k_{DC,2,+}\theta_{EtOH,DH}^{a}\theta_{*,DC}^{b}z_{DC}C_{tot,DC} + k_{DC,2,-}\theta_{AcH,DH}^{c}\theta_{H,DH}^{d}z_{DC}C_{tot,DC}$$

Equation 1

$$\frac{\partial F_{AcH}}{\partial W} = k_{DH,3,+}\theta_{EtO,DH}\theta_{*,DH}z_{DH}C_{tot,DH} - k_{DH,3,-}\theta_{AcH,DH}\theta_{H,DH}z_{DH}C_{tot,DH} - k_{DH,4,+}\theta_{AcH,DH}\theta_{*,DH}z_{DH}C_{tot,DH} + k_{DC,2,+}\theta_{EtOH,DC}^{a}\theta_{*,DC}^{b}z_{DC}C_{tot,DC} + k_{DC,2,-}\theta_{AcH,DC}^{c}\theta_{H,DC}^{d}z_{DC}C_{tot,DC} - k_{DC,3,+}\theta_{AcH,DC}^{e}\theta_{*,DC}^{f}z_{DC}C_{tot_{DC}} + k_{DC,3,-}\theta_{CH_4,DC}^{g}\theta_{CO,DC}^{h}z_{DC}C_{tot,DC}$$

Equation 2

$$\frac{\partial F_{EtAc}}{\partial W} = k_{DH,5,+}\theta_{Ac,DH}\theta_{EtO,DH}z_{DH}C_{tot,DH} - k_{DH,5,-}\theta_{EtAc,DH}\theta_{*,DH}z_{DH}C_{tot,DH}$$

Equation 3

$$\frac{\partial F_{H_2}}{\partial W} = \frac{1}{2}\left(k_{DH,2,+}\theta_{EtOH,DH}\theta_{*,DH}z_{DH}C_{tot,DH} - k_{DH,2,-}\theta_{EtO,DH}\theta_{H,DH}z_{DH}C_{tot,DH} + k_{DH,3,+}\theta_{EtO,DH}\theta_{*,DH}z_{DH}C_{tot,DH} - k_{DH,3,-}\theta_{AcH,DH}\theta_{H,DH}z_{DH}C_{tot,DH} + k_{DH,4,+}\theta_{AcH,DH}\theta_{*,DH}z_{DH}C_{tot,DH} - k_{DH,4,-}\theta_{Ac,DH}\theta_{H,DH}z_{DH}C_{tot,DH}\right) + k_{DC,2,+}\theta_{EtOH,DC}^{a}\theta_{*,DC}^{b}z_{DC}C_{tot,DC} + k_{DC,2,-}\theta_{AcH,DC}^{c}\theta_{H,DC}^{d}z_{DC}C_{tot,DC}$$

Equation 4

$$\frac{\partial F_{CH_4}}{\partial W} = k_{DC,3,+}\theta_{AcH,DC}^{e}\theta_{*,DC}^{f}z_{DC}C_{tot_{DC}} - k_{DC,3,-}\theta_{CH_4,C}^{g}\theta_{CO,DC}^{h}z_{DC}C_{tot,DC}$$ **Equation 5**

$$\frac{\partial F_{CO}}{\partial W} = k_{DC,3,+}\theta_{AcH,DC}^{e}\theta_{*,DC}^{f}z_{DC}C_{tot_{DC}} - k_{DC,3,-}\theta_{CH_4}^{g}\theta_{CO}^{h}z_{DC}C_{tot,DC}$$ **Equation 6**

$$\begin{aligned}\frac{\partial \theta_{EtO}}{\partial W} = {} & k_{DH,2,+}\theta_{EtOH,DH}\theta_{*,DH}z_{DH}C_{tot,DH} - k_{DH,2,-}\theta_{EtO,DH}\theta_{H,DH}z_{DH}C_{tot,DH} \\ & - k_{DH,3,+}\theta_{EtO,DH}\theta_{*,DH}z_{DH}C_{tot,DH} \\ & + k_{DH,3,-}\theta_{AcH,DH}\theta_{H,DH}z_{DH}C_{tot,DH} \\ & - k_{DH,5,+}\theta_{EtO,DH}\theta_{Ac,DH}z_{DH}C_{tot,DH} \\ & + k_{DH,5,-}\theta_{EtAc,DH}\theta_{*,DH}z_{DH}C_{tot,DH}\end{aligned}$$ **Equation 7**

$$\begin{aligned}\frac{\partial \theta_{Ac}}{\partial W} = {} & k_{DH,4,+}\theta_{AcH,DH}\theta_{*,DH}z_{DH}C_{tot,DH} - k_{DH,4,-}\theta_{Ac,DH}\theta_{H,DH}z_{DH}C_{tot,DH} \\ & - k_{DH,5,+}\theta_{EtO,DH}\theta_{Ac,DH}z_{DH}C_{tot,DH} \\ & + k_{DH,5,-}\theta_{EtAc,DH}\theta_{*,DH}z_{DH}C_{tot,DH}\end{aligned}$$ **Equation 8**

$$\theta_{*,DH} = \frac{1 - \theta_{EtO,DH} - \theta_{Ac,DH}}{1 + K_{EtOH}p_{EtOH} + K_{AcH}p_{AcH} + K_{EtAc}p_{EtAc} + \sqrt{K_{H_2}p_{H_2}}}$$ **Equation 9**

$$\theta_{*,DC} = \frac{1}{1 + K_{EtOH}p_{EtOH} + K_{AcH}p_{AcH} + K_{CH_4}p_{CH_4} + K_{CO}p_{CO} + \sqrt{K_{H_2}p_{H_2}}}$$ **Equation 10**

2. *Analytical determination of initial intermediate concentration*

The initial concentration of the ethoxyl species can, a priori, be calculated from a set of algebraic equations. Firstly, the sum of the surface fractions of all adsorbed species and free sites should equal one at all time.

$$1 = \theta_{EtOH,DH} + \theta_{EtO,DH} + \theta_{AcH,DH} + \theta_{Ac,DH} + \theta_{EtAc,DH} + \theta_{H,DH} + \theta_{*,DH}$$ **Equation 11**

With:

θ	molar fraction (-)
EtOH	Ethanol
EtO	Ethoxyl
AcH	Acetaldehyde
Ac	Acetyl
EtAc	Ethyl acetate
H	Hydrogen atom
*	Free sites

Taking into account that all adsorption steps of the gas phase species are considered in quasi equilibrium, the above site balance is transformed into:

$$\mathbf{1} = \left(\boldsymbol{K_{EtOH}p_{EtOH}} + \boldsymbol{K_{AcH}p_{AcH}} + \boldsymbol{K_{EtAc}p_{EtAc}} + \sqrt{\boldsymbol{K_{H_2}p_{H_2}}} + \mathbf{1}\right)\boldsymbol{\theta_{*,DH}} + \boldsymbol{\theta_{EtO,DH}} + \boldsymbol{\theta_{Ac,DH}} \quad \textbf{Equation 12}$$

With:

K	Adsorption equilibrium coefficient
p	Pressure
H_2	Hydrogen gas

Initially, the partial pressures of acetaldehyde (AcH), ethylacetate (EtAc) and hydrogen (H_2) equal zero and also the fraction of acetyl species (Ac) is zero. This reduces the equation further.

$$\boldsymbol{\theta_{*,DH}} = \frac{\mathbf{1} - \boldsymbol{\theta_{EtO,DH}}}{\mathbf{1} + \boldsymbol{K_{EtOH}p_{EtOH}}} \quad \textbf{Equation 13}$$

Furthermore, the formation rate of the intermediate ethoxyl species is described as follows.

$$\frac{d\theta_{EtO,DH}}{dW} = k_{DH,2,+}\theta_{EtOH,DH}\theta_{*,DH}z_{DH}C_{tot,DH} - k_{DH,2,-}\theta_{EtO,DH}\theta_{H,DH}z_{DH}C_{tot,DH} - k_{DH,3,+}\theta_{EtO,DH}\theta_{*,DH}z_{DH}C_{tot,DH} + k_{DH,3,-}\theta_{AcH,DH}\theta_{H,DH}z_{DH}C_{tot,DH} - k_{DH,5,+}\theta_{EtO,DH}\theta_{Ac,DH}z_{DH}C_{tot,DH} + k_{DH,5,-}\theta_{EtAc,DH}\theta_{*,DH}z_{DH}C_{tot,DH}$$ **Equation 14**

With:

W catalyst mass (kg_{cat})

k rate coefficient (s^{-1})

z_{DH} number of nearest neighbors

$C_{tot,DH}$ number of active dehydrogenation sites ($mol\ kg_{cat}^{-1}$)

Taking into account that only the ethanol and ethoxyl fraction are different from zero and that, based on the pseudo-steady state approximation, the formation rate of intermediates should be approximately equal to zero, Equation 14 can be rewritten as:

$$0 = k_{DH,2,+}\theta_{EtOH,DH}\theta_{*,DH} - k_{DH,3,+}\theta_{EtO,DH}\theta_{*,DH}$$ **Equation 15**

Combining Equation 13 and Equation 15, yields an analytical expression for the initial ethoxyl and free dehydrogenation site fraction, see Equation 16 and Equation 17.

$$\theta_{EtO,DH} = \frac{k_{DH,2,+}K_{EtOH}p_{EtOH}}{k_{DH,3,+}(1 + K_{EtOH}p_{EtOH}) + k_{DH,2,+}K_{EtOH}p_{EtOH}}$$ **Equation 16**

$$\theta_{*,DH} = \frac{1}{1 + K_{EtOH}p_{EtOH} + \frac{k_{DH,2,+}K_{EtOH}p_{EtOH}}{k_{DH,3,+}}}$$ **Equation 17**

Appendix C:

List of publications

1. A1 publications

1.1. Published

PdZn nanoparticle catalyst formation for ethanol dehydrogenation: active metal impregnation vs incorporation (Chapter 3)

De Waele, J.; Galvita, V.V.; Poelman, H.; Detavernier, C.; Thybaut, J.W.
Applied Catalysis A General
555, 12-19, 2018
SCI-IF: 3.942 (2014), ranking: 22/221, quartile: Q1
doi: 10.1016/j.apcata.2018.02.005

Formation and stability of an active PdZn nanoparticle catalyst on a hydrotalcite-based support for ethanol dehydrogenation (Chapter 4)

De Waele, J.; Galvita, V.V.; Poelman, H.; Detavernier, C.; Thybaut, J.W.
Catalysis Science & Technology
7 (17), 3715-3727, 2017
SCI-IF: 5.287 (2015), ranking: 28/144, quartile: Q1
doi: 10.1039/C7CY01105A

1.2. To be submitted

Effect of water on the ethanol dehydrogenation performance of PdZn/Mg(Al)(Pd)(Zn)O_x (Chapter 5)

To be submitted

Promotion of Cu catalysts with Ni via NiCu formation for (bio-)ethanol dehydrogenation (Chapter 6)

To be submitted

2. C3 contributions

2.1. *Oral presentations*

PdZn/Mg(Al)(Pd)(Zn)O_x for ethanol conversion: reconstruction of the active phase upon a water containing feed

De Waele, J.; Galvita, V.V.; Poelman, H.; Thybaut, J.W.
13th European Congress on Catalysis (EUROPACAT 2017)
Florence, Italy, August 27-31, 2017
Book of Abstracts, 168 pages, 17

2.2. *Poster presentations*

Ni-Cu/MgAlO_x catalysts for ethanol dehydrogenation

Gabrovska, M.; Nikolova, D.; Damyanova, S.; De Waele, J.; Thybaut, J.W.; Galvita, V.V.
15th National Conference on Catalysis (NCC)
Sofia, Bulgaria, November 30, 2017

PdZn active metal impregnation vs. incorporation for ethanol dehydrogenation

De Waele, J.; Poelman, H.; Galvita, V.V.; Thybaut, J.W.
17th Netherlands' Catalysis and Chemistry Conference (NCCC XVII)
Noordwijkerhout, Netherlands, March 7-9, 2016
Book of Abstracts, 1 page, 215

PdZn nanoparticle formation for ethanol dehydrogenation: impregnation vs. co-precipitation

De Waele, J.; Poelman, H.; Galvita, V.V.; Thybaut, J.W.
IAP Annual Meeting 2016
Liège, Belgium, September 12, 2016

Ethanol dehydrogenation on PdZn/Mg(Al)Ox: the effect of incorporation and impregnation on the catalyst behavior

De Waele, J.; Poelman, H.; Galvita, V.V.; Thybaut, J.W.
IAP Annual Meeting 2015-1
Hasselt, Belgium, September 11, 2015